New Analytical Techniques for the Investigation of Alpha Clustering in Nuclei

A Study of ^{18}F and ^{44,48,52}Ti using Resonant Scattering

Sam Bailey

UNIVERSITY OF BIRMINGHAM

A thesis submitted to
the University of Birmingham
for the degree of
Doctor of Philosophy

Nuclear Physics Group
School of Physics and Astronomy
College of Engineering and Physical Sciences
University of Birmingham
September 22, 2016

Abstract

This thesis presents the analysis of two experiments, one measuring the ^{4}He(^{14}N,α) and ^{4}He(^{14}N,d)^{16}O reactions and a second measuring the ^{4}He(^{40}Ca,α), ^{4}He(^{44}Ca,α) and ^{4}He(^{48}Ca,α) reactions. These measurements were used to investigate ^{18}F and ^{44,48,52}Ti respectively. In both experiments the Thick Target Inverse Kinematics technique was used and the analysis focused on the investigation of α-clustering.

The measurements of ^{4}He(^{14}N,α) and ^{4}He(^{14}N,d)^{16}O were performed between E_x[^{18}F] = 5.5 - 16 MeV, and evaluated using a full $\boldsymbol{R}$-matrix analysis up to 9 MeV. From this nine new states in ^{18}F were extracted and the α-cluster structure of ^{18}F was explored by comparison with nuclear models.

The measurements of ^{4}He(^{40}Ca,α), ^{4}He(^{44}Ca,α) and ^{4}He(^{48}Ca,α) were made over the ranges E_x[^{44}Ti] = 9 - 17 MeV, E_x[^{48}Ti] = 13.5 - 24 MeV and E_x[^{52}Ti] = 12 - 20 MeV. The experimental data were analysed using a novel technique developed in this thesis for the identification of fragmented α-clustered states, known as the spectral signature analysis. From this analysis nine such states were identified in ^{44}Ti, in good agreement with previous work. None were identified in ^{48}Ti and three in ^{52}Ti. The implications of these results for α-clustering in the *fp*-shell are discussed.

To my parents.

Acknowledgements

Looking back on the last four years I have spent working towards my PhD, there are many people who have made this experience so very rewarding, and to whom I owe my deepest gratitude.

Firstly and most importantly I would like to thank my supervisors Tzany Kokalova-Wheldon and Martin Freer, from whom I have learned so much. Martin, who has a seemingly superhuman knowledge of all aspects of nuclear physics, and Tzany, who is both enthusiastic and patient, and who has always been available to provide advice and encouragement when I have needed it most. Their continual and unwavering guidance has been invaluable throughout my studies. Furthermore, I, think, Tzany, has, finally, (after, many, attempts), taught, me, the, proper, use, of, commas.

In addition to my formal supervisors, I have received much help from the many other members of the nuclear physics research group. Specifically, I would like to thank Carl Wheldon for repeatedly helping me with VirtualBox, and being my de facto Linux mentor, and Neil Curtis, who's understanding of the accelerators and detectors used in nuclear physics is unparalleled.

I am also grateful to the other residents of the nuclear physics PhD office: Joe, Robin, Jack, Harry, Matt, Dan, Nima and Tanya, as well as those we adopted from other groups: Chris, Andy, Rob, Lyndsie and many others. Whether it was playing elaborate deception based games, building my robotic replacement from a desk lamp (Mecha Sam - RIP), or discussing at length the similarities between the words nuclear and unclear, you have made the past four years unforgettable.

I would also like to thank the members, past and present, of Birmingham University Korfball Club, with whom I spent a considerable amount of my free time. It is with this club that I have had some of the most enjoyable experiences of my life so far, whether that was competing in tournaments as far away as Edinburgh and Eindhoven, sampling the finest night life Birmingham has to offer (the Guild and Snobs) or attending weekly training sessions at the Munrow Sports Centre at 7am on a Wednesday morning, it has all been excellent.

There are countless others who have contributed to maintaining my sanity throughout the past four years. Special mention goes to my housemates at Kenilworth court, who have made living in Birmingham an incredibly easy and enjoyable experience, and introduced me to the wonders of Geordie

Shore, the Great British Bake Off and Ex on the Beach. I would also like to thank Teo and Dotto Wheldon, who's unexpected appearances in the office and fascination with Nerf guns never failed to keep me on my toes.

Finally I would like to thank my parents, who have been excellent role models for me throughout my life, and have made me who I am today. I am certain that without their guidance and support I would not have made it to this point. I would also like to thank my brother, Harry, for kindly allowing me to take all of our Friends DVD's to University (and keep them for the entire 8 years, very generous), and my girlfriend, Rachel, who for the last couple of years has made everything I do worthwhile. Also she introduced me to gin, which I feel positively about. For these reasons, and many more, I am extremely grateful.

Research Outcomes

The work presented in this thesis has led to the following outcomes:

Peer-reviewed Publications

- Bailey, S. *et al.* Energy levels of ^{18}F from the ^{14}N+α resonant reaction. *Phys. Rev. C* **90,** 024302 (2 Aug. 2014)
- Bailey, S. *et al.* Alpha clustering in ^{18}F. *J. Phys. Conf. Ser.* **569,** 012053 (2014)
- Bailey, S. *et al.* Alpha clustering in Ti isotopes: ^{40,44,48}Ca + α resonant scattering. *EPJ Web of Conferences* **113,** 08002 (2016)

Conference Presentations

- 'Investigating the Structure of ^{18}F through the Study of the Resonant Reaction ^{14}N + α'. (Oral presentation) Institute of Physics Annual Nuclear Physics Conference, York, UK. April 2013.
- 'Investigating the Structure of ^{18}F'. (Oral presentation) STFC Nuclear Physics Summer School, Bristol, UK. Sept 2013.
- 'Investigating the Structure of ^{18}F'. (Oral presentation) Institute of Physics Annual Nuclear Physics Conference, Croydon, UK. April 2014.
- 'Investigating the Structure of ^{18}F using the ^{14}N + α Resonant Reaction'. (Poster presentation) State of the Art in Nuclear Cluster Physics, Yokohama, Japan. May 2014.
- 'Alpha Clustering in *fp*-shell Nuclei: the ^{40,44,48}Ca + α Resonant Reaction'. (Oral presentation) Institute of Physics Particle, Astroparticle, and Nuclear Physics Conference, Manchester, UK. March 2015.

- 'Alpha Clustering in Ti isotopes: the ^{40,44,48}Ca + α Resonant Reaction'. (Poster presentation) Few Body Physics Conference, Chicago, USA. May 2015.
- 'Alpha Clustering in Ti isotopes: the ^{40,44,48}Ca + α Resonant Reaction'. (Poster presentation) Euroschool on Exotic Beams, Dubrovnik, Croatia. Sept 2015.
- 'Extracting the Spectral Signature of Alpha Clustering in Medium Mass Nuclei'. (Oral presentation) Institute of Physics Annual Nuclear Physics Conference, Liverpool, UK. April 2016.

Contents

List of Figures

List of Tables

Acronyms

ACM Alpha Cluster Model. 9, 10, 13, 14

AMD Antisymmetrized Molecular Dynamics. 9, 13–15

AUC Area Under the Curve. 126

CWT Continuous Wavelet Transform. 91, 101, 103–106, 108, 111, 113, 116–120, 122, 126, 139–141, 144

DT Decision Tree. 121, 122, 124, 126

LDM Liquid Drop Model. 1, 3, 9

RF Random Forest. 122–127, 129, 131–134, 141, 144

ROC Receiver Operating Characteristic. 123, 125, 126

TTIK Thick Target Inverse Kinematics. 17, 18, 21, 22, 25, 27, 28, 31, 32, 34, 35, 51, 58, 66, 74, 88, 91, 92, 99, 116, 141, 143

Chapter 1

Introduction

1.1 Overview of Nuclear Structure and Clustering

The atomic nucleus resides at the centre of the atom, with a size of the order of femtometers (10^{-15} m), and is constructed of Z protons and N neutrons. A nucleus is usually defined in terms of Z, which is often known as the atomic number of the nucleus, and A, which is the sum of Z and N and is known as the atomic mass number. The protons and neutrons interact via a short range interaction known as the residual strong force, which consists of a short range repulsive component and a slightly longer range attractive component [4, 5]. This is a very complex interaction, which depends not only on the distance between the nucleons but also on their spins and isospins, and also includes higher order contributions such as three-body terms. The combination of this rather complex interaction and the quantum many body nature of the nucleus leads to the formation of a broad range of intricate and exotic structures within the nucleus. The field of nuclear structure physics is concerned with developing a clear understanding of this variety of structures, looking in particular at the development of different structures as a function of Z and A. The diverse behaviour of different nuclei has so far prohibited the development of a universally successful theoretical model of nuclear structure and instead a range of different models exist, each based on certain simplifying assumptions, and successful only in a subset of cases. Consequently, the field relies heavily on experimental data to constrain and inform theoretical advances.

One of the earliest successful nuclear models is the Liquid Drop Model(LDM), originally developed in 1935 by Weizsäcker [6] and in 1936 by Bethe & Bacher [7]. In this very simplistic picture, nuclei are modelled as a charged liquid sphere, rather than as individual protons and neutrons. This model was very successful in predicting the overall behaviour of the binding energies of the most stable nuclei as a function of A and Z, and has also been used as the basis for more sophisticated collective models of

nuclear structure, for example to predict the fission of heavy nuclei [8, 9].

The first truly quantum mechanical description of the nucleus was developed in 1949 and is known as the nuclear shell model, referred to henceforth as the shell model. This model was originally formulated by Mayer [10] and Haxel *et al.* [11] as the Independent Particle Model (IPM), and has since been extensively developed, and refined, producing the modern nuclear shell model. An extensive overview of the latter is given in Ref. [12]. The fundamental underlying assumption of the shell model is that the forces felt between the individual nucleons average out, allowing each nucleon to be treated independently of all others, moving in a mean-field potential which reflects the average interaction with all of the other nucleons.

The shell model takes its name from the fact that it predicts sets of energy levels, known as shells, with each shell separated from neighbouring shells by a large energy gap, shown on the left hand side of Figure 1.1. The nucleons fill these energy levels according to the Pauli exclusion principle [13]. Nuclei which have the number of protons or neutrons required to fill an entire shell are known as closed-shell nuclei or magic nuclei (in the case that both the proton and neutron shells are filled they are known as doubly-magic). Enhancements in the nuclear binding energy for these predicted magic nuclei have been observed experimentally, shown in Figure 1.1, suggesting that the independent particle assumption upon which the shell model is based is a reasonable one.

The shell model has been used extensively to predict the properties of the ground and excited states of a variety of nuclei, over the entire range of A and Z, with significant success [16–18]. It does, however, fail in certain situations, specifically where nucleons exhibit collective behaviours, whereby many or all of the nucleons in the nucleus become correlated, effectively invalidating the underlying independent particle assumption of the shell model. One specific example of a phenomenon that the shell model struggles to reproduce is nuclear clustering, and this is discussed in detail in the review papers by Freer & Merchant [19] and von Oertzen *et al.* [20].

Nuclear clustering, abbreviated henceforth as clustering, refers to the concept of nucleons forming sub-structures within the nucleus, known as clusters. This model was originally formulated as the Alpha Particle Model by Hafstad & Teller [21], where it was proposed that nuclei may be composed of configurations of α-particles. This was based, in part, upon an analysis of the binding energies of light α-conjugate nuclei[a], which were shown to vary approximately linearly with the expected number of α-α bonds, shown on the left hand side of Figure 1.2. The Alpha Particle Model was further justified by observations of the spontaneous α-decay of heavy nuclei, which indicated that α-particles may exist inside the nucleus for some time before being emitted.

The Alpha Particle Model has found much success when applied to light α-conjugate nuclei, par-

[a]Alpha-conjugate nuclei are nuclei with $A = 4N_\alpha$ and $Z = 2N_\alpha$ which can therefore be split into N_α α-particles

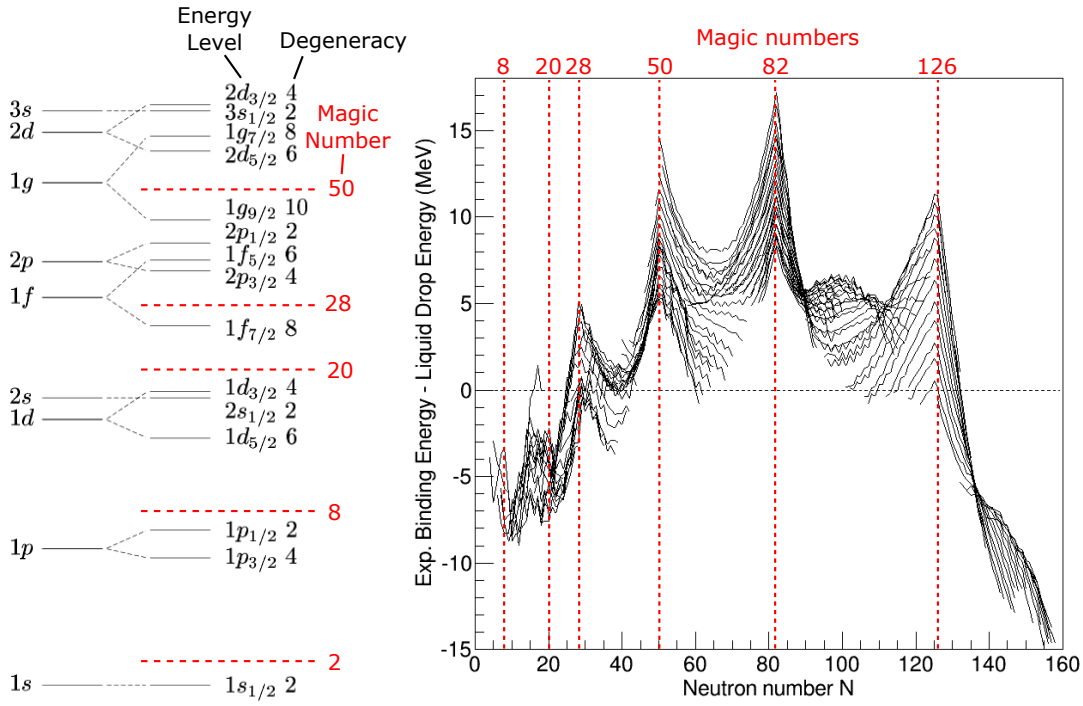

Figure 1.1: The single particle energy levels, degeneracies and magic numbers produced by the nuclear shell model (left), and a comparison between the magic numbers and the difference between the measured nuclear binding energies and those predicted by the LDM (right). This figure is adapted from Refs. [14, 15].

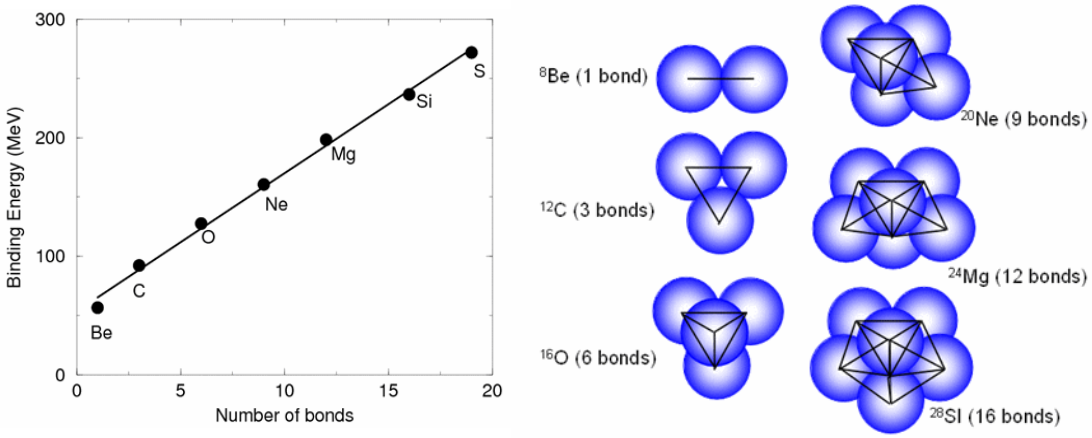

Figure 1.2: The binding energies of light α-conjugate nuclei as a function of the predicted number of α-α bonds (left), based on the α-particle configurations shown (right). This figure is adapted from Ref. [22] and based on the work by Hafstad & Teller [21].

ticularly ^{8}Be and ^{12}C. The α-α structure of ^{8}Be was first suggested based on the instability of its ground state to decay via breakup into two α-particles [23]. More recently, *ab initio* calculations[b] of ^{8}Be show a clear α-α structure in its ground state [24], and its excited states can be described well as the dynamics of two interacting α-particles [25].

Following this, it is natural to suggest the existence of the α-α-α structure in ^{12}C. This structure has, however, proved a significant challenge to understand. It was originally predicted by Hoyle [26], who argued that such a state ought to exist close to the 3α-decay threshold, based on the enhancement that such a state would provide to the astrophysical reaction rate calculations of the 3α-process in stars. After much experimental work, this state (known as the Hoyle state) was identified experimentally [27–29] and the experimental results are in good agreement with the results of *ab initio* calculations [30, 31]. More recently a significant portion of the low-lying energy levels in ^{12}C have been shown to be reproduced by excitations of an α-α-α structure, where the clusters are arranged in an equilateral triangle configuration [32], as opposed to a linear chain or 'bent arm' configuration as proposed in previous studies [33].

While there has been work done to investigate the 4-α structure in ^{16}O [34], it has yet to be conclusively measured experimentally. Heavier configurations of α-particles have also been predicted [19, 35], but have been similarly difficult to observe.

Since its initial inception as the Alpha Particle Model, the cluster model has been generalised beyond simple configurations of α-clusters. The observation of the Hoyle state close to the 3α-decay threshold suggests that a variety of exotic cluster structures may emerge in nuclei as the excitation energy increases, close to the energy required to separate the clusters, E_{sep}. This separation energy is calculated as the difference in binding energies between the ground state configuration and the constituent clusters, written explicitly as

$$E_{\text{sep}} = \text{BE}(A, Z) - \sum_i \text{BE}(A_i, Z_i) \tag{1.1}$$

where i denotes the clusters, $\text{BE}(A, Z)$ dictates the binding energy of a given nucleus, and $A = \sum_i A_i$ and $Z = \sum_i Z_i$. This modern approach to clustering is summarised well for light α-conjugate nuclei by Ikeda in the famous Ikeda diagram [36], shown in Figure 1.3.

This suggestion that nuclei other than the α-particle may form within other nuclei as clusters leads to the question of which nuclei are most likely to do so? Good cluster candidates are often defined as having a high binding energy per nucleon, as well as a high first excited state [19]. Together these attributes allow the cluster to easily form and exist unperturbed for a significant period of time within

[b] *Ab initio* calculations are those that solve the entire A-body system of interacting nucleons rigorously, and therefore they make no *a priori* assumptions about the structure of the nucleus.

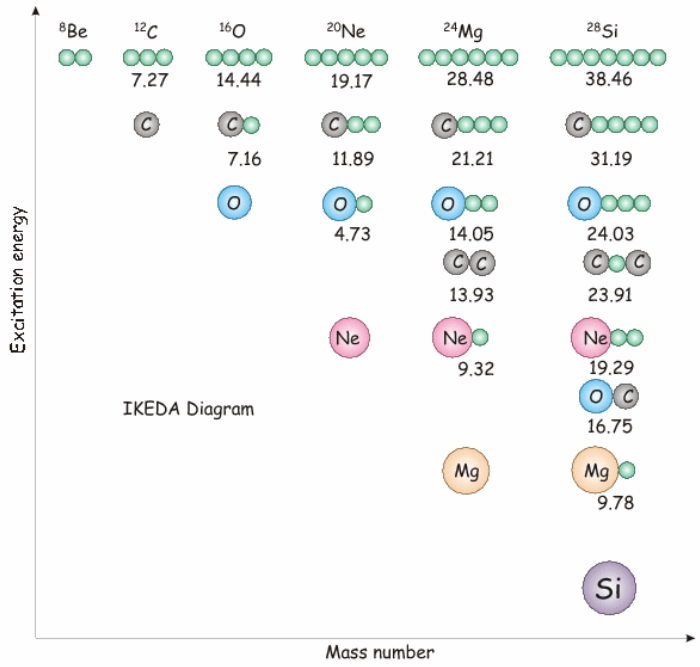

Figure 1.3: The Ikeda diagram, displaying the possible cluster configurations of light α-conjugate nuclei vs the excitation energy at which they ought to manifest. Alpha-particles are represented by green circles and E_{sep} is given in MeV underneath each structure. Based on the work by Ikeda [36], this figure is reprinted from Ref. [20].

the nucleus. These properties are compared in Figure 1.4 for all light nuclei up to $A = 20$. It is clear from this figure that the α-particle is an outstanding cluster candidate, while ^{12}C, ^{14}C, ^{14}O, ^{15}N and ^{16}O are also likely to form as clusters inside nuclei.

The most commonly observed cluster structure is the α-core cluster structure, which refers to a nucleus which clusters into two bodies: a large core and an α-particle. It is usually energetically favourable for the nucleus to form an α-core cluster structure as opposed to clustering into a system of many α-particles, leading to α-core clustering being observed in a variety of nuclei, and especially prominently in light α-conjugate nuclei.

The most famous and well understood α-core cluster structure is the α-^{16}O structure observed in ^{20}Ne. This structure has been observed both as a component of the ground state of ^{20}Ne [37] and in excited states [38], and this is understood by comparison with theoretical models [39]. This structure is especially dominant because both the α-particle and ^{16}O are doubly-magic nuclei. This makes them both good cluster candidates, and introduces a large energy gap in the shell-model picture between the nucleons in the core and those in the α-particle. This energy separation has the effect of disentangling the dynamics of the cluster and the core. In this case the nucleons which form the ^{16}O core fill up the *s* and *p*-shells, and the additional two protons and two neutrons are placed in the *sd*-shell, forming the α-particle.

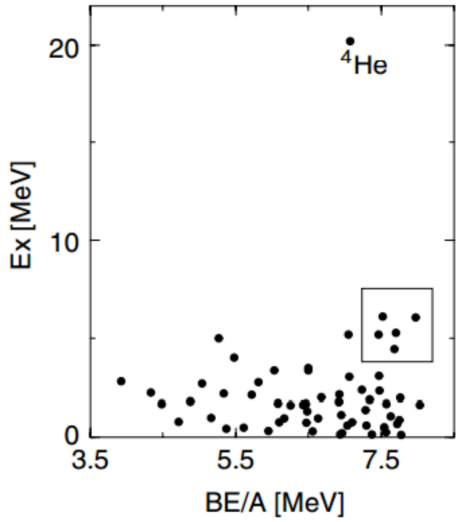

Figure 1.4: The energy of the first excited state as a function of binding energy per nucleon for all nuclei up to $A = 20$. Helium-4 is annotated, and the box indicates ^{12}C, ^{14}C, ^{14}O, ^{15}N and ^{16}O. This figure is reprinted from Ref. [19].

This tendency for the α-core cluster structure to form following the addition of two protons and two neutrons to a doubly-magic nucleus has been further confirmed by investigating the α-^{40}Ca structure in ^{44}Ti, discussed in this thesis in Section 5.1.1, and the α-^{208}Pb structure in ^{212}Po [40], and by theoretical works such as the successful description of ^{20}Ne, ^{44}Ti, ^{60}Zn and ^{212}Po using an α-core model of clustering by Wang *et al.* [41].

The discussion up to this point has focussed on clustering in α-conjugate nuclei, however, the behaviour of clustering in nuclei that deviate from α-conjugation is an interesting topic, and in particular the addition of neutrons has been the subject of great research interest.

It is often the case that additional neutrons act as valence particles on top of the underlying cluster structure, providing additional binding to the clusters in a similar way to that observed for valence electrons in atomic molecules. This behaviour is clearly exhibited by neutron rich Beryllium isotopes, with the persistence of the α-xn-α structure into isotopes as heavy as ^{12}Be [25, 42–44]. The additional binding provided by the valence neutrons is demonstrated by comparing ^{8}Be, which is unstable to break-up into two α-particles, with ^{9}Be, where the α-n-α structure is stable in the ground state [23]. Furthermore, Figure 1.5 shows the predicted proton and neutron density distributions for the ground states of a range of Beryllium isotopes [39], which clearly demonstrate the persistence of the α-α structure in the proton densities up to ^{14}Be.

Further examples of valence neutrons have also been observed in ^{13}C, which exhibits the α-α-n-α structure[c] [45], ^{18}O which exhibits the α-$2n$-^{12}C [46], and ^{21,22}Ne, which exhibit the α-xn-^{16}O structure

[c]It should be noted that the notation used here to refer to specific cluster structures has no relation to the geometrical configuration of the clusters and valence neutrons. It simply serves to list the constituent clusters.

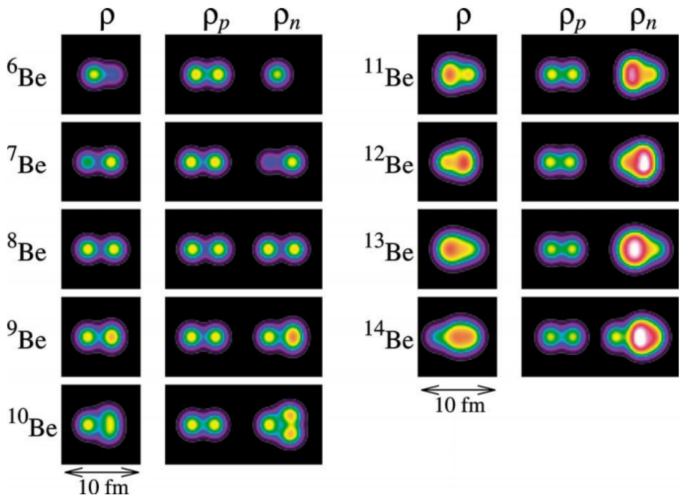

Figure 1.5: Density distributions of protons (ρ_p) and neutrons (ρ_n) and the total density distribution (ρ) calculated using the Antisymmetrized Molecular Dynamics (AMD) model for $^{6\text{-}14}$Be. The α-α structure is observed clearly in all neutron rich cases. AMD is discussed in Section 2.1.3. This figure is reprinted from Ref. [39].

[47, 48].

1.2 Motivation for the Present Work

Reported in this thesis are the results of two separate experiments, one investigating the α-^{14}N structure in ^{18}F and another investigating the α-^{40,44,48}Ca structures in ^{44,48,52}Ti.

While the role that valence neutrons play in light nuclear molecules is relatively well understood, the degree to which other particles act as valence particles on an underlying cluster structure is not clear. It is this aspect of nuclear clustering which cultivates interest in ^{18}F. In this work the α-^{14}N cluster structure is investigated and compared with the similar α-^{16}O cluster structure in ^{20}Ne. It is reasonable to think of the cluster structure in ^{18}F as an α-^{16}O cluster structure plus one proton hole and one neutron hole, and it therefore presents an opportunity to investigate the interplay between nucleon holes and cluster structures.

Much research has been carried out to investigate and understand clustering in light nuclei, however the work on medium and heavy mass nuclei is limited. The question of the extent to which α-clustering continues beyond light nuclei is addressed here by investigating ^{44,48,52}Ti. Titanium isotopes present an excellent opportunity to understand the nature of α-clustering in the *fp*-shell, and a comparison between the α-cluster structure of these nuclei and Ne isotopes, which represent the equivalent structure in the *sd*-shell, may provide some insight into how clustering develops in heavier systems.

While a simple comparison with ^{20}Ne suggests that one ought to expect the doubly-magic ^{40}Ca

core to introduce a dominant cluster component to the structure of ^{44}Ti and neutron rich Ti isotopes, this structure will be in competition with mean-field type structures, which are observed to dominate in the medium and heavy mass region [49]. This suggests that Ti isotopes may present an excellent opportunity to observe the interplay between α-clustering and the nuclear mean-field.

Previous work has often focused on attempting to investigate the α-^{40}Ca structure in ^{44}Ti, much of which is discussed in Section 5.1.1, however in this thesis ^{48,52}Ti are compared with ^{44}Ti experimentally, in an effort to identify whether the cluster structure persists following the addition of valence neutrons, as it does in the *sd*-shell. Furthermore, the next shell-closure exists in ^{48}Ca, and so investigating Ti isotopes in the mass range A = 44 - 52 allows the evolution of the α-cluster structure and its relationship with the mean-field contribution to be investigated throughout the entire *fp*-shell.

The study of Titanium isotopes required the development of a novel analytical technique, referred to in this thesis as the spectral signature analysis, which expedited the extraction of α-clustered states from the experimental measurements, previously a difficult task in heavy systems.

Chapter 2

Theoretical and Experimental Techniques in Nuclear Clustering

In this section some of the theoretical and experimental techniques used to investigate clustering in nuclei are summarised.

2.1 Theoretical Nuclear Models

There have been a plethora of theoretical models developed which attempt to describe nuclear clustering. Here some of the most influential models are summarised, specifically those that are most relevant to this work, namely the Nilsson-Strutinsky model, the Alpha Cluster Model (ACM) and Anti-symmetrized Molecular Dynamics(AMD).

2.1.1 The Nilsson-Strutinsky Model

The Nilsson-Strutinsky model is a shell-model type calculation, which predicts potential energy surfaces as a function of nuclear deformation. The potential energy surfaces are calculated using a combination of a macroscopic term, which is calculated using the LDM, and a microscopic term, which is calculated using the shell model with a deformed harmonic oscillator basis. Shell-effects often introduce secondary minima in these potential energy surfaces, from which the existence of deformed structures can be inferred.

The microscopic contribution is calculated using the Nilsson energy levels, discussed in detail in Ref. [50]. These are a set of single particle energy levels constructed by solving the Schrödinger equation in the presence of the mean field potential, $U_{\text{def}}(\vec{r})$, which is a deformed harmonic oscillator po-

tential with a surface correction and a spin-orbit correction, defined as

$$U_{\text{def}}(\vec{r}) = \frac{1}{2}m\left(\omega_x^2 x^2 + \omega_y^2 y^2 + \omega_z^2 z^2\right) + C\vec{l}\cdot\vec{s} + D\vec{l}^2 \tag{2.1}$$

where $\vec{l}$ represents the orbital angular momentum of the nucleon, $\vec{s}$ represents the spin of the nucleon, $\vec{r}$ dictates the position of the nucleon with respect to the center of the nucleus, ω_i is the harmonic oscillator frequency along axis $i = \{x, y, z\}$ and m is the mass of the nucleon. C and D are constants which dictate the strengths of the spin-orbit and surface correction terms, respectively.

The oscillator frequencies are appropriately chosen so as to produce the desired nuclear deformation, which in standard notation is defined by (ϵ, γ). These parameters allow the definition of any prolate, oblate or triaxial deformation, with the degree of axial deformation defined by ϵ, where $\epsilon = 0$ indicates no deformation, and γ defining the nature of the deformation ($\gamma = 0°$: prolate, $\gamma = 60°$: oblate, $0° < \gamma < 60°$: triaxial). In the simple case of a prolate deformation the oscillator frequencies in the x and y directions are equal, $\omega_{x,y} = \omega_x = \omega_y$, and ϵ is defined as

$$\epsilon = \frac{\omega_{x,y} - \omega_z}{\omega_0} \tag{2.2}$$

where $\omega_0 = 2\omega_{x,y} + \omega_z$, and is fixed to ensure that the nuclear volume is conserved. The Nilsson levels in the case of prolate deformations are shown in Figure 2.1. The discussion here has been restricted to quadrupole deformations ($\epsilon = \epsilon_2$), however it is possible to generalise this technique to higher order deformations, for example octupole deformations, ϵ_3.

The microscopic and macroscopic terms are combined using the Strutinsky procedure [52], which treats the microscopic term as a correction to the macroscopic energy surface. It does this by essentially comparing the levels produced by the Nilsson model with a set of uniformly spaced energy levels, allowing the effects produced by the shell gaps to be extracted.

Nilsson-Strutinsky calculations have been performed for a range of light α-conjugate nuclei by Leander & Larsson [53]. An example of a Nilsson-Strutinsky calculation for ^{24}Mg is shown in Figure 2.2, which shows multiple deformation minima and assigns them to a variety of α-cluster structures calculated using the ACM (discussed in Section 2.1.2), based on their deformation. The justification for these assignments is detailed in Ref. [54], and the argument is made that the consistency observed between the two models is a clear justification for the cluster picture of light α-conjugate nuclei.

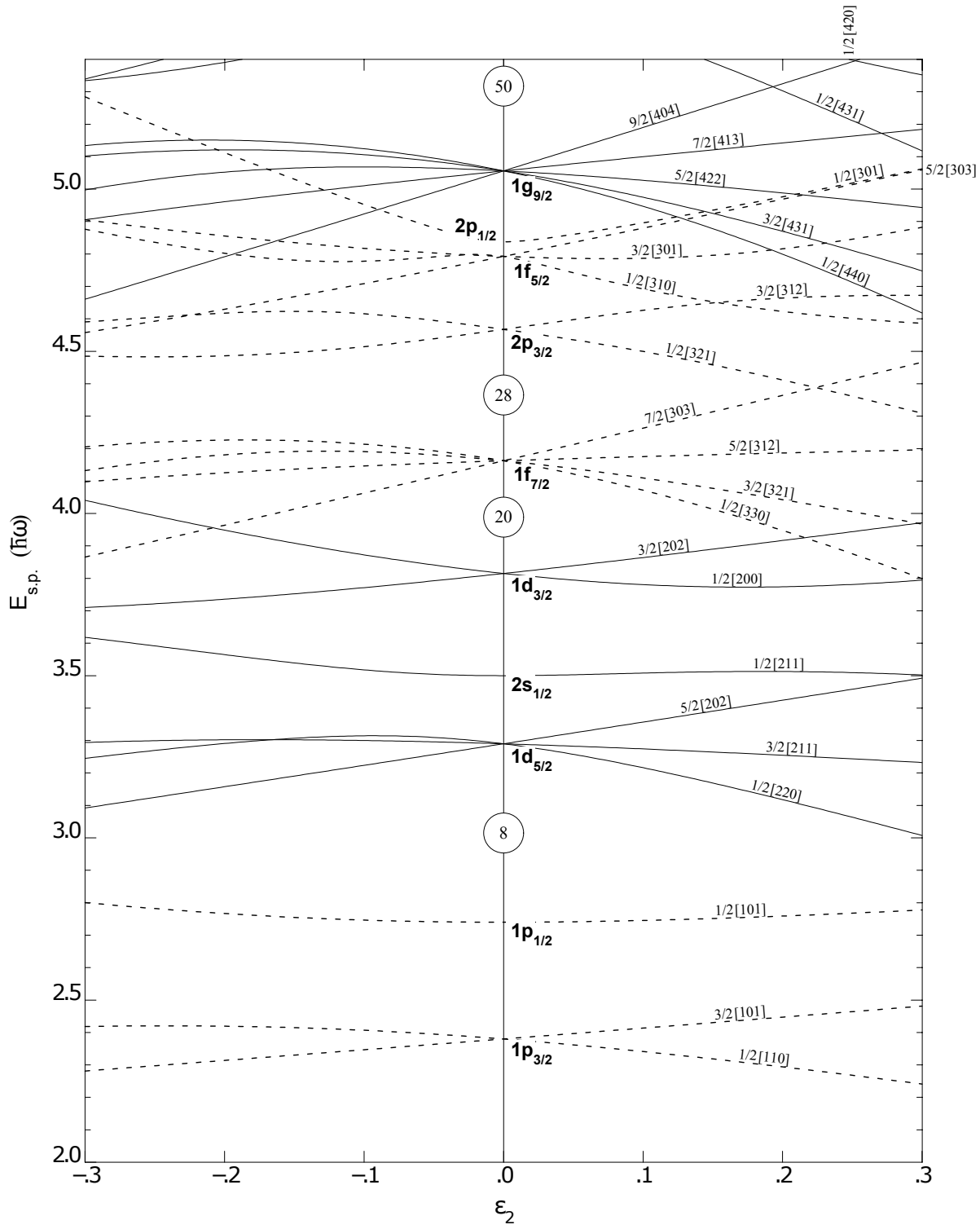

Figure 2.1: Nilsson energy levels for $\gamma = 0$, where ϵ_2 defines the quadrupole deformation, $\epsilon_2 > 0$ corresponds to prolate deformations and $\epsilon_2 < 0$ to oblate deformations. The energies are given in units of $\hbar\omega$. This figure is reprinted from Ref. [51].

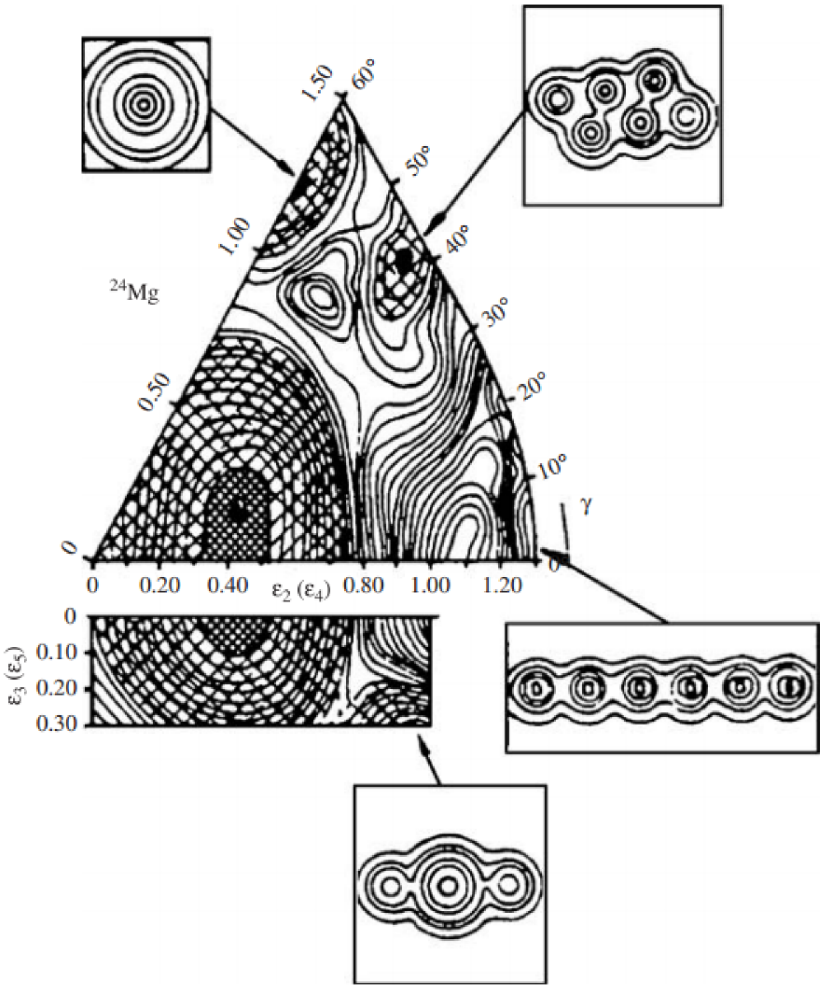

Figure 2.2: A Nilsson-Strutinsky calculation for ^{24}Mg, and the Alpha Cluster Model (ACM) configurations associated with each minimum. The triangular plot shows the potential energy surface as a function of quadrupole deformation, ϵ_2, radially and the triaxiality, γ, azimuthally. In all cases the hexadecapole deformation, ϵ_4, is varied and the minimum value is plotted. The rectangular plot shows the potential energy surface as a function of ϵ_2 in the x direction and the octupole deformation, ϵ_3, in the y direction, and at all points ϵ_4 and ϵ_5 are minimised. This figure is reprinted from Ref. [20].

2.1.2 Alpha Cluster Model (ACM)

The ACM was first proposed by Brink, and was heavily influenced by the ideas of Bloch, thus is often refered to as the Bloch-Brink model [55]. This is a semi-microscopic model which assumes protons and neutrons condense into α-particles and consequently treats the nucleus as a system of interacting α-clusters rather than independent nucleons. This assumption limits the applicability of this model to α-conjugate nuclei.

It is assumed that the α-clusters are constructed from pairs of protons and neutrons which couple to form a state with zero total angular momentum. The wavefunction for the i^{th} α-cluster, $|\phi_i(\vec{R}_i)\rangle$, is modelled in the harmonic oscillator framework as

$$\langle \vec{r}|\phi_i(\vec{R}_i)\rangle = \sqrt{\frac{1}{b^3\pi^{3/2}}}\exp\left(\frac{-(\vec{r}-\vec{R}_i)^2}{2b^2}\right) \tag{2.3}$$

where the center of the α-cluster is given by $\vec{R}_i$, and $b = (\hbar/m\omega)^{1/2}$ is a scale parameter which determines the size of all the α-clusters. The total wavefunction, $|\Phi_{\text{ACM}}\rangle$, is constructed by antisymmetrising the product of N α-cluster wavefunctions, where $N = A/4$. The antisymmetrisation is performed using the antisymmetrisation operator, $\mathcal{A}$, and produces a Slater determinant of the α-cluster wavefunctions. This is written explicitly as

$$|\Phi_{\text{ACM}}\rangle = \mathcal{A}\prod_{i=1}^{N}|\phi_i(\vec{R}_i)\rangle\,. \tag{2.4}$$

The α-α interaction is usually calculated by folding an effective nucleon-nucleon interaction with the α-particle density distributions, and $\{\vec{R}_i\}$ and b are determined variationally by minimising the total energy of the system. It is often the case that $|\Phi_{\text{ACM}}\rangle$ is treated as an intrinsic wavefunction, from which states with a specific spin and parity are projected using the techniques developed by Peierls & Yoccoz [56].

The α-cluster model was used in many early theoretical studies of α-clustering [57, 58], and an example of some of the density distributions produced using this method are shown in Figure 2.3.

2.1.3 Antisymmetrised Molecular Dynamics (AMD)

AMD is an example of an *ab initio* nuclear model. *Ab initio* models retain all of the degrees of freedom of the A-body nuclear system, down to the level of individual nucleons. These models do not make any assumptions *a priori* about the structure of the nucleus, and instead allow the nuclear structure to emerge unguided. *Ab initio* models are very powerful models, however they usually encompass a

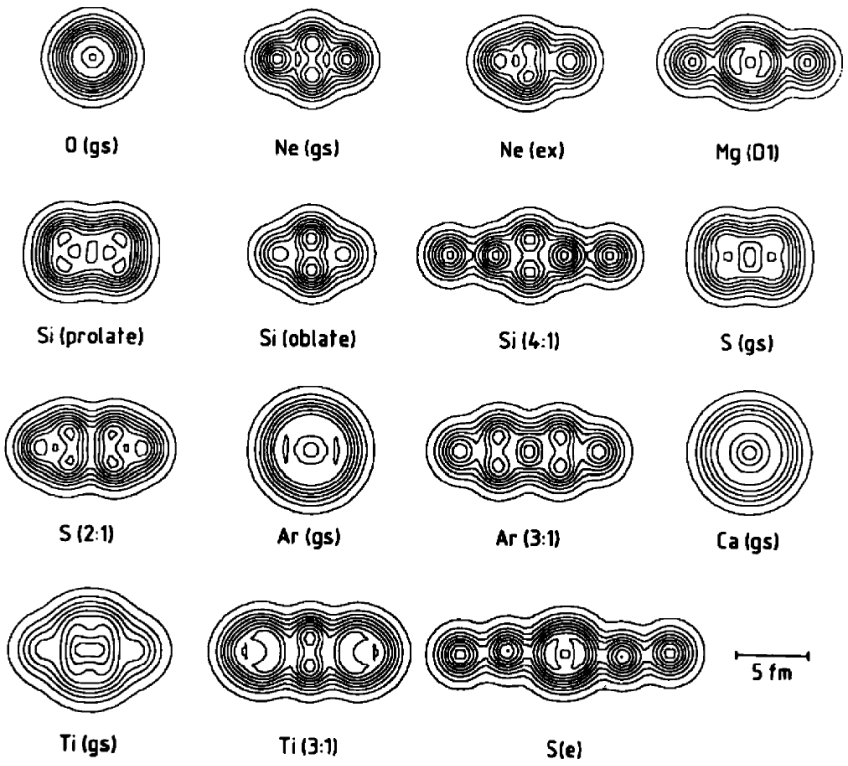

Figure 2.3: Density profiles of a range of light to medium mass nuclei calculated using the ACM. This figure is reprinted from Ref. [57].

very large model space, and so are usually very computationally intensive, limiting them to systems with small A.

The AMD wavefunction is similar to that of the ACM, however in AMD the nucleons are treated individually, rather than as preformed α-clusters. This allows AMD to describe both clustered and non-clustered structures, and allows the investigation of non-α-conjugate nuclei, which is not possible in the ACM framework. The wavefunction of the i^{th} nucleon, $|\psi_i\rangle$, is constructed from a spatial contribution $|\phi_i(\vec{R}_i)\rangle$, spin contribution, $|\chi_i\rangle$, and isospin contribution, $|\tau_i\rangle$,

$$|\psi_i\rangle = |\phi_i(\vec{R}_i)\rangle|\chi_i\rangle|\tau_i\rangle\,. \tag{2.5}$$

The spatial contribution $|\phi_i(\vec{R}_i)\rangle$ is assumed to be a Gaussian wavepacket, centred at $\vec{R}_i$, as was the case for the individual α-clusters in the ACM in Equation (2.3). The total wavefunction is produced by antisymmetrising the product of the nucleon wavefunctions using a Slater determinant

$$|\Phi_{\text{AMD}}\rangle = \mathcal{A}\prod_{i=1}^{A}|\psi_i\rangle\,. \tag{2.6}$$

The nucleons interact via an effective nucleon-nucleon potential, and the positions of the nucleons

are calculated variationally, minimising the total energy of the system. As for the ACM, angular momentum and parity projection are often used to extract good states of angular momentum and parity from $|\Phi_{\mathrm{AMD}}\rangle$.

AMD has been applied to a range of light nuclei [31, 39] with great success, predicting energy levels, binding energies and transition rates in excellent agreement with experimental observations. Additionally AMD calculations have been shown to predict the existence of α-clustering in many light nuclei. An example of the emergence of the α-α structure from AMD calculations is shown in Figure 1.5. The exceptional usefulness of the AMD model for studies of α-clustering comes from its ability to model both clustered states and shell-model type states within the same framework, meaning that the emergence of clustered wavefunctions from these calculations provides considerable evidence that clustering plays an important role in nuclear structure.

2.2 Experimental Techniques

In this section three of the most common experimental techniques used to investigate α-clustering are introduced, namely α-transfer reactions, inelastic scattering and resonant reactions. The concept of an α-clustered rotational band is introduced as one of the most commonly observed experimental signatures of α-clustering.

2.2.1 Transfer Reactions

Alpha-transfer reactions are a type of direct nuclear reaction whereby two protons and two neutrons are transferred from the beam to the target. Following the transfer, the residual target+α system is left in an excited state, and what remains of the beam-like nucleus (known as the ejectile) is subsequently measured in a detection system. The excitation energy of the residual nucleus is calculated from the measured energy of the ejectile, leading to a measurement of the reaction cross-section as a function of excitation energy.

The beam is usually chosen such that the reaction has a large α-spectroscopic factor [59, 60], with common examples being the (^{6}Li,d) and (^{7}Li,t) reactions[a], as well as reactions using heavier beams such as (^{14}N,^{10}B) [59] and (^{16}O,^{12}C) [61]. Heavier beams do however lead to complications in the analysis of the results [62], as compared with the light deuteron or triton produced when Lithium ions are used, the heavier outgoing particles will lead to a poorer experimental resolution due to the increased energy loss in the target. Therefore Lithium beams are usually preferred. These reactions are likely to preferentially populate α-cluster states, since the α-particle is more likely to be transferred as a co-

[a] Here d represents the deuteron and t represents the triton

herent structure rather than as individual nucleons [62]. They do not however populate all clustered states equally, with a preference for high spins states due to the selectivity of the reaction process with respect to the angular momentum and reaction Q-value [59], and dependencies on other experimental factors such as the beam energy.

The cross-sections of α-transfer reactions are peaked at the grazing angle, which usually corresponds to a small scattering angle, and so by making measurements at these angles α-transfer reactions are preferentially selected over contributions from other reaction processes. The extraction of spin assignments and spectroscopic factors, where large α-spectroscopic factors indicate α-clustered states, is usually done by a comparison between the angular distributions of the ejectile and Distorted Wave Born Approximation (DWBA) calculations [63, ch. 3]. DWBA calculations are built upon the optical model of nuclear reactions, which treats nuclear scattering as the interaction of an incoming wave with a spherical potential composed of both real and imaginary parts. These optical model potentials are usually constrained by elastic scattering measurements, and are then used in conjunction with calculations of single particle wavefunctions made using the shell-model to calculate the differential cross-section of the transfer reaction.

This technique was originally developed for the transfer of either a single neutron or proton, where the angular distributions are heavily dependant on the spin of the state populated in the residual nucleus. This dependency is not so clear when transferring an α-particle however, as this introduces a large number of possible orbital angular momenta that may contribute incoherently to the reaction, increasing the ambiguity of the results. This difficulty is discussed in the analysis of the ^{14}N(^{7}Li,t)^{18}F reaction by Cobern & Parker [64]. Often the approximation is made that α-clustered states ought to produce a high cross-section, and so an α-cluster structure is simply assigned to states which have a large yield.

Another limitation of this technique is that DWBA calculations are model-dependant, and therefore the extracted spectroscopic factors and spin assignments are dependent on the model parameters used in the DWBA calculations. A significant advantage, however, is that α-transfer reactions can populate the entire excitation energy range of the nucleus of interest, whereas the other techniques discussed in this section are limited to investigating α-clustering above the α-decay threshold. Further details on α-transfer reactions can be found in Refs. [37, 62].

2.2.2 Inelastic Scattering Break-up

In this technique the beam is scattered from the target, leaving the target in an excited state. The target may then decay by break-up into multiple nuclei, which are measured along with the scattered beam. This technique is especially appropriate for the study of clustered states, due to their increased

likelihood of breaking up into their constituent clusters. It is possible to extract the spins and parities of the excited states by analysing the correlations between the angles of the decay products measured in these reactions.

This is a very powerful technique, and it is very selective of clustered states. However the results are very sensitive to the resolution of the detector set-up, and the angular correlation analysis can be extremely complicated in the case that the outgoing nuclei are not spin-zero. Furthermore, using the break-up to select the clustered states limits the investigation to states that exist above the α-decay threshold. These difficulties often limit the applicability of this technique.

This technique has been used to great effect to study the α-cluster structure of the Hoyle state and its excitations in ^{12}C, by making a measurement of the ^{12}C(α,3α)^{4}He reaction [32].

2.2.3 Resonant scattering

Resonant scattering is an experimental technique which populates excited states in the nucleus formed by the fusion of the beam and target nuclei, known as the compound nucleus. The compound nucleus decays shortly after being formed, and the outgoing decay products are measured, providing measurements of the reaction cross-section as a function of the excitation energy populated in the compound nucleus. Energy levels in the compound nucleus manifest themselves in the reaction cross-section as resonances, and it is the analysis of these resonances that leads to the extraction of the spins and parities, J^{π}, and partial widths, Γ_i, of the energy levels, from which conclusions about the underlying nuclear structure can be drawn. The analysis of these measurements is underpinned by $\boldsymbol{R}$-matrix theory, which is discussed in detail in Section 3.2.

In order to develop a full understanding of a given compound nucleus, it is necessary to make measurements using a range of entrance and exit channels, and at a range of scattering angles. Measurements of multiple entrance and exit channels allow the constraint of all of the partial widths, with the reaction A(B,C)D constraining Γ_{AB} and Γ_{CD}. The angular distributions of the decay products as a function of scattering angle are used to constrain the spins of the compound states.

Resonant scattering is used to investigate α-clustering by measuring reactions that proceed via the α-channel, either in normal kinematics, $A(\alpha,y)R$, or inverse kinematics, ^{4}He(A,y)R. Here R is the residual nucleus, A is either the target (normal kinematics) or the beam (inverse kinematics) and y is the decay product that is measured in these reactions. The decay product is often an α-particle, and in the case that both the α-particle and the residual nucleus are left in their ground states the measurement corresponds to elastic α-particle scattering. This technique explores states with an α-A cluster structure, as one would expect any such levels to have raised α-decay widths, Γ_{α}, and should therefore be preferentially populated by reactions which proceed via the α-channel. This is especially

true in the case of elastic α-particle scattering, since the α-channel is both the incoming and outgoing channel.

Resonant scattering measurements can be classified as either thin-target or thick-target measurements. Thin target measurements are classically performed in normal kinematics, using an accelerated α-particle beam impinging on an appropriately chosen target. The target thickness is chosen to be small enough such that the energy loss by the beam through the target is minimal. This allows the approximation to be made that for a given beam energy, the reactions between the beam and target all populate a single excitation energy in the compound nucleus, E_x. The decay products are measured by a detection system at a scattering angle in the center of mass frame, $\theta_{\text{c.m.}}$. Many measurements are taken at different beam energies, and with the detectors in different positions, from which the cross-section is constructed as a function of E_x and $\theta_{\text{c.m.}}$.

Thick target measurements, by contrast, are usually made in inverse kinematics, giving rise to the name Thick Target Inverse Kinematics(TTIK) technique. Here the reaction chamber is filled with a ^{4}He gas, and it is the beam that must be appropriately chosen to populate the required reaction. Rather than attempting to minimise the energy loss through the target, as is done in thin target measurements, the TTIK technique actually exploits this energy loss to make cross-section measurements over a range of E_x from a single beam energy. As the beam traverses the ^{4}He gas it loses energy, meaning that the compound nucleus is populated at a range of E_x along the path of the beam through the reaction chamber. The beam energy and ^{4}He gas pressure are chosen to ensure that the beam is entirely stopped in the gas, meaning that E_x will range between the decay threshold energy and some maximum value dictated by the initial energy of the beam upon reaching the reaction chamber. The highest beam energies occur close to the entrance to the reaction chamber, and they decrease along the beam path. It is common practice to place detectors at 0° to the beam line, and at the opposite end of the chamber to the beam entrance, beyond the range of the beam in the gas. This allows measurements to be made of the light reaction decay products at a scattering angle of 180°.

The TTIK technique was first introduced by Artemov *et al.* [65], and has since been used with much success for the study of α-clustering. For example it was used extensively by Norrby *et al.* [66, 67], Lonnroth *et al.* [68] and Goldberg *et al.* [69] to investiage the medium mass nuclei ^{32}S, ^{34}S, ^{36}Ar and ^{40}Ca (all of which is detailed in the thesis by Norrby [70]), by Freer *et al.* [71, 72] to investiagte ^{11}C and ^{14}C, and by Avila *et al.* [46] to study ^{18}O. It has also been used to study proton resonance reactions with a ^{1}H gas [73]. A comparison between two independent measurements of the ^{4}He + ^{20}Ne resonant reaction is made in Ref. [74], one made using the TTIK technique and another using the thin target technique.

The TTIK technique is the experimental technique used throughout this thesis. It is a very powerful

technique, with the following advantages over thin target resonant scattering:

- It allows measurements to be made at a scattering angle of 180°, which corresponds to a maximum for the resonant contributions to the spectrum, and a minimum for the Rutherford contribution, producing the clearest possible resonances in cross-section. This is ideal since it is the resonances which contain the nuclear structure information, and this measurement cannot usually be made using the thin target technique.
- It produces a continuous measurement of cross-section, as opposed to discrete measurements that are produced by the thin target technique. While discrete measurements have the potential to be just as powerful as continuous measurements, this requires a high sampling rate to ensure that no features are missed, which often requires a very long experimental run.
- Thin target resonant scattering measurements are limited to reactions with a stable target, whereas it is possible to implement the TTIK technique using radioactive beams, greatly extending the range of measurements that can be made.

There are also some disadvantages which ought to be noted. These are as follows:

- The extraction of the cross-section from the raw TTIK measurements requires a significant amount of data processing, which can introduce additional uncertainties. In this work special care has been taken to overcome this, detailed in Section 3.1.
- The quality of the measurements are highly dependent on the experimental resolution, and this has been observed to degrade at scattering angles away from 180°, causing accurate and reliable measurements of angular distributions to be challenging. This is discussed in Section 3.1.4.

2.3 Alpha-clustered Rotational Bands

Cluster structures are often described as solid-phase structures in nuclei, as opposed to liquid-phase (Liquid Drop Model) and gaseous-phase (Shell Model). If the cluster structure is indeed assumed to be rigid, then any collective excitations must consist purely of rotational energy. This is achieved by combining the classical expression for rotational energy, given in Equation (2.7), with the quantum mechanical operator for total angular momentum, $\hat{J}^2$, producing an expression for the excitation energy, E_x, of quantized rotational energy levels:

$$E(J) = \frac{1}{2} I\omega^2 = \frac{J^2}{2I} \tag{2.7}$$

$$E_x = \frac{\hbar^2}{2I} j(j+1) \tag{2.8}$$

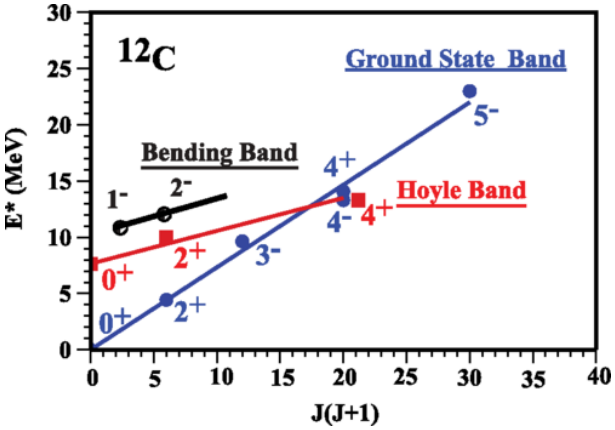

Figure 2.4: Rotational bands in ^{12}C, showing the clear linear behaviour as a function of $J(J+1)$. This figure is reprinted from Ref. [32].

where ω is the angular frequency of the rotation, I is the nuclear moment of inertia, and j is the total angular momentum quantum number. If this idea is combined with the idea that some energy is required to initially form the clustered state, given by Equation (1.1), then a simple expression for the energy levels of a clustered rotational band can be formulated, given in Equation (2.9). It can be seen that E_x should vary linearly with $j(j+1)$, with a gradient that is inversely proportional to the moment of inertia of the structure and an intercept which gives the threshold energy for the structure, E_0.

$$E_x = E_0 + \frac{\hbar^2}{2I} j(j+1) \tag{2.9}$$

Additionally an α-clustered rotational band has the property that all of the states should have raised α-decay widths, indicating that the α-particle is preformed within the nucleus. Rotational bands are discussed in Ref. [4], and examples of clustered rotational bands have been seen in many light nuclei, including the α-α structure in Be isotopes [25, 42] and the α-^{16}O structure in ^{20}Ne [38]. An example of the rotational bands in ^{12}C can be seen in Figure 2.4.

In the case that the angular momentum projection onto the axis of deformation, K, is non-zero and there exists at least one unpaired neutron or proton, Coriolis decoupling is often observed in the rotational band. This arises due to the interaction of the spins of the single particle wavefunctions of the uncoupled protons and neutrons with the collective rotational motion of the nucleus, with a preference for the alignment of these two quantities. This leads to the mixing of states with different K and manifests as the zig-zagging of consecutive band members, and is discussed in Ref. [20]. It is particularly evident in the $K = 1/2^+$ rotational bands in ^{9}Be and ^{11}Be, shown in Figure 2.5.

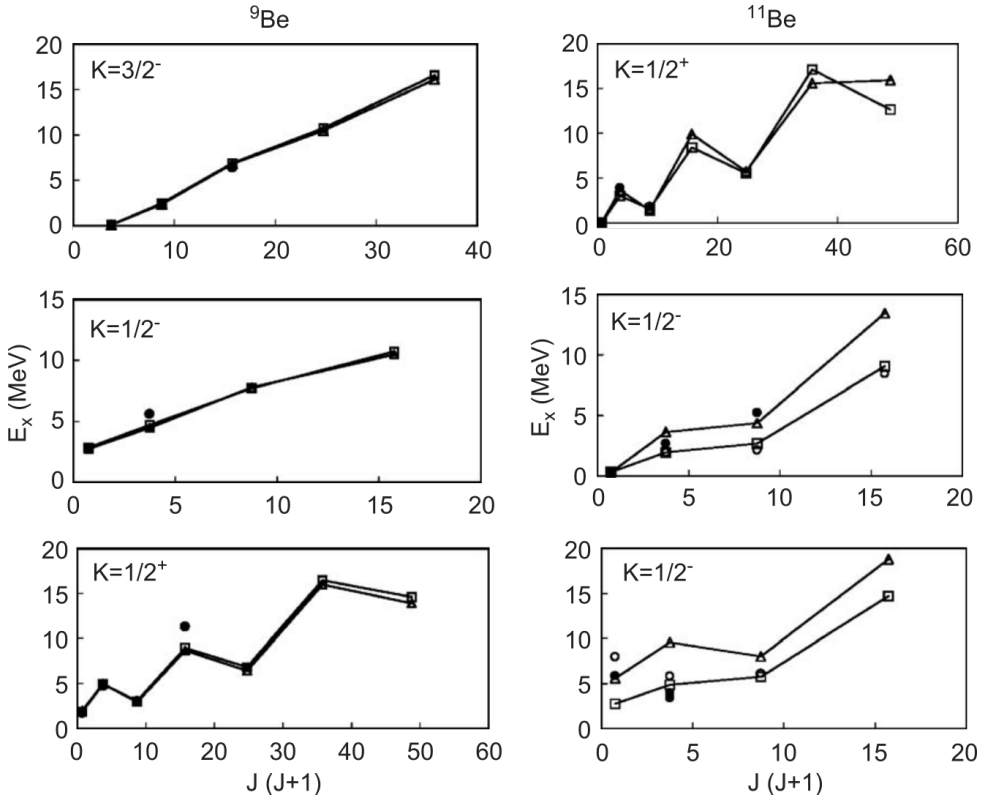

Figure 2.5: Examples of rotational bands in ^{9}Be and ^{11}Be, showing clear Coriolis decoupling in $K = 1/2^{+}$ rotational bands. Here the filled circles are measured states, and the open squares and triangles are two different model calculations, connected by lines. This figure is reprinted from Ref. [20].

Chapter 3

Resonant Scattering in Inverse Kinematics

The TTIK technique, detailed in Ref. [65], is used for all of the experimental work in this thesis to provide measurements of the differential reaction cross-section, $d\sigma/d\Omega$, over a range of energies and scattering angles. These measurements are then understood and interpreted in terms of the underlying nuclear structure using $\boldsymbol{R}$-matrix theory. The details of the TTIK methodology used here, and specifically how it is applied to the investigation of α-clustering is explored in Section 3.1, and $\boldsymbol{R}$-matrix theory is discussed in detail in Section 3.2.

3.1 The Thick Target Inverse Kinematics Technique

The TTIK technique is exceptionally powerful when applied to the investigation of α-clustering, as discussed in Section 2.2.3. It does however require a range of corrections and considerations unique to such measurements. In the sections that follow, the tools necessary to understand and analyse TTIK measurements are discussed.

3.1.1 Generic Experimental Set-up and Detection System

A generic TTIK experiment for the measurement of resonant scattering from α-particles can be defined in terms of the beam particle, A, decay product, y, and residual nucleus, R. The reaction that is measured in these experiments is given as

$$^{4}\mathrm{He}(A,y)R\,. \tag{3.1}$$

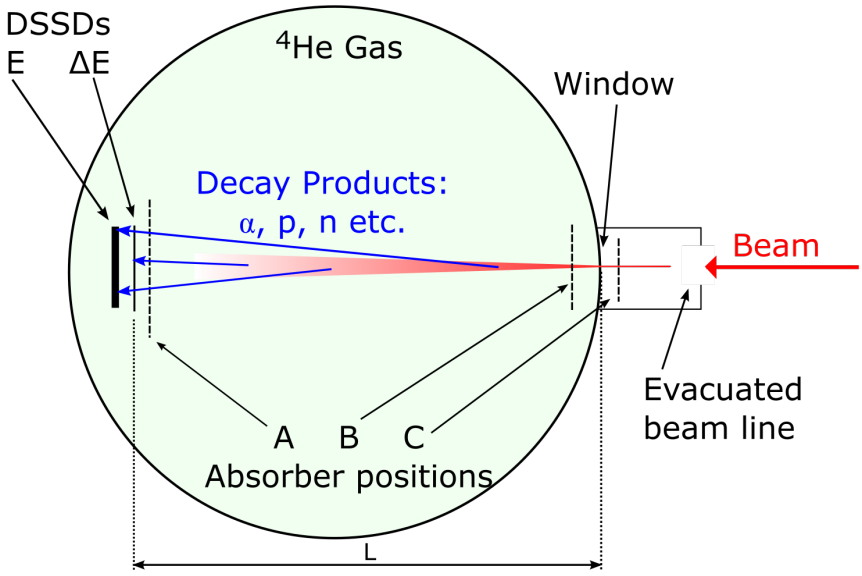

Figure 3.1: A generic TTIK experimental set up. Here the ^{4}He gas fills the green region, the beam is shown in red, and the dashed lines indicate the possible locations of the absorber, denoted as A, B and C. L indiactes the distance between the window and the detectors. This figure is adapted from my work in Ref. [1].

A typical experimental set-up is shown schematically in Figure 3.1. It is necessary to isolate the reaction chamber from the beam line using a thin window, often constructed from Havar or Mylar, in order to separate the gas target from the evacuated beam line. An absorber is often used either before the detectors, after the window, or before the window, to provide additional flexibility on the measured energy range. These absorber positions are labelled as positions A, B and C respectively in Figure 3.1. Positions B and C reduce the beam energy before it interacts with the gas, reducing the energies populated in the measurements without requiring the retuning of the accelerator. Position A allows high beam energies to be used, which would otherwise hit the detectors.

In all of the experimental work in this thesis, silicon detectors were used. Silicon is a semiconductor, and semiconductor charged particle detectors make use of the depleted region in a p-n junction to measure charged particles. Semiconductors are usually doped, producing an excess of either electrons (n-type) or holes (p-type). By joining a p-type semiconductor to an n-type semiconductor one creates a p-n junction, shown schematically in Figure 3.2a. At the point where the two types of semiconductor meet, the excess electrons are attracted to the excess holes, cancelling each other out and creating what is known as the depleted region of the p-n junction, with no free electrons or holes. Any charged particles which pass through the depleted region create electron-hole pairs via ionisation, causing them to lose energy, and since it takes a fixed amount of energy to create an electron-hole pair, the

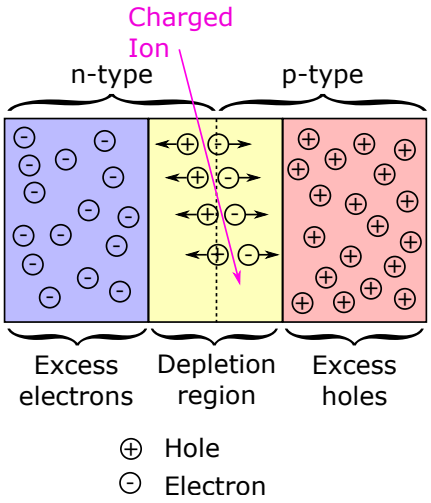

(a) P-n junction.

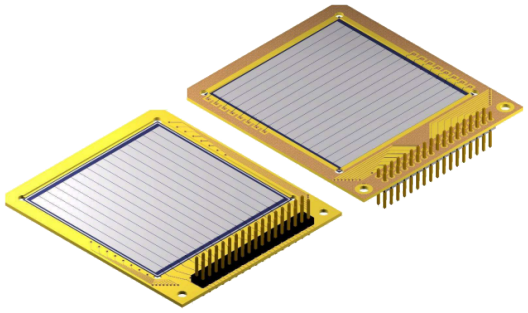

(b) DSSD.

Figure 3.2: A schematic diagram of the use of a p-n junction for the detection of charged particles (left), and a rendering of a typical Double Sided Silicon Strip Detector, adapted from Ref. [76] (right).

number created will be proportional to the energy deposited by the charged particle, to within the uncertainty of counting statistics.

A potential difference is placed across the p-n junction, known as a 'reverse bias', which increases the size of the depletion region such that it covers the entire depth of the detector. The potential difference allows the electron-hole pairs to be counted, by attracting the electrons to one side and holes to another. This generates a charge pulse for each charged particle that passes through the detector, the magnitude of which is proportional to the energy of the charged particle. For more detail on semiconductors, p-n junctions and their use as charged particle detectors please refer to Ref. [75].

In this work the detectors used are the W1 Double-sided Silicon Strip Detectors (DSSD), produced by Micron Semiconductor, shown in Figure 3.2b. These are square silicon detectors with a side length of 50mm. The front and back faces are split into 3 mm strips, with 16 vertical strips on the front and 16 horizontal strips on the back. This allows position information to be extracted for each event, assigning each event to an effective 3 by 3 mm pixel.

Particle identification is performed by using a $\Delta E - E$ setup. Here two DSSDs are used, one in front of the other. The front DSSD is usually a very thin detector, and is known as the ΔE detector. The rear DSSD is a thick detector, and is know as the E detector. For each event the decay products usually pass through the ΔE detector, depositing a small amount of energy, before being absorbed by the E detector where the remainder of its energy is deposited.

The amount of energy deposited in the ΔE detector is dictated by the Bethe-Bloch formula for stopping power [77]. This was discussed in detail by Ziegler [78], and is used to calculate the energy

loss of charged ions through matter as

$$\frac{dE}{dx} = -\kappa Z^2 \frac{Z_m}{A_m} \frac{1}{\beta} L(\beta) \tag{3.2}$$

where dE/dx is the energy loss per unit distance, $\beta = v/c$ is the velocity of the ion relative to the speed of light, Z_m and A_m are the atomic and atomic mass numbers respectively of the medium within which the ion is travelling, Z is the atomic number of the ion and $\kappa = 0.3071$ is a constant which produces stopping powers in units of keV/(mg/cm^2). $L(\beta)$ is known as the stopping number, and is traditionally expanded in terms of Z as

$$L(\beta) = L_0(\beta) + ZL_1(\beta) + Z^2 L_2(\beta) + ... \tag{3.3}$$

where L_0 is the largest contribution, and L_1 and L_2 are corrections, known respectively as the Barkas and Bloch correction. The details of the stopping number can be found in Ref. [78], and depends in part on the atomic mass number of the ion.

It is clear that the energy loss depends heavily on the energy and Z of the ion, and to a lesser extent on the mass of the ion. Therefore by a comparison of the energy deposited in the ΔE detector with the energy deposited in the E detector it is possible to uniquely identify the measured decay product. This is done in this work by producing particle identification plots, by plotting for each event the amount of energy deposited in the ΔE detector against the total energy deposited in both detectors. An example of a particle identification plot is shown in Figure 3.3. This technique clearly separates light decay products with different Zs and As.

3.1.2 Excitation Spectrum Reconstruction

Following some preliminary analysis, detailed in Section 4.3, each experimental event can be characterised by three pieces of information: the measured decay product energy, E_m, the two dimensional position of the measurement on the detector, $\vec{R}_m$, and the identity of the measured decay product based on $\Delta E - E$ particle identification. Since the DSSDs only constrain the position to within a 3 by 3 mm pixel, $\vec{R}_m$ is randomized uniformly within the pixel boundaries to synthesize continuous values. This set of raw values must be converted to the properties of the nuclear reaction; the excitation energy populated in the compound nucleus, E_x, the position of the reaction in the chamber (measured as the distance from the chamber entrance), x, and centre of mass scattering angle, $\theta_{\text{c.m.}}$. This requires the simulation of the energy loss of the beam and decay products through the ^{4}He gas and the calculation of the reaction kinematics.

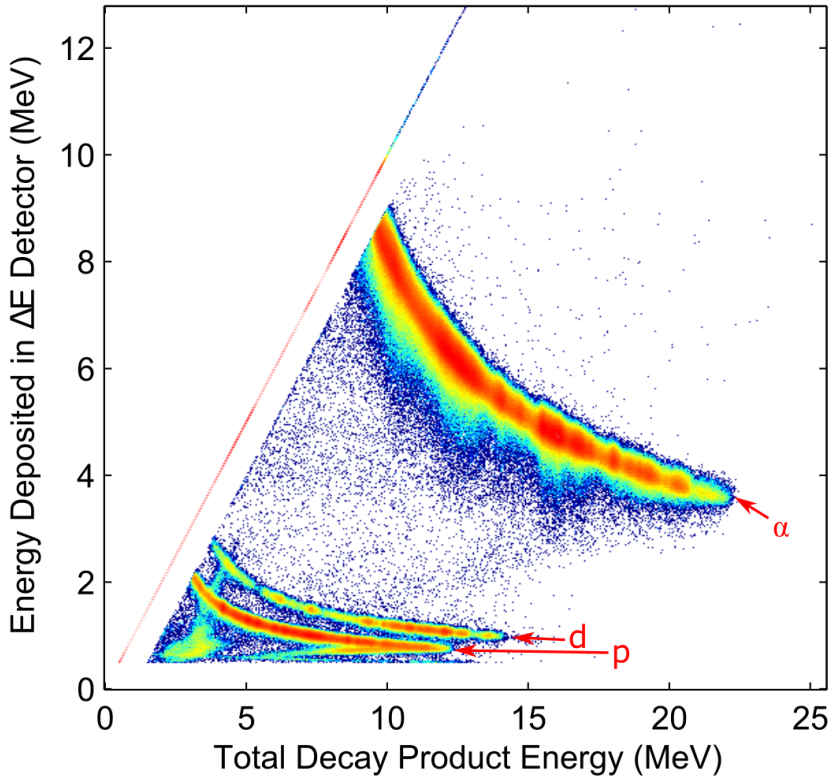

Figure 3.3: An example particle identification plot, taken from the experimental work on ^{18}F discussed in Section 4. Alpha-particles, deuterons and protons are clearly separated, annotated in red. The fine details of this plot are discussed in Section 4.3.4.

3.1.2.1 Energy Loss

The energy loss is calculated by numerically integrating the stopping power, defined in Equation (3.2). This process proceeds by moving the nucleus through the material with many small steps, and at each step calculating the energy that is lost by the nucleus during that step, based on the energy at the start of that step. In practice this is done in `python` using the integration subpackage in `SciPy` [79].

Stopping powers are notoriously difficult to calculate accurately, and so experimental measurements are often used to constrain them. In the present work the stopping powers were extracted from `Lise++` [80] and the in house code `dedx`. `Lise++` has three different stopping powers, `He-base`, `H-base` and `ATIMA 1.2`, and these are compared with `dedx` in Figure 3.4. The differences between each of these stopping powers arise from the application of the numerous phenomonological corrections to the Bethe-Bloch formula, many of which are detailed in Ref. [78], which are applied using different constraining data and parametrisations in each case. The `Lise++` documentation [81] recommends the use of the `H-base` stopping powers, which are based on the work by Ziegler [78], for low and intermediate energies (below 100-300 MeV/A), and specifically for gas targets, making them ideal for the present work.

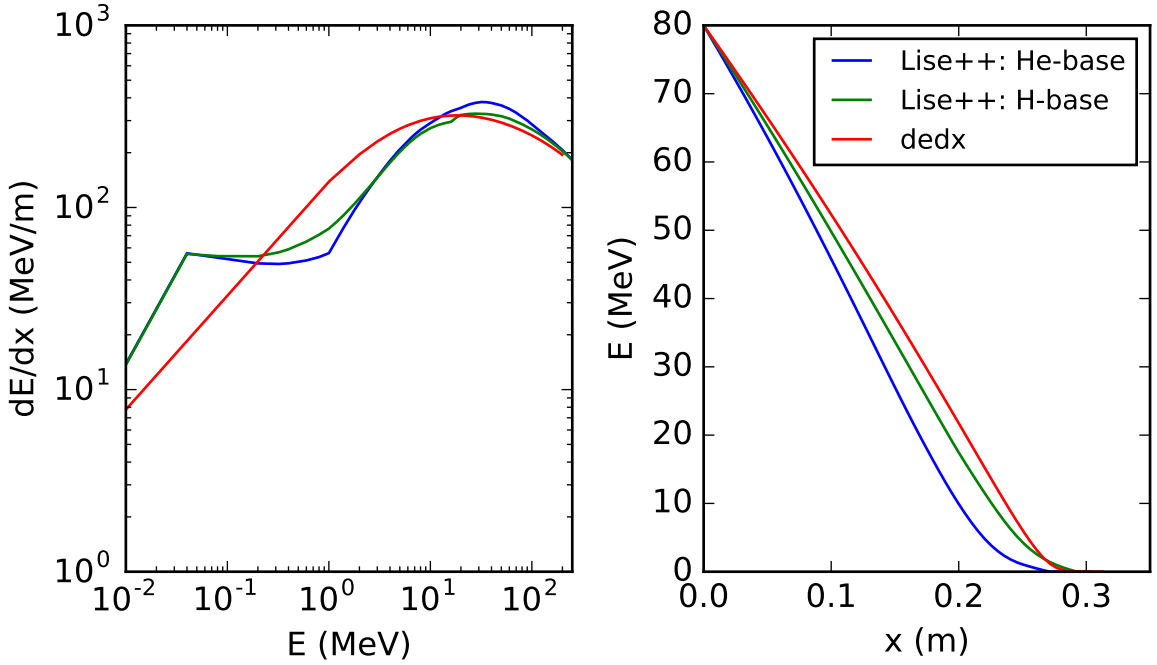

Figure 3.4: A comparison of the stopping powers from `Lise++` and `dedx`. Stopping powers calculated for ^{40}Ca ions in a ^{4}He gas at a pressure of 550 mbar, with an initial energy of 80 MeV. Stopping power (left) and corresponding numerical integration (right). The stopping power produced by `ATIMA 1.2` is identical in this case to `H-base`, since these differ only at very high energies.

The experimental analysis of ^{18}F, detailed in Section 4.3.4, was performed using each stopping power code, and the results were compared with previous measurements. It was found that `H-base` did indeed produce the results most consistent with the previous measurements. Based on this the `H-base` stopping powers are used throughout this thesis.

3.1.2.2 Two-Body Kinematics

The two-body kinematics required to deal with the nuclear reactions in TTIK measurements are derived in the general case in Ref. [4]. Here the important results of that derivation are adapted specifically for TTIK measurements using a ^{4}He gas target, where the reactions are of the type given in Equation (3.1).

At the reaction point it is assumed that initially the target nucleus, ^{4}He, is stationary, and A is travelling towards the target with a kinetic energy E_A, in the $+\hat{x}$ direction. After the reaction R and y have energies E_R and E_y respectively in the laboratory frame, and y is scattered by θ_y with respect to $+\hat{x}$. In the centre of mass frame, all of the parameters are denoted by a prime. The centre of mass scattering angle, $\theta_{\text{c.m.}}$, is the angle in the centre of mass that the incoming nuclei are scattered by. Since the total linear momentum is zero in the centre of mass frame, conservation laws ensure that y and R

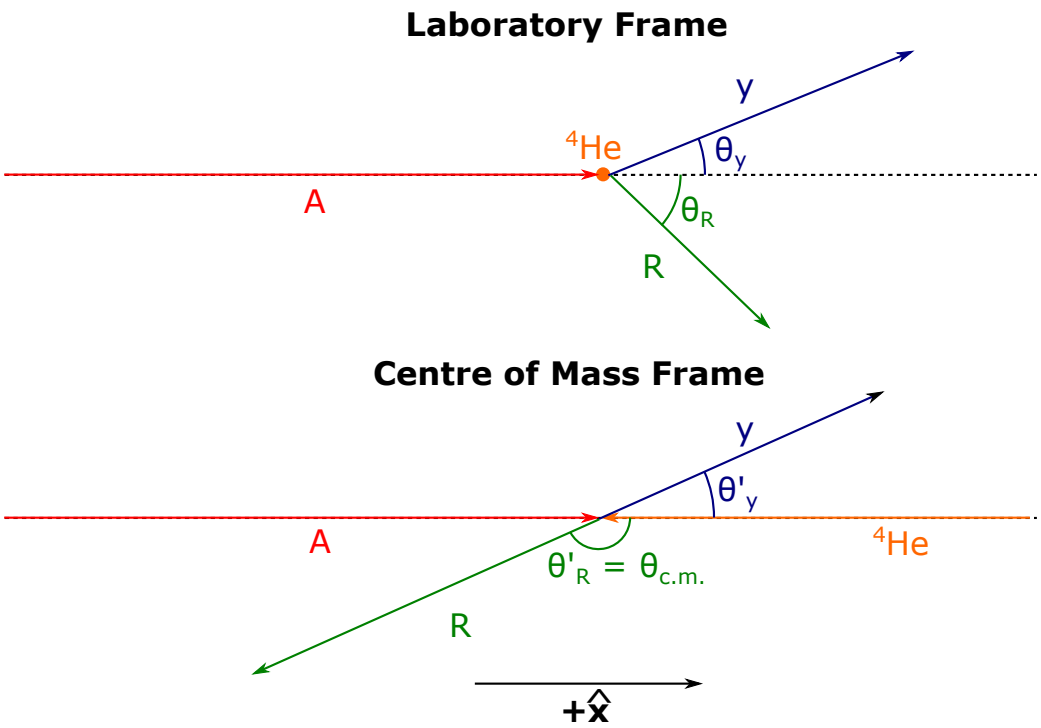

Figure 3.5: The laboratory and centre of mass frame kinematics of a typical TTIK reaction with a ^{4}He target. Here A is the beam, y is the measured decay product and R is the residual nucleus. The parameters in the centre of mass frame are denoted by a prime.

are emitted back to back in that frame. However, the conversion back to the laboratory frame removes this symmetry. This is depicted in Figure 3.5.

The centre of mass energy is calculated from the beam energy, E_A, and is directly related to the excitation energy, E_x, populated in the compound nucleus, C. These relationships are defined as

$$E_{\text{c.m.}} = \frac{m_\alpha}{m_A + m_\alpha} E_A \tag{3.4}$$

$$E_x = E_{\text{c.m.}} + Q_f \tag{3.5}$$

where Q_f is the Q-value of the fusion reaction $A + \alpha \rightarrow C$, and m_A and m_α are the masses of A and the α-particle, respectively.

The energy of y in the lab frame, E_y, is calculated in terms of γ, which is the ratio of the centre of

mass velocity, $v_{\text{c.m.}}$, to the velocity of y in the centre of mass frame, v'_y. These are defined as

$$E_y = E_A \frac{m_y m_A}{(m_A + m_\alpha)^2} \left(\gamma^4 + 2\gamma^3 \cos\theta_{\text{c.m.}} + \gamma^2\right) \tag{3.6}$$

$$\gamma = \frac{v_{\text{c.m.}}}{v'_y} = \left[\frac{m_A m_y}{m_R m_\alpha} \frac{E_A}{E_A + (Q_r - E^*_y - E^*_R)\left(1 + \frac{m_A}{m_\alpha}\right)}\right]^{\frac{1}{2}} \tag{3.7}$$

where Q_r is the Q-value for the full reaction $A + \alpha \rightarrow y + R$. If either y or R are left in an excited state, then E^*_y and E^*_R denote these energies. The scattering angles are also related in terms of γ as

$$\tan\theta_y = \frac{\sin\theta'_y}{\cos\theta'_y + \gamma} \tag{3.8}$$

$$\theta'_y = 180^\circ - \theta_{c.m.}\,. \tag{3.9}$$

It is possible to invert Equation (3.8) using the trigonometric identity $\sin(A - B) = \sin A \cos B - \cos A \sin B$, giving

$$\theta'_y = \sin^{-1}(\gamma \sin\theta_y) + \theta_y \tag{3.10}$$

These calculations are greatly simplified in the case of elastic scattering, whereby $y = \alpha$, $R = A$ and $Q_r = 0$. In this situation, $\gamma = 1$, which reduces Equations (3.6) - (3.10), giving

$$E_\alpha = 4E_A \frac{m_\alpha m_A}{(m_A + m_\alpha)^2} \cos^2\frac{\theta_{\text{c.m.}}}{2} \tag{3.11}$$

$$\theta'_\alpha = 2\theta_\alpha \tag{3.12}$$

$$\theta_{\text{c.m.}} = 180^\circ - 2\theta_\alpha\,. \tag{3.13}$$

3.1.2.3 Full Experimental Simulation

Using the energy loss and kinematics a single experimental event is simulated, given a specific reaction ^{4}He$(A, y)R$, and the definition of the parameters E_0, $\theta_{\text{c.m.}}$, and x. This simulation outputs the values for E_x, E_m and $\vec{R}_m$ for that specific event. The simulation proceeds as follows: the energy loss of A is calculated between the chamber entrance and x. At that point kinematics calculations are performed to calculate E_x, E_y and θ_y. The energy loss of y is then calculated between x and the detectors, giving E_m. $\vec{R}_m$ is calculated geometrically from x and θ_y. This process is shown as a flow diagram in Figure 3.6.

This is repeated for many events, covering a range of values of x and θ. Since the detectors are

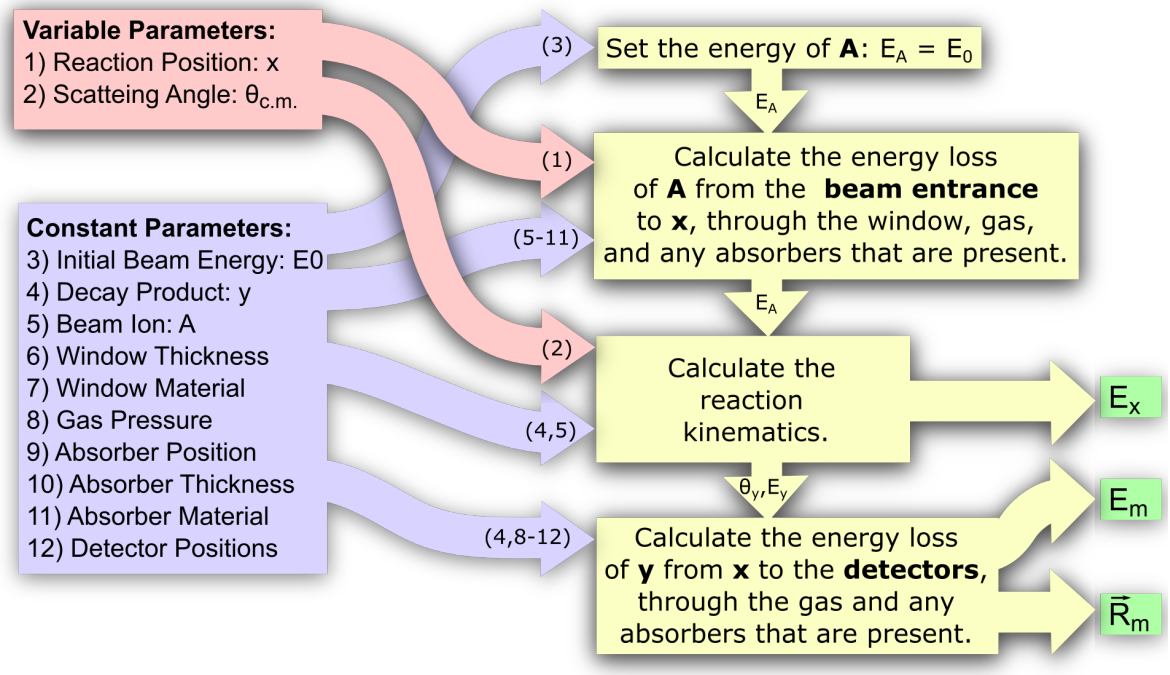

Figure 3.6: A flow diagram showing the process of simulating a TTIK event, showing inputs (red and blue), calculation steps (yellow) and outputs (green). In order to generate the data from which the polynomials f_{E_x}, f_x and f_θ (see text) are constructed, the variable parameters (red) are varied over a suitable range. The constant parameters (blue) remain fixed for a given polynomial. The numbers on the arrows indicate the parameters required.

placed along the beam line, it is clear from the symmetry of the reaction that only the radial distance of the measurement from the centre of the detector, r_m, is important. This allows r_m to be used instead of $\vec{R}_m$, which reduces the dimensionality of the problem. It is then possible to fit a 2-dimensional polynomial to the data produced by these simulations, to approximate the functions:

$$E_x = f_{E_x}\left(E_m, r_m\right) \tag{3.14}$$

$$\theta_{\text{c.m.}} = f_{\theta_{\text{c.m.}}}\left(E_m, r_m\right) \tag{3.15}$$

$$x = f_x\left(E_m, r_m\right) . \tag{3.16}$$

These polynomials may then be used to convert E_m and $\vec{R}_m$ to x, E_x and $\theta_{\text{c.m.}}$. These polynomials will vary depending on the reaction, gas pressure, the position and properties of the absorber, the properties of the window and the position of the detectors in the chamber. Examples of these polynomials are shown in Figures 3.7, 3.8 and 3.9.

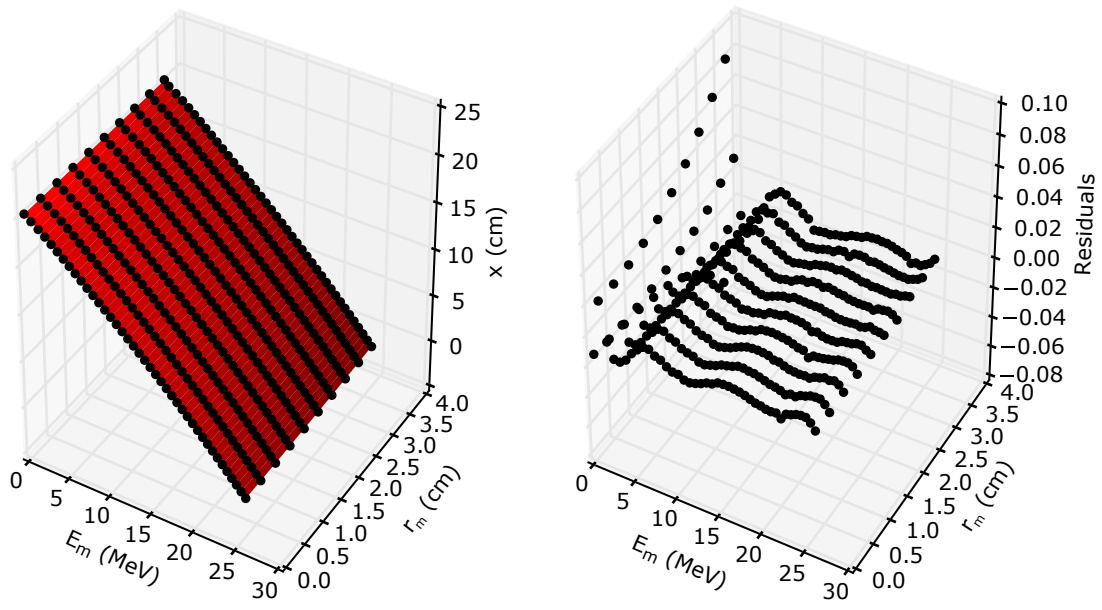

Figure 3.7: The data (black circles) and polynomial fit (red surface) used to produce $f_x(E_m, r_m)$. Shown in this case for measurement 1 of the reaction ^{4}He(^{40}Ca,α). The details of this are given in Table 5.4.

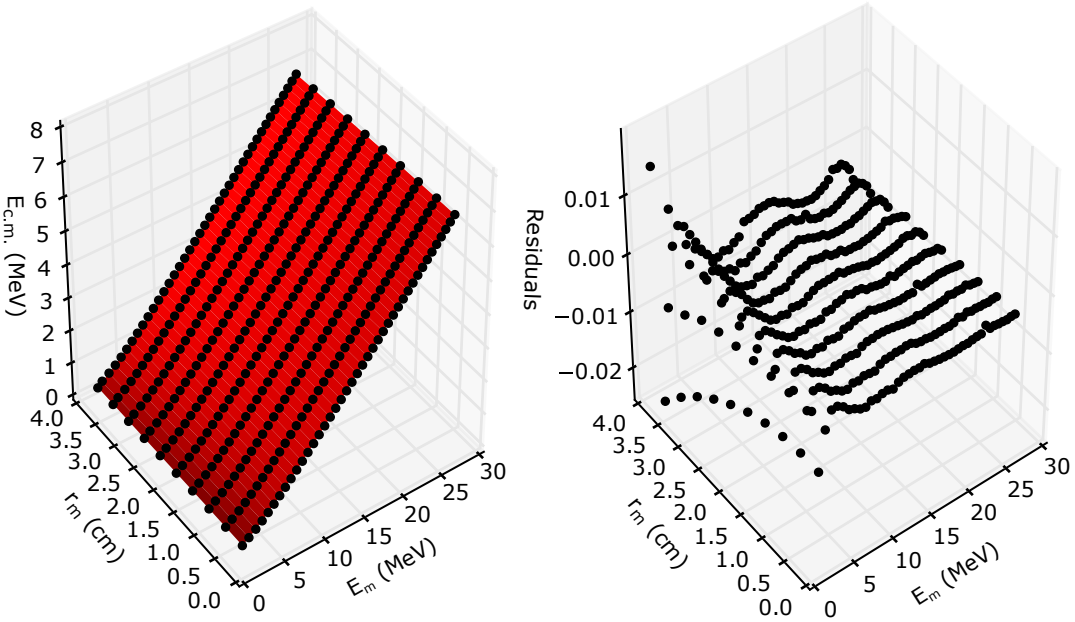

Figure 3.8: The data (black circles) and polynomial fit (red surface) used to produce $f_{E_{\text{c.m.}}}(E_m, r_m)$. From this it is trivial to calculate E_x using Equation (3.5). Shown in this case for measurement 1 of the reaction ^{4}He(^{40}Ca,α). The details of this are given in Table 5.4.

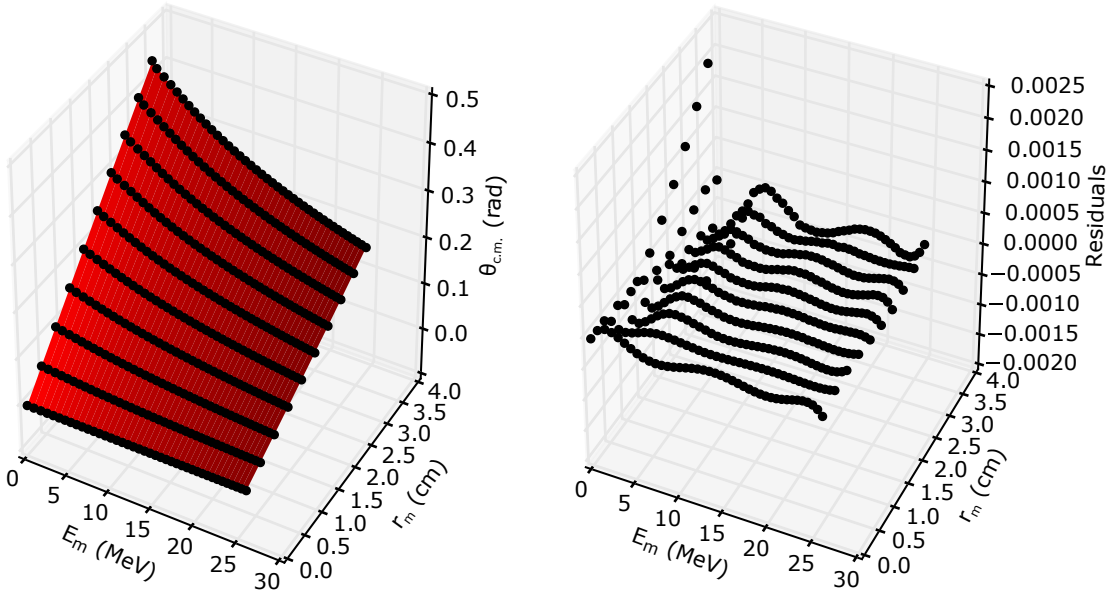

Figure 3.9: The data (black circles) and polynomial fit (red surface) used to produce $f_{\theta_{\text{c.m.}}}(E_m, r_m)$. Shown in this case for measurement 1 of the reaction ^{4}He(^{40}Ca,α). The details of this are given in Table 5.4.

3.1.3 Efficiency Correction

It is important to correct for energy dependant efficiency components in TTIK measurements before extracting $d\sigma/d\Omega$. There are two important corrections to be made: the geometrical correction and the effective target thickness correction. The geometrical correction is the dominant effect, whereas the effective target thickness is a much smaller effect, often assumed to be negligible in the analysis of other TTIK measurements.

3.1.3.1 Geometrical Correction

The technique reported here for the correction of the geometrical efficiency was developed collaboratively with J. Walshe [74].

Since it is mainly the energy loss through the ^{4}He target that produces the range of measured energies, the high energy events should occur close to the window, far from the detectors, and the low energy events close to the detectors. This combined with the finite size of the detectors introduces an energy dependent geometrical efficiency, depicted in Figure 3.10, whereby the detectors subtend a smaller solid angle for high energy events than for low energy events. This is corrected for by setting a fixed maximum value for $\theta_{\text{c.m.}}$, $\theta^{\text{max}}_{\text{c.m.}}$, and rejecting any events which are measured at $\theta_{\text{c.m.}} > \theta^{\text{max}}_{\text{c.m.}}$. This

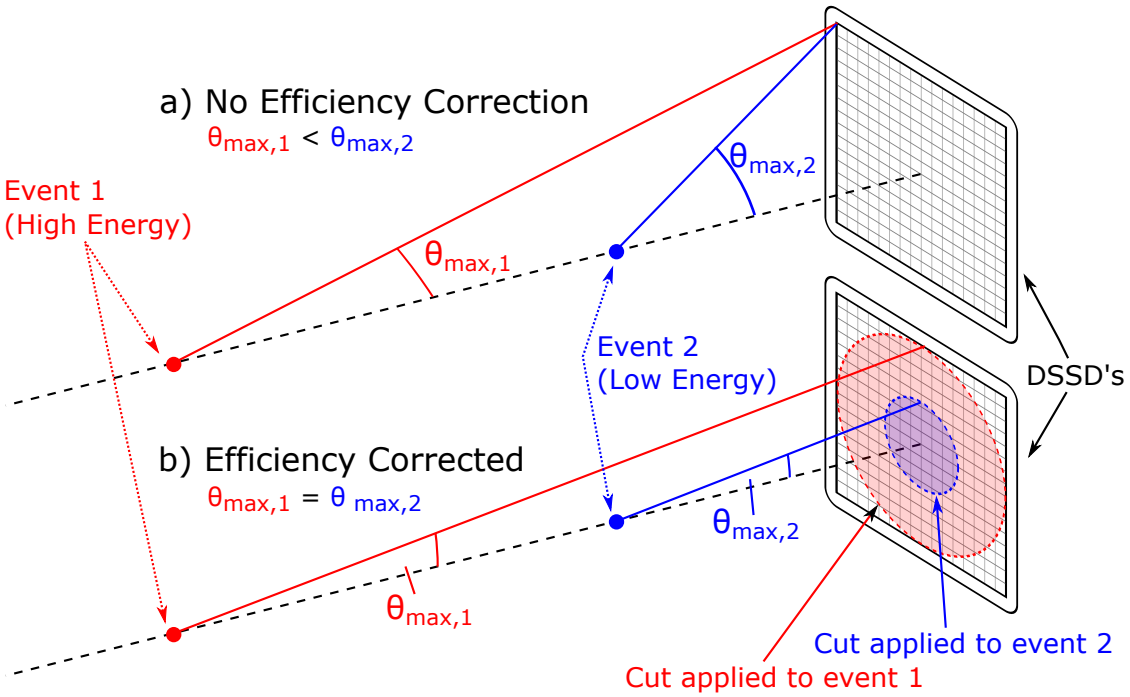

Figure 3.10: A schematic diagram depicting the geometrical efficiency effect (a) and its correction (b). Two events are shown, event 1 is a high energy event (red), and event 2 is a low energy event (blue). It is important to note here that for the correction the maximum angle is set in the centre of mass frame, however for clarity this diagram depicts a fixed laboratory frame scattering angle. This figure is adapted from Figure 4.7 in Ref. [74].

effectively produces a circular cut on the DSSDs, the radius of which is dependant on the distance of the event from the detectors, and hence on the energy of the event. The yield produced by this efficiency correction is proportional to the cross-section in the centre of mass frame, $d\sigma/d\Omega$.

Since $\vec{R}_m$ is only constrained to a pixel in the detector, in cases where the circular cut bisects the active pixel it is impossible to determine whether the event should be recorded or rejected. It is then the randomization of $\vec{R}_m$ within the pixel that determines whether that event is recorded or rejected, introducing a degree of uncertainty into the method. A Monte Carlo simulation was performed to analyse the effect that this has on the resulting efficiency correction. This simulation was similar to the full experimental simulation shown in Figure 3.6, with the difference here that the reaction position, x, and scattering angle, $\theta_{\text{c.m.}}$ were randomised to produce a uniform cross-section as a function of both $E_{\text{c.m.}}$ and $\theta_{\text{c.m.}}$. The resulting $\vec{R}_m$ was then randomised to account for the finite pixel size on the DSSDs. The 'measured' scattering angle was then computed from the randomised value of $\vec{R}_m$, and the efficiency correction applied, allowing the effect that the finite DSSD pixel size has on the quality of the efficiency correction to be analysed. Effects of the resolution of the system, such as the energy and angular straggling of the nuclei in the gas and window, and the intrinsic energy resolution of the

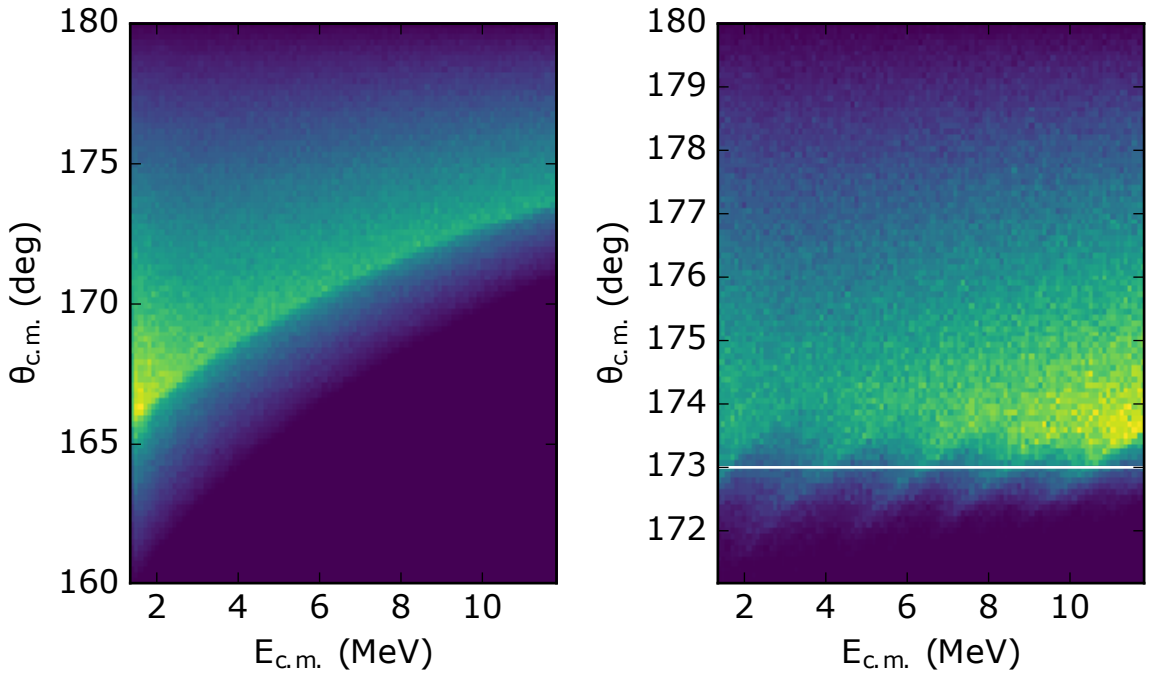

Figure 3.11: The resulting yields as a function of $\theta_{\text{c.m.}}$ and $E_{\text{c.m.}}$ of the Monte Carlo simulation detailed in the text. The yields before (left) and after (right) the application of the geometrical efficiency correction are shown, where $\theta_{\text{c.m.}}^{\text{max}} = 173°$ is marked by a white line. This particular simulation was performed for the ^{4}He(^{40}Ca,α) reaction, using the parameters for measurement 4, given in Chapter 5.

detector were ignored for the purposes of this simulation, but are discussed in detail in Section 3.1.4.

Here the simulation was performed for the ^{4}He(^{40}Ca,α) reaction, detailed in Chapter 5, however one would expect the results to be applicable to all TTIK measurements. The results are shown in Figure 3.11. In this simulation it is clear that the efficiency correction successfully limit the measurements of scattering angles to a fixed $\theta_{\text{c.m.}}^{\text{max}}$. The aberrations at $\theta_{\text{c.m.}} \sim \theta_{\text{c.m.}}^{\text{max}}$ in the efficiency corrected plot in Figure 3.11 are caused by the finite pixel size, however these produce a comparatively small effect, fluctuating by generally less than a degree. They do, however, get larger at low $E_{\text{c.m.}}$. This is because at lower energies, where the reactions are occurring close to the DSSDs, each pixel on each DSSD subtends a larger solid angle. This means that the uncertainty of $\vec{R}_m$ over a single pixel corresponds to a larger effective uncertainty in $\theta_{\text{c.m.}}$ for low energy events than it does for high energy events, causing the aberrations to increase in size. It can therefore be concluded that this is an effective efficiency correction as long as the events do not occur too close to the detectors. Another feature of these simulations is that the yield seems to increase at high $E_{\text{c.m.}}$ in the corrected spectrum. This is due to the effective target thickness component to the experimental efficiency, which was not corrected for here and is discussed in the next section. This Monte Carlo simulation is used to assess the applicability of the geometrical efficiency correction for each of the experiments performed in this thesis in the

appropriate chapters to ensure its validity for each case. This method does however discard many events, which is reasonable in all of the experiments in this thesis since they all were measured with good statistics, however in experiments which have a limited count rate a different efficiency correction would be necessary.

It is also worth noting that while the detectors are nominally referred to as being placed at $\theta_{\text{c.m.}} = 180°$, in fact they measure a finite range of angles, the average of which is smaller than 180°. It is possible to produce an analytic formula to calculate the average measured $\theta_{\text{c.m.}}$, $\bar{\theta}_{\text{c.m.}}$, under the simplifying assumptions that the decay products are emitted uniformly and there are no aberrations at $\theta^{\text{max}}_{\text{c.m.}}$, i.e. the positions of the detected events are known exactly. While this second assumption is not strictly true, if the aberrations are small then it is a reasonable approximation. It is the possible to calculate the average scattering angle by evaluating the mean scattering angle over all measured angles in the centre of mass frame, Ω_m, which gives

$$\begin{aligned}
\bar{\theta}_{\text{c.m.}} &= \frac{\int_{\Omega_m} \theta_{\text{c.m.}} d\Omega}{\int_{\Omega_m} d\Omega} \\
\bar{\theta}_{\text{c.m.}} &= \frac{\int_{\theta^{\text{max}}_{\text{c.m.}}}^{180} \theta_{\text{c.m.}} \sin\theta_{\text{c.m.}} d\theta_{\text{c.m.}} \int_0^{2\pi} d\phi}{\int_{\theta^{\text{max}}_{\text{c.m.}}}^{180} \sin\theta_{\text{c.m.}} d\theta_{\text{c.m.}} \int_0^{2\pi} d\phi} \\
&= \frac{\pi - \sin\theta^{\text{max}}_{\text{c.m.}} + \theta^{\text{max}}_{\text{c.m.}} \cos\theta^{\text{max}}_{\text{c.m.}}}{1 + \cos\theta^{\text{max}}_{\text{c.m.}}} .
\end{aligned} \tag{3.17}$$

3.1.3.2 Effective Target Thickness Correction

The second efficiency correction required deals with the varying effective target thickness as a function of energy. The measurement of cross-section made by the TTIK technique is made by binning the events as a function of E_x into equally sized bins. However because the energy loss of the beam through the target is not a linear function, a constant bin width will correspond to a variable target thickness. This is shown schematically in Figure 3.12. In order to understand and correct for this, the problem is treated in detail mathematically here.

The full TTIK measurement can be thought of as many thin target measurements at different energies, each directly next to each other. If it is assumed that each hypothetical thin target is of equal width, given by Δx, then the yield produced by each target, Y_i, can be defined as

$$Y_i = N.n.\Delta x.\Omega.\frac{d\sigma}{d\Omega}(E_{x,i}, \theta_{\text{c.m.}}) \tag{3.18}$$

where N is the total number of incident beam ions, n is the number of target nuclei per meter cubed,

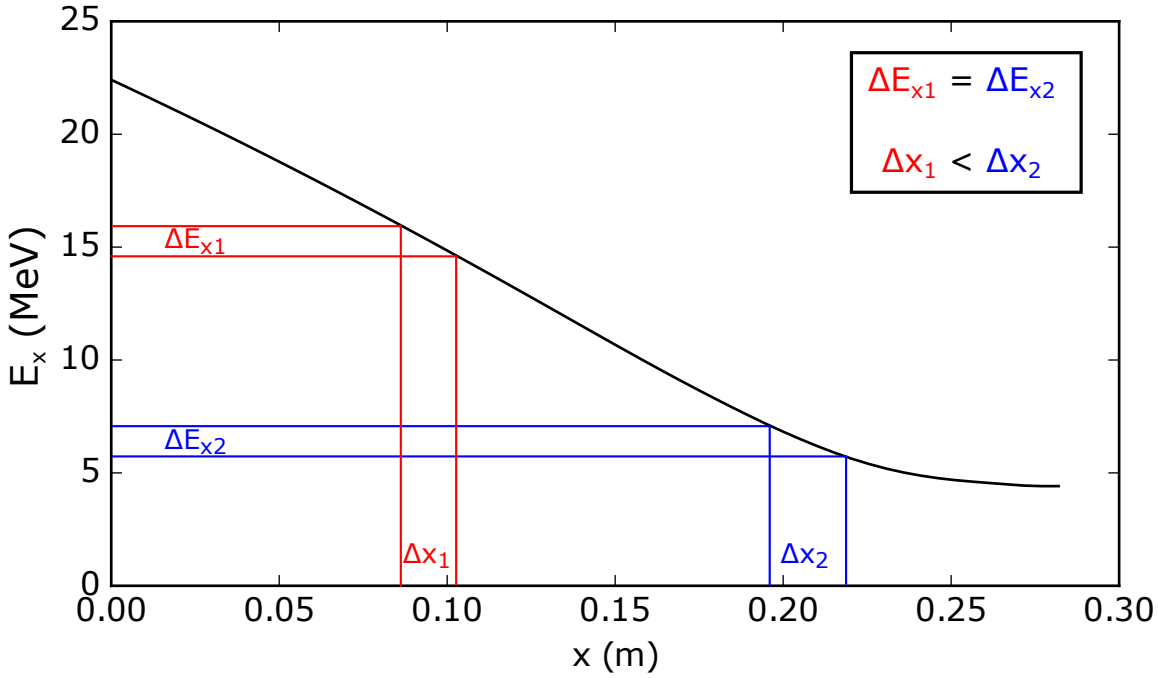

Figure 3.12: Shown here is E_x as a function of x for the ^{4}He(^{14}N,α) reaction, using the parameters for 'Measurement 1', given in Section 4. Annotated are two E_x bins with fixed bin widths, showing how this corresponds to an unequal effective target thickness.

$E_{x,i}$ is the excitation energy at the centre of target i, and Ω is the solid angle subtended by the detectors, centred on $\theta_{\text{c.m.}}$. Here it is assumed that the geometrical efficiency correction discussed in the previous section has been applied, such that Ω can be considered to be constant, and small enough such that $d\sigma/d\Omega$ is approximately constant across it. Now taking the limit that the target thickness goes to 0 gives the differential yield, dY/dx, defined as

$$\frac{dY}{dx}(E_x) = N.n.\Omega.\frac{d\sigma}{d\Omega}(E_x, \theta_{\text{c.m.}})\,. \tag{3.19}$$

However, since the TTIK measurements are made by binning the measured yield as a function of E_x, with a constant bin width, it is actually the derivative of the yield with respect to E_x that is measured, dY/dE_x. Given a bin width of ΔE_x, the yield measured in a bin centred on $E_{x,j}$, where the bins are indexed by j, is defined as

$$Y_j = \frac{dY}{dE_x}(E_{x,j})\Delta E_x\,. \tag{3.20}$$

under the assumption that the bin width is small enough that the yield does not change dramatically

across a given bin. It is possible then to use the chain rule to relate the two derivatives of yield, giving

$$\frac{dY}{dx} = \frac{dY}{dE_x}\frac{dE_x}{dx}\,. \tag{3.21}$$

The quantity dE_x/dx is related to the stopping power of the beam in the ^{4}He gas target, dE_A/dx, by Equations (3.4) and (3.5), giving

$$\frac{dE_x}{dx}(E_x) = \frac{m_\alpha}{m_A + m_\alpha}\frac{dE_A}{dx}\left((E_x - Q_f)(1 + \frac{m_A}{m_\alpha})\right)\,. \tag{3.22}$$

Finally by combining Equations (3.19), (3.20) and (3.21), an expression can be constructed giving $d\sigma/d\Omega$ in terms of Y_j

$$\frac{d\sigma}{d\Omega}(E_{x,j}, \theta_{\text{c.m.}}) = \frac{Y_j}{Nn\Omega\Delta E_x}\frac{dE_x}{dx}(E_{x,j})\,. \tag{3.23}$$

This shows that to correct for the variable target thickness, the yield must be multiplied by the stopping power of the beam in the target. This is demonstrated using the geometrical efficiency Monte Carlo simulation, discussed in the previous section. Shown in Figure 3.13 is a comparison of the results of applying only the geometrical efficiency correction and both efficiency corrections. It is evident that both corrections are required to produce the desired uniform distribution.

3.1.4 Experimental Resolution

The experimental resolution, σ_R, plays a crucial role in TTIK measurements. The spectra that are extracted from TTIK measurements are in fact a convolution of the true $d\sigma/d\Omega$ with the experimental resolution σ_R. There are many experimental factors which contribute to the observed experimental resolution in TTIK measurements:

Beam properties The beam used to make the measurements will have an intrinsic energy spreading and angular spreading, and the beam spot will have a finite size. All of these factors are dependant on the method of beam production.

Energy and angular straggling in the window, gas and absorbers The individual nuclei in the beam will be deflected slightly by interactions in the window, gas and absorbers, leading to a spreading in the energies and trajectories that the beam follows. These effects are known as energy and angular straggling, details on energy straggling can be found in Ref. [82] and on angular straggling in Ref. [83].

Intrinsic detector energy and position resolution The DSSDs will have an intrinsic energy resolution dependent on the electronics set-up and counting statistics for the electron-hole pairs. They

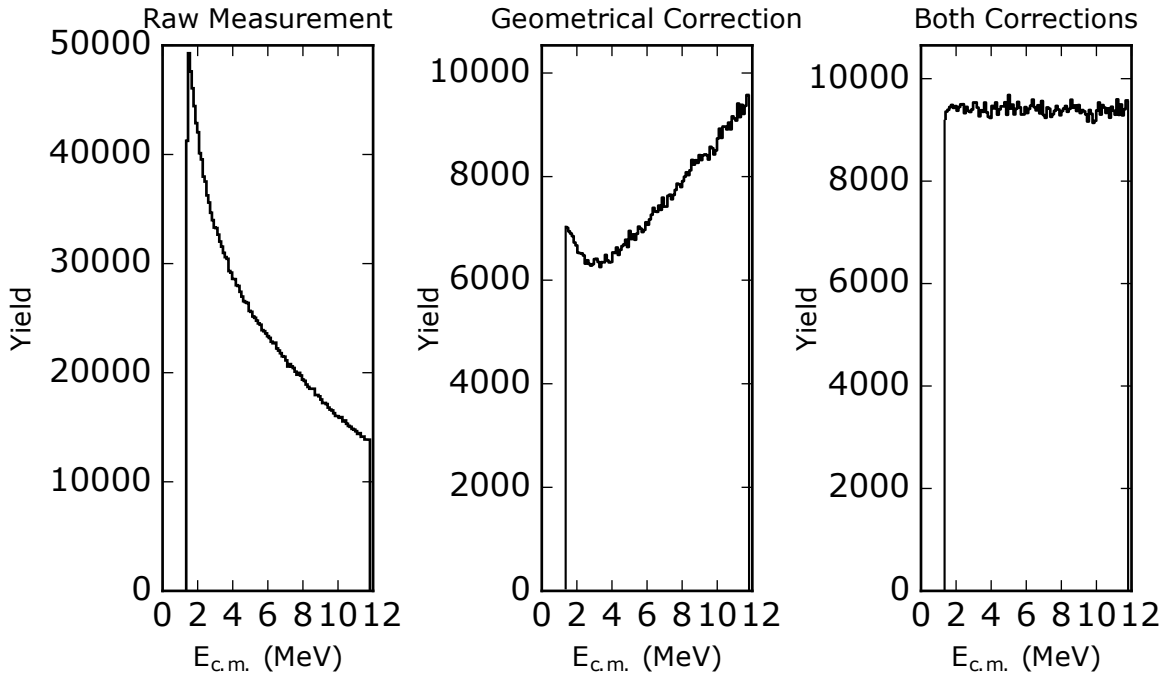

Figure 3.13: A Monte Carlo simulation of the ^{4}He(^{40}Ca,α) reaction assuming a uniform cross-section. The raw data (left), the data following only the geometrical efficiency correction (middle) and the data following both the geometrical and variable target thickness corrections (right). It is evident that both corrections are required to reproduce the expected uniform cross-section.

also have a position resolution since they can only constrain the measurements to a given pixel on the detector. This position resolution leads to an effective uncertainty on the energy via the kinematics calculations.

The degree to which each of these factors contribute to the overall experimental resolution was analysed in a review of TTIK measurements by Curtis & Walshe [84]. Here a Monte Carlo simulation was compared with TTIK measurements of the ^{4}He(^{20}Ne,α) reaction, which uses a very similar set up to both of the TTIK measurements made in this thesis. It was found in that work that the largest contribution to the overall experimental resolution, by a significant margin, was angular straggling in the window. The influence of angular straggling is minimised in measurements that are made using the 0° detectors, i.e. events at $\theta_{\text{c.m.}} = 180°$, however it causes a rapid degradation of the experimental resolution at $\theta_{\text{c.m.}}$ away from 180°.

This makes the measurement of angular distributions of individual resonances very difficult, as nearby resonances will overlap and eventually become indistinguishable as the resolution degrades at smaller $\theta_{\text{c.m.}}$. This is especially a problem for measurements of heavier systems, where one would expect the level density to be higher [63]. These angular distributions are often crucial for the assignments of spins and parities, as is discussed in Section 3.2.

There has been a variety of attempts to circumvent this problem. The most common of these is to incorporate σ_R into the analysis using a convolution, as was done for TTIK measurements of ^{32}S, ^{34}S, ^{36}Ar and ^{40}Ca [66–69]. Here a Simplified $\boldsymbol{R}$-matrix fit was performed on the data, which were taken over a range of E_x and $\theta_{\text{c.m.}}$. This method is discussed in Section 3.2.4, however in cases of poor resolution it is a very slow and difficult analysis and often leads to ambiguous results since many of the details in the spectrum remain hidden. A similar process was performed for the TTIK measurement of ^{28}Mg [74], however here only resonances which could be clearly separated from the other resonances in the spectrum were analysed. This allowed the assumption to be made that only one resonance contributed to the spectrum in that region, which reduced the ambiguities in the analysis, but lead to large amounts of the measurements being discarded. Another possible solution would be to attempt to deconvolve the measured experimental spectra prior to the analysis. Deconvolution is a process which is used extensively in image analysis and astronomy [85], however it is rarely applied to measurements of this type.

Finally one may simply constrain the analysis to only the measurements that are made at $\theta_{\text{c.m.}} = 180^\circ$, hence ensuring optimal resolution. The difficulty here is that the analysis must then proceed without any angular distribution measurements, precluding the identification of spins and parities of states using traditional methods. In some cases the shapes of the resonance and the interference between the resonances at 180° can be used to identify the spins, by simply trying various spin/parity combinations for all of the states in the relevant energy region until the $\boldsymbol{R}$-matrix calculation matches the observed spectrum. This technique however is limited to spectra with a low level density, producing ambiguous results when applied to more complex spectra.

3.1.5 Inelastic Contaminants

As discussed previously, ΔE-E particle identification is used to separate out the different decay products and hence different reactions in TTIK measurements. A difficulty encountered in TTIK measurements is that this technique relies on the different masses and charges of the decay products to separate them, which means it cannot distinguish between reactions which emit nuclei in their ground states (elastic reactions) and those which emit nuclei in excited states (inelastic reactions). This is a problem since it means that measurements of $^4\text{He}(A, y_0)R$ may be contaminated by the reactions $^4\text{He}(A, y_{1,2,3\ldots})R$. Here the notation $^4\text{He}(A, y_i)R$ refers to the i^{th} lowest excitation of either y or R. In the following discussion a technique is developed to distinguish between the reaction which proceeds via the lowest excited state, $^4\text{He}(A, y_1)R$, from the ground state reaction, since if this is achieved then the spectrum will also be necessarily clean from all higher excitations.

There are two regions of the measured spectra which are guaranteed energetically to be clean of

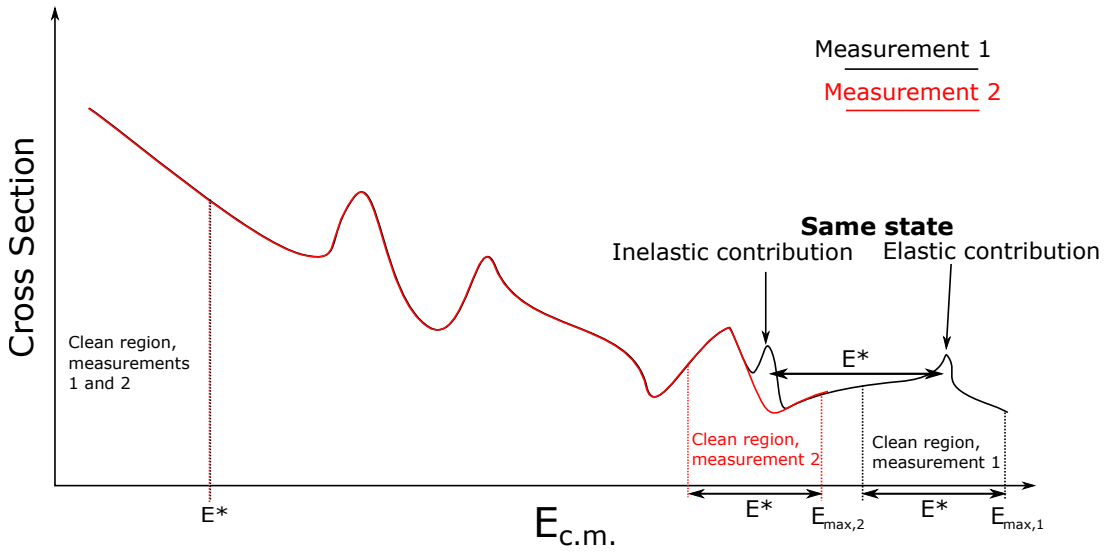

Figure 3.14: A schematic diagram depicting two experimental runs with different maximum measured energies. The regions of the measurements that are free from inelastic contributions are annotated as clean regions, and the identification of an inelastic contribution is shown. Here $E*$ represents the excitation energy of the inelastic decay channel and E_{max} represents the maximum measured energy for a given measurement.

inelastic contaminants. These both occur due to the energy that is lost to the internal excitation of the decay product, referred to here as E^*. The first of these is the region of the spectrum where $E_{\text{c.m.}}$ is smaller than E^*. This is guaranteed to be free from inelastic contaminants since there is not enough energy in the system to excite the decay product. The second inelastic free region is found close to the highest measured $E_{\text{c.m.}}$, referred to as $E_{\text{c.m.}}^{\text{max}}$. In the case that $E_{\text{c.m.}} + E^* > E_{\text{c.m.}}^{\text{max}}$, the sum of the energy required to populate the excited state plus the kinetic energy given to the decay product is larger than the maximum centre of mass energy generated in the measurement, making it impossible to populate the inelastic channel. These two regions are depicted schematically in Figure 3.14.

If E^* is very large, then these clean regions will often cover the entire measured energy range, ensuring that it is entirely clean of inelastic contaminants. However in the case that E^* is small, these clean regions may only cover a small range of the measured energies. In this case the low energy clean region is often not useful, as it only covers the low energy portion of the spectrum, which is dominated by Rutherford scattering rather than resonances. The high energy clean region can still be used effectively however. This is done by making multiple measurements with varying $E_{\text{c.m.}}^{\text{max}}$, producing clean regions which span different energy ranges for each measurement. By the comparison of the spectrum in the clean region of one measurement with the same region in a different measurement, any inelastic contributions will show up as differences in the spectra. This is shown in Figure 3.14. The dif-

ferent energy ranges are often generated using a variety of combinations of absorber thicknesses, initial beam energies and gas pressures. If many measurements are made it is possible to ensure that the entire measurement is clean of inelastic contaminants, or making fewer measurements simply allows the evaluation of the order of magnitude of the inelastic contributions at various points throughout the spectrum.

3.2 R-Matrix Theory

$\boldsymbol{R}$-matrix theory is a method of computing the differential cross-section, $d\sigma/d\Omega$, of a given two body reaction. This formalism is based on the compound nucleus picture of nuclear reactions, whereby the incoming nuclei fuse to form an intermediate 'compound' nucleus before decaying into the outgoing particles, shown in Figure 3.15. The argument is made that the compound nucleus is long lived compared to the time-scale of the reaction and as a consequence the outgoing particles have no dependence on the properties of the incoming particles, only on the compound nucleus [86].

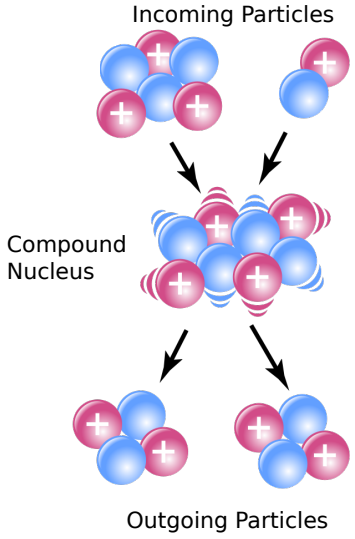

Figure 3.15: A schematic diagram of the three stages of a compound nucleus reaction, adapted from [87]

$\boldsymbol{R}$-matrix theory generates $d\sigma/d\Omega$ from the energies, E_λ, spins, J_λ, parities, π_λ, and reduced widths, $\gamma_{\mu\lambda}$, of resonant states in the compound nucleus, indexed by λ. It can be used in one of two ways. The first of these is the calculable $\boldsymbol{R}$-matrix, whereby the properties of the states are calculated from some appropriately chosen nuclear model, and then $\boldsymbol{R}$-matrix theory is used to generate the reaction cross-sections which can be compared with experimental data. The second method is the phenomenological $\boldsymbol{R}$-matrix. In this instance, the properties of the states of the compound nucleus are treated as free parameters, and $\boldsymbol{R}$-matrix theory is used to generate a reaction cross-section which is then fitted

to experimental data. Once the fit has been completed, the parameters are then taken to be the true levels and widths of the compound nucleus, and it is these levels and widths that are compared to theory. In this work the phenomenological $\boldsymbol{R}$-matrix is used in Section 4 and a simplified version of the calculable $\boldsymbol{R}$-matrix is used in Section 5.

The cross-section produced by $\boldsymbol{R}$-matrix theory consists in general of up to three components. These are the Rutherford contribution, potential contribution and resonant contribution. The Rutherford contribution reproduces classical Rutherford scattering, which arises from the scattering of two point charges, and is only present in the elastic scattering cross-section (i.e. the case where the outgoing nuclei are identical to the incoming nuclei). The potential contribution arises due to the finite size of the nuclei involved in the scattering, which is not taken into account by the Rutherford contribution, and is also only present in the elastic scattering cross-section. In standard $\boldsymbol{R}$-matrix theory it is the hard-sphere potential contribution which arises naturally, and this is discussed in Section 3.2.2.5. Finally the resonant contribution is the contribution from the resonances which arise from the states in the compound nucleus. It is the analysis of these resonances in particular that lead to the extraction of structural information. Both the potential and Rutherford contribution are slowly varying as a function of energy.

$\boldsymbol{R}$-matrix theory was first introduced by Kapur and Peierls in 1938 [88], and then by Wigner and Eisenbud in 1947 [89]. It was also summarised extensively in the review by Lane and Thomas in 1958 [86]. Since then $\boldsymbol{R}$-matrix theory has proved to be a very effective tool for extracting quantitative information about the underlying structure of nuclei from measurements of the differential cross-section of nuclear reactions. The greatest advantage of $\boldsymbol{R}$-matrix theory is that it is a rigorous theory, based on very few assumptions. The assumptions it does make are discussed in detail in Ref. [86], and are as follows:

1. Non-relativistic quantum mechanics is applicable.

2. Absence or unimportance of all processes which proceed via the production of more than two nuclei.

3. Absence or unimportance of all processes of creation or destruction. The main implication of this is that photons may not be described by $\boldsymbol{R}$-matrix theory, however it is possible to introduce photon channels using pertubation theory [86].

4. The existence of a finite radial separation, beyond which the nuclear force may be ignored. This limit is known as the interaction radius.

The most important and useful results of $\boldsymbol{R}$-matrix theory and their applications to the analysis of

experimental data are discussed in detail in the book Nuclear Reactions for Astrophysics by Thompson and Nunes [63]. This is referenced extensively in the following sections.

3.2.1 Defining the Problem

The assumptions upon which $\boldsymbol{R}$-matrix theory is derived lead to two main concepts: reaction channels and the interaction radius. If the full n-nucleon quantum mechanical problem were to be solved rigorously, it would need to be solved in 3n-dimensional space. To simplify this problem, reaction channels are introduced such that within these channels the nucleons form two distinct nuclei. The wavefunction in the configuration space outside the channels is set to zero, which effectively removes any probability of the reaction proceeding by any other route, reducing the n-body problem to a 2-body problem. The 2-body reaction is then defined by specifying an entrance channel, μ, and an exit channel, μ'. In the following sections the reactions are defined as: $t_\mu(p_\mu, p_{\mu'})t_{\mu'}$, where t represents the target nucleus and p represents the projectile nucleus for each reaction channel.

The reaction channels are defined primarily by the particle pair, tp, noting here that if either of the outgoing nuclei are left in an excited state this is considered to be a unique particle pair. However, the reaction channels are also defined by their angular momentum couplings:

- The channel spin, $\vec{S_\mu}$, and projection, s_μ, are defined by the coupling of the projectile and target spins, $\vec{I_{p_\mu}}$ and $\vec{I_{t_\mu}}$, and their projections i_{p_μ} and i_{t_μ}.
- The total spin and parity of the compound nucleus, J^π, is calculated by the coupling of the channel spin, $\vec{S_\mu}$, to the relative orbital angular momentum of the particle pair, $\vec{L_\mu}$, with the angular momentum projection M_μ.

These couplings are defined mathematically as

$$\vec{S_\mu} = \vec{I_{t_\mu}} + \vec{I_{p_\mu}} \qquad s_\mu = i_{t_\mu} + i_{p_\mu} \tag{3.24}$$

$$\vec{J} = \vec{L_\mu} + \vec{S_\mu} \qquad M_J = M_\mu + s_\mu \qquad \pi = (-1)^{L_\mu}\pi_{t_\mu}\pi_{p_\mu}\,. \tag{3.25}$$

Since angular momenta couple via vector addition, there may be more than one possible S_μ and L_μ for a given tp, which leads to multiple channels for that particle pair, each with a unique channel spin and orbital angular momentum. Hence the definition of an $\boldsymbol{R}$-matrix channel requires the definition of both the channel spin and orbital angular momentum as well as the particle pair, i.e. μ defines $\{t_\mu p_\mu S_\mu L_\mu\}$. The full $\boldsymbol{R}$-matrix calculation sums over all of the possible values of S_μ and L_μ to produce the overall cross-section for the reaction.

The interaction radius, R_μ, is defined for each reaction channel as

$$R_\mu = r_0 \left(A_{t_\mu}^{\frac{1}{3}} + A_{p_\mu}^{\frac{1}{3}} \right) \tag{3.26}$$
$$r_0 \sim 1.3\,\text{fm}\,.$$

It is argued that the nuclear force is only relevant at nuclear separations smaller than this interaction radius. Outside of this range the nuclear force is ignored, and only the Coulomb force is considered, which can be solved exactly for a 2-body system giving the *external* wavefunction. At separations smaller than the interaction radius, all the nucleons are assumed to be interacting via the nuclear force. This is considered to be the compound nucleus stage of the reaction, and it is in this region that the $\boldsymbol{R}$-matrix is defined and used to calculate the *internal* wavefunction. The cross-section, $d\sigma/d\Omega$, is then calculated by matching the *internal* and *external* wavefunctions at the interaction radius, for both the entrance and exit channels. These ideas are displayed schematically in Figure 3.16.

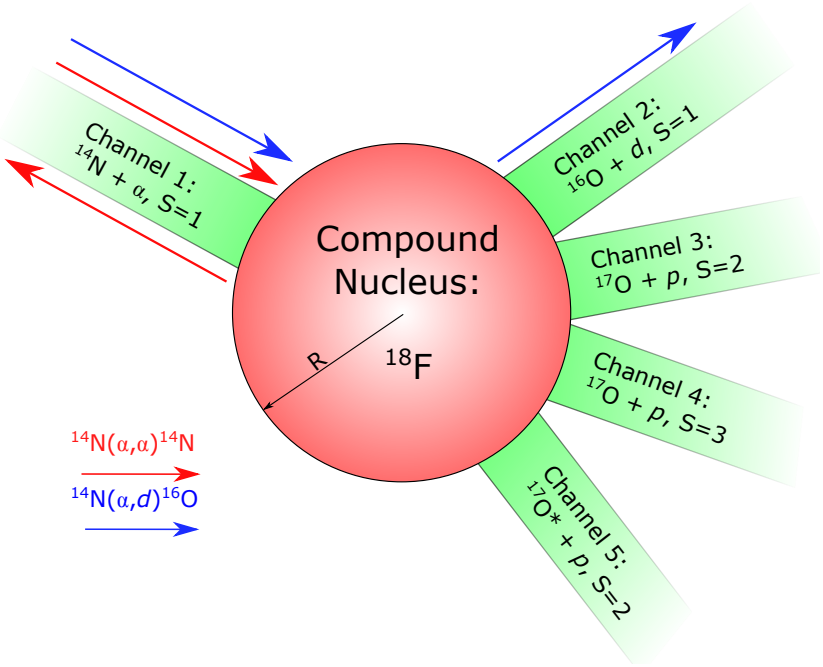

Figure 3.16: A schematic diagram of reaction channels in configuration space, using the example of the ^{18}F compound nucleus. S = channel spin, R = interaction radius.

Everything is calculated in the centre of mass (c.m.) frame. The centre of mass energy of the nuclei in a given channel μ, E_μ, is related to the centre of mass energy in another channel, μ', simply by the Q-value of the relevant reaction, $E_{\mu'} = E_\mu + Q_{\mu\mu'}$. For simplicity the centre of mass energy of the entrance channel is referred to as E, dropping the index μ. The reduced mass, m_μ, and momentum,

k_μ, for a given channel are then defined as

$$m_\mu = \frac{m_{p_\mu} m_{t_\mu}}{m_{p_\mu} + m_{t_\mu}} \tag{3.27}$$

$$k_\mu = \frac{\sqrt{2 m_\mu E_\mu}}{\hbar} . \tag{3.28}$$

3.2.2 The General Case of Non-Zero Spins and Multiple Channels

3.2.2.1 Cross-section Calculation

The differential cross-section, $d\sigma/d\Omega$, is defined by combining a complex nuclear amplitude, f_N, and Coulomb, or Rutherford, amplitude f_R. All of these quantities depend both on E and the centre of mass scattering angle, $\theta_{\text{c.m.}}$, referred to as θ in this section for simplicity. The Rutherford amplitude occurs only in the elastic reaction channel, and if used alone reproduces the classical Rutherford scattering formula [90]. The nuclear amplitude is dependent on the elements of the scattering matrix, $\widetilde{\boldsymbol{S}}$, which is calculated from the $\boldsymbol{R}$-matrix and contains all of the properties pertaining to the underlying structure of the compound nucleus.

The nuclear amplitude is dependent on the spin projection (polarisation) of the nuclei involved. Here it is assumed that an unpolarised beam is used, so the final cross-section is given by averaging over all of the incident polarisations and summing over all of the outgoing polarisations. The Rutherford amplitude only contributes if the polarisation does not change during the reaction. The cross-section is defined as [63]

$$\frac{d\sigma}{d\Omega}(\theta, E) = \frac{1}{(2I_{t_\mu}+1)(2I_{p_\mu}+1)} \sum_{i_{p\mu'} i_{t\mu'} i_{p\mu} i_{t\mu}} \left| \delta_{i_{t\mu} i_{t\mu'}} \delta_{i_{p\mu} i_{p\mu'}} \delta_{\mu\mu'} f_R(\theta, E) + f_N(\theta, E) \right|^2 \tag{3.29}$$

The Rutherford amplitude is calculated by considering the point Coulomb potential between the target and projectile nuclei

$$V_{C\,\mu}(r) = \frac{e^2}{4\pi\epsilon_0} \frac{Z_{t_\mu} Z_{p_\mu}}{r} \tag{3.30}$$

where r is their separation. The solutions of the 3-dimensional Schrödinger equation in the presence of this potential are the regular and irregular Coulomb wavefunctions, $F_L(\eta_\mu, \rho_\mu)$ and $G_L(\eta_\mu, \rho_\mu)$ respectively, where L is the orbital angular momentum of the two-body system and η_μ is the Sommerfield parameter. Both η_μ and ρ_μ are defined as

$$\eta_\mu = \frac{e^2}{4\pi\epsilon_0 \hbar^2} \frac{Z_{t_\mu} Z_{p_\mu} m_\mu}{k_\mu} \tag{3.31}$$

$$\rho_\mu = k_\mu r . \tag{3.32}$$

The regular and irregular wavefunctions are distinguished by the fact that they go to 0 and infinity at $\rho_\mu = 0$ respectively. The Coulomb wavefunctions are defined in Ref. [63], and discussed in more detail in Appendix A. The external wavefuncion may be constructed in general as a linear combination of $F_L(\eta_\mu, \rho_\mu)$ and $G_L(\eta_\mu, \rho_\mu)$. $\boldsymbol{R}$-matrix theory is derived by matching this external wavefunction to the internal wavefunction at R_μ, so the Coulomb wavefunctions are evaluated at $\rho_\mu = k_\mu R_\mu$.

Following this it is possible to derive f_R. This is done in Ref. [63], and leads to the following expression for the Rutherford amplitude

$$f_R(\theta, E) = -\frac{\eta_\mu}{2k_\mu \sin^2\left(\frac{\theta}{2}\right)} \exp\left[-i\eta_\mu \ln\left(\sin^2\left(\frac{\theta}{2}\right)\right) + 2i\sigma_0(\eta_\mu)\right] . \tag{3.33}$$

where $\sigma_0(\eta)$ is the Coulomb phase shift, $\sigma_L(\eta)$, at $L = 0$. This is defined as follows, where $\Gamma(x)$ is the standard mathematical Gamma function

$$\sigma_L(\eta) = \arg\left[\Gamma\left(1 + L + i\eta\right)\right] . \tag{3.34}$$

The nuclear amplitude is calculated by summing the $\widetilde{\boldsymbol{T}}$-matrix, which is a simple reparametrisation of the scattering matrix, $\widetilde{\boldsymbol{S}}$, over all of the possible angular momentum couplings, combined with the appropriate coefficient, K, which is dependant on the angular momentum coupling and scattering angle, and a phase factor

$$f_N(\theta, E) = \frac{4\pi}{k_\mu} \sum_{\substack{L_\mu L_{\mu'} S_\mu S_{\mu'} \\ s_\mu s_{\mu'} M_J J}} K^{JM_J}_{L_\mu L_{\mu'} S_\mu S_{\mu'} s_\mu s_{\mu'}}(\theta) \widetilde{\boldsymbol{T}}^{J^\pi}_{\mu\mu'}(E) e^{i\left[\sigma_{L_\mu}(\eta_\mu) + \sigma_{L_{\mu'}}(\eta_{\mu'})\right]} \tag{3.35}$$

The K coefficient is defined using a combination of Clebsch-Gordan coefficients [91] and spherical harmonics. The Clebsch-Gordan coefficient, $\langle S_1 s_1, S_2 s_2 | S_3 s_3 \rangle$, describes the angular momentum coupling of S_1 to S_2 to produce S_3. It arises here from the coupling of the intrinsic nuclear spin of the target and projectile to produce the channel spin, and the coupling of the channel spin to the orbital angular momentum to produce the spin of the compound nucleus. The spherical harmonics, $Y^M_L(\vec{k})$, define the angular distribution of the decay products. The K coefficient is defined in terms of these as

$$\begin{aligned} K^{JM_J}_{L_\mu L_{\mu'} S_\mu S_{\mu'} s_\mu s_{\mu'}}(\theta) =& \langle I_{p_\mu} i_{p_\mu}, I_{t_\mu} i_{t_\mu} | S_\mu s_\mu \rangle \langle L_\mu M_\mu, S_\mu s_\mu | J M_J \rangle \langle I_{p_{\mu'}} i_{p_{\mu'}}, I_{t_{\mu'}} i_{t_{\mu'}} | S_{\mu'} s_{\mu'} \rangle \\ & \times \langle L_{\mu'} M_{\mu'}, S_{\mu'} s_{\mu'} | J M_J \rangle Y^{M_\mu}_{L_\mu}(\vec{k}_\mu)^* Y^{M_{\mu'}}_{L_{\mu'}}(\vec{k}_{\mu'}) . \end{aligned} \tag{3.36}$$

This expression can be simplified by setting the co-ordinates such that the incident projectile is travelling in the $+\hat{\boldsymbol{z}}$ direction. This fixes the first spherical harmonic, and then the second can simply

be written in terms of the centre of mass scattering angles θ, ϕ

$$Y_{L_\mu}^{M_\mu}(\hat{z}) = \delta_{M_\mu 0}\sqrt{\frac{2L_\mu+1}{4\pi}} \tag{3.37}$$

$$Y_{L_{\mu'}}^{M_{\mu'}}(\theta,\phi) = \sqrt{\frac{2L_{\mu'}+1}{4\pi}\frac{(L_{\mu'}-M_{\mu'})!}{(L_{\mu'}+M_{\mu'})!}}P_{L_{\mu'}}^{M_{\mu'}}(\cos\theta)\mathrm{e}^{i\phi}\,. \tag{3.38}$$

where the associated Legendre polynomial, P_L^M, is normalised such that $P(1) = 1$. The $\widetilde{\boldsymbol{T}}$-matrix is defined in terms of the $\widetilde{\boldsymbol{S}}$-matrix as

$$\widetilde{\boldsymbol{T}}_{\mu\mu'}^{J^\pi} = \frac{i}{2}\left[\delta_{\mu\mu'} - \widetilde{\boldsymbol{S}}_{\mu\mu'}^{J^\pi}\right]\,. \tag{3.39}$$

The $\widetilde{\boldsymbol{S}}$-matrix is calculated using the $\boldsymbol{R}$-matrix in the following section. There is a separate $\widetilde{\boldsymbol{S}}$-matrix and $\boldsymbol{R}$-matrix for each J^π.

3.2.2.2 The R-Matrix and A-Matrix

The $\boldsymbol{R}$-matrix is defined in terms of the reduced widths, $\gamma_{\mu\lambda}$, and pole energies, e_λ, of the states of the compound nucleus, $|X_\lambda\rangle$. The reduced widths are defined in terms of the value of the wavefunction at the matching radius in decay channel μ as

$$\gamma_{\mu\lambda} = \sqrt{\frac{\hbar^2}{2m_\mu R_\mu}}\langle R_\mu|X_\lambda\rangle\,. \tag{3.40}$$

Equation (3.40) is usually only used in the case of the calculable $\boldsymbol{R}$-matrix, whereas with the phenomenological $\boldsymbol{R}$-matrix the reduced widths are simply treated as free parameters. The $\boldsymbol{R}$-matrix is then calculated as follows, summing over all the levels of a given J^π,

$$\boldsymbol{R}_{\mu\mu'}^{J^\pi} = \sum_\lambda \frac{\gamma_{\mu\lambda}\gamma_{\mu'\lambda}}{e_\lambda - E}\,. \tag{3.41}$$

From this the $\widetilde{\boldsymbol{S}}$-matrix is calculated by matching the internal and external wavefunctions at the matching radius. The mathematics of this wavefunction matching is not shown here, for more detail see Ref. [63]. The $\widetilde{\boldsymbol{S}}$-matrix is defined as

$$\widetilde{\boldsymbol{S}}_{\mu\mu'}^{J^\pi} = \Omega_\mu\left[\delta_{\mu\mu'} + 2iP_\mu^{1/2}(\boldsymbol{I} - \boldsymbol{R}^{J^\pi}(\boldsymbol{S}^0 + i\boldsymbol{P}))_{\mu\mu'}^{-1}\boldsymbol{R}_{\mu\mu'}^{J^\pi}P_{\mu'}^{1/2}\right]\Omega_{\mu'} \tag{3.42}$$

where $\boldsymbol{I}$ is the identity matrix, $\delta_{\mu\mu'}$ is the kronecker delta, and $\boldsymbol{S}^0$ and $\boldsymbol{P}$ are diagonal matrices with elements S_μ^0 and P_μ respectively. The shift function, S_μ^0, penetrability, P_μ, and hard-sphere phase

shift Ω_μ are all energy and angular momentum dependent quantities calculated from the Coulomb wavefunctions. These are defined in Appendix A. Of these, P_μ is of particular physical significance, as it is the barrier penetrability through the combined Coulomb and centrifugal barriers in channel μ.

It is possible to redefine the $\boldsymbol{R}$-matrix as a level matrix, rather than a channel matrix. This is the $\boldsymbol{A}$-matrix. Using the $\boldsymbol{A}$-matrix produces identical results to the $\boldsymbol{R}$-matrix, however it is more computationally efficient in the case that there are many open channels and few compound levels. The $\boldsymbol{A}$-matrix is defined and used to calculate the $\widetilde{\boldsymbol{S}}$-matrix as follows:

$$(\boldsymbol{A}^{J^\pi\,-1})_{\lambda\lambda'} = \delta_{\lambda\lambda'}(e_\lambda - E) - \sum_\mu \gamma_{\mu\lambda}\left(S^0_\mu + iP_\mu\right)\gamma_{\mu\lambda'} \tag{3.43}$$

$$\widetilde{\boldsymbol{S}}^{J^\pi}_{\mu\mu'} = \Omega_\mu\left[\delta_{\mu\mu'} + 2i\sum_{\lambda\lambda'} P^{1/2}_\mu \gamma_{\mu\lambda}\boldsymbol{A}^{J^\pi}_{\lambda\lambda'}P^{1/2}_\mu\gamma_{\mu'\lambda'}\right]\Omega_{\mu'}\,. \tag{3.44}$$

3.2.2.3 R-Matrix Observables

The parameters used to generate the $\boldsymbol{R}$-matrix, e_λ and $\gamma_{\mu\lambda}$, are not themselves physical observables. They are instead related to the actual physical observables, the resonance energy, E_λ, and partial widths, $\Gamma_{\mu\lambda}$, by S^0_μ and P_μ as

$$\Gamma_{\mu\lambda} = 2P_\mu\gamma^2_{\mu\lambda} \tag{3.45}$$

$$E_\lambda = e_\lambda - \sum_\mu S^0_\mu\gamma^2_{\mu\lambda}\,. \tag{3.46}$$

It is important to note here however that S^0_μ and P_μ are both energy dependent quantities, which means that the resonance energy and partial widths will also vary as a function of energy. In the literature the values for these observables are usually quoted as being their values at the resonance energy E_λ, which must be calculated iteratively using Equations (3.45) and (3.46). The total width for a given state is defined as the sum over all partial widths, $\Gamma_\lambda = \sum_\mu \Gamma_{\mu\lambda}$. It is often preferable to use the physical observables, E_λ and $\Gamma_{\mu\lambda}$, as the input parameters to $\boldsymbol{R}$-matrix theory, instead of e_λ and $\gamma_{\mu\lambda}$, especially when it is being used phenomenologically to fit experimental data. This can be done using the Brune transformation [92], which uses matrix algebra to provide either the calculation of e_λ and $\gamma_{\mu\lambda}$ from E_λ and $\Gamma_{\mu\lambda}$, or the calculation of the $\widetilde{\boldsymbol{S}}$-matrix directly from E_λ and $\Gamma_{\mu\lambda}$.

Factoring the penetrability out of $\Gamma_{\mu\lambda}$ leaves behind only $\gamma^2_{\mu\lambda}$. This suggests that $\gamma^2_{\mu\lambda}$ is related to the preformation factor for channel μ. It is important to remember here that the channel, μ, is dependent not only on the particle pair and excitations of the outgoing nuclei, but also on channel spin and orbital angular momentum. These latter two parameters are unimportant, and one would ideally look to extract an overall $\Gamma_{tp\lambda}$ and $\gamma_{tp\lambda}$ for a given particle pair, tp, which may contain many channels, μ.

This is straightforward for the partial width, as it is simply the sum over the partial widths for all valid channels,

$$\Gamma_{tp\lambda} = \sum_{\mu} \Gamma_{\mu\lambda} \,. \tag{3.47}$$

The overall reduced width is then calculated by defining an average penetrability for tp, $P_{tp\lambda}$, as the weighted sum over all valid channels

$$P_{tp\lambda} = \frac{\sum_{\mu} \gamma^2_{\mu\lambda} P_{\mu}}{\sum_{\mu} \gamma^2_{\mu\lambda}} \,. \tag{3.48}$$

Then if it is assumed that $\Gamma_{tp\lambda}$ is related to $\gamma_{tp\lambda}$ via this average penetrability in exactly the same way as it is for the channel reduced width in Equation (3.45), it follows that $\gamma^2_{tp\lambda}$ must be defined as the sum over all valid $\gamma^2_{\mu\lambda}$. This is presented explicitly as

$$\Gamma_{tp\lambda} = 2 P_{tp\lambda} \gamma^2_{tp\lambda} \tag{3.49}$$

$$\gamma^2_{tp\lambda} = \sum_{\mu} \gamma^2_{\mu\lambda} \,. \tag{3.50}$$

The overall reduced width, $\gamma_{tp\lambda}$, is interpreted as being related to the likelihood of the particle pair tp forming within the compound nucleus. It is often informative to compare $\gamma^2_{tp\lambda}$ with the Wigner limit, γ^W_{tp}, which is a theoretical upper limit for the overall reduced width. It is calculated under the assumption that the wavefunction is constant inside R_{μ} and zero outside [63]. It is defined as

$$\gamma^W_{tp} = \sqrt{\frac{3\hbar^2}{2 m_{\mu} R^2_{\mu}}} \,. \tag{3.51}$$

The ratio to the Wigner limit, $\theta^2_{tp\lambda}$, is often used to indicate the importance of the particle pair tp to the structure of the state λ [63], and is defined explicitly as

$$\theta^2_{tp\lambda} = \frac{\gamma^2_{tp\lambda}}{\gamma^{W\,2}_{tp}} \,. \tag{3.52}$$

This is especially common in studies of α-clustering, where the ratio to the Wigner limit for the α-channel, $\theta^2_{\alpha\lambda}$, is used as an indicator of the degree of α-clustering in that state.

3.2.2.4 Convolution with Experimental Resolution

In order to accurately compare the predicted cross-section with the experimental data, it must first be convoluted with the experimental resolution, σ_R. This is done by assuming that the point spread

function for the experimental set up is a Gaussian, which leads to

$$\frac{d\sigma}{d\Omega}'(E) = \frac{1}{\sqrt{2\pi\sigma_R^2}} \int_0^\infty \exp\left(-\frac{(E-\epsilon)^2}{2\sigma_R^2}\right) \frac{d\sigma}{d\Omega}(\epsilon) d\epsilon \,. \tag{3.53}$$

In general σ_R may depend on E, however in the cases presented in this work it is reasonably approximated as a constant.

3.2.2.5 Hard Sphere Phase Shift

The parameter Ω_μ is the hard sphere phase shift, and is used in Equations 3.42 and 3.44. It dictates primarily the type of interference between each of the partial waves of the nuclear amplitude, and the Coulomb amplitude, and in the case of elastic scattering it also defines the potential contribution to the cross-section. It is known as the hard sphere phase shift because it is the same phase shift that is produced in the case of the scattering of two hard spheres, i.e. in the case that there is zero probability of the two spheres inter-penetrating each other. This arises because of the fixed interaction radius used to match the boundary conditions in $\boldsymbol{R}$-matrix theory.

The hard sphere phase shift is usually not a good approximation to the true phase shifts observed in nuclear reactions, and so it is often changed in one of two ways. The first way is to use the optical model to produce more accurate phase shifts, and then simply replace Ω_μ with those. This is done in the analysis of the resonant reactions ^{14}N(α,α) resonant reaction [93]. The second way is to introduce background poles at high excitation energies, and then allow the properties of these poles to vary, essentially allowing the phase shifts to be fitted to the data. This technique has the additional benefit that the background poles also serve to imitate the effect produced by the interference of higher energy resonances with resonances in the energy range under investigation.

3.2.2.6 Boundary Condition and Interaction Radius Consistency

The derivation of $\boldsymbol{R}$-matrix theory, which is detailed in Ref. [63], requires the definition of a fixed boundary condition, β, which fixes the value of the logarithmic derivative of the internal wavefunction at the interaction radius, R_μ. This ensures the orthogonality of the internal wavefunctions. The value of β may be any real number, and may take a different value for each unique J^π.

It is important to note, however, that both β and R_μ are not physically significant parameters, they are just products of the derivation of $\boldsymbol{R}$-matrix theory. It is reasonable to suggest, therefore, that the physical observables which are extracted from an $\boldsymbol{R}$-matrix fit, E_λ and $\Gamma_{\mu\lambda}$, ought to be independent of these quantities. This is in contrast to the $\boldsymbol{R}$-matrix parameters, e_λ and $\gamma_{\mu\lambda}$, which one would expect to depend heavily on β and R_μ. This fact is often used to test the robustness of an $\boldsymbol{R}$-matrix

analysis, by varying the interaction radius and boundary conditions and observing any variations in the extracted physical observables. If the fit is robust the physical parameters ought to change by an amount consistent with their error bars.

3.2.3 The Spin Zero Single Channel Case

$\boldsymbol{R}$-matrix theory is greatly simplified in the case that all of the nuclei involved are spin-0, and that there is only one open decay channel. The existence of only one decay channel simplifies the $\boldsymbol{R}$-matrix and $\widetilde{\boldsymbol{S}}$-matrix, since they are both reduced to 1x1 matrices. These are defined as follows, where the index μ has been dropped in all cases,

$$\boldsymbol{R}^L = \sum_\lambda \frac{\gamma_\lambda^2}{e_\lambda - E} \tag{3.54}$$

$$\widetilde{\boldsymbol{S}}^L = \Omega^2 \frac{1 - \boldsymbol{R}^L(S^0 - iP)}{1 - \boldsymbol{R}^L(S^0 + iP)} \,. \tag{3.55}$$

The calculation of f_N and the cross-section $d\sigma/d\Omega$ are simplified by the fact that the nuclei involved are spin-0. This removes much of the angular momentum coupling required in the general formulae, as the channel-spin is necessarily also 0, meaning that the total spin is equal to the orbital angular momentum, $J = L$, and therefore only natural parity states are allowed. This reduces many of the summations and simplifies the calculation, leading to the following expressions, where the $\boldsymbol{R}$-matrix and $\widetilde{\boldsymbol{S}}$-matrix are calculated for each L separately,

$$f_N(\theta) = \frac{1}{2ik} \sum_{L=0}^{\infty} (2L+1) P_L(\cos(\theta) e^{2i\sigma_L(\eta)} (\widetilde{\boldsymbol{S}}^L - 1) \tag{3.56}$$

$$\frac{d\sigma}{d\Omega}(\theta) = |f_R(\theta) + f_N(\theta)|^2 \,. \tag{3.57}$$

Here P_L is the Legendre polynomial, the Rutherford amplitude is defined as before in Equation (3.33).

3.2.4 The Simplified R-Matrix

An $\boldsymbol{R}$-matrix calculation is performed by first calculating either the $\boldsymbol{R}$-matrix or $\boldsymbol{A}$-matrix, then calculating the $\widetilde{\boldsymbol{S}}$-matrix, before finally calculating $d\sigma/d\Omega$, which is then convoluted with the experimental resolution before it is compared with data. This process is shown schematically in Figure 3.17. This is quite a complex calculation to perform in the general case described here, and can be quite computationally intensive. Therefore in many cases a simplified version of the calculation is performed.

The majority of the computational time in an $\boldsymbol{R}$-matrix calculation is spent on calculating the

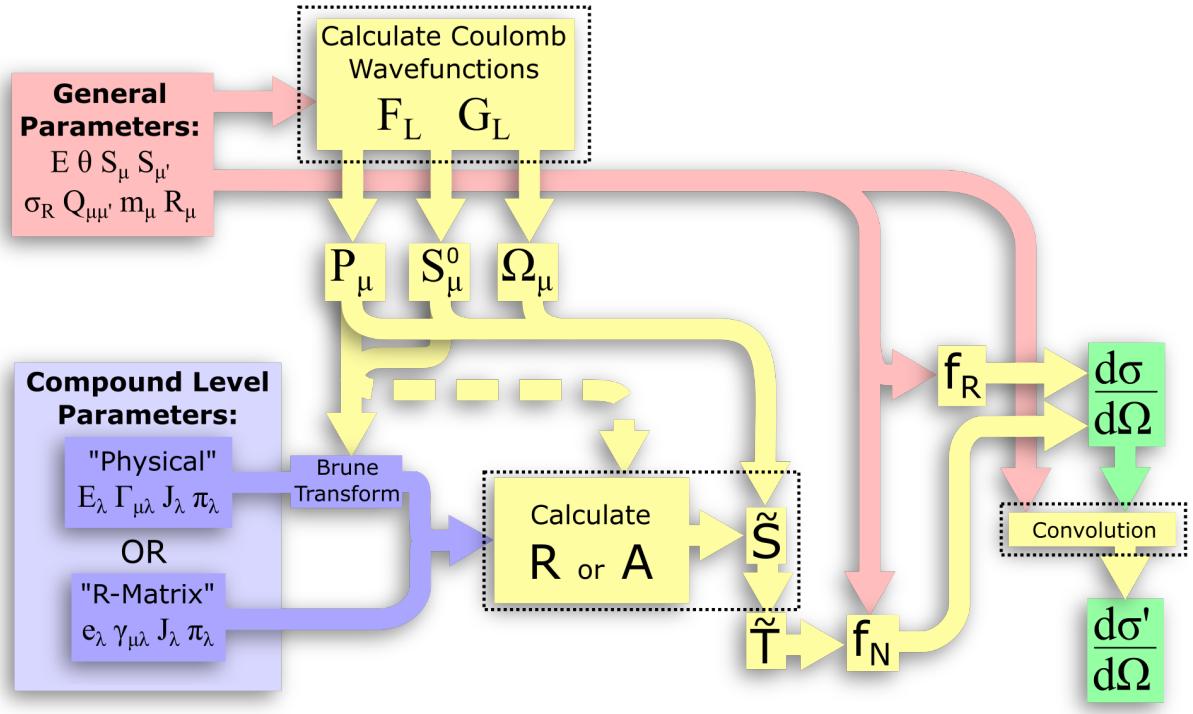

Figure 3.17: A flow diagram depicting a full $\boldsymbol{R}$-matrix calculation, using either the $\boldsymbol{R}$-matrix or $\boldsymbol{A}$-matrix, and either standard $\boldsymbol{R}$-matrix parameters or physical parameters via the Brune transformation. Showing input parameters (red and blue), calculation steps (yellow) and outputs (green). Computationally intensive parts of the calculation are highlighted with a black dashed box. The dashed arrow is only required for an $\boldsymbol{A}$-matrix calculation.

Coulomb wavefunctions, performing the matrix inversions required to calculate the $\widetilde{\boldsymbol{S}}$-matrix, and on performing the convolution with the experimental resolution. The last of these is unavoidable, however it is possible to optimise this by performing the convolution in Fourier space using the FFT, [94]. The first two are unavoidable in a full $\boldsymbol{R}$-matrix calculation, however it is possible to use an alternative technique which approximates the $\boldsymbol{R}$-matrix, which avoids both of these computationally heavy processes. This is known as the Simplified $\boldsymbol{R}$-matrix, and is discussed in detail in Ref. [95] and used in Refs. [66–69].

The Simplified $\boldsymbol{R}$-matrix is valid only for spin-0 nuclei, and while it does allow for the existence of multiple decay channels, and hence the definition of partial decay widths $\Gamma_{\mu\lambda}$, it is not a true multi-channel calculation in that it does not calculate the cross-section consistently over multiple channels.

The Simplified $\boldsymbol{R}$-matrix avoids the matrix inversions by making the assumption that there is no interference between the states in the compound nucleus. Under the $\boldsymbol{A}$-matrix formalism, this is equivalent to setting all of the off-diagonal terms in the $\boldsymbol{A}$-matrix to 0, which makes the matrix inversion trivial. It then removes the necessity to calculate the Coulomb wavefunctions by replacing their contributions by variables which are fit to the experimental data. These assumptions mean that

while the Simplified $\boldsymbol{R}$-matrix can produce spectra which are very similar (or identical in certain special cases) to the spectra that would be produced by a full $\boldsymbol{R}$-matrix calculation, it is also possible to produce unrealistic spectra. Therefore, while the improvements in computational efficiency achieved by the Simplified $\boldsymbol{R}$-matrix are significant, the levels that are extracted by a fit to experimental data are not as reliable as those that would be produced by the full $\boldsymbol{R}$-matrix. The Simplified $\boldsymbol{R}$-matrix is defined as

$$\begin{aligned}\frac{d\sigma}{d\Omega} = \Big|\delta_{\mu\mu'}\left(f_R(E,\theta)+\rho(E,\theta)e^{i\chi(E\,\theta)}\right) \\ -\frac{i}{2k_\mu}\sum_\lambda(2L_\lambda+1)\frac{\Gamma_{\mu\lambda}}{\Gamma_\lambda}(e^{2i\beta_\lambda(E)}-1)e^{2i\phi_{L_\lambda}}P_{L_\lambda}(\cos\theta)\Big|^2\end{aligned} \tag{3.58}$$

where f_R is the Rutherford amplitude, defined in Equation (3.33), and ρ and χ are the amplitude and phase shift of the potential contribution, and are both in general dependent on E and θ. All of these contributions are only relevant in the elastic scattering channel. In full $\boldsymbol{R}$-matrix theory the potential contribution is generated automatically in f_N, from the hard sphere phase shifts, Ω_μ, whereas here it is treated as a free parameter and fit to the data. The resonant contribution here is represented as a sum over the compound levels. The resonant phase shift, $\beta_\lambda(E)$, is defined as

$$\beta_\lambda(E) = \arctan\left(\frac{\Gamma_\lambda/2}{E_\lambda - E}\right). \tag{3.59}$$

The partial wave phase shift, ϕ_{L_λ}, is unique to each L, and dictates the interference observed between each partial wave in the resonant contribution and the background contributions. In full $\boldsymbol{R}$-matrix theory this is again dictated by the hard sphere phase shifts, whereas here it is unconstrained and allowed to be fit to the data. The partial widths and resonant energy, $\Gamma_{\mu\lambda}$ and E_λ, are constants, and do not vary with E as they do in full $\boldsymbol{R}$-matrix theory. The other variables in Equations (3.58) and (3.59) have the same definitions as they do in full $\boldsymbol{R}$-matrix theory.

3.2.5 The Azure2 Code

The full $\boldsymbol{R}$-matrix was implemented in this work using the code `Azure2`, which was developed by De Boer [96], largely based on the earlier version, `Azure`, discussed in Ref. [97]. This is a very powerful program, providing the functionality to perform a full $\boldsymbol{R}$-matrix fit to experimental data, with multiple decay channels and many levels, via either the $\boldsymbol{R}$ or $\boldsymbol{A}$-matrix formalism. It also allows the use of the physical resonance parameters as the variables rather than the $\boldsymbol{R}$-matrix parameters, via the Brune transformation. It is possible to perform the fitting procedure simultaneously over many data sets, with any combinations of entrance and exit channels, and allows the treatment of experimental reso-

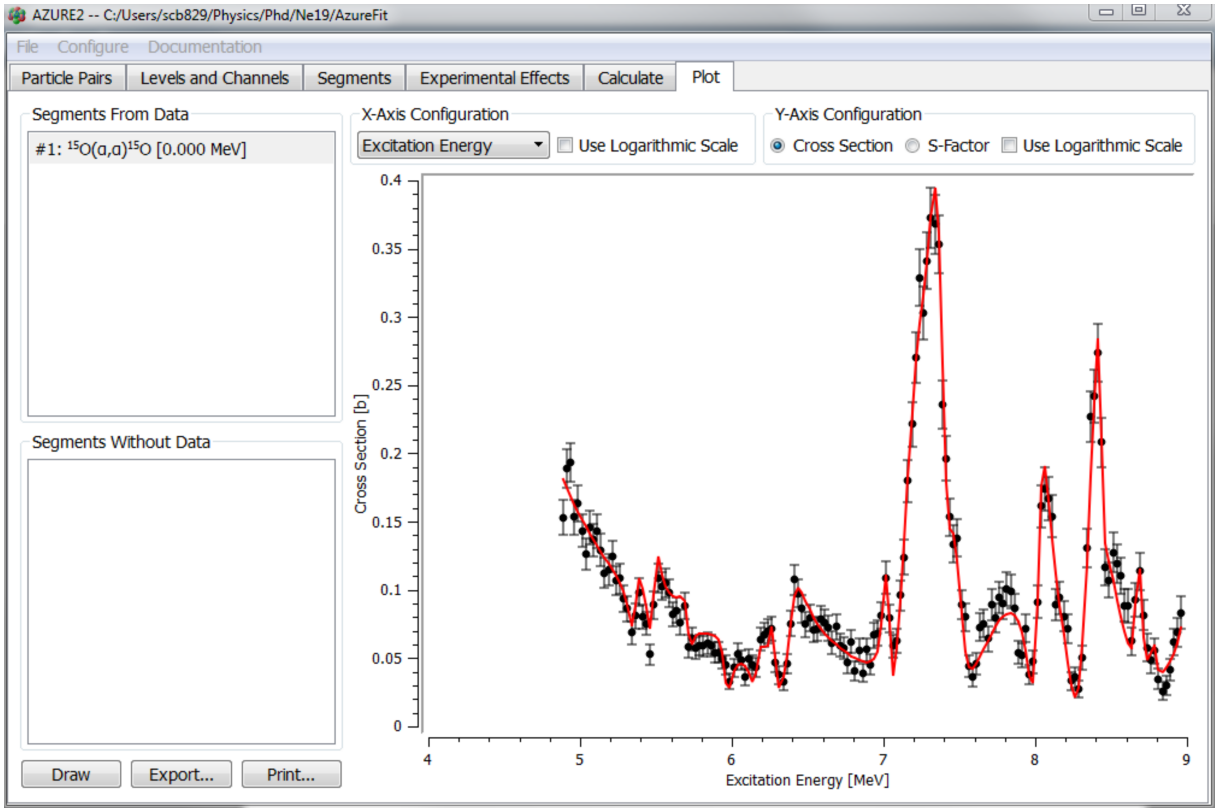

Figure 3.18: A screenshot of the R-matrix fitting program `Azure2`.

lution using the convolution procedure. Finally it provides the functionality to extract the resonance parameters and errors on those parameters from the final fit. A screenshot of this program is shown in Figure 3.18.

Chapter 4

An Investigation of ^{18}F with a Full R-Matrix Analysis

This chapter describes an experiment which was performed to investigate α-clustering in ^{18}F, using the TTIK technique to measure the ^{14}N + α resonant reaction. The results were interpreted using a full $\boldsymbol{R}$-matrix analysis to extract structural information on ^{18}F. This chapter has been adapted from my publications:

- Bailey, S. *et al.* Energy levels of ^{18}F from the ^{14}N+α resonant reaction. *Phys. Rev. C* **90,** 024302 (2 Aug. 2014) (Appendix F)
- Bailey, S. *et al.* Alpha clustering in ^{18}F. *J. Phys. Conf. Ser.* **569,** 012053 (2014) (Appendix G)

4.1 Previous Work

4.1.1 Clustering

In this work the α-^{14}N structure is explored. As discussed previously in Section 1, from a shell-model perspective α-core structures are emphasised in the case that two protons and two neutrons exist above a shell-closure, providing a clear energy separation between the α-cluster and the core. In the case of ^{18}F this suggests that α-cluster states ought to arise following the promotion of one additional proton and one additional neutron from the *p*-shell to the *sd*-shell, resulting in sets of states known as 4 particle, 2 hole ($4p$-$2h$) excitations. This shell structure is very similar to that of ^{20}Ne, with the addition of one proton hole and one neutron hole to the p-shell, and is displayed in Figure 4.1.

There exists a large amount of work characterising ^{18}F, much of which is summarised in [98], how-

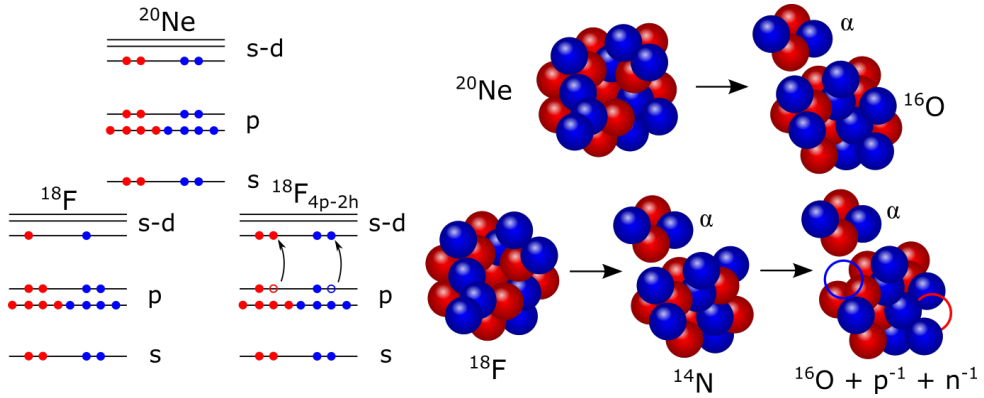

Figure 4.1: ^{18}F and ^{20}Ne from a shell model (left) and cluster model (right) perspective. Here protons are red and neutrons are blue, and open circles indicate holes. This figure is adapted from my work in Ref. [2].

ever here only the work that is relevant to α-clustering and $4p$-$2h$ excitations is discussed. Much of this section is taken from my publication: Bailey, S. *et al.* Alpha clustering in ^{18}F. *J. Phys. Conf. Ser.* **569,** 012053 (2014) (Appendix G).

4.1.1.1 Hole-particle Coupling

The regime which governs the coupling between the p shell holes and the s-d shell particles in $4p$-$2h$ states is extremely important for understanding the structure of ^{18}F. This coupling can either be described as weak-coupling or strong-coupling. In the weak-coupling picture, the particle wavefunctions are assumed to be similar to the eigenfunctions of ^{20}Ne, and the hole wavefunctions like that of the ^{14}N ground state [99–101]. This is interpreted as weak coupling since the interaction is expected to be well described as a small perturbation on these wavefunctions, leading to a structure very similar in nature to ^{20}Ne with some additional core excitations.

The strong-coupling model takes the opposite approach, asserting that the interaction between the holes and particles is too strong for the wavefunctions to be approximated in such a way. Instead more robust techniques are required, leading to more varied and exotic deformations and structures.

One of the earliest experimental investigations of hole-particle states in ^{18}F was performed in 1968 Middleton *et al.* [99] using the ^{14}N(^{7}Li,t)^{18}F α-transfer reaction. It is expected that α-transfer reactions preferentially excite states formed by transferring all four nucleons into the same shell, leading to an amplified cross-section for $4p$-$2h$ states. In this work it was argued that this allowed the $4p$-$2h$ excitations to be identified by selecting states which were strongly populated by this reaction but weakly populated by one or two nucleon transfer reactions. However this may be an overly simplistic interpretation since it ignores the effects that the matching conditions have on the cross-section [102]. Additionally the non-zero spins of the nuclei involved in this reaction often lead to ambiguous angular

distributions, making experimental J^π assignments very difficult [64].

Middleton *et al.* [99] reported six states to be likely $4p$-$2h$ candidates at 1.70, 2.52, 3.36, 4.23, 5.30 and 6.55 MeV using this technique. They go on to argue that these states can be well described by the weak-coupling model, coupling the ^{20}Ne ground state band to the $(1p_{1/2})_{1+}{}^{-2}$ hole configuration. The application of this model led to the following spin-parity assignments for the observed $4p$-$2h$ states, respectively: $J^\pi = 1^+, 2^+, 3^+, 1^+, 3^+$ and $(4^+, 5^+)$.

This weak-coupling description of the $4p$-$2h$ states was challenged following an extensive study of the structure of ^{18}F in 1973 by Rolfs *et al.* [98]. In this work the hole-particle states were investigated in detail using the ^{14}N(α,γ)^{18}F, ^{17}O(p,γ)^{18}F and ^{16}O(^{3}He,pγ)^{18}F reactions [98, Part III]. Following these measurements 5 states were identified as being members of a $K^\pi = 1^+$ rotational band of predominantly $4p$-$2h$ nature, at 1.701, 2.523, 3.358, 5.298 and 6.567 MeV. Spin-parity assignments were made based on measured branching ratios and angular distributions to be respectively $J^\pi = 1^+, 2^+, 3^+, 4^+$ and 5^+. The reduced α-widths were extracted for the 4^+ and 5^+ members, and in both cases were found to be exceptionally large.

It is clear that these states are the same states as those measured by Middleton *et al.* [99], with the exception that the 4.23 MeV state was found by Rolfs *et al.* [98, Part IV] to be unlikely to be $4p$-$2h$ in nature, and was instead assigned to be a $J^\pi = 2^{(-)}$ state of 3p-1h structure. Additionally the spin-parity assignment for the 5.298 MeV state disagrees with the assignment made based on the weak-coupling model by Middleton *et al.* [99]. These considerations led Rolfs *et al.* [98] to reject the weak-coupling model in favour of the strong-coupling model.

A comparison was made between this band and a strong-coupling calculation performed in 1965 by Bassichis *et al.* [103], which predicted a $K^\pi = 1^+$, $4p$-$2h$ rotational band in ^{18}F. The gradient of the predicted band was found to be in excellent agreement with the measurements and it reproduced the observed zig-zagging in excitation energy, however the predicted band was shifted $\approx$ 2.5 MeV higher in energy. Rolfs *et al.* [98, Part III] speculated that based on the exceptionally large reduced α-widths observed for the 4^+ and 5^+ members, α-particle clustering may in fact play a prominent role in the structure of this band, and perhaps the explicit inclusion of α-clustering in the microscopic description of the band may reconcile this energy shift.

Based on these results it seems likely that the strong-coupling regime better describes the hole-particle coupling in ^{18}F, since the work by Rolfs *et al.* [98, Part III] is more extensive, allowing the spin-parity assignments to be made based on experimental measurements. Further to this, more α-transfer measurements have been made by Cobern & Parker [64] and Etchegoyen *et al.* [104], extending the $K^\pi = 1^+$ rotational band observed by Rolfs *et al.* [98, Part III] from $J^\pi = 5^+$ up to 8^+. This rotational band is displayed in Figure 4.2, with the band calculated using the strong-coupling model by Bassichis *et al.*

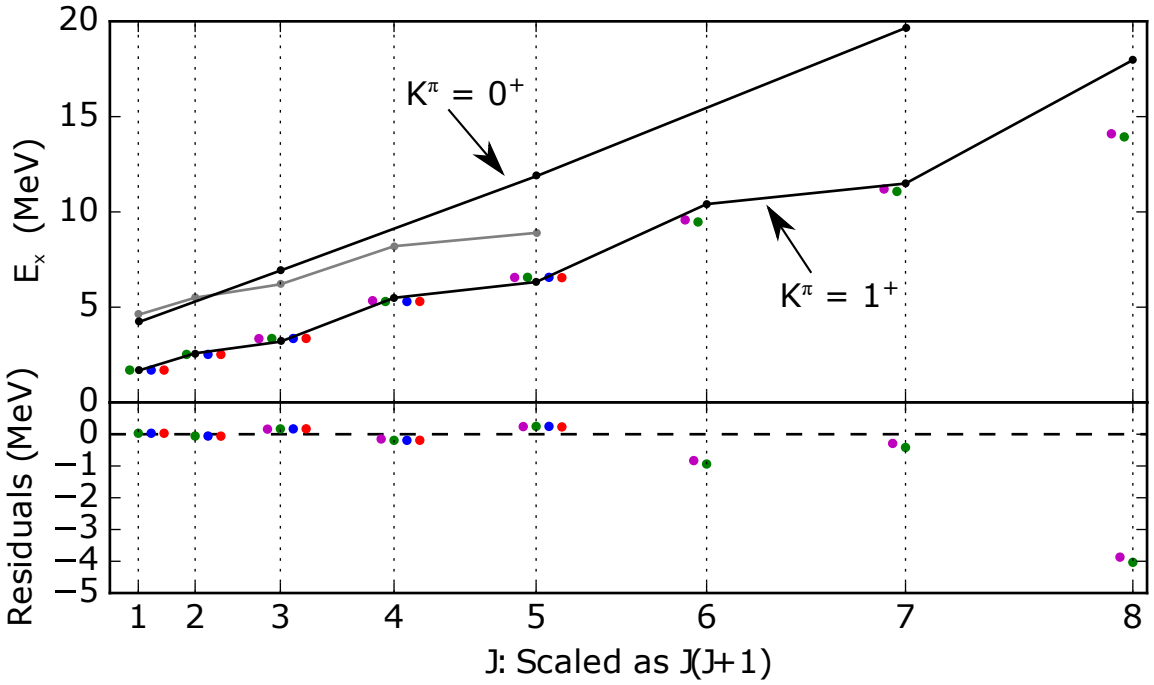

Figure 4.2: A comparison between the previous experimental measurements and theoretical calculations of the positive alpha clustered rotational bands in ^{18}F. Data points refer to experimental work by Middleton *et al.* [99] (red), Rolfs *et al.* [98] (blue), Cobern & Parker [64] (green) and Etchegoyen *et al.* [104] (magenta). The black points connected by lines refer to the two α-clustered rotational bands predicted by Buck *et al.* [105], and the grey points connected by lines refer to the shell-model type calculation of $4p$-$2h$ states assuming strong coupling between the holes and states by Bassichis *et al.* [103]. The top panel shows the rotational bands, and the bottom panel shows the difference between the experimental measurements and the K^π=1$^+$ α-clustered rotational band predicted by Buck *et al.* [105]. The experimental data points are shifted horizontally for clarity.

[103] for comparison.

4.1.1.2 Alpha Clustering

Based on the work by Rolfs *et al.* [98, Part III] it seems likely that there is a large α-cluster component to the structure of the $K^\pi = 1^+$ rotational band. A semi-microscopic calculation of α-cluster states in ^{18}F was performed in 1979 by Buck *et al.* [105]. In this work all four nucleons from which the α-particle is built up are placed in the s-d shell, enforcing the experimentally determined $4p$-$2h$ structure discussed previously. This leads to the formulation of the wavefunction of the ^{14}N core as two p shell holes in the ^{16}O closed shell.

This model produced two distinct rotational bands, one with $K^\pi = 1^+$ and one with $K^\pi = 0^+$. The states in the $K^\pi = 1^+$ band agreed exceptionally well with the experimentally determined states up to $J^\pi = 5^+$, however above this they began to diverge, with the calculated levels shifted higher in energy compared with the experimentally observed levels. This can be seen in Figure 4.2. It was however

Table 4.1: A table of the previously known levels in ^{18}F thought to have an α-clustered structure. Both experimental and theoretical results are shown, and these are discussed in detail in the text.

K^π	J	Middleton *et al.* [99]	Rolfs *et al.* [98]	Cobern *et al.* [64]	Etchegoyen *et al.* [104]	Strong-Coupling Model [103]	Alpha-Cluster Model [105]
1^+	1	1.70	1.701	1.701		4.6	1.67
1^+	2	2.52	2.523	2.523		5.5	2.58
1^+	3	3.36	3.358	3.358	3.35	6.2	3.19
1^+	4	5.30	5.298	5.298	5.34	8.2	5.49
1^+	5	6.55	6.567	6.567	6.56	8.9	6.32
1^+	6			9.472	9.58		10.41
1^+	7			11.074	11.2		11.49
1^+	8			13.937	14.1		17.97
0^+	1						4.21
0^+	3						6.92
0^+	5						11.87
0^+	7						19.65

explained by Buck *et al.* [105] that this may be due to the way the nuclear potential was modelled, since similar discrepancies have arisen in other calculations involving the same potential.

The extremely good agreement between observed and calculated levels in the $K^\pi = 1^+$ band leads to the belief that this is indeed an α-clustered $4p$-$2h$ rotational band. However if this model is correct, it should also be possible to identify the $K^\pi = 0^+$ rotational band. Buck *et al.* [105] assigned the 1^+ state in this band to two experimentally observed 1^+ states at 3.724 and 4.361 MeV. It is argued that this is due to mixing between this state and a $2p$ shell model state predicted to exist at a similar energy, causing the $4p$-$2h$ strength to be shared between both states. This hypothesis is confirmed to an extent experimentally by the slightly reduced cross-section for these states in α-transfer measurements [99]. However Buck *et al.* [105] were unable to confidently assign any of the other members of this band.

4.1.2 Resonant Scattering Measurements

In this section previous resonant scattering measurements which proceed via the ^{18}F compound nucleus are discussed.

The reaction ^{14}N(α,p)^{17}O was the first observation of an α induced nuclear transmutation, observed by Rutherford in 1919 [106]. Since then there has been a lot of work on reactions which proceed via the ^{18}F compound nucleus below an excitation energy of 9 MeV.

The ^{14}N(α,α) and ^{14}N(α,p)^{17}O reactions were measured in 1958 by Herring *et al.* [107] over excitation energies ranging between 6 and 7.5 MeV. The errors on the excitation spectra recorded ranged between 3% and 10%, and the excitation energy errors ranged between ± 0.6 keV and ± 10 keV. The ^{14}N(α,α) data was analysed by Herring [108] using the single level approximation to $\boldsymbol{R}$-matrix theory.

The ^{16}O(d,α)^{14}N reaction was studied amongst others in 1963 by Seiler *et al.* [109]. In this work

the differential cross section was measured at 166° in the centre of mass frame, covering excitation energies ranging from 8.15 MeV to 9.39 MeV. The measurements were made using a thin ^{16}O gas target and a deuteron beam. The errors on the measured cross-sections were reported to be less than 5%, and the uncertainty on the beam energy were ± 5 keV which corresponds to ± 4.4 keV in excitation energy.

The ^{17}O(p,α_0)^{14}N, ^{17}O(p,$p_1\gamma$)^{17}O and ^{17}O(p,γ)^{18}F reactions were measured by Sens *et al.* [110, 111] in 1978, populating excitation energies between 7.1 and 8.3 MeV in ^{18}F. The protons were accelerated using a 3 MV Van de Graff accelerator, and the target used was a 45 μg/cm^2 enriched SiO target. The energies of the incident protons were reported to within an error of ± 1.5 keV, corresponding to a ± 1.4 keV error on the excitation energy. The beam energy variation through the target was reported to be approximately 3 keV. These data were analysed using a Breit-Wigner analysis, which is a simplification to $\boldsymbol{R}$-matrix theory similar to the simplified $\boldsymbol{R}$-matrix detailed in Section 3.2.4. From this analysis 19 levels in ^{18}F were extracted.

In 1979 the ^{16}O(p,α)^{14}N reaction was measured by Kieser *et al.* [112] between E_x = 6 and 7 MeV, and this data was analysed in conjunction with other data sources using $\boldsymbol{R}$-matrix theory, leading to the extraction of resonances between E_x = 6 and 7.3 MeV.

Both the ^{14}N(α,α) and ^{14}N(α,p)^{17}O reactions were measured in 2008 by Terwagne *et al.* [113]. The α channel cross section was measured at 169° in the centre of mass, and measurements of the proton channel were made at three different angles: 99°, 141° and 167°. All of the measurements were made for excitation energies from 7.1 MeV to 9.1 MeV. The measurements were made using an α beam and a thin TaN target, produced by nitrogen implantation into tantalum. The total error on the cross section was reported to be between 7%-10%, and the beam energy uncertainty was less than ± 1 keV.

Finally a measurement was made in 2011 of the ^{14}N(α,α) reaction by Gurbich *et al.* [93]. Measurements were taken at 165°, 150° and 118°, over an excitation energy range of 6.36 MeV to 7.53 MeV. An α beam was used with a thin 200 nm SiN target. These measurements were then used in conjunction with several other ^{14}N(α,α)^{14}N data sources and an $\boldsymbol{R}$-matrix analysis was performed, from which the properties of the energy levels in ^{18}F were extracted up to ~ 8 MeV. The $\boldsymbol{R}$-matrix fit is shown in Figure 4.3.

4.2 Experimental Set-up

This experiment was carried out using the MC40 Cyclotron at the University of Birmingham. The cyclotron was used to produce a ^{14}N beam at ~46 MeV and ~62 MeV, with beam currents typically ranging between 0.5 and 0.75 nA. This was the first time a ^{14}N beam had been produced at this facility,

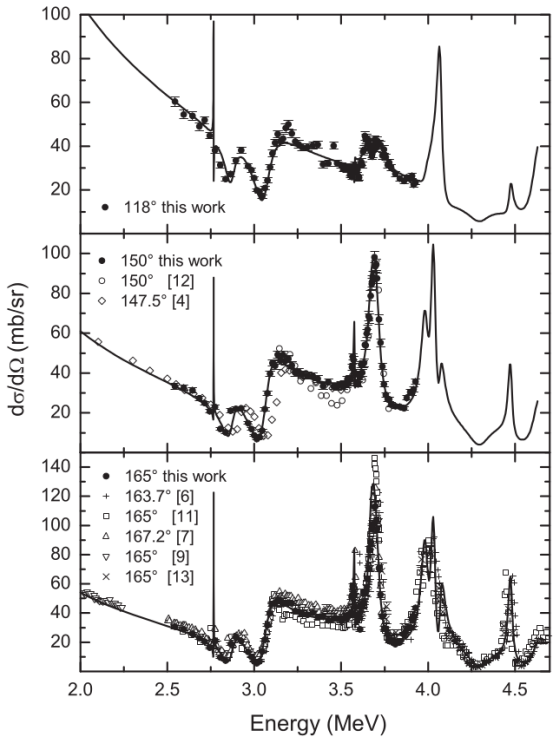

Figure 4.3: Differential cross-section data for the ^{14}N(α,α) reaction with $\boldsymbol{R}$-matrix fit from Ref. [93], energies are α beam energies. This figure is reprinted from Ref. [93].

and as no direct measurement of the beam energy was made, these energies were calculated theoretically using the cyclotron formulae detailed in Appendix B. These calculations are very sensitive to the radius at which the beam was extracted from the cyclotron. This leads to an uncertainty on the beam energy of 10% [114], and as such these values only serve as nominal beam energies. This uncertainty is, however, resolved through the data analysis discussed in Sections 4.3.4.

Upon extraction the beam passed to the reaction chamber. The reaction chamber was set up following the typical TTIK configuration discussed in Section 2.2.3. The specifics of this experimental set-up are detailed here, and shown in Figure 4.4. The reaction chamber was filled with ^{4}He gas, and the detectors were placed at 0° to the beam line, producing measurements at $\theta_{\text{c.m.}} = 180°$. Particle identification was performed using the standard ΔE-E set-up, with a 1 mm thick DSSD for the E detector, and a 70 µm thick DSSD for the ΔE detector. The ΔE detector was placed 490 mm from the entrance window, and the E detector was placed 15 mm behind the ΔE detector. The window was 5 µm thick, and made from Havar, and one 12 µm thick Mylar absorber was used either just after the window or just before the ΔE detector, depending on the measurement.

The decay products measured in this experiment were the α-particle, deuteron and proton, and the heavy residual nuclei, ^{14}N, ^{16}O and ^{17}O, were stopped in the ^{4}He gas before reaching the detectors. This in principle ought to have led to the measurement of the ^{4}He(^{14}N,α), ^{4}He(^{14}N,d)^{16}O and ^{4}He(^{14}N,p)^{17}O

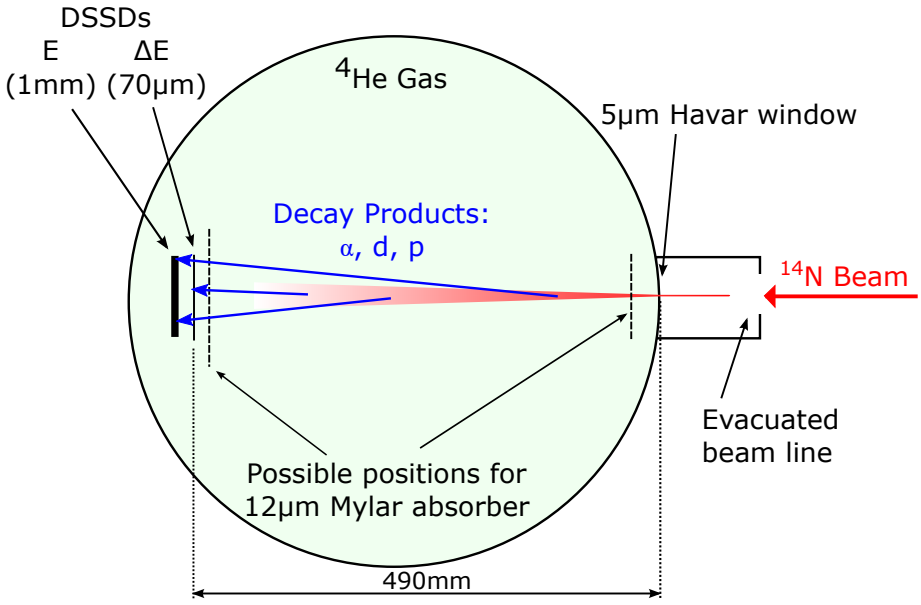

Figure 4.4: A schematic drawing of the reaction chamber used in the ^{18}F experiment. This figure is adapted from my work in Ref. [1]

reactions, however the ^{4}He(^{14}N,p)^{17}O reaction was contaminated by protons that were knocked out of the Mylar absorber and Havar window, rendering the data useless, and only the ^{4}He(^{14}N,α) and ^{4}He(^{14}N,d)^{16}O reactions are presented. In total 6 measurements were made, using different beam energies, gas pressures and absorbers, to allow for the assessment of the contribution of inelastic contaminants to the spectra. The details of each measurement are given in Table 4.2, and the assessment of the inelastic contamination is discussed in Section 4.3.5.

Table 4.2: The details of each of the measurements; all energies in MeV. The beam intensity is given in particles per second.

Measurement	Theoretical beam energy	Gas pressure (mbar)	Absorber position	^{14}N Charge state	Beam current (nA)	Beam intensity (pps)
1	46	620	None	4+	0.5	7.8×10^8
2	46	420	Window	4+	0.5	7.8×10^8
3	62	900	Detectors	5+	0.5	6.3×10^8
4	62	900	Detectors	5+	0.25	3.1×10^8
5	62	900	Window	5+	$<$0.75	$<9.4\times10^8$
6	62	850	Window	5+	0.75	9.4×10^8

The current pulses produced by the DSSDs upon measurement of a charged particle were converted into digital signals which could be stored and analysed on a computer using an analogue signal processing chain. Each strip on the DSSDs acted like an independent detector, and so 64 independent signal processing chains were required to utilise all 16 strips in both faces of both detectors. In each of

these signal processing chains the raw current from the silicon detector strip was first passed to a pre-amplifier which integrated the charge pulse into a voltage pulse, where the peak height of the voltage pulse is proportional to the energy of the measured charged particle. This pulse was then passed to a CAEN N568LC shaping amplifier which reshaped the signal into 'Gaussian-like' form, with a rounded peak, which is the optimum form to be read by an Analogue to Digital Converter (ADC). The ADC used was a Silena S9418, which converts the analogue pulse to a binary signal. This binary signal was then passed to and stored on the data acquisition computer.

Two CAEN V895 discriminators were used, one for each detector, to determine if a significant signal had been recorded. It was assumed that if a measurement were made in one face of a detector, then it must also have been measured in the other face, meaning that for each detector only one face was used to signal an event. If a signal was recorded in any strip of the face connected to the discriminator, then the data from all of the strips in both detector faces in both detectors was recorded. This signal processing chain is shown schematically in Figure 4.5.

4.3 Preliminary Analysis

Here the preliminary analysis refers to the process of producing the excitation spectra from the raw measurements, which may then be analysed using $\boldsymbol{R}$-matrix theory. This was done using a combination of Matlab scripts and the groups in-house analysis package, named Sunsort as it was originally written for Sun workstations.

4.3.1 Data Cleaning

It was first necessary to calibrate and clean the data, to ensure that the events that were measured were good events, and not produced by defects in the experimental set-up or detections system. The initial calibration was performed using a 3α-source ^{239}Pu^{241}Am^{244}Cm. For the calibration runs the reaction chamber was evacuated and the detectors separated so that each had a clear, unobstructed view of the 3α-source. This source produced three peaks in the measured spectra at the known energies 5.138, 5.457 and 5.759 MeV [115], to which a linear fit was performed independently for each detector strip. This calibration was only used as an initial rough calibration, and it was refined before the final spectra were produced. This recalibration is discussed in Section 4.3.3. Following this initial calibration an energy threshold was set at 1.5 MeV for the E detector and 0.5 MeV for the ΔE detector, and events which were recorded with an energy lower than this were discarded, ensuring that any statistical background or noise in the detectors was ignored.

It was important to prevent events associated with pile-up and charge sharing in the DSSDs from

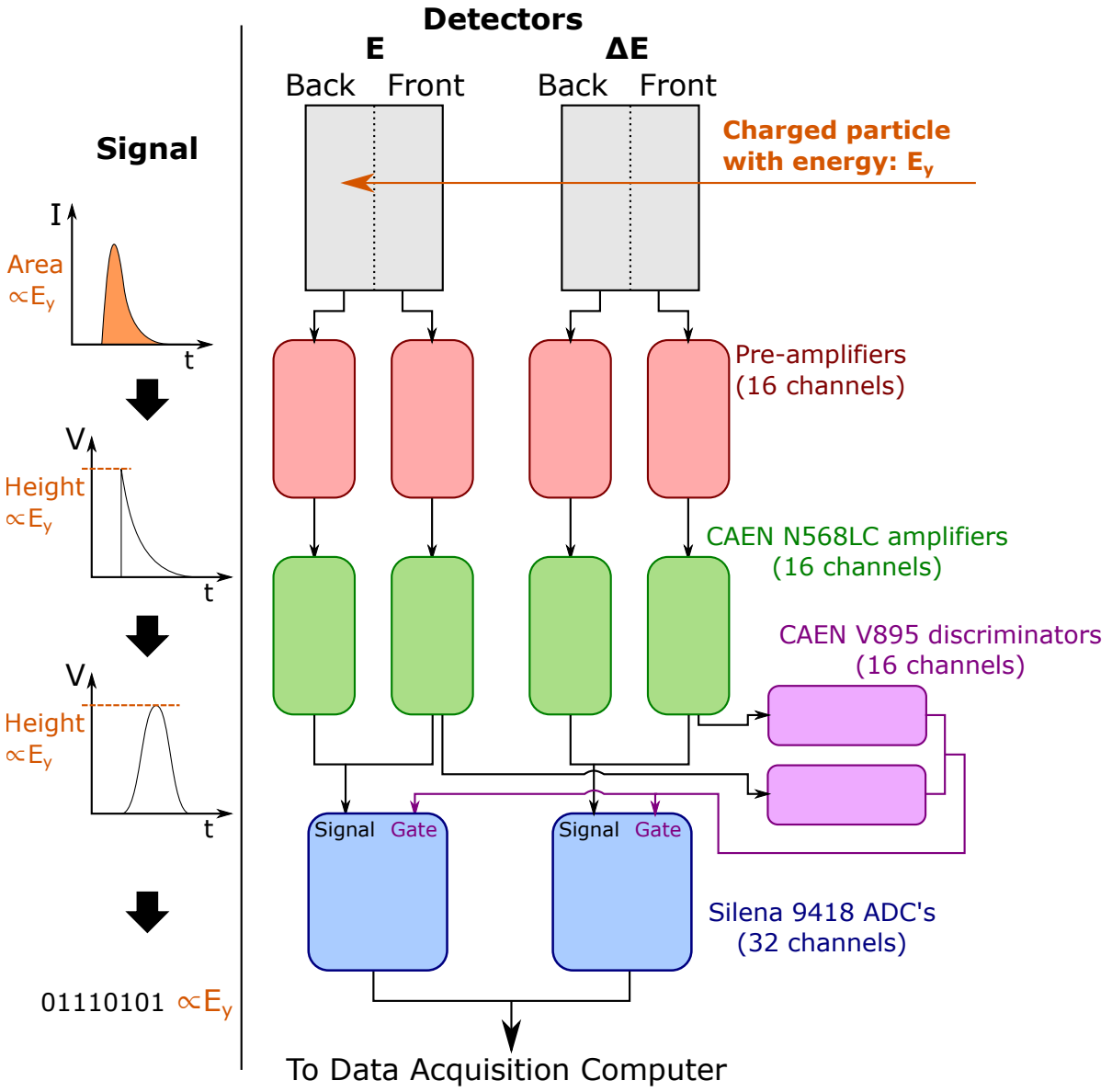

Figure 4.5: A schematic drawing of the signal processing chain used in the ^{18}F experiment (right), and how the signal develops through the chain (left).

contaminating the data. Pile-up occurs when two or more events are measured in the same strip simultaneously. In this case the strip will produce a single signal equivalent to the total energy of all measured events. Charge sharing occurs in the case that a particle interacts on the boundary between two strips, leading to the energy being shared over both strips. Events associated with these phenomena were rejected in most cases by only counting events in which *both* faces of the detector only have one active strip. This minimises pile-up since if two events are measured in the same strip but not the same pixel, i.e. the same strip on one face but not on both faces, then the detector will register more than one active strip in one of the faces, and the events will be discarded. It removes charge sharing in most cases since in one face the two strips over which the charge is shared are activated, leading to the events being discarded.

This technique works well to remove the vast majority of both pile-up and charge sharing, with the exception of the following cases:

1. If pile-up occurs in the same pixel, i.e. the same strip on both faces of the detector, then only one event will be measured in each face, and this will be recorded. The likelihood of measuring two events in the same pixel is very low, however. It was estimated that approximately 3% of all pile-up events should occur in the same pixel, meaning that this technique will correctly remove 97% of pile-up events. The details of this calculation are given in Appendix C.

2. If charge sharing occurs such that the amount of energy in one of the active strips is less than the energy threshold, then this will produce only one strip signal, which will be recorded but with a smaller energy than it should have. This is again expected to be a very small proportion of all charge sharing events, and therefore have a small effect on the results.

4.3.2 Particle Identification

The measured decay product was identified for each event using ΔE-E particle identification. This was discussed in Section 3.1.1, and an example of a particle identification plot is shown in Figure 4.6. This technique clearly separates the measured α-particles, deuterons and protons into three separate bands, which can then be gated on to produce spectra containing only those decay products. In this work gates A and C were used to produce the ^{4}He(^{14}N,α) spectrum and gate D was used to produce the ^{4}He(^{14}N,d)^{16}O spectrum.

Using gate A in addition to gate C allowed the ^{4}He(^{14}N,α) spectrum to be extended to lower energies. This was justified by analysing the Q-values for reactions which emit decay products heavier than the α-particle and the energy losses of those decay products through the gas and absorbers. It was found that no decay products heavier than the α-particle ought to reach the detectors, and so

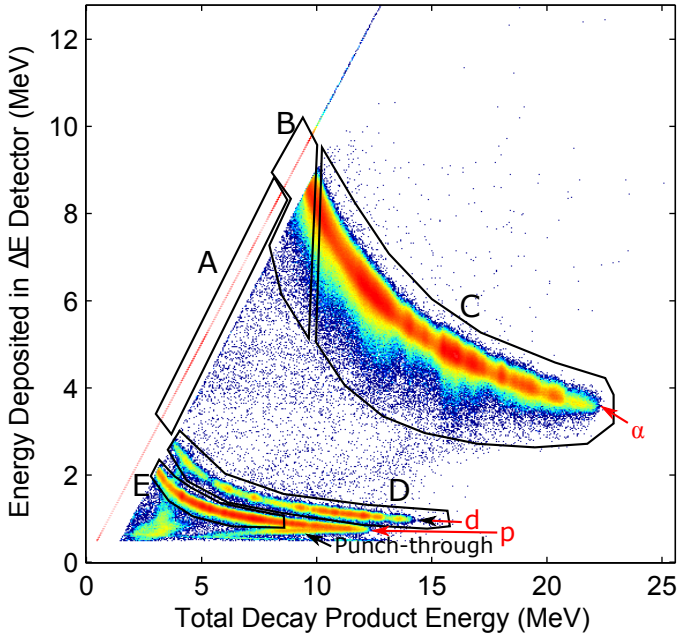

Figure 4.6: The ΔE-E particle identification plot for measurement 1. Here the energy deposited in the ΔE detector is plotted as a function of the sum of the energies deposited in both detectors. The thin diagonal line corresponds to particles that were stopped entirely by the ΔE detector. Annotated are a set of gates, which are explained in the text, labelled A-E, and the α, deuteron and proton lines (red labels). The tail characteristic of punch-through is shown for the proton line. This figure was adapted from my work in Ref. [1].

would not be observed in these measurements, meaning that gate A will consist purely of α-particle events. The 1.5 MeV energy threshold on the E detector manifests itself in the particle identification plot as the gap between the thin line of events which were absorbed by the ΔE detector and the particle bands. This gap introduces a systematic skew to the ^{4}He(^{14}N,α) spectrum inside gate B, since if an α-particle has enough energy to pass through the ΔE detector, but has less than 1.5 MeV remaining upon reaching the E detector, that remaining energy will not be recorded and the event will be moved artificially into the diagonal line. This led to the data within gate B being discarded, producing a gap in the measurement of the ^{4}He(^{14}N,α) spectrum.

'Punch-through' events are observed in Figure 4.6 at the end of the proton band. Here there is an additional tail on the end of the band which comes back across the band. This corresponds to events which arrived at the detectors with sufficient energy to pass through both the ΔE and E detectors without being stopped, leading to only a fraction of their energies being recorded. The overlap of the punch through events with the normal particle band leads to the contamination of the good high energy events. In this example, if one wished to extract the proton spectrum, then gate E would have to be used, which is shortened to avoid these punch-through contaminants. Punch through events

were present in measurements 3-6 of the ^{4}He(^{14}N,d)^{16}O spectrum, and as such limited the high energy measurements in this spectrum.

4.3.3 Energy Recalibration

The DSSDs are backed by a 1 µm thick Aluminium contact, which is used to conduct the current pulse produced by the measurement of a charged particle from the silicon to the signal processing circuit. This Aluminium strip however acts as an additional absorber, absorbing some of the energy of the decay products before they reach the depletion-region in the Silicon, where their energy is measured. In addition to this, if the depletion-region does not cover the full depth of the detector, then there will be a certain amount of Silicon which does not produce a measurable signal, known as a 'dead layer'. This dead layer will also act as an absorber. The affect of the Aluminium backing and the Silicon dead layer was accounted for by recalibrating the measurements with a particle-dependent calibration, which took into account the energy loss through these regions. In the following discussion the 'dead layer' refers to the combination of both the Aluminium backing and the Silicon dead layer, as both have an identical effect of absorbing a fraction of the energy of the decay product.

The particle-dependent calibration was performed again using the same 3α-source as was used for the initial calibration. Here however a dead layer was assumed to exist, with a thickness, D_{DL}, and the energy lost by the α-particles produced by the 3α-source through that dead layer was subtracted off their known values prior to fitting. A linear fit was then performed to these new values, giving the 'true response' of the active DSSD. The calibration curves were then calculated as this true response plus the calculated energy lost in the dead layer. This produced three different calibrations, one for each decay product, since each decay product will lose a different amount of energy to the dead layer. The calibration is shown in Figure 4.7.

The effect of this new calibration is to shift the spectra produced in the α and deuteron channels relative to each other. Since D_{DL} was not measured directly, it was treated as a free parameter in the reconstruction of the excitation function, and varied to produce the best possible agreement with previous work. This process is discussed in Section 4.3.4, and resulted in the identification of a 2 µm dead-layer on both DSSDs, representing the 1 µm Aluminium contact and a 1 µm silicon dead layer.

4.3.4 Reconstruction of the Excitation Function

Following these initial corrections the raw spectra were extracted via the gates on the particle identification plot, as a function of measured energy. The raw data from Measurement 1 is shown in Figure 4.8. The techniques discussed in Sections 3.1.2 and 3.1.3 were used to reconstruct the ^{4}He(^{14}N,α) and

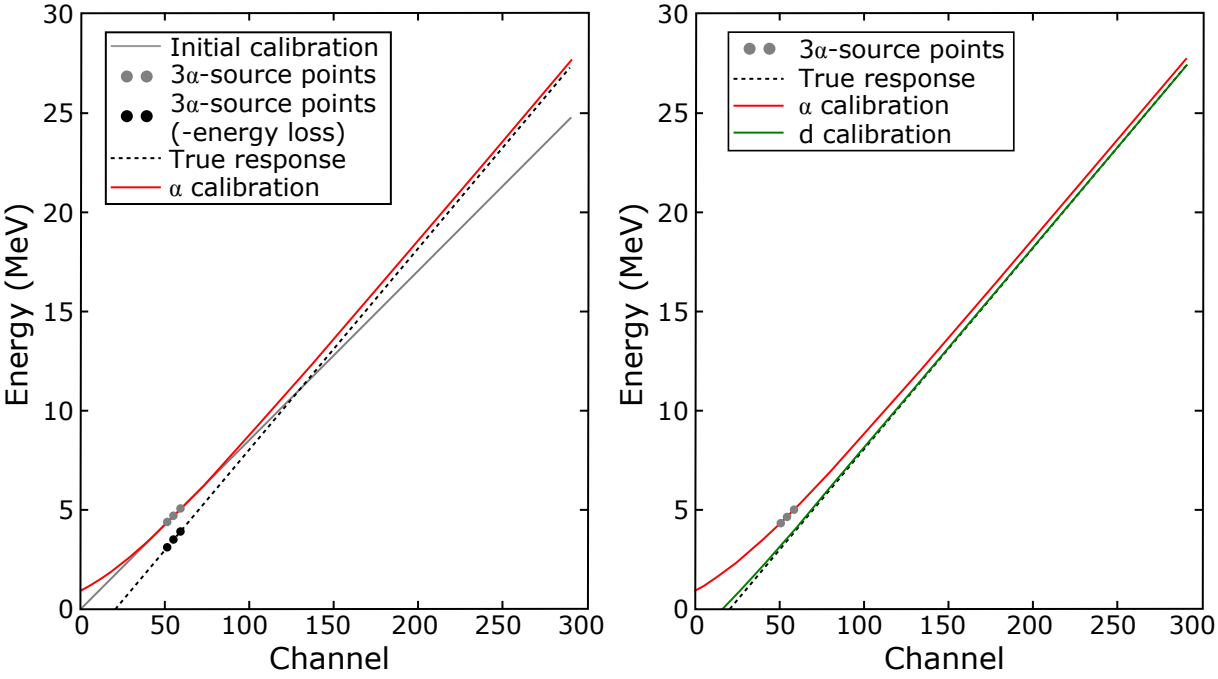

Figure 4.7: A comparison between the initial calibration which did not account for the detector dead-layer and the recalibration which does. Showing both a comparison between the initial and new calibrations (left) and the recalibration for α-particles and deuterons (right). This example is calculated for $D_{\mathrm{DL}} = 10\,\mu$m. This corresponds to a very large dead layer, chosen to exaggerate the effect for clear visualisation.

^{4}He(^{14}N,d)^{17}O spectra by converting these raw spectra from Yield as a function of measured energy to $d\sigma/d\Omega$ as a function of E_x. As mentioned previously, the contaminated proton data was discarded.

The reconstruction requires the definition of the beam energies, E_0, for each measurement, and the thickness of the dead layer in the DSSDs, D_{DL}. However these values were not known to a high degree of accuracy. Therefore these parameters were treated as free parameters, and were varied to produce an optimal agreement with previous measurements of the same spectra. The ^{4}He(^{14}N,α) spectrum was compared with measurements of the ^{14}N(α,α) reaction made by Terwagne *et al.* [113], and the ^{4}He(^{14}N,d)^{16}O reaction was compared with a measurement of ^{16}O(d,α)^{14}N made by Seiler *et al.* [109]. These were chosen because both have a very low uncertainty on E_x, with the work by Terwagne *et al.* [113] reporting an uncertainty of ± 1 keV and the work by Seiler *et al.* [109] reporting an uncertainty of ± 4.4 keV. One would not expect the cross-sections of the spectra to match perfectly, as they are made at slightly different scattering angles, and the ^{16}O(d,α)^{14}N reaction is the inverse of the ^{4}He(^{14}N,d)^{16}O reaction from present work. However the same resonances and features ought to be present in both, and the spectra can be matched by comparing the positions of these features in E_x.

Following this process the silicon dead layer was identified as 1 µm, in addition to the 1 µm Aluminium backing, and the true beam energies were found to agree with the theorised beam energies to within 2 MeV, which is within the maximum expected deviation of 10%. The true beam energies are

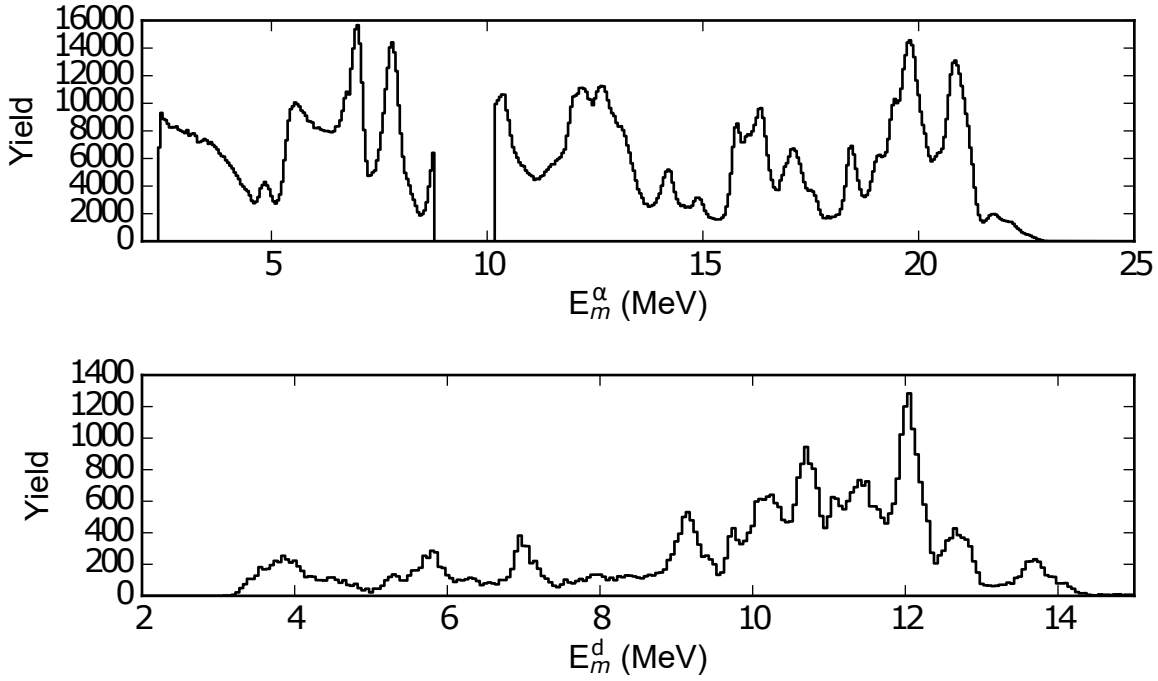

Figure 4.8: The raw data collected in Measurement 1, showing the measured energies of α-particles (top) and deuterons (bottom).

given in Table 4.4.

Following this, the efficiency corrections detailed in Section 3.1.3 were implemented here, setting the maximum centre of mass scattering angle to be 175°. This produces measurements with an average $\theta_{\text{c.m.}}$ of 176.6°. These efficiency corrections produce a spectrum which is proportional to $d\sigma/d\Omega$, but in order to extract an absolute measurement of $d\sigma/d\Omega$ a reference point is required. In this case the ^{4}He(^{14}N,α) spectrum was scaled to provide an optimal agreement with the $\boldsymbol{R}$-matrix fit which is performed on the low energy portion of this spectrum in Section 4.4. The scale factor extracted using this method was then used to scale the ^{4}He(^{14}N,d)^{16}O spectrum.

A comparison between all of the reconstructed measurements is shown in Figures 4.9 and 4.10 for the ^{4}He(^{14}N,α) and ^{4}He(^{14}N,d)^{16}O spectra respectively. The excellent agreement between the different experimental measurements suggests that the reconstruction procedure is robust, with the exception of measurements 3 and 4 at low E_x in the ^{4}He(^{14}N,α) spectrum. Here it is clear that below the gap at 8 MeV these measurements deviate considerably from the others. This is because the geometrical efficiency correction fails for measurements 3 and 4 at low energies. Measurements 3 and 4 were both made with the absorber next to the detectors, shifting all of the reactions closer to the detectors, and as such for a given E_x each pixel on the detectors subtends a much larger solid angle than they do in the other measurements, making the geometrical efficiency correction unreliable. This is demonstrated

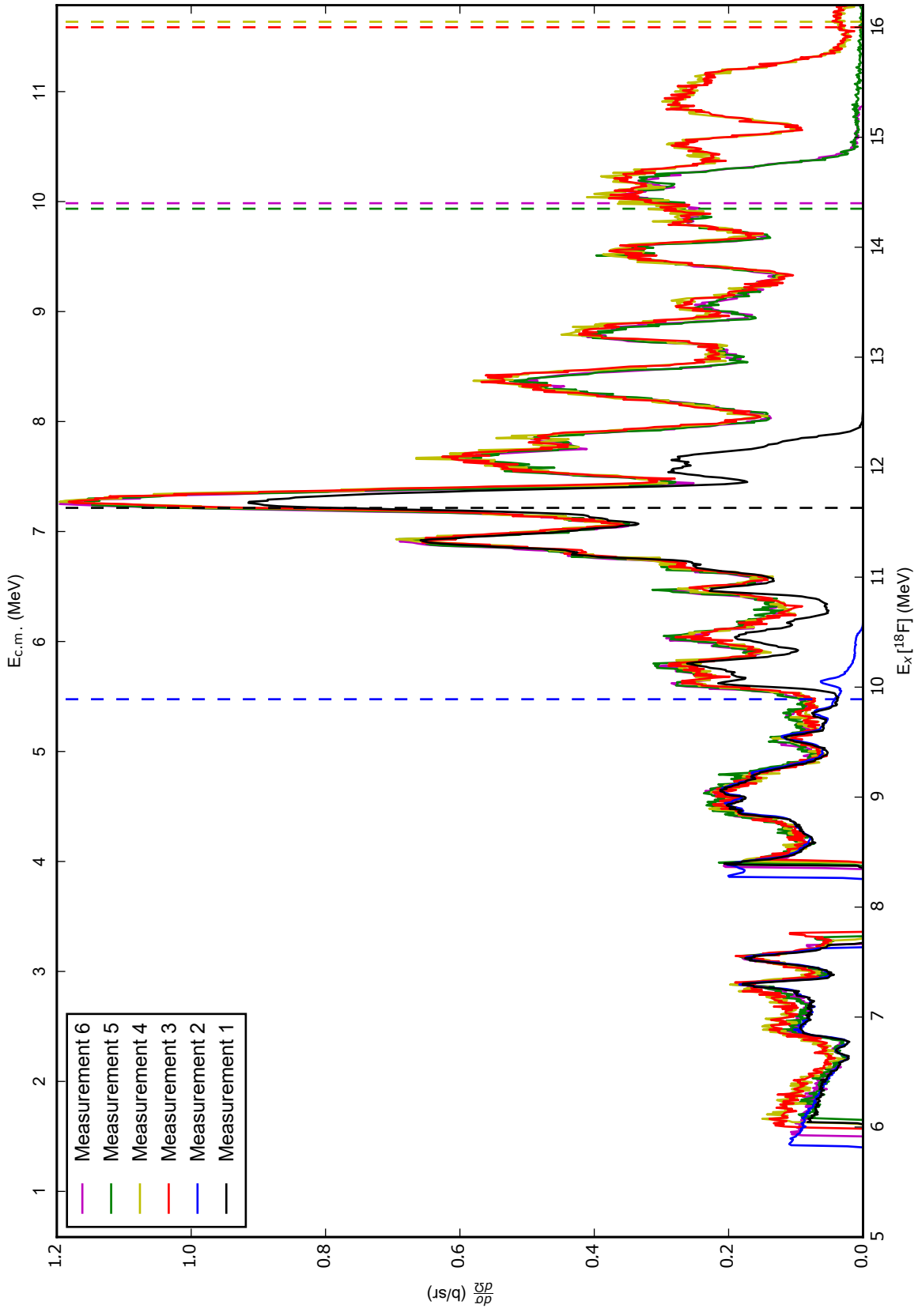

Figure 4.9: The reconstructed excitation functions for all measurements of the ^{4}He(^{14}N,α) reaction. The dashed lines indicate the predicted maximum excitation energy that ought to be populated in that measurement. In the cases of measurements 3/4 and measurements 5/6 the dashed lines are displaced horizontally slightly, for clarity.

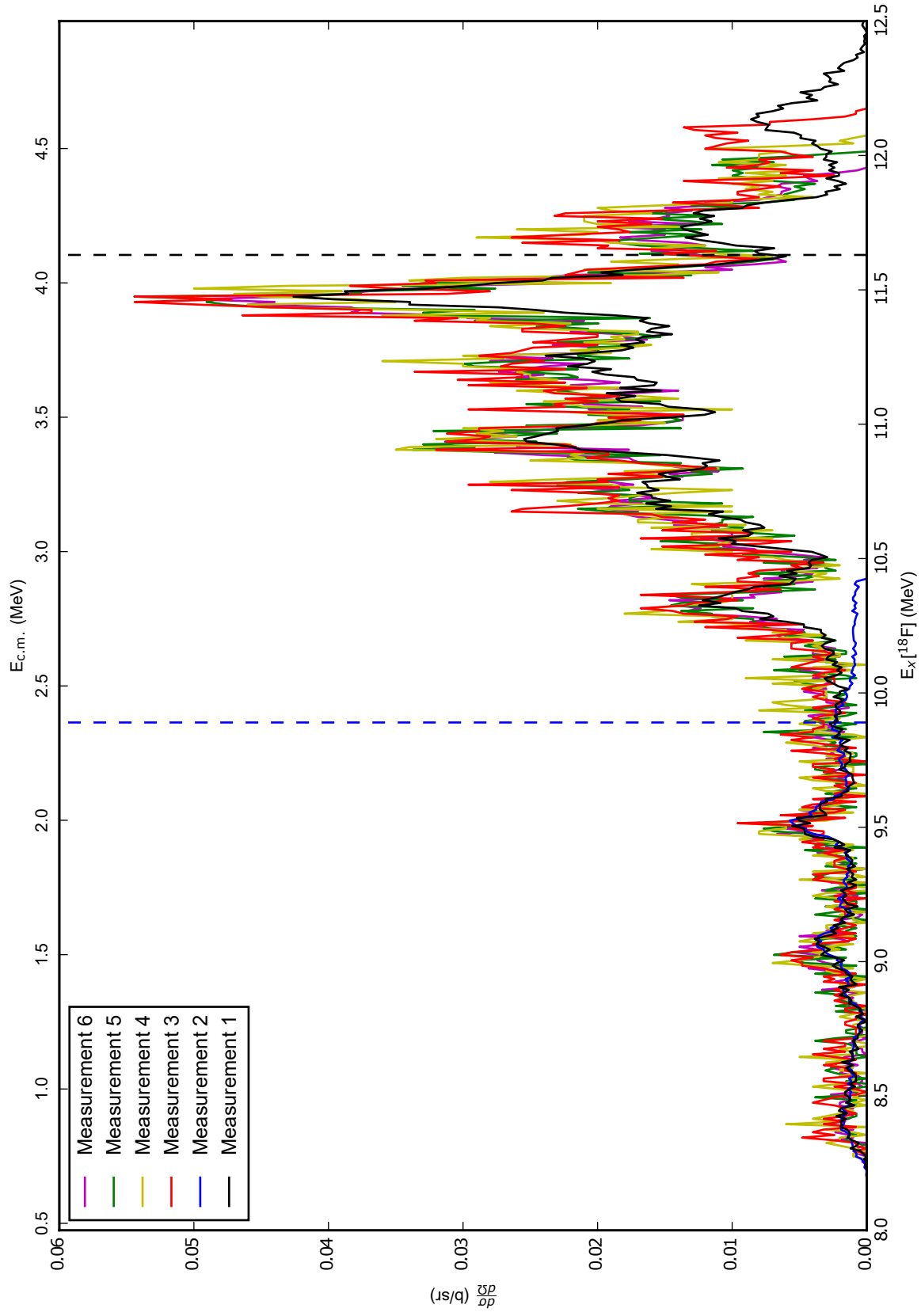

Figure 4.10: The reconstructed excitation functions for all measurements of the ^{4}He(^{14}N,d)^{16}O reaction. The dashed lines indicate the predicted maximum excitation energy that ought to be populated in that measurement. In the cases of measurements 3-6 the measurements do not reach the theoretical maximum because the high energy portion is contaminated by punch-through events, and so their corresponding maximum excitation energies are located beyond the energy range of this graph.

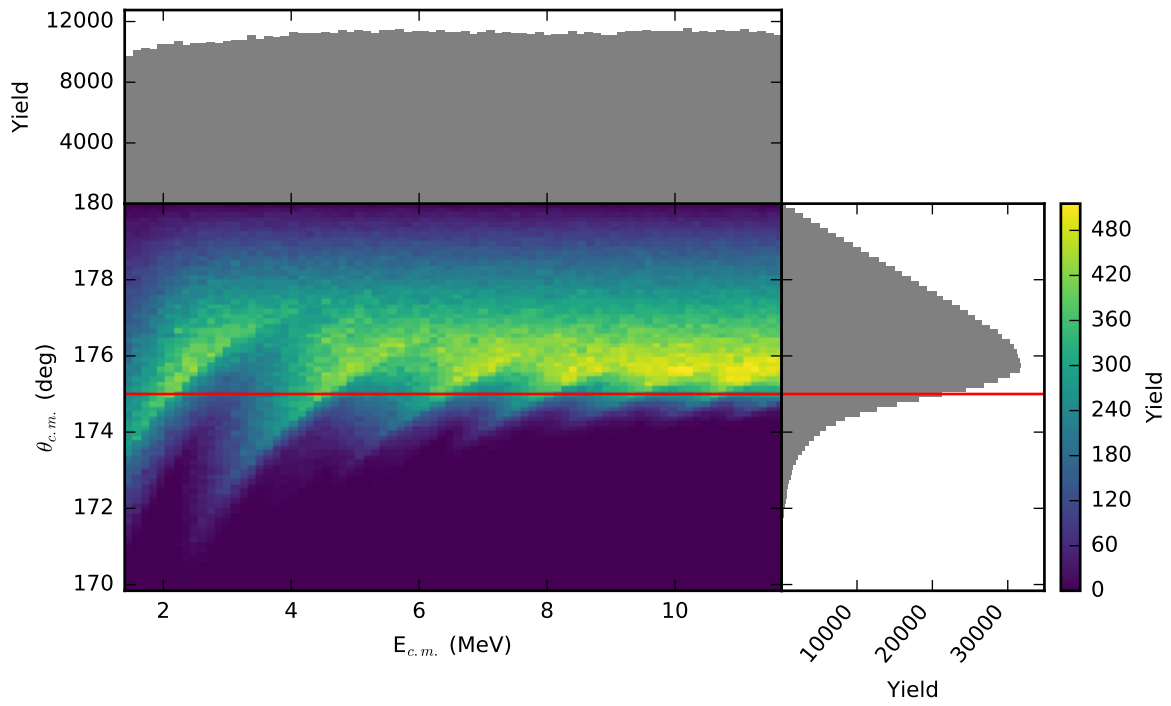

Figure 4.11: A Monte Carlo simulation of the application of the efficiency correction to measurements 3 and 4 of the ^{4}He(^{14}N,α) reaction. The grey histograms show the projections of the yield as a function of energy and scattering angle. The red line indicates the maximum centre of mass scattering angle. It is clear here that the aberrations about the red line increase in size dramatically at low energies.

using the Monte Carlo simulation detailed in Section 3.1.3 in Figure 4.11, which shows that at low energies the algorithm fails to constrain the scattering angles to the limit of 175°. For this reason, measurements 3 and 4 were discarded below 8 MeV.

4.3.5 Inelastic Contributions

As was discussed in Section 3.1.5, in TTIK measurements it is possible for inelastic reactions, i.e. reactions which leave the outgoing nuclei in excited states, to contaminate the measurements. The spins and parities of the ground and first excited states of the nuclei relevant to the present work are given in Table 4.3. The deuteron has no bound excited states, and the first excited states of the closed-shell nuclei ^{16}O and ^{4}He are too high to be populated in these measurements. This leaves only the first excited state of ^{14}N that can be populated in these measurements, and therefore it is only the ^{4}He(^{14}N,α) spectrum which may be contaminated by inelastic processes, while the ^{4}He(^{14}N,d)^{16}O is automatically clean of inelastic contamination.

The extent to which these inelastic contaminants impact the ^{4}He(^{14}N,α) spectrum was investigated by comparing the different measurements made in this experiment, the details of which are given in Table 4.2. These 6 measurements covered 4 unique excitation energy ranges, and therefore provide

Table 4.3: Spin/parity of the ground and first excited states of each decay product in the ^{18}F experiment.

Reaction	Decay product	Energy (MeV)	J^π
^{4}He(^{14}N,α)	α	g.s.	0^+
		20.21[a]	0^+
	^{14}N	g.s.	1^+
		2.313	0^+
^{4}He(^{14}N,d)^{16}O	d	g.s.	1^+
	^{16}O	g.s.	0^+
		6.049[a]	0^+

[a] State too high to be populated in these measurements

4 different energy ranges which are guaranteed kinematically to be clean of inelastic contaminants. These are detailed in Table 4.4.

Table 4.4: The energetics of each of the measurements; all energies in MeV. The inelastic free region refers to the ^{18}F excitation energy range for which the ^{4}He(^{14}N,α) reaction is free from inelastic contributions. The true beam energies are those extracted by a comparison of the data measured in the present work with previous measurements. This process is detailed in Section 4.3.4.

Measurement	Theoretical beam energy	True beam energy *(after window)*	Max. ^{18}F excitation energy	Inelastic free region
1	46	44.4 *(32.5)*	11.63	9.22 - 11.63
2	46	45.9 *(34.2)*	9.89	7.57 - 9.89
3,4[a]	62	62.2 *(52.5)*	16.0	13.69 - 16.0
5,6[b]	62	61.8 *(52.1)*	14.35	12.03 - 14.35

[a] Identical energy ranges, but with a different beam current.

[b] Identical energy ranges, but with a different gas pressure.

By comparing the spectra that are clean of inelastic contaminants with those that are not, one can investigate the contribution that the inelastic processes make to the spectrum. This is done by looking at the difference between measurement 1 and measurement 2 inside the measurement 2 clean region, the difference between measurements 3, 4, 5 and 6 and measurement 1 inside the measurement 1 clean region, and the difference between measurements 3 and 4 and measurement 6 inside the measurement 6 clean region. Measurement 6 may be replaced with measurement 5 in this final region and identical results would be produced, however measurement 6 was used as it has superior statistics. These differences are shown in Figure 4.12. While these comparisons allow the inelastic contributions to be identified in these energy regions, at energies below 7.57 MeV and between 11.63 and 12.03 MeV there are no clean measurements, and so the results must be extrapolated to incorporate these regions.

There evidently exists a noticeable inelastic contribution between 9.5 and 11 MeV, and at 13 and 13.5 MeV. The inelastic contribution is negligible below 9.5 MeV, suggesting that the low energy region

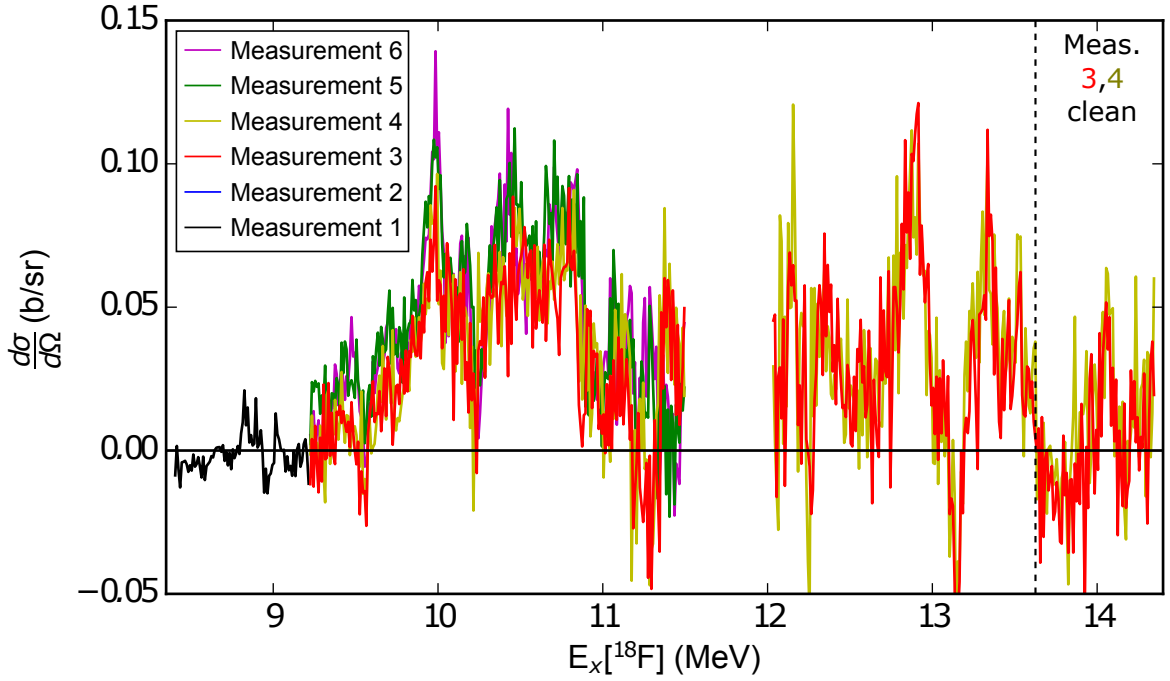

Figure 4.12: Difference between the unclean and clean measurements over the appropriate regions, demonstrating the contribution from inelastic scattering to the ^{4}He(^{14}N,α) spectrum. Between 8.4 and 9.22 MeV: measurement 1 - measurement 2. Between 9.22 and 11.5 MeV: measurements 3,4,5,6 - measurement 1. Between 12.03 and 14.35 MeV: measurements 3,4 - measurement 6. Above 13.69 MeV measurements 3 and 4 are also kinematically clean, so no inelastic contribution would be expected.

of the spectrum which is not covered by a kinematically clean region is likely still clean of inelastic contaminants. Above 13.69 MeV all measurements are kinematically clean, and this is evident in Figure 4.12 as the contribution goes to zero here. The inelastic contribution either side of the unclean gap between 11.63 and 12.03 MeV is approximately $d\sigma/d\Omega \sim 0.05$ b/sr, which is about 5% of the value of the cross-section in the elastic channel in that energy range. Therefore the inelastic contribution here was assumed to be negligible in this region.

The final, full ^{4}He(^{14}N,α) and ^{4}He(^{14}N,d)^{16}O spectra are shown in Figures 4.13 and 4.14 respectively. These were generated by averaging the different measurements, except in the case where inelastic contributions were present, in which case only the clean measurements were used. It is these spectra that are analysed in the following $\boldsymbol{R}$-matrix analysis.

4.3.6 Experimental Resolution

The experimental resolution on the measured energies, σ_{E_m}, is calculated in terms of the intrinsic detector resolution on the ΔE and E detectors, $\sigma_{\Delta E}$ and σ_E respectively. As E_m is given by the sum of the energies in each detector, σ_{E_m} is calculated by summing the detector resolutions in quadrature.

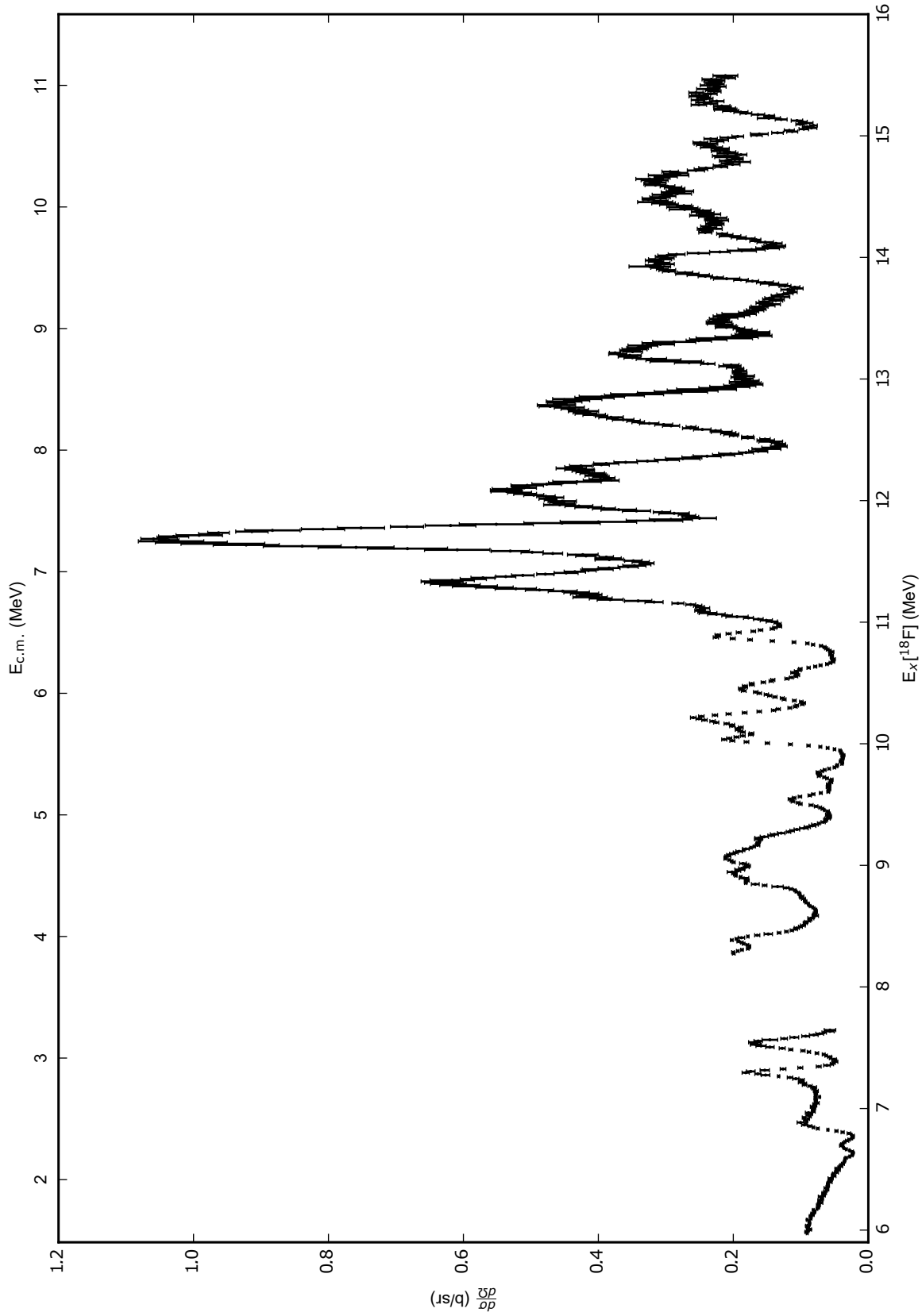

Figure 4.13: The averaged ^{4}He(^{14}N,α) spectrum.

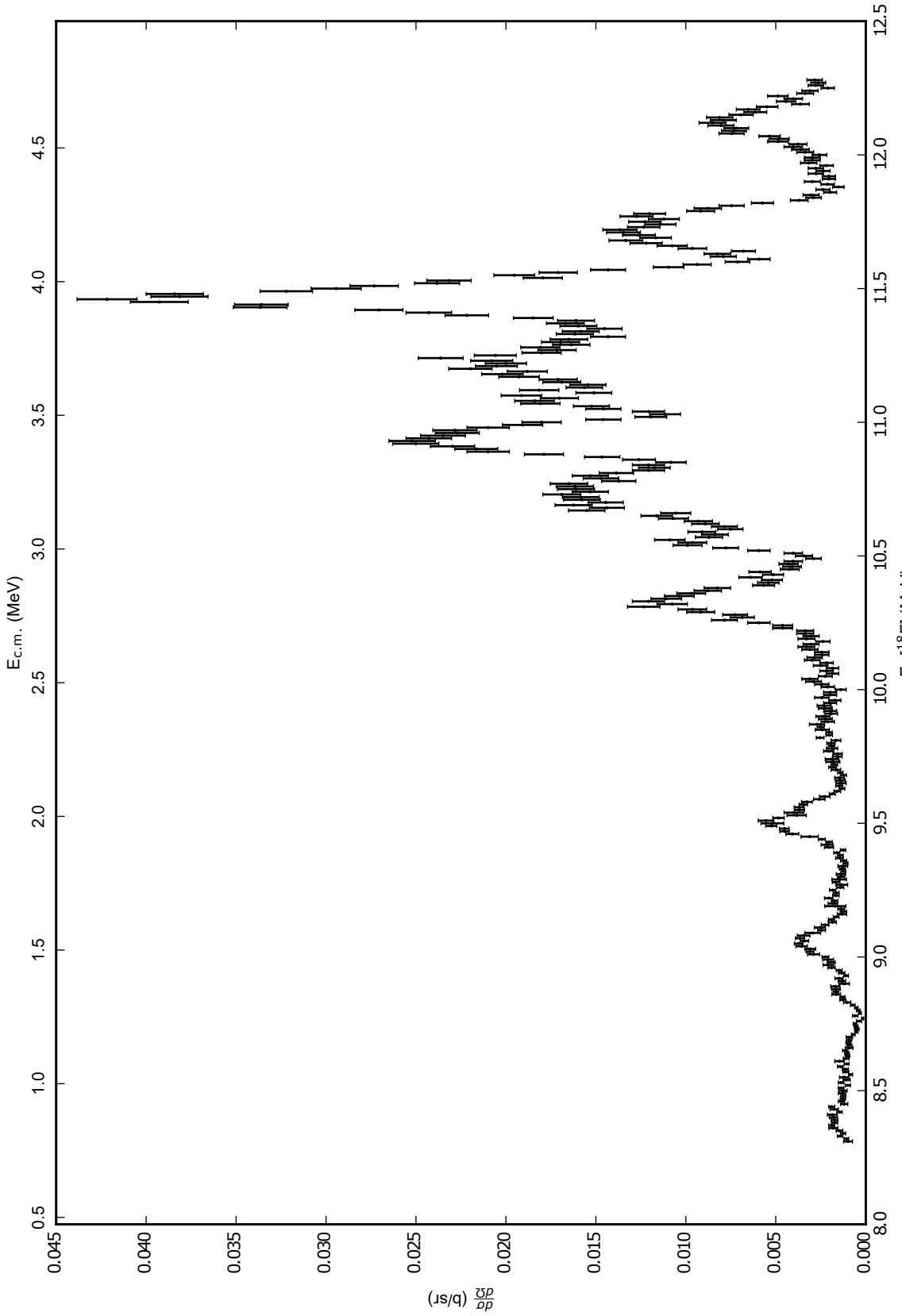

Figure 4.14: The averaged ^{4}He(^{14}N,d)^{16}O spectrum.

From this, the resolution on E_x, σ_{E_x}, was calculated using the gradient of the polynomial f_{E_x}, given in Equation (3.14). This process is defined mathematically as

$$\sigma_{E_m} = \sqrt{\sigma_{\Delta E}^2 + \sigma_E^2} \tag{4.1}$$

$$\sigma_{E_x} = \frac{df_{E_x}}{dE_m}\sigma_{E_m} \,. \tag{4.2}$$

The intrinsic detector resolutions were measured by fitting gaussians to the peaks in the spectra generated by the 3α-source, and extracting their widths. This was found to be between 30 keV and 40 keV for each detector strip, with an average of 36 keV for both the ΔE and E detectors. This led to the following resolutions on the experimental measurements: in the ^{4}He(^{14}N,α) spectrum $\sigma_{E_x} =$ 11 keV below $E_x = 8$ MeV, and $\sigma_{E_x} = 14$ keV above $E_x = 8$ MeV. In the ^{4}He(^{14}N,d)^{16}O spectrum $\sigma_{E_x} =$ 15 keV. The resolution was reduced below 8 MeV in the ^{4}He(^{14}N,α) spectrum because the energies were measured entirely in the ΔE detector, which meant that it was not necessary to sum the detector resolutions in quadrature, and instead $\sigma_{E_m} = \sigma_{\Delta E}$.

4.4 R-Matrix Analysis

A full $\boldsymbol{R}$-matrix analysis was performed in order to extract the energy levels of ^{18}F from these measurements. This section discusses this analysis and compares the results with previously measured states in ^{18}F, and is adapted from my publication: Bailey, S. *et al.* Energy levels of ^{18}F from the ^{14}N+α resonant reaction. *Phys. Rev. C* **90,** 024302 (2 Aug. 2014) (Appendix F).

The multi-channel $\boldsymbol{R}$-matrix was used phenomenologically to fit the spectra produced in this experiment, using the code `Azure2`, using the physical parameters E_λ, J_λ^π and $\Gamma_{\mu\lambda}$ as the fit parameters via the Brune transformation. It was found that the spectra measured in the present work were not sufficient alone to constrain the $\boldsymbol{R}$-matrix fit, since the spins of the states could not be uniquely identified. This was due to the lack of angular measurements, meaning that angular distributions could not be used to constrain the spins of the states. It is often possible in the absence of angular distributions to use the shape of the resonances and interference effects at a single scattering angle to constrain the spins of the states, however here the non-zero spins of ^{14}N and the deuteron led to many different possible channel spins and orbital angular momenta for a state with a given J_λ^π, making this process of producing spin assignments unreliable.

To resolve this issue, data from the literature discussed in Section 4.1.2 was used in conjunction with the data from the present work, further constraining the fit. The data sources used are summarised in Table 4.5. For the data from the present work, the fit was convoluted with the appropriate

Table 4.5: A summary of the data used to constrain the $\boldsymbol{R}$-matrix fit.

Reaction	$\theta_{\text{c.m.}}$	E_x[^{18}F] range (MeV)	Measurement type	Reference
^{4}He(^{14}N,α)	176.6°	6-15.5	TTIK	Present work
^{4}He(^{14}N,d)^{16}O	176.6°	8.2-12.3	TTIK	Present work
^{14}N(α,α)	169°	7-9.1	Thin target	[113]
^{14}N(α,p)^{17}O	167°	7-9.1	Thin target	[113]
^{14}N(α,p)^{17}O	141°	7-9.1	Thin target	[113]
^{14}N(α,p)^{17}O	99°	7-7.9	Thin target	[113]
^{16}O(d,α)^{14}N	166°	8.2-9.1	Thin target	[109]

experimental resolution, however this was not necessary for the other measurements as they were all thin target measurements. It was noticed that the ^{16}O(d, d) measurement from Ref. [109] did not agree with the predicted Rutherford cross-section at low energies. This was corrected for by scaling both the ^{16}O(d, d) and ^{16}O$(d, \alpha)^{14}$N data from the same work by a factor of 1.1 prior to fitting. While the use of previous measurements permitted the application of $\boldsymbol{R}$-matrix theory, it limited the fit to only be performed below E_x = 9 MeV, as above this there were no previous measurements available to provide the necessary additional constraint.

Fitting these data sources simultaneously was not only sufficient to constrain the fit across the ^{14}N + α_0 and ^{16}O + d_0 channels, but the inclusion of the ^{14}N(α,p)^{17}O measurements by Terwagne *et al.* [113] allowed the fit to be extended to include the ^{17}O + p_0 channel, and should therefore produce reliable assignments for $\Gamma_{\alpha 0}$, Γ_{d0} and Γ_{p0}. One would however expect the ^{17}O + p_1 channel to also contribute significantly to the decays of states in ^{18}F. This was expected since the ground state of ^{17}O has a spin of $\frac{5}{2}^+$, while the first-excited state has a low energy of 0.871 MeV and a spin of $\frac{1}{2}^+$. This may introduce a preference for low spins states in ^{18}F to decay via the ^{17}O + p_1 channel rather than the ^{17}O + p_0 channel, since the decay products would carry away a smaller amount of angular momentum, reducing the size of the centrifugal barrier. Therefore the ^{17}O + p_1 channel was included without any data to directly constrain it. Since Γ_{p1} would contribute to the total widths of the states, including it in the parameter space provides a more accurate description of the data and more reliable results. As this channel contains nuclei with non-zero intrinsic spins, multiple channel spins are possible, and therefore multiple orbital angular momenta. For a given state, the choice of channel spin and orbital angular momentum will only significantly affect the spectrum in the ^{17}O + p_1 channel, which is unconstrained. Therefore for this work the smallest orbital angular momentum available was used in all cases, corresponding to the highest penetrability factor and therefore allowing for the largest possible Γ_{p1} given a reasonable γ_{p1}. This was important mainly for the $\boldsymbol{R}$-matrix calculation, as exceptionally large values for γ_{p1} make the calculation difficult, slowing the computational speed. It was observed that the introduction of the ^{17}O + p_1 channel significantly improved the χ^2/d.o.f. of the fits, reducing it by between 10% and

Table 4.6: Details of the channels used in the $\boldsymbol{R}$-matrix calculation. Here Q_f refers to the Q-value for the fusion reaction producing ^{18}F, and the channel radii were calculated from Equation (3.26) with $r_0 = 1.35$.

Channel	Light Particle			Heavy Particle			Q_f	Channel Radius	Channel
	Particle	J^π	E^* (MeV)	Particle	J^π	E^* (MeV)	(MeV)	(fm)	Spins
^{14}N + α_0	α	0^+	0	^{14}N	1^+	0	4.415	5.3967	1
^{16}O + d_0	d	1^+	0	^{16}O	0^+	0	7.526	5.1027	1
^{17}O + p_0	p	$\frac{1}{2}^+$	0	^{17}O	$\frac{5}{2}^+$	0	5.607	4.8212	2, 3
^{17}O + p_1	p	$\frac{1}{2}^+$	0	^{17}O	$\frac{1}{2}^+$	0.8707	5.607	4.8212	0, 1

50% for each data set. The channel radii were calculated for each decay channel using Equation (3.26), setting r_0 to 1.35 fm. The decay channels used in this $\boldsymbol{R}$-matrix fit are summarised in Table 4.6.

The $\boldsymbol{R}$-matrix fit was performed simultaneously to all data sets, using previously measured levels as a starting point for the parameters and then adding the fewest new energy levels possible to produce an optimal fit. The best fits for each data set are shown in Figures 4.15, 4.16 and 4.17. It should be noted that, while the $\boldsymbol{R}$-matrix fits generally reproduce the data very well, with the χ^2/d.o.f. ranging between 1.6 and 2.9, there are some discrepancies at very low energies with the data from this work, where the data is shifted to slightly lower energies compared with the fit. This can be seen below 8.5 MeV in the ^{4}He(^{14}N,d)^{16}O spectrum in Figure 4.15. This is probably due to inadequacies of the energy loss formulae produced by `Lise++` at low energies, since the fit perfectly reproduces the same region in the ^{16}N(d,α)^{14}N spectrum from Ref. [109].

The parameters extracted from these calculations are given in detail in Appendix D, and compared with previously measured states in Table 4.7. The systematic uncertainty on the resonance energies was estimated to be $\pm$10 keV. Uncertainties on the widths were calculated by using the `Minos` erorr analysis function in `Azure2`. In the cases that the error was larger than the width, only an upper limit is given. The results in Appendix D show that the effect produced by varying the channel radii is consistent with the errors extracted on the parameters, indicating a robust analysis. In the following subsections some of the key results of this analysis are discussed with reference to previous work.

4.4.1 Comparisons with Previously Measured States

Upon comparison with previous measurements of states in ^{18}F it became clear that some of the results extracted from this $\boldsymbol{R}$-matrix analysis were contrary to the understanding of ^{18}F at the time of writing. There were several discrepancies between the spins extracted in this work and those extracted from the $\boldsymbol{R}$-matrix fit performed by Gurbich *et al.* [93], and the present analysis seems to overestimate the widths of several states compared with previous measurements. Both of these discrepancies and other state assignments which were not straightforward are discussed here.

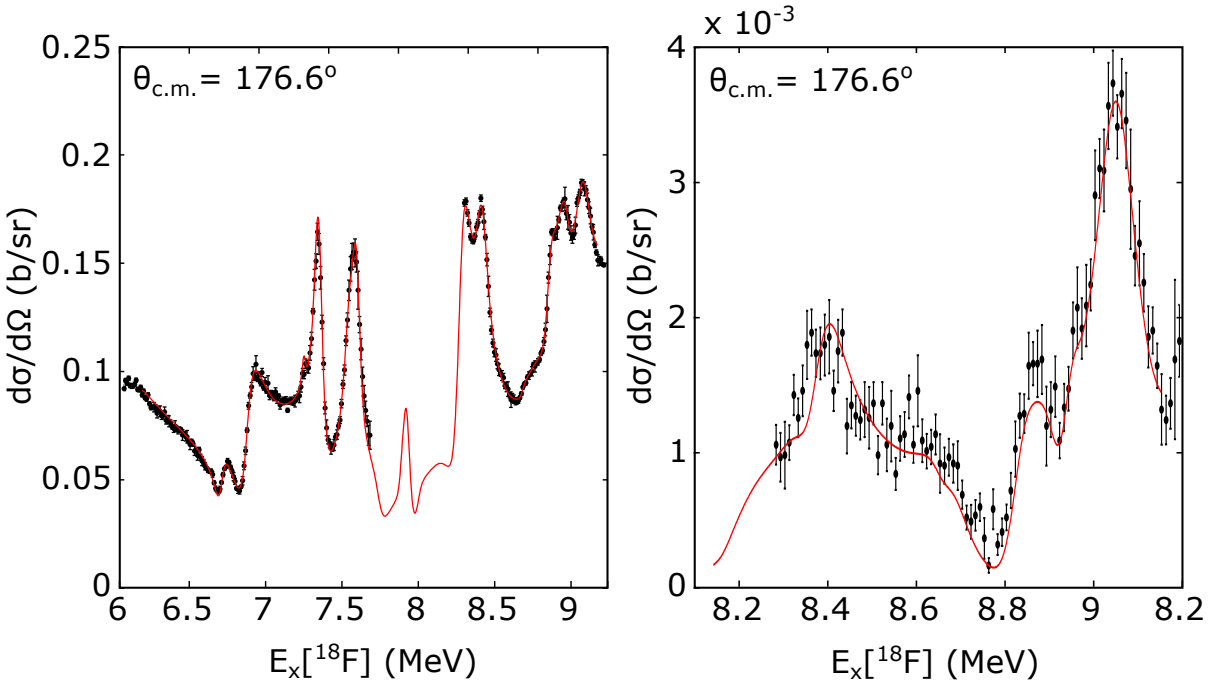

Figure 4.15: $\boldsymbol{R}$-matrix fits to the data from the present work. Fit shown in red. Left: ^{4}He(^{14}N,α) spectrum, χ^2/d.o.f. = 2.6. Right: ^{4}He(^{14}N,d)^{16}O spectrum, χ^2/d.o.f. = 1.8. In both cases the $\boldsymbol{R}$-matrix fit is convoluted with the experimental resolution. These figures were adapted from my work in Ref. [1].

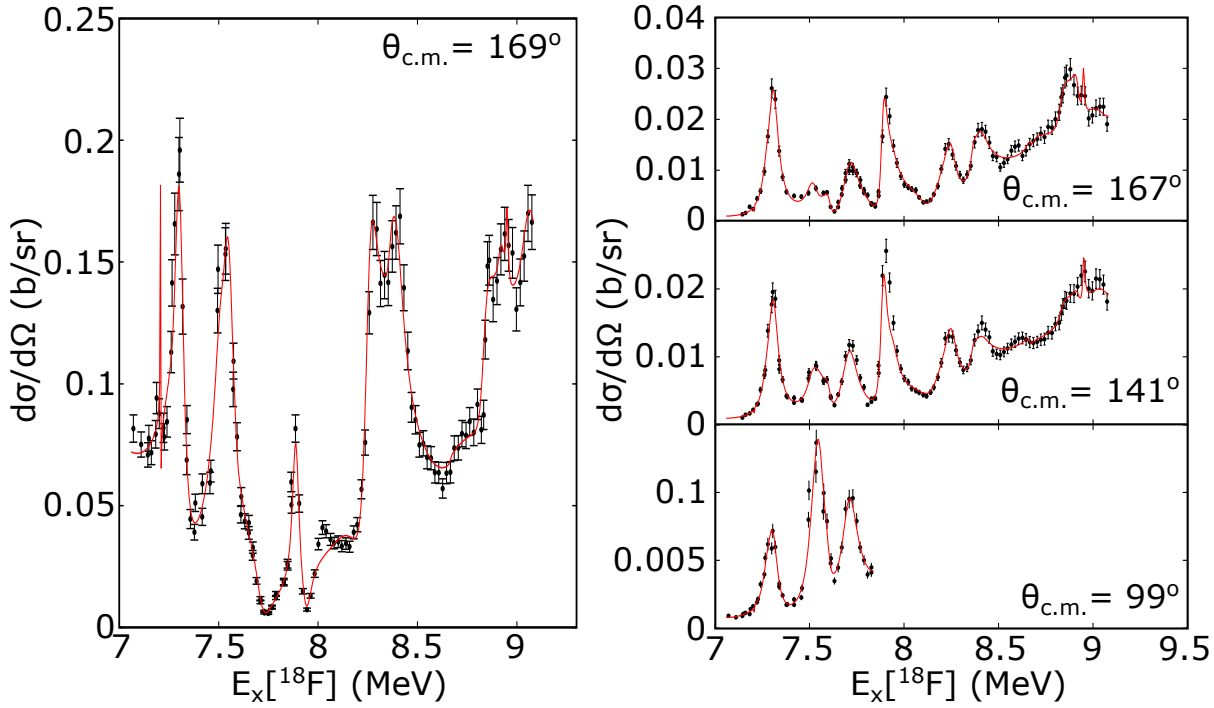

Figure 4.16: $\boldsymbol{R}$-matrix fits to the data from the work by Terwagne *et al.* [113]. Fit shown in red. Left: ^{14}N(α,α) spectrum, χ^2/d.o.f. = 2.2. Right: ^{14}N(α,p)^{17}O spectra, χ^2/d.o.f. = 1.6. These figures were adapted from my work in Ref. [1].

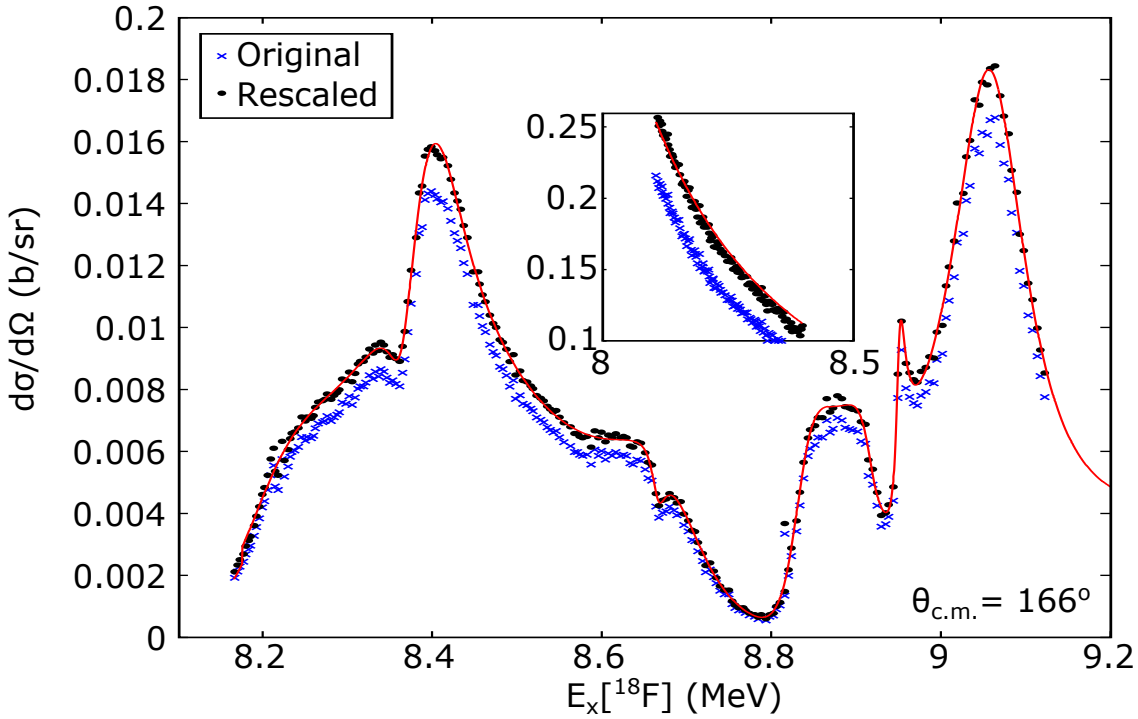

Figure 4.17: $\boldsymbol{R}$-matrix fit to the ^{16}N(d,α)^{14}N spectrum from the work by Seiler *et al.* [109]. Fit shown in red, χ^2/d.o.f. = 2.9. Inset shows the ^{16}O(d,d) spectrum from the same work, at $\theta_{\text{c.m.}}$ = 166.5°, compared with pure Rutherford scattering (red). Data rescaled by a factor of 1.1, as explained in the text. This figure was adapted from my work in Ref. [1].

Table 4.7: A comparison of the states identified in the present work with those in the tabulations compiled by Tilley *et al.* [116] and those from previous R-Matrix fits by Gurbich *et al.* [93] to ^{14}N(α,α) data, Kieser *et al.* [112] to ^{17}O(p,α)^{14}N data and Herring [108] to ^{14}N(α,α) data. The states from the tabulations are shown in bold.

Present Work							Previous Measurements				
E_λ (MeV)	J$^\pi$	Γ (keV)	$\Gamma_{\alpha 0}$ (keV)	Γ_{d0} (keV)	Γ_{p0} (keV)	$\theta^2_{\alpha 0}$	E_λ (MeV)	J$^\pi$	Γ (keV)	Decay	Ref.
6.654[a]	1^-	60 ± 6	39 ± 3	-	21 ± 2	0.216	6.647	1^-	59		[93]
							6.635	1^-	80		[112]
							6.664	1	93		[108]
							6.633	**1**	**80**	p, α	**[116]**
6.832[a]	2^-	118 ± 4	109 ± 3	-	9 ± 2	0.44	6.811	2^-	93		[93]
							6.807	2^-	88		[112]
							6.664	2	101		[108]
							6.809	$\mathbf{2^-}$	**88**	p, α	**[116]**
(7.208)[c]	(3^-)	(0.6 ± 0.3)	(0.6 ± 0.3)	-	(< 0.02)	(0.006)	7.20	3^-	3.1		[93]
							7.213	$3, 4, 5$	< 4		[108]
							7.201	$\mathbf{(4^+)}$	**<6.5**	p, α	**[116]**
7.260	1^+	61 ± 6	53 ± 6	-	3.3 ± 1.1	0.082	7.269	4^+	35		[93]
							7.246	(1^+)	60		[112]
							~7.29	$1, 2, 3$	~ 62		[108]
							7.247	$\mathbf{(1^+)}$	**46.5**	p, α	**[116]**
7.306[a]	3^-	63 ± 3	42 ± 3	-	20 ± 2	0.85	7.326	4^-	57		[93]
							7.294	3^-	60		[112]
							~ 7.32	$2, 3, 4$	~ 31		[108]
							7.315	$\mathbf{(3^-)}$	**52**	p, α	**[116]**
7.515	2^-	62 ± 5	53 ± 4	-	9 ± 3	0.11	7.518	3^-	39		[93]
							7.528	$\mathbf{2^-}$	**16.5**	γ, p, α	**[116]**
7.553[a]	3^-	75 ± 2	62 ± 2	-	12 ± 1	0.994	7.565	4^-	35		[93]
							7.532		**75**	p, α	**[116]**
7.595	1^-	46 ± 13	5 ± 1	-	40 ± 12	0.005	7.592	4^+	31		[93]
							7.555	$\mathbf{(1^-)}$	**30**	p	**[116]**
7.711	3^+	106 ± 12	56 ± 10	-	39 ± 7	0.067	7.814	2^-	140		[93]
							7.685	$\mathbf{3^+, 4^+}$	**36**	p, α	**[116]**
							7.729	$\mathbf{> 0}$	**66**	p, α	**[116]**
7.895	3^-	45 ± 5	26 ± 2	-	19 ± 5	0.088	7.915	3^-	23		[93]
							7.899	$\mathbf{(2^-)}$	**38**	p, α	**[116]**
7.947	1^+	70 ± 11	49 ± 6	-	22 ± 10	0.027	8.016	1^+	93		[93]
							7.941	$\mathbf{(1^+)}$	**112**	p, α	**[116]**
-	-	-	-	-	-	-	8.071	4^+	62		[93]
							8.064	$\mathbf{> 3}$	**60**	p, α	**[116]**
8.108	4^+	100 ± 35	1.7 ± 0.9	-	95 ± 35	0.14	**8.115**		**96**	p	**[116]**
8.212[b]	2^-	170 ± 15	90 ± 8	2.8 ± 0.2	55 ± 12	0.165	**8.209**	$\mathbf{2^-}$	**52**	p, α	**[116]**
8.260[a]	4^+	100 ± 25	65 ± 20	-	32 ± 8	0.86	8.261	4^+	23		[93]
							8.238	$\mathbf{4^+}$	**20**	p	**[116]**
8.326	1^+	450 ± 110	430 ± 110	6 ± 2	15 ± 5	0.16					
8.363[b]	3^+	32 ± 5	4 ± 1	0.119 ± 0.002	6 ± 5	0.011					
8.505[a]	2^-	440 ± 45	270 ± 40	10 ± 2	150 ± 20	0.37					
8.667[b]	2^-	< 50	0.9 ± 0.5	< 50	< 11	0.001					
8.678[b]	1^+	220 ± 20	130 ± 20	8 ± 3	7 ± 4	0.041					
8.801	1^+	280 ± 15	250 ± 15	6.8 ± 0.3	13 ± 5	0.055					
8.858[a]	3^+	410 ± 60	310 ± 50	0.027 ± 0.001	95 ± 20	0.37					
8.917[b]	0^-	43 ± 6	30 ± 4	2.9 ± 0.5	< 4	0.011					
8.951	3^-	< 21	1.2 ± 0.7	0.4 ± 0.2	< 20	0.001					
8.996	1^+	450 ± 115	430 ± 115	13 ± 7	12 ± 10	0.089	**9.02**	$\mathbf{(5^-)}$			**[116]**

[a] Raised Wigner ratio in the α channel $\theta^2_{\alpha 0}$ suggests large α-cluster component in the structure.

[b] Fit suggests a significant ^{17}O + p$_1$ contribution to the total width.

[c] State is too narrow for the present data to provide a confident fit.

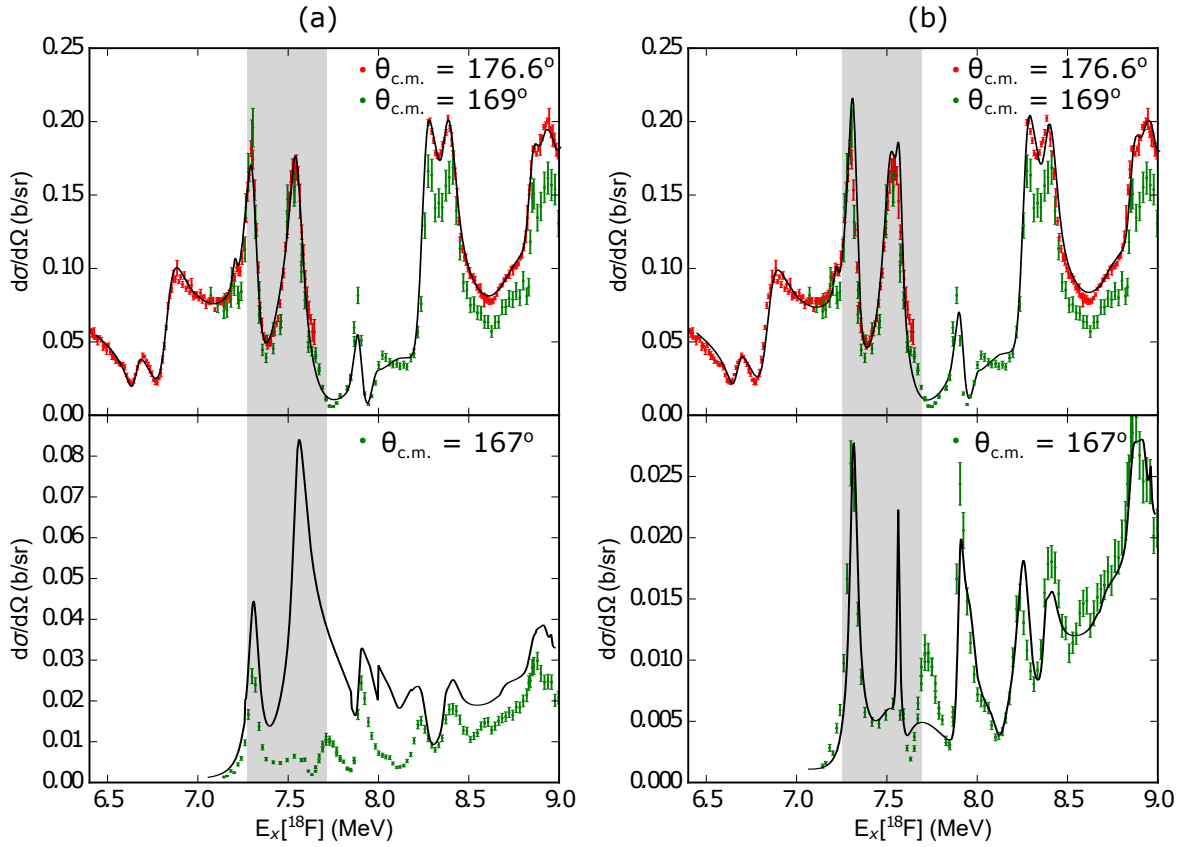

Figure 4.18: The result of altering the spins from the present work to agree with those produced by Gurbich *et al.* [93] on the $\boldsymbol{R}$-matrix fit (black line) to the data in the α_0 (top) and p_0 (bottom) channels. (a) Fit only constrained by data in the α-channel, and the χ^2/d.o.f. calculated for the α-channel only was 4.3. (b) Fit constrained by all data sets; χ^2/d.o.f. $\sim$ 100. Data shown from present work (red), and from Terwagne *et al.* [113] (green). Grey region indicates the location of the altered states. This figure was adapted from my work in Ref. [1].

4.4.1.1 States between 7.26 and 7.712 MeV

The spin assignments for the 6 states between 7.26 and 7.712 MeV were observed to disagree with a previous $\boldsymbol{R}$-Matrix fit by Gurbich *et al.* [93]. A likely explanation for this is that their fit was performed on a more limited data set, constraining only the α channel, and the introduction of more data from different decay channels in the present analysis led to a better constrained fit. It was found that if the alternative spins used by Gurbich *et al.* [93] were used in the present fit, and only the data pertaining to the α-channel was used as a constraint in order to mimic the fit produced by Gurbich *et al.* [93], a good fit can be achieved with an overall χ^2/d.o.f. of 4.3. However if the data constraining the proton and deuteron channels is added it became clear that fitting with these alternative spins cannot sufficiently reproduce the data, with the χ^2/d.o.f. rising to $\sim$100. The results from these fits are shown in Figure 4.18.

Additionally, while the spin assignments disagreed with those made by Gurbich *et al.* [93], they

did agree with the spin assignments from the tabulations [116], suggesting that it is in fact the results produced by Gurbich *et al.* [93] that are anomalous, rather than those produced in the present work.

4.4.1.2 The 2^- State at 6.832 MeV

This state was measured in this work to have a width of 118 keV, compared with 88 keV, 93 keV or 101 keV from previous measurements. This is only a relatively small increase, and may be due to the lack of ^{14}N(α,p)^{17}O data in this region, leading to a poorly constrained Γ_{p0} in the present fit.

4.4.1.3 The 3^- State at 7.208 MeV

This is a very narrow state, with a width extracted from the present fit of 0.6$\pm$0.3 keV. This width is significantly smaller than the experimental resolution here, which is 11 keV. This leads to this state being largely washed out by the experimental resolution, leaving behind only a very small fluctuation in the ^{4}He(^{14}N,α) spectrum to which a resonance may be fit. This resonance is also not well constrained by the thin target measurement of the ^{14}N(α,α) and ^{14}N(α,p)^{17}O spectra by Terwagne *et al.* [113], since the data point spacing in this region is $\sim$11 keV, which is larger than the width of the state. This considerations led to only tentative assignments for this state.

4.4.1.4 The 1^+ State at 7.26 MeV

The width of this state is larger than expected from previous measurements. Here the width was measured to be 61 keV, compared to 46.5 keV in the tabulations by Tilley *et al.* [116] and 35 keV in the work by Gurbich *et al.* [93]. However the result is consistent with the $\boldsymbol{R}$-matrix analysis performed by Kieser *et al.* [112], which produced a width of 60 keV, as well as that performed by Herring [108] which produced a width of 62 keV. It seems likely that the $\boldsymbol{R}$-matrix fit by Gurbich *et al.* [93] may underestimate the width since they assign a spin of 4^+ to the state, which would significantly increase the centrifugal barrier and limit the width. Also the widths given by Gurbich *et al.* [93] seem to be consistently underestimated for every state with spin assignments higher than in the present work and the tabulations [116]. Taking this into account, with the exception of the tabulations by Tilley *et al.* [116] the width from the present work seems consistent with the majority of other sources.

4.4.1.5 The 2^- State at 7.515 MeV

The width of the this state is also larger than previous measurements suggest, with the present work recording a width of 62 keV compared with 39 keV in the work by Gurbich *et al.* [93] and 16.5 keV in the tabulations by Tilley *et al.* [116]. Again it is likely that Gurbich *et al.* [93] underestimate the width due to an incorrect spin assignment, however the width from the tabulations is more difficult to explain. It

may be that there are in fact two states here with the same spin and parity, which cannot be resolved in this analysis. Another state was observed in a Breit-Wigner analysis of ^{17}O(p,α_0)^{14}N, ^{17}O(p,p$_1\gamma$)^{17}O and ^{17}O(p,γ)^{18}F data by Sens *et al.* [111] at 7.446 MeV with undetermined spin and a width of 140 keV, which would be an appropriate candidate if it was measured to be the correct spin. If that was the case it may require a new measurement with improved resolution in order to separate the two states.

4.4.1.6 The 3^+ State at 7.711 MeV

This state may correspond to another possible unresolved doublet. In this case there are two possible states in the tabulations by Tilley *et al.* [116] at 7.685 MeV and 7.729 MeV, each with ambiguous spin assignments and widths of 36 keV and 66 keV. In comparison the present analysis provides a width of 106 keV. Again a repeat measurement with improved resolution may disentangle this doublet, allowing the widths to be accurately extracted.

4.4.1.7 The 4^+ State at 8.108 MeV

In the previous work by Gurbich *et al.* [93] a 4^+ state was observed at 8.071 MeV with a width of 62 keV, which agrees with a state in the tabulations by Tilley *et al.* [116] at 8.064 MeV. While it is tempting to assign the 4^+ state at 8.108 MeV from the present work to these states, the partial widths indicate otherwise. A very small $\Gamma_{\alpha 0}$ and large Γ_{p0} extracted from the present work implies that this state is in fact the 8.115 MeV state from the tabulations by Tilley *et al.* [116] which had previously only been measured to proton decay. Additionally the total width of this state matches the width from the present work far better.

4.4.1.8 The 2^- and 4^+ States at 8.212 and 8.26 MeV

The widths of both of these states are dramatically overestimated when compared with both the tabulations by Tilley *et al.* [116] and the parametrisation by Gurbich *et al.* [93], with widths of 170 keV and 100 keV in the present work, compared with 52 keV and 23 or 20 keV measured previously. However in the present work 9 new states have been observed ranging from 8.236 MeV to 9 MeV, and the introduction of these new states to the $\boldsymbol{R}$-matrix calculation may strongly interfere with the states close to the boundary. This suggests that the properties of these two states extracted in the present work are in fact more reliable than those from previous measurements.

4.4.1.9 The 1^+ State at 8.996 MeV

This state has only been tentatively assigned to the state from the tabulations by Tilley *et al.* [116] at 9.02 MeV. While this state is very close in excitation energy, the spin is significantly higher and oppo-

Table 4.8: The possible α-clustered states measured in the present work, identified by having $\theta^2_{\alpha 0} > 0.2$.

E_x[^{18}F] (MeV)	J^π	$\theta^2_{\alpha 0}$
6.654	1-	0.216
6.832	2-	0.44
7.306	3-	0.85
7.553	3-	0.994
8.260	4+	0.86
8.505	2-	0.37
8.858	3+	0.37

site parity in the tabulations, and there is no measured total width with which a comparison could be made. Additionally this state has only been observed in the ^{17}O(α,t)^{18}F proton transfer reaction [117], which implies a large single particle component to the state which is not what is observed in the present analysis. If this assignment is incorrect, then the state from the present work would in fact correspond to a 10$^{\text{th}}$ newly observed state in ^{18}F.

4.5 Clustering Discussion

By examining the Wigner ratios for the states decaying to the ^{14}N + α_0 channel, seven possible candidates for α-clustered states were identified, shown in Table 4.8, and compared with predicted α-clustered states in Figure 4.19.

As discussed in Section 4.1.1, the semi-microscopic calculation performed by Buck *et al.* [105] predicts two positive parity α-clustered rotational bands, one with $K = 1$ and another with $K = 0$. It does not however predict any negative parity states, which given the existence of positive parity rotational bands, ought to exist also. In the following section these predictions are compared with the results from the present work, and the negative parity states are discussed.

4.5.1 The Predicted 5^+ Member of the $K^\pi = 1^+$ Rotational Band

The first predicted state in the relevant energy range is the 5^+ member of the K$^\pi = 1^+$ rotational band. This state was predicted to have an energy of 6.32 MeV [105], and was assigned to a 5^+ state which was found to be very strongly populated by the ^{14}N(^{7}Li,t)^{18}F α-transfer reaction at 6.567 MeV [64, 99]. This state was also observed in α elastic scattering measurements performed previously by Gurbich *et al.* [93], and was fit using $\boldsymbol{R}$-matrix theory as a 5^+ state at 6.567 MeV, with a width of 0.5 keV and $\Gamma_\alpha/\Gamma = 1$. This state was not observed, however, in the present work due to its very narrow width, which would have been entirely washed out by the experimental resolution.

Despite this, it is expected that this state has been correctly assigned based on the previous experimental measurements. It is likely that its narrow width is simply a product of the state being close to

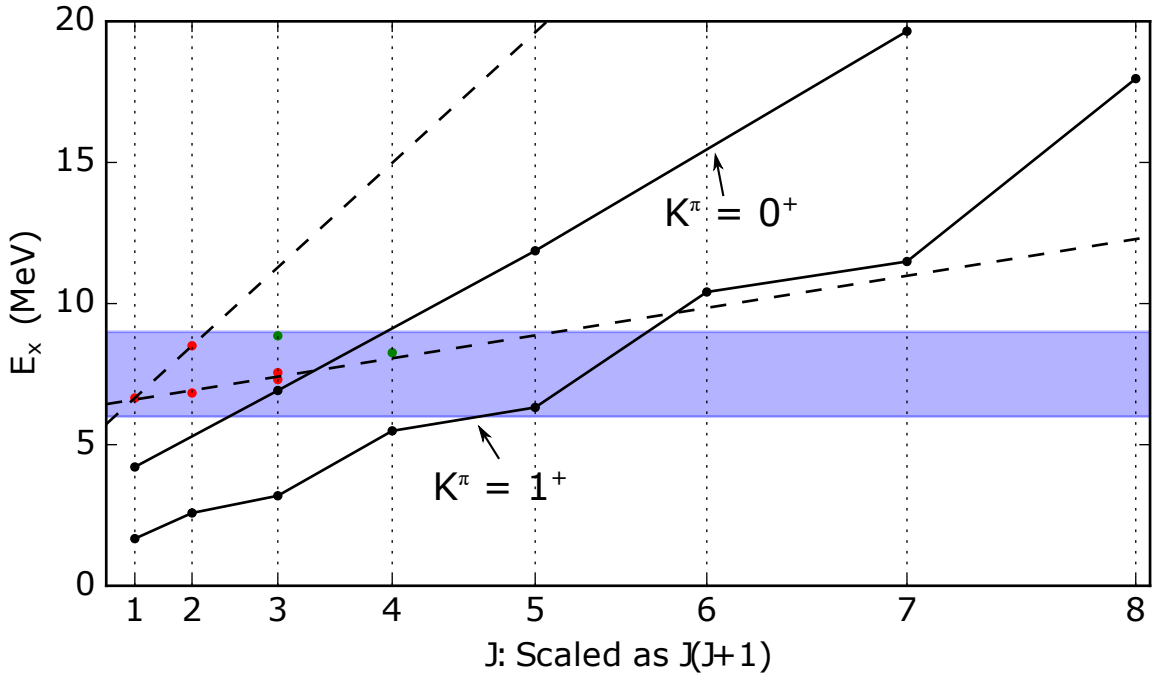

Figure 4.19: The α-clustered states identified in the present $\boldsymbol{R}$-matrix fit (red dots: $\pi = -$, green dots: $\pi = +$), compared with the rotational bands predicted by Buck *et al.* [105] (black dots and solid lines). Two possible negative parity rotational bands are shown (dashed line), and discussed in the text. The blue region indicates the range of the present $\boldsymbol{R}$-matrix fit.

the particle decay threshold and having a large spin, producing a very large centrifugal barrier, rather than any structural affects.

4.5.2 The Predicted 3^+ Member of the $K^\pi = 0^+$ Rotational Band

Another predicted α-clustered state is the 3^+ member of the K$^\pi = 0^+$ rotational band. This state was predicted to have an energy of 6.92 MeV [105]. Some attempts have been made to assign this state to experimental measurements. The first candidate was a 3^+ state at 6.48 MeV, however this has been discounted as it has been observed to contain considerable two-particle components [118], and additionally this would place the state below the 5^+ member of the K$^\pi = 1^+$ band, which is the opposite of what is predicted by the calculation. Another candidate has been suggested at 7.26 MeV by Middleton *et al.* [99]. This was observed to be very strongly populated in α-transfer reactions, however further analysis by Sens *et al.* [111] suggested that this may in fact be a 3^- state, and this was confirmed in the present $\boldsymbol{R}$-matrix analysis.

The present analysis has identified three 3^+ states at 7.712, 8.363 and 8.858 MeV. The 7.712 MeV state is the closest match to the theorised state in excitation energy, however it has a small Wigner ratio of $\theta^2_{\alpha 0} = 0.067$, which is uncharacteristic of α-clustered states. Additionally, this ratio may be reduced

further since when comparing this state to the tabulations it seems likely that this may actually be an unresolved doublet, with two 3^+ states at 7.685 MeV and 7.729 MeV. If this is the case then each would be expected to have even smaller widths and hence smaller Wigner ratios than was produced in the present fit. The second candidate at 8.363 MeV also has a very small Wigner ratio of $\theta^2_{\alpha_0} = 0.011$, and there seems to be some evidence for a large Γ_{p1} component, suggesting that this is also not a good candidate. This leaves the 3^+ state at 8.858 MeV which does present a large Wigner ratio of $\theta^2_{\alpha_0} = 0.37$, indicative of an α-clustered state. However the energy of this state is 1.93 MeV higher than the predicted value.

4.5.3 The Predicted 5^+ Member of the $K^\pi = 0^+$ Rotational Band

The 5^+ member of the K$^\pi = 0^+$ band was predicted by Buck *et al.* [105] to exist at 11.87 MeV, and has yet to be assigned experimentally. This is outside of the range of the present $\boldsymbol{R}$-matrix analysis, but inside the range of the measured spectrum.

A calculation was performed to predict what an α clustered state at the Wigner limit ($\theta^2_{\alpha 0} = 1$), with the predicted energy and spin would look like in the $\alpha(^{14}\text{N},\alpha)$ spectrum. The result is shown in Figure 4.20. The peak is very broad, and so it is unlikely that it could be assigned to any of the strong, sharp resonances observed in this energy region. However by taking the moving average of the data, using an interval of 1 MeV, averages out these narrow resonances, leaving behind only the structures in the spectrum that are broader than 1 MeV. It is clear that there is a good agreement between the shape and amplitude of the predicted 5^+ state and the moving average. While this is indicative of the existence of this state, a full $\boldsymbol{R}$-matrix analysis is required to see specifically how a state in this region would impact the spectrum. This, in turn, would require all the decay channels to be measured at this energy, at a range of scattering angles.

4.5.4 Negative Parity States

While there has been little work done to investigate negative parity α-clustered states, it is possible to put the observed negative parity states with raised $\theta^2_{\alpha 0}$ into context by comparing them with the systematics of the positive parity rotational bands.

The gradient of a rotational band is inversely proportional to the moment of inertia of the nucleus, evident from Equation (2.9). Given a specific cluster structure, one would expect to observe both positive and negative rotational bands, and as they are based on the rotation of the same structure they ought to have a similar moment of inertia, and therefore similar gradients.

It can be seen from Figure 4.19 that two possible rotational bands can be constructed by looking

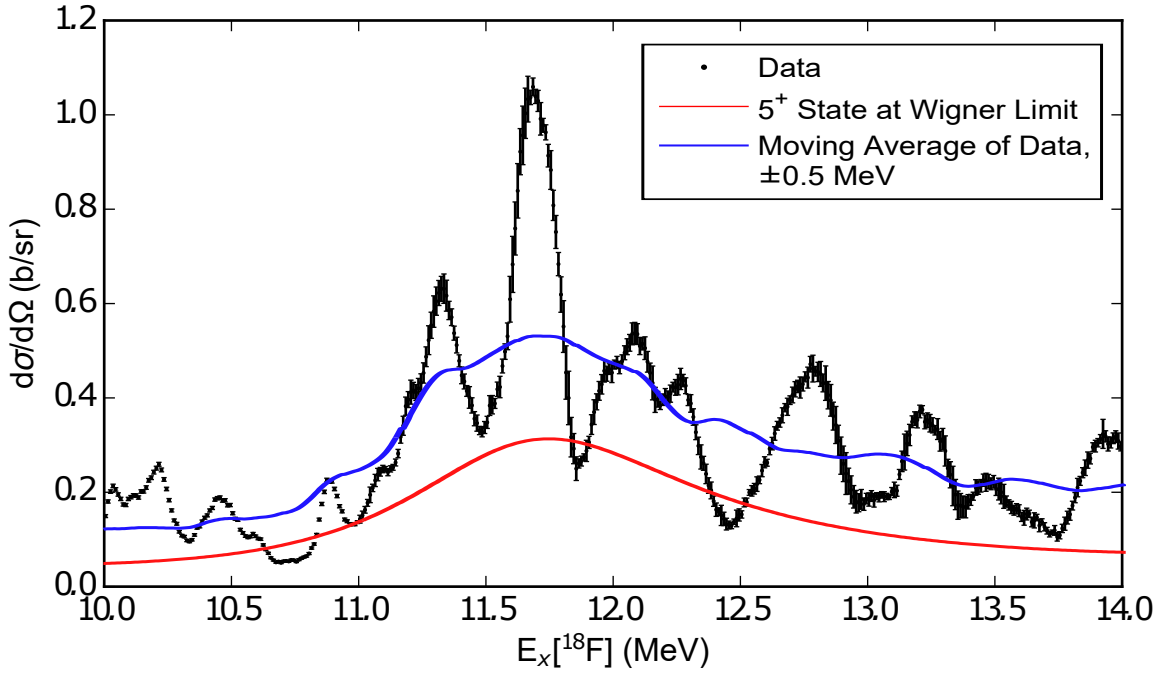

Figure 4.20: The ^{4}He(^{14}N,α) spectrum in the vicinity of the 5^+ α-clustered state predicted by Buck *et al.* [105], compared with a theoretical calculation of the predicted state, described in the text, and the moving average of the data taken over a 1 MeV interval. This figure was adapted from my work in Ref. [1].

for a linear dependence on J(J+1). The rotational band candidate with a shallower gradient is however unlikely because if it were indeed a α-clustered rotational band then the 4^- and 5^- members ought to have been measured in the present $\boldsymbol{R}$-matrix fit, and they were not. Additionally the gradient is significantly shallower than that observed for the positive parity states.

The band candidate with a larger gradient may be a more reasonable option, however it is very tentative, with only two data points to constrain it. It should also be noted that this analysis is based upon the bands being perfectly linear, when in fact it is clear from previous measurements that coriolis decoupling is present, causing zig-zagging in the bands. Overall it is clear that without the measurements of higher spin candidates this analysis is inconclusive.

4.6 Conclusion

Measurements were made of the ^{4}He(^{14}N,α) and ^{4}He(^{14}N,d)^{16}O resonant reactions, populating excitation energies in ^{18}F between 6 and 15.5 MeV and 8.4 and 12.3 MeV respectively. These were analysed, in conjunction with previous measurements of reactions covering the ^{14}N + α_0, ^{16}O + d_0 and ^{17}O + p_0 channels by Terwagne *et al.* [113] and Seiler *et al.* [109], using a multi-channel $\boldsymbol{R}$-matrix analysis be-

tween E_x[^{18}F] = 6 and 9 MeV. This led to the extraction of 24 energy levels in ^{18}F, at least 9 of which had not been previously observed. For each level $\Gamma_{\alpha 0}$, Γ_{d0}, Γ_{p0} and Γ_{p1} were extracted.

Following this, the degree to which α-clustering persists in ^{18}F was analysed, by comparison of the present work with predictions made using a semi-microscopic α-cluster model of ^{18}F. This comparison confirmed the existence of the 3^+ state in the $K^\pi = 0^+$ rotational band, however it was measured in this work at a significantly higher energy than was predicted, indicating that the α-cluster structure of ^{18}F is not yet fully understood. Further to this, the 5^+ member of the same rotational band was compared with the data in the present work. While this state fell outside the range of the present $\boldsymbol{R}$-matrix analysis, a simplified analysis was employed, and suggested that the level may indeed exist at its predicted energy.

Four negative parity states were extracted from the $\boldsymbol{R}$-matrix fit with raised α decay widths, indicative of α-clustering. There has however been little theoretical work done to investigate negative parity α-clustered states, meaning that conclusions could not be drawn from these results.

Chapter 5

An Investigation of $^{44,\ 48,\ 52}$Ti using the Spectral Signature Approach

In this chapter ^{44}Ti, ^{48}Ti and ^{52}Ti are investigated using the TTIK technique to measure the ^{40}Ca + α, ^{44}Ca + α and ^{48}Ca + α reactions. These were then analysed using a novel technique, developed throughout this chapter and referred to as the spectral signature analysis. Parts of this chapter are adapted from my publication: Bailey, S. *et al.* Alpha clustering in Ti isotopes: ^{40,44,48}Ca + α resonant scattering. *EPJ Web of Conferences* **113,** 08002 (2016) (Appendix H).

5.1 Introduction

5.1.1 Previous Work

There has been a lot of work investigating the α-cluster structure of ^{44}Ti both experimentally and theoretically. Much of this is discussed in Refs. [119–121]. Here some of the most relevant results are briefly summarised.

A review of the experimental work on α-clustering in ^{44}Ti by Ohkubo [119] identified many states with a possible α-cluster configuration up to $E_x[^{44}\text{Ti}]\sim$ 18 MeV. These levels are compared with α-cluster model calculations in Figure 5.1, details of which can be found in Ref. [120], and show generally a good agreement, indicating that the structure of ^{44}Ti may have a significant α-^{40}Ca component.

The α-clustered states are defined in terms of the principle quantum number, $N = 2n_r + l$, where n_r denotes the number of nodes in the radial wavefunction and l denotes the orbital angular momentum. The rotational bands are labelled by the value of N at the band head. The bands of interest for this work are the $N = 14$ and $N = 15$ bands. The 0^+, 2^+ and 4^+ states in the $N = 14$ band and the

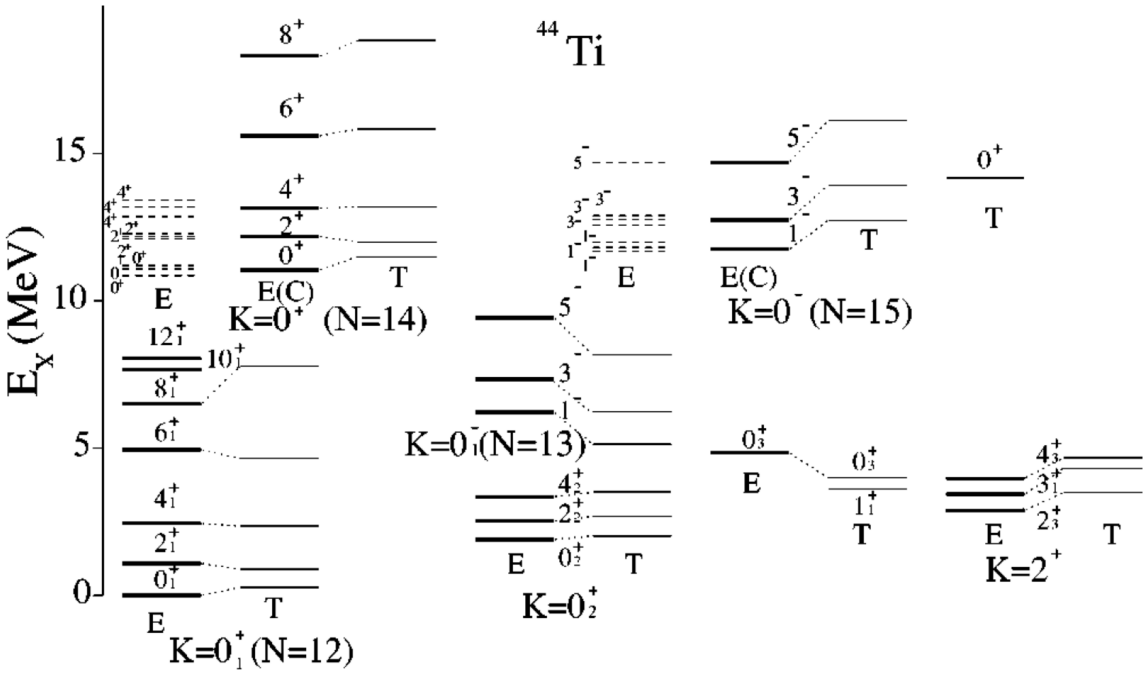

Figure 5.1: Energy levels of ^{44}Ti, compared with predictions from an α-cluster model. Theoretical energy levels (thin solid lines, labelled T) are compared with the experimental data (thick solid lines and labelled E). The fragmented experimental energy levels (E) are displayed by dashed lines and their centroid is indicated by the thick solid lines with label E(C). This figure is reprinted from Ref. [120].

1^-, 3^- and 5^- states in the $N = 15$ band were measured experimentally using a range of α-transfer reactions by Artemov *et al.* [122] and Yamaya *et al.* [123] and α-elastic scattering reactions by Frekers *et al.* [124, 125]. With the exception of the 5^- state, these states are well understood to manifest as sets of fragmented α-clusered states, split by the coupling of the α-clustered states to non-clustered states. It is likely the 5^- state manifests in a similar way, however this state was measured only by Artemov *et al.* [122], and in those measurements the fragmentation of the energy levels was not observed. The higher spin members of the $N = 14$ band are not as well understood. The 6^+ and 8^+ members were assigned based on the analysis of oscillations in the α+^{40}Ca fusion cross-section with the optical model [126]. Full details of the energy levels of these bands can be found in Table 5.1.

In addition to these two bands, a 0^+ bandhead at 14 MeV was predicted by the α-cluster model for a core-excited higher nodal band with an α + ^{40}Ca(0^+, 3.35 MeV) structure by Ohkubo *et al.* [120]. This state has not yet been identified experimentally.

The structure of ^{44}Ti can be further understood by a comparison with a deformed basis AMD calculation [121]. This is a more sophisticated version of the AMD calculations discussed in Section 2.1.3, which allows the Gaussian wavepackets which define each nucleon to be non-spherical. The deformations of each wavepacket are then treated as a free parameters in the calculation, in addition

Table 5.1: Previous measurements of α-clustered states in ^{44}Ti. Showing values for fragmented excitation energies (E), the centroid energy of the fragmented states (E(C)), and theoretically predicted excitation energies denoted by T. All energies given in MeV. The work by Ohkubo *et al.* [120] is an extensive summary of previous experimental measurements, rather than another independent measurement. In the work by Ohkubo [119], Ohkubo *et al.* [120], and Michel *et al.* [126] some excitation energies were not stated in the text. In these cases the excitation energies were extracted from figures.

Band	J^π	Frekers *et al.* [124, 125]		Artemov *et al.* [122]	Michel *et al.* [126]	Ohkubo *et al.* [119, 120]		
		E	E(C)	E(C)	E(C)	E	E(C)	T
$N = 14$	0^+	10.44 10.63 10.71 10.84 11.04 (11.1) (11.15)	11.05	11.7		10.86 11.08 11.19	11.04	
	2^+		12.17	12.28	12.3	12.12 12.18 12.28	12.19	
	4^+		13.18	13.42	13.6	12.86 13.18 13.42	13.15	
	6^+			16.1	15.5		15.58	
	8^+				18.2		18.28	
$N = 15$	1^-		11.69	11.8		11.69 11.73 11.8		
	3^-		12.77	12.86		12.57 12.78 12.88		
	5^-			14.7		14.7		
Core Excited	0^+							14.0

to the positions of the wavepackets. This calculation is very powerful as it is able to describe both deformed mean-field and α-cluster type structures without the *a priori* assumption of either structure. This calculation predicts the coexistence of both superdeformed mean-field bands and α-cluster bands in ^{44}Ti, in good agreement with experimental work. It predicts both the $N = 14$ and $N = 15$ α-clustered bands, consistent with previous experimental measurements, and also the fragmentation of the $N = 15$ states due to coupling with mean-field type states. The fragmentation of the $N = 14$ states is not predicted, however this is explained by a deficiency in the calculation.

By comparison there has been little work investigating ^{48}Ti, ^{52}Ti, or other neutron rich Titanium isotopes, however the work that has been done has been unable to find substantial evidence for α-clustering in this region. A DWBA analysis of a range of α-transfer reactions has indicated that the α-spectroscopic factors decrease with increasing A for the ground states of ^{44,46,48,52}Ti [127, 128]. The work by Fukada *et al.* [129] measuring the ^{40,42,48}Ca(^{7}Li,$t\alpha$)^{40,42,48}Ca reaction does identify α-clustered states in ^{46}Ti, however they are not as strongly populated as those in ^{44}Ti. They were, however, unable to populate any such states in ^{52}Ti. The ^{48}Ca(α,α) elastic scattering measurement was made by Frekers *et al.* [124], and resonant structure identified, yet no analysis was made of that structure.

Studies of other nuclei in this mass region (^{32}S, ^{34}S, ^{36}Ar and ^{40}Ca) using the TTIK technique by

Lonnroth *et al.* [68] and Goldberg *et al.* [69] and Norrby *et al.* [66, 67] have shown a fragmented α-cluster structure, indicating that the manifestation of α-clustered states as sets of fragmented states is a common phenomenon in this mass region.

5.1.2 The Spectral Signature Approach

Difficulties arise in the application of the phenomenological $\boldsymbol{R}$-matrix when the data used to constrain the fit is incomplete or inadequate, with the procedure becoming incredibly time-intensive as well as producing ambiguous results. As discussed in Section 3.1.4, a significant difficulty encountered when attempting to analyse TTIK measurements using $\boldsymbol{R}$-matrix theory is the degradation of the experimental resolution for scattering angles away from 180°. This is especially problematic for spectra with a high level density, such as would be expected in the present experiment, leading to ambiguous angular distribution measurements and spin/parity assignments, and therefore precluding a full $\boldsymbol{R}$-matrix fit.

In order to circumvent this problem a new technique was developed, which avoids using $\boldsymbol{R}$-matrix theory directly and instead attempts to identify certain features or 'signatures' in the spectra indicative of the underlying nuclear structure. Here the spectral signature to be identified is that of fragmented α-clustering, often also known as doorway states or the fine structure of a resonance, and this is done using the Continuous Wavelet Transform(CWT) [130]. The major benefit of this technique is that there is no need extract the properties of the underlying level structure; the aspect of nuclear structure of interest, in this case the existence of fragmented α-clustering, is extracted directly from the measurements. This means that it is not necessary to make angular distribution measurements, as spin/parity assignments are not required, allowing the analysis to be performed on the optimal resolution measurements at $\theta_{\text{c.m.}} = 180°$ alone[a].

This technique is similar to the correlation analysis used in Ref. [124]. Here the correlation function, $C(E,\epsilon)$, is defined as

$$C(E,\epsilon) = C_{ik} = \frac{\langle y_i y_k\rangle - \langle y_i\rangle\langle y_k\rangle}{\langle y_i\rangle\langle y_k\rangle} \tag{5.1}$$

where y_i and y_k correspond to the values of the measured cross-section at E and $(E+\epsilon)$ respectively, and $\langle\ \ \rangle$ indicates an average over a suitably chosen interval. The correlation function is then used to analyse the average behaviour of the fluctuations in the spectrum as a function of E, and from this conclusions can be drawn about the existence of fragmented states. This process is limited, however, by the arbitrarily chosen interval over which the averages must be calculated. The size of this interval ought to be chosen such that it is larger than the widths of the fragmented states, but small enough to

[a] This is not to say that this approach would not benefit from angular distribution measurements, simply that they are not a fundamental necessity for the procedure.

Table 5.2: The properties of the beams produced at the GANIL facility for this experimental work. Here the beam intensity is given in particles per second, and the charge state refers to the number of electrons ionised from the nucleus.

Ion	Charge State	Energy (MeV)	Beam Current (nA)	Beam Intensity (pps)
^{40}Ca	7+	179.83	0.3-0.9	2.5×10^8 - 8×10^8
^{44}Ca	8+	206.59	0.1-0.2	8×10^7 - 1.5×10^8
^{48}Ca	9+	234.01	0.2-1.0	1.5×10^8 - 7×10^8

ensure that groups of fragmented states can be identified, as any features smaller than the averaging interval will be lost. The use of the CWT in this work plays a similar role to the correlation function, however as a transformation it does not rely on the definition of an averaging interval or equivalent, and instead simply transforms the data into a new representation, with minimal loss of information.

5.2 Experimental Work

The experimental work and preliminary analysis follow an almost identical process as was detailed in Sections 4.2 and 4.3 for the ^{18}F experiment, and so to avoid repetition the following section simply summarises the key features of this experiment.

Measurements were made using the TTIK technique of the three resonant reactions ^{40,44,48}Ca + α, to facilitate the investigation of ^{44,48,52}Ti. These measurements were performed at the GANIL experimental facility in Caen, France. Here three ion beams were produced, accelerating ^{40}Ca, ^{44}Ca and ^{48}Ca ions to 179.83, 206.59 and 234.01 MeV respectively. These beams were accelerated using the CSS1 cyclotron, and the properties of each beam are given in Table 5.2. More details on the beam production can be found in Appendix B, and on the GANIL accelerator facility in Ref. [131].

Following extraction from the accelerator the beam passed into the reaction chamber. The reaction chamber was very similar to that used for ^{18}F, with some differences. The window was constructed from a slightly thinner sheet of Havar, at 4.5 µm thick. The absorber was placed in the beam line, before the window, and was constructed of Havar with thicknesses of either 2, 4 or 8 µm. A schematic diagram of the reaction chamber is shown in Figure 5.2.

The detection system used here involved two 1 mm thick DSSDs placed at zero degrees to the beam line, at the opposite end of the chamber to the window and in the ΔE-E configuration, as well as a 'lampshade' detector array. This is shown in Figure 5.3. The lampshade array consists of 6 single sided silicon detectors. These detectors are wedge shaped with 16 curved strips, and combine to produce an array which looks like a lampshade, where each detector is at an angle of 45° to the beam line. The silicon detectors are Micron Semiconductor YY1 detectors, and the lampshade array is discussed in detail in Ref. [84]. These detectors were designed to be used to extract angular distribution mea-

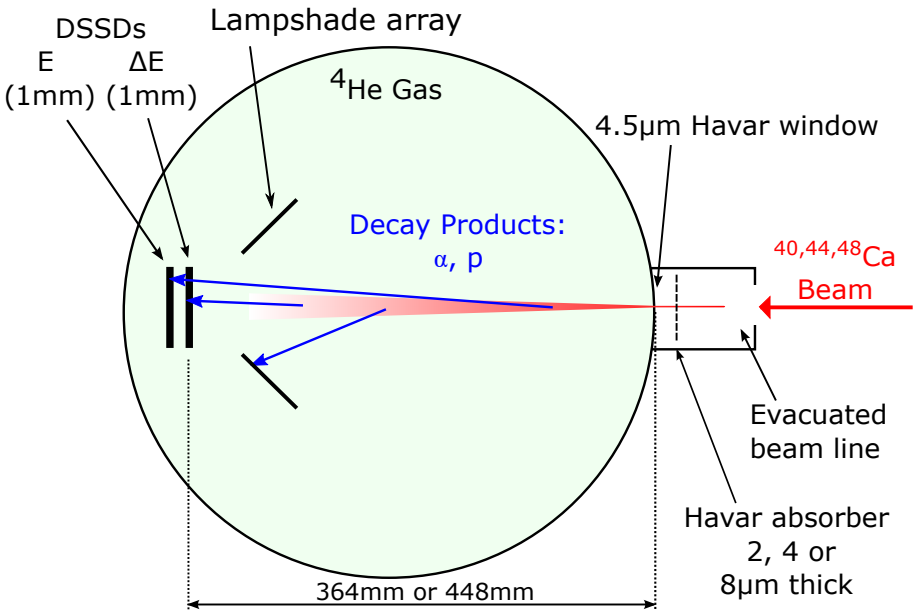

Figure 5.2: The set-up of the reaction chamber used for the ^{40,44,48}Ca + α measurements. This figure was adapted from my work in Ref. [1].

surements, however in the present analysis the data from these were not used, and so they are not discussed further.

The priority for these measurements was to optimize the quality of the ^{4}He(^{40,44,48}Ca,α) spectra, rather than attempting to use particle identification to measure all available decay channels, as was done in the case of ^{18}F. This led to the configuration of the ΔE-E DSSD set-up with two thick detectors, rather than a thin ΔE detector. By considering the maximum excitation energy that was populated in these measurements, and the open decay channels given in Table 5.3, it was clear that only α-particles and protons would have a significant impact on the measurements. The DSSDs are charged particle detectors, and as such cannot measure neutrons, and the deuteron channels only opened at very high excitation energies, meaning that they would not contribute significantly to the measurements. It was therefore decided that using a thick ΔE-detector ought to be sufficient to separate out the α and proton channels, as it will be sufficiently thick to stop all of the α-particles, but the light protons will pass through and be measured in the E-detector. By rejecting all events that are measured in the E-detector it was possible to veto the proton events, producing a clean α spectrum above $E_{\text{c.m.}} \sim 3$ MeV in all measurements. It was crucial that the measurement veto proton events as they will come not only from the reactions with the gas but also from protons that are knocked out of the Havar window and absorber.

This technique has the advantage of improving the resolution on the measured energies, measured

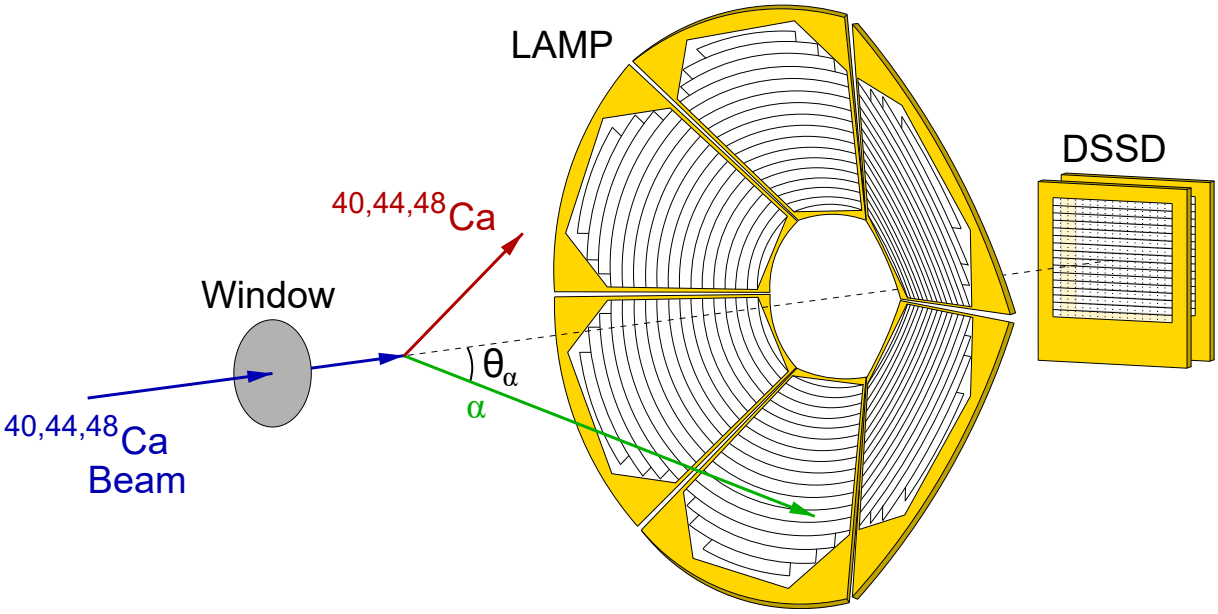

Figure 5.3: The detector set-up used for the ^{40,44,48}Ca + α measurements. The data from the Lamp array was not used in the present work. θ_α is the scattering angle of the α-particle in the laboratory frame. This figure was adapted from Ref. [84].

in this work as 45 keV at Full Width Half Maximum, as they will be measured entirely in one detector, and also allows the measurements of the α-particles to be extended to low energies, while avoiding the gap in the spectrum that was present in the ^{18}F experiment. In total 10 measurements were made of the ^{4}He(^{40,44,48}Ca,α) spectra, using different beams, gas pressures and absorbers. These are detailed in Table 5.4. For each of these measurements the preliminary data analysis was identical to that detailed in Section 4.3, with the exception that the data was not recalibrated to correct for the dead layer in the DSSDs. This correction was not made because without the measurement of multiple decay channels or the direct measurement of the dead-layer, its thickness could not be adequately constrained. This correction was not considered to be necessary, however, as all the measurements made were of α-particles, and so the energy lost to the dead-layer was partially accounted for automatically by the fact that the detectors were calibrated with a 3α-source, and therefore with the same decay product.

5.3 Results and Spectra

The ^{4}He(^{40,44,48}Ca,α) spectra were produced by converting the raw data from Yield as a function of measured energy to $d\sigma/d\Omega$ as a function of excitation energy E_x using the techniques detailed in Sections 3.1.2 and 3.1.3. Following this reconstruction process the absolute values for $d\sigma/d\Omega$ were extracted for each spectrum by scaling the measurements to provide an optimal agreement with the

Table 5.3: The decay channels populated in the present measurements. Here threshold E_x indicates the excitation energy above which the channel is open, and max E_x the maximum excitation energy populated in that nucleus.

Nucleus	Max E_x (MeV)	Channel	Threshold E_x (MeV)
^{44}Ti	17.3	^{40}Ca + α_0	5.127
		^{43}Sc + p_0	8.649
		^{43}Ti + n_0	16.299
^{48}Ti	22.2	^{44}Ca + α_0	9.447
		^{47}Sc + p_0	11.445
		^{47}Ti + n_0	11.626
		^{46}Sc + d_0	19.867
^{52}Ti	19.9	^{48}Ca + α_0	7.669
		^{51}Ti + n_0	7.808
		^{51}Sc + p_0	13.529
		^{50}Sc + d_0	18.057

Table 5.4: A summary of the measurements made in this experiment. Max E_x indicates the maximum excitation energy populated in the compound nucleus in that measurement.

Measurement	Beam	Gas Pressure (mbar)	Absorber Thickness (μm)	Window → Detectors Distance (mm)	Max E_x (MeV)
1	^{40}Ca	550	4	364	12.49
2	^{40}Ca	750	2	364	14.79
3	^{40}Ca	750	2	448	14.79
4	^{40}Ca	800	None	448	16.95
5	^{44}Ca	849	None	448	22.59
6	^{44}Ca	849	2	448	20.67
7	^{44}Ca	849	4	448	18.66
8	^{48}Ca	790	4	448	18.44
9	^{48}Ca	790	8	448	14.58
10	^{48}Ca	920	2	448	20.24

typical Rutherford scattering cross-section at low energies, given by

$$\frac{d\sigma}{d\Omega}_R = \left(\frac{Z_1 Z_2 e^2}{4\pi\epsilon_0}\right)^2 \left(\frac{1}{4E_{\text{c.m.}}}\right)^2 \frac{1}{\sin^4 \frac{\theta_{\text{c.m.}}}{2}} \tag{5.2}$$

where Z_1 and Z_2 denote the atomic numbers of the nuclei involved, e is the charge of the electron and ϵ_0 is the permittivity of free space. The geometrical efficiency correction was performed by setting a maximum scattering angle in the centre of mass frame of 175°, which leads to a mean measured scattering angle of 176.6° using Equation (3.17). In this experiment Monte Carlo simulations of the geometrical efficiency correction, discussed in Section 3.1.3, indicated that the correction worked well for all measurements.

The results of this process are shown for each measurement in Figures 5.4, 5.5 and 5.6. The reconstructed excitation energies show very good agreement between the different measurements, with all resonances and features in the spectra lining up in excitation energy. However a poorer agreement is observed between the cross-sections of the different measurements. This is thought to be due to background contaminants in the spectra, and is discussed in Section 5.3.1. While the good agreement in excitation energy indicates that the analysis was robust, the variations in cross-section made the identification of inelastic contaminants impossible using the techniques described in Section 3.1.5, as any differences in the cross-section between measurements due to the inelastic processes will be indistinguishable from differences due to the background contaminants.

The degree to which inelastic contributions ought to influence the ^{4}He(^{40,48}Ca,α) spectra should, however, be small. The first excited states for each of the reactions are given in Table 5.5. Both the first excited states of ^{40}Ca and ^{48}Ca are quite high excitations, meaning that the barrier penetrability will be on average significantly smaller that it would be in the elastic channel, leading to a small contribution from the inelastic channel. This is however not so clearly the case for ^{44}Ca, and so it is possible that the ^{4}He(^{44}Ca,α) spectrum may include significant inelastic contributions. While this is not an ideal situation, the spectral signature analysis is not especially sensitive to contaminants as it focuses on the dominant contribution to the spectrum, and while inelastic contributions may be significant they are unlikely to dominate the elastic contribution.

Furthermore, because of the disparity in cross-section measurements, they could not be averaged to produce a suitable single cross-section measurement. Averaging the measurements is only useful when the individual measurements are independent measurements of the same quantity. However in this case the measurements are not strictly the same quantity as they have different background levels, and therefore averaging them may introduce artificial features arising due to the different combinations of backgrounds. Therefore in the spectral signature analysis detailed in Section 5.4 the measure-

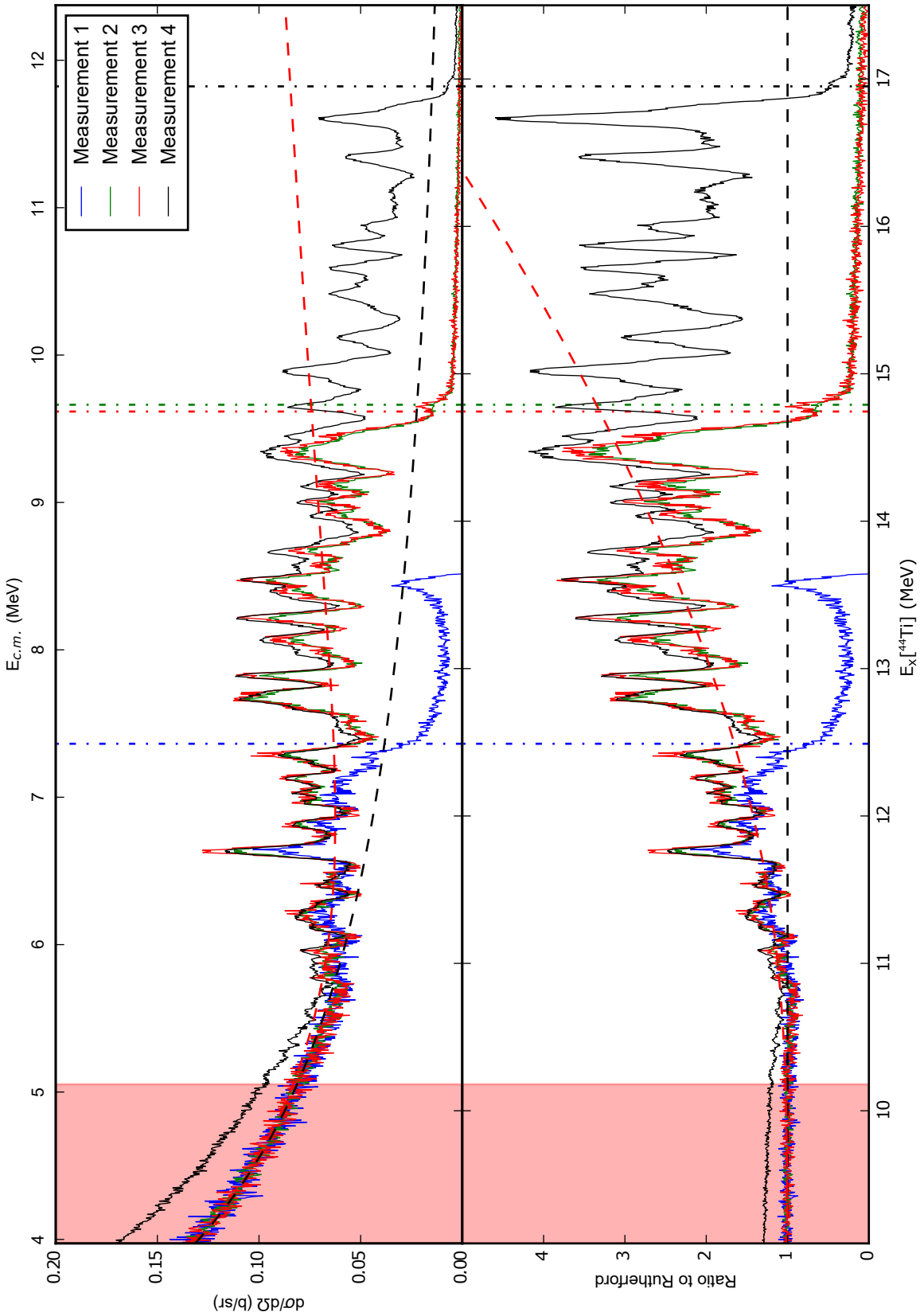

Figure 5.4: The reconstructed excitation function for the measurements of the ^{4}He(^{40}Ca,α) spectrum (top) and the ratio to the Rutherford cross-section (bottom). Shaded red region indicates the energy range used to match the measurement to the Rutherford cross-section. The dot-dashed lines indicate the predicted maximum energy that ought to be populated in the correspondingly coloured measurements. In the case of measurements 2/3 the dot-dashed lines are displaced horizontally slightly, for clarity. Also shown is the Rutherford cross-section (black dashed line) and the combination of the Rutherford and hard-sphere potential contribution (red dashed line).

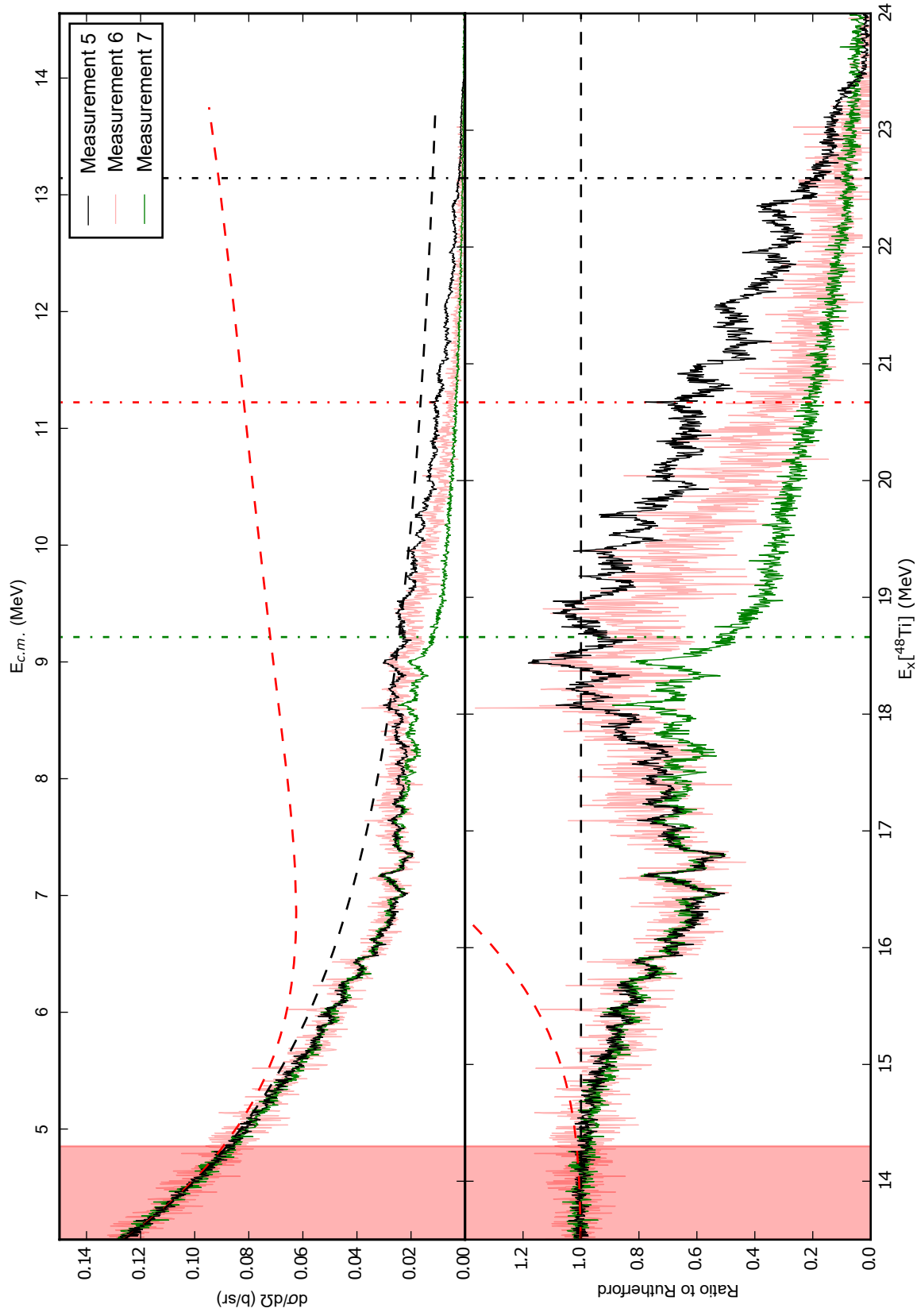

Figure 5.5: The reconstructed excitation function for the measurements of the ^{4}He(^{44}Ca,α) spectrum (top) and the ratio to the Rutherford cross-section (bottom). Shaded red region indicates the energy range used to match the measurement to the Rutherford cross-section. The dot-dashed lines indicate the predicted maximum energy that ought to be populated in the correspondingly coloured measurements. Also shown is the Rutherford cross-section (black dashed line) and the combination of the Rutherford and hard-sphere potential contribution (red dashed line).

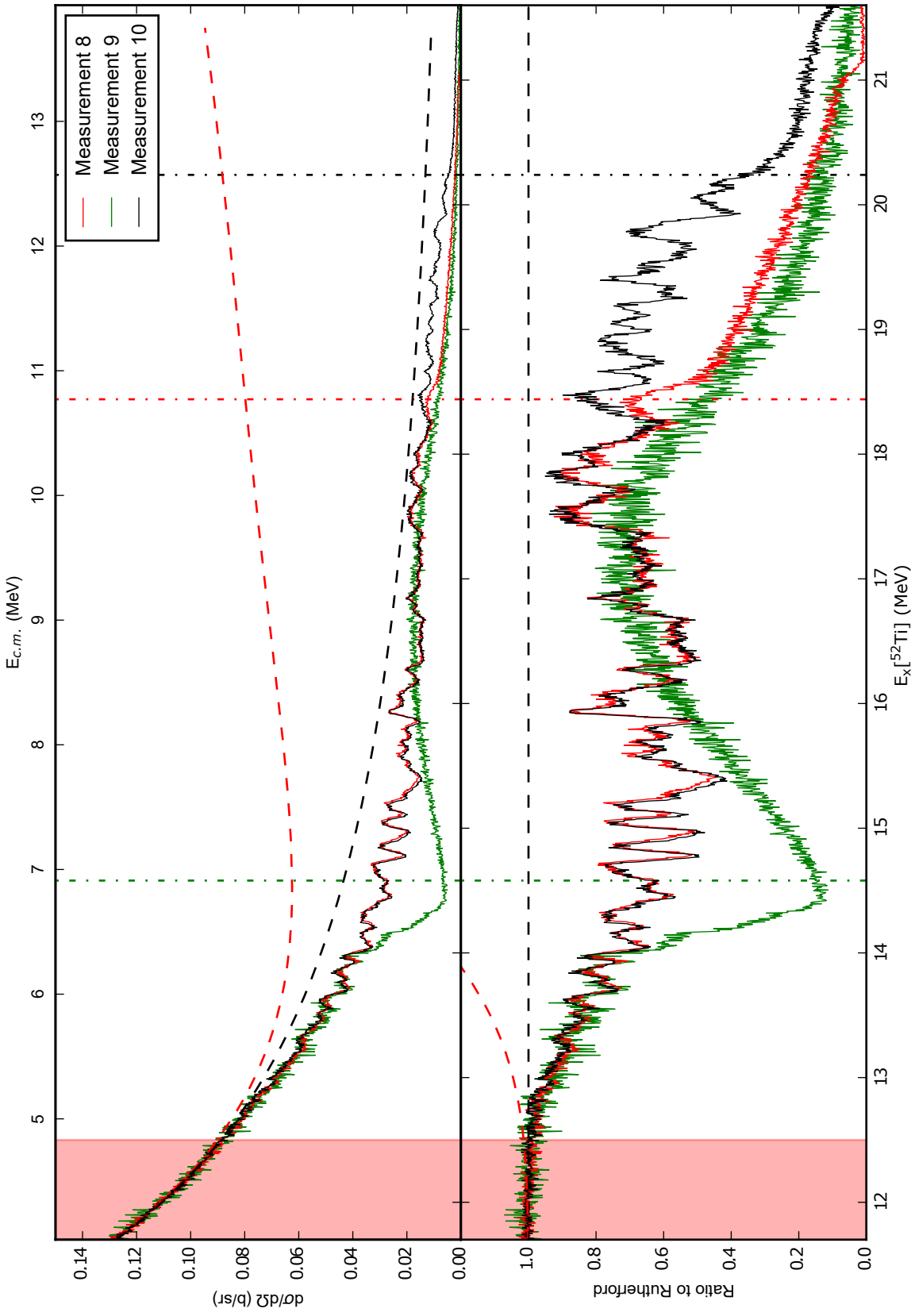

Figure 5.6: The reconstructed excitation function for the measurements of the ^{4}He(^{48}Ca,α) spectrum (top) and the ratio to the Rutherford cross-section (bottom). Shaded red region indicates the energy range used to match the measurement to the Rutherford cross-section. The dot-dashed lines indicate the predicted maximum energy that ought to be populated in the correspondingly coloured measurements. Also shown is the Rutherford cross-section (black dashed line) and the combination of the Rutherford and hard-sphere potential contribution (red dashed line).

Table 5.5: The ground and first excited states of each decay product in the ^{44,48,52}Ti experiments.

Decay product	Energy (MeV)	J^π
α	g.s.	0^+
	20.21[a]	0^+
^{40}Ca	g.s.	0^+
	3.352	0^+
^{44}Ca	g.s.	0^+
	1.157	2^+
^{48}Ca	g.s.	0^+
	3.831	2^+

[a] State too high to be populated in these measurements

ments which extend to the highest excitation energies (measurements 4, 5 and 10) were used alone.

5.3.1 Background Contaminants

In TTIK measurements it is possible to introduce background contaminants to the spectra which arise from interactions between the beam and the window or absorbers. In an ideal situation this could be accounted for by taking a measurement with the target ^{4}He gas removed from the chamber, however as the target is used to stop the beam from reaching the detectors, without it the beam would hit the detectors, and the high beam intensity would damage them. It is possible to overcome this by using an identical beam with a much lower inensity, which would therefore not damage the detectors and allow such a measurement to be made, however this was not done in this experiment due to beam time constraints.

With no direct measurement of the background contributions, they were analysed qualitatively. At low energies the background contribution seems to be insignificant in all measurements except measurement 4, since the shape of the spectrum matches that expected for pure Rutherford scattering. This is evidenced by the constant ratio of the cross-section to the Rutherford scattering cross-section (shown in the bottom panel in Figures 5.4, 5.5 and 5.6) at low energies in all measurements with the exception of measurement 4. Based on this, measurement 4 was not scaled to match the Rutherford cross-section at low energies, and instead was scaled to match the resonant contribution as best as possible with measurements 1, 2 and 3.

At high energies it is clear that there is often a significant background contribution to the measurements, especially in the ^{4}He(^{44,48}Ca,α) measurements, as above the maximum excitation energies that ought to be populated in each measurement there is often still a significant yield. Measurement 9, which was made using the thickest absorber available (8 µm), shows the possible shape of the background contributions to these measurements. The yield here is small at low energies, and peaks at approximately 17 MeV, before slowly tailing off at high energies as is observed in the other measure-

ments.

This analysis suggests that the background varies slowly with energy. The spectral signature analysis is not sensitive to these slowly varying features, and focuses only on the sharply varying resonant contribution to each spectrum. It was therefore assumed that these background contributions would not have a significant detrimental effect on the results of the analysis.

5.3.2 Potential Contribution

As discussed in Section 3.2 there are three principle components to any resonant scattering reaction. These are the Rutherford contribution, the potential contribution and the resonant contribution. Here the potential contribution to each of the measured reactions is discussed.

The sum of the hard sphere potential contribution and the Rutherford contribution is calculated using $\boldsymbol{R}$-matrix theory with no resonances, and this is compared with the measurements in Figures 5.4, 5.5 amd 5.6. For all three reactions the calculated hard sphere potential contribution interferes constructively with the Rutherford contribution, however this only matches the ^{4}He(^{40}Ca,α) spectrum. By contrast, in both the ^{4}He(^{44}Ca,α) and ^{4}He(^{48}Ca,α) spectra the potential contribution destructively interferes with the Rutherford contribution. These results are in good agreement with Ref. [124].

5.4 Spectral Signature Analysis

5.4.1 The Continuous Wavelet Transform

The CWT provides the decomposition of a spectrum into a continuous range of scales, δE. It was originally developed for use in signal processing and image analysis, however more recently has been used in nuclear structure physics to extract the fine structure of giant resonances [132, 133] and in the analysis of inelastic α-particle scattering on ^{16}O [134]. In the present work it is used as a location-dependent Fourier transform. In this formulation δE is analogous to the period in Fourier analysis, and the CWT identifies both the degree to which a given scale δE contributes to the spectrum and *where* in the spectrum it contributes. Much of the following section is based on Ref. [130]

The wavelet transform, $W_\Psi(E,\delta E)$, represents the contribution of a given scale to the spectrum at a specific energy, E, and is calculated by convoluting the measured spectrum $\sigma(E)$ with an appropriately chosen wavelet $\Psi(E)$. This is defined explicitly as

$$W_\Psi(E,\delta E) = \frac{1}{(\delta E)^n}\int_{-\infty}^{\infty}\sigma(\epsilon)\Psi\left(\frac{\epsilon - E}{\delta E}\right)d\epsilon \tag{5.3}$$

where ϵ is a dummy variable used to facilitate the integration. The variable n is a normalisation factor,

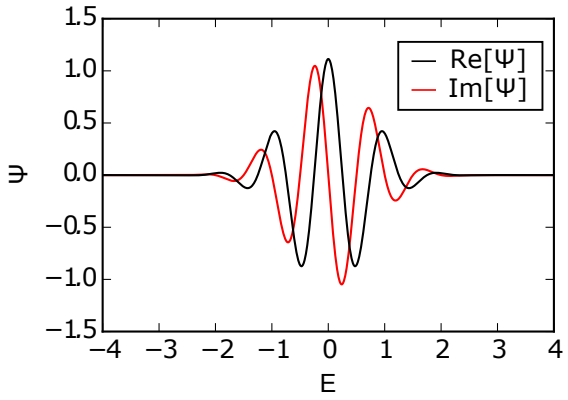

Figure 5.7: The Complex Morlet wavelet, with the wavelet scale $d = 0.8$. Both the real and imaginary parts are shown.

and may be defined to be any real number, and is taken in much of the literature to be either 0, 0.5 or 1 [130]. In the present work $n = 0.5$ is used, since this ensures that the L^2-norm of Ψ is 1 [130, p. 229]. The wavelet power spectrum, $P_\Psi(\delta E)$, is defined as the integral of $|W_\Psi(E, \delta E)|^2$ over the entire energy range, and represents the contribution of a given scale to the entire spectrum

$$P_\Psi(\delta E) = \int_{-\infty}^{\infty} |W_\Psi(E, \delta E)|^2 dE \,. \tag{5.4}$$

It is also possible to reconstruct the original spectrum from W_Ψ and the complex conjugate of Ψ using the following equation [130]

$$\sigma(E) = \frac{1}{c_\Psi} \int_{-\infty}^{\infty} d\epsilon \int_0^{\infty} \frac{d\,\delta E}{\delta E^{3-2n}} W_\Psi(\epsilon, \delta E) \Psi^* \left(\frac{\epsilon - E}{\delta E} \right) . \tag{5.5}$$

Here c_Ψ is a normalisation quantity, calculated from the Fourier transform of the wavelet, $\hat{\Psi}(\omega, \delta E)$, as

$$c_\Psi = \int_{-\infty}^{\infty} \left| \hat{\Psi}(\omega, \delta E) \right|^2 |\omega|^{-1} \, d\omega \,. \tag{5.6}$$

For the purposes of identifying fragmented alpha clustering the Complex Morlet wavelet is used, which is specialised for extracting periodic information from spectra. The Complex Morlet wavelet, displayed in Figure 5.7, consists of an oscillatory term multiplied by a Gaussian window, and is defined in Ref. [130, p. 229] as

$$\Psi(E) = \underbrace{(d\sqrt{\pi})^{\frac{1}{2}}}_{\text{Normalisation}} \overbrace{\left(e^{-i2\pi E} - c_0\right)}^{\text{Oscillatory}} \underbrace{e^{-\frac{E^2}{2d^2}}}_{\text{Window}} \tag{5.7}$$

where the factor c_0 is a normalisation factor, $c_0 = \exp\left(-2\pi^2 d^2\right)$. The variable d determines the size of the gaussian window. A typical visualisation of $|W_\Psi|$ and P_Ψ is presented in Figure 5.8 for an example

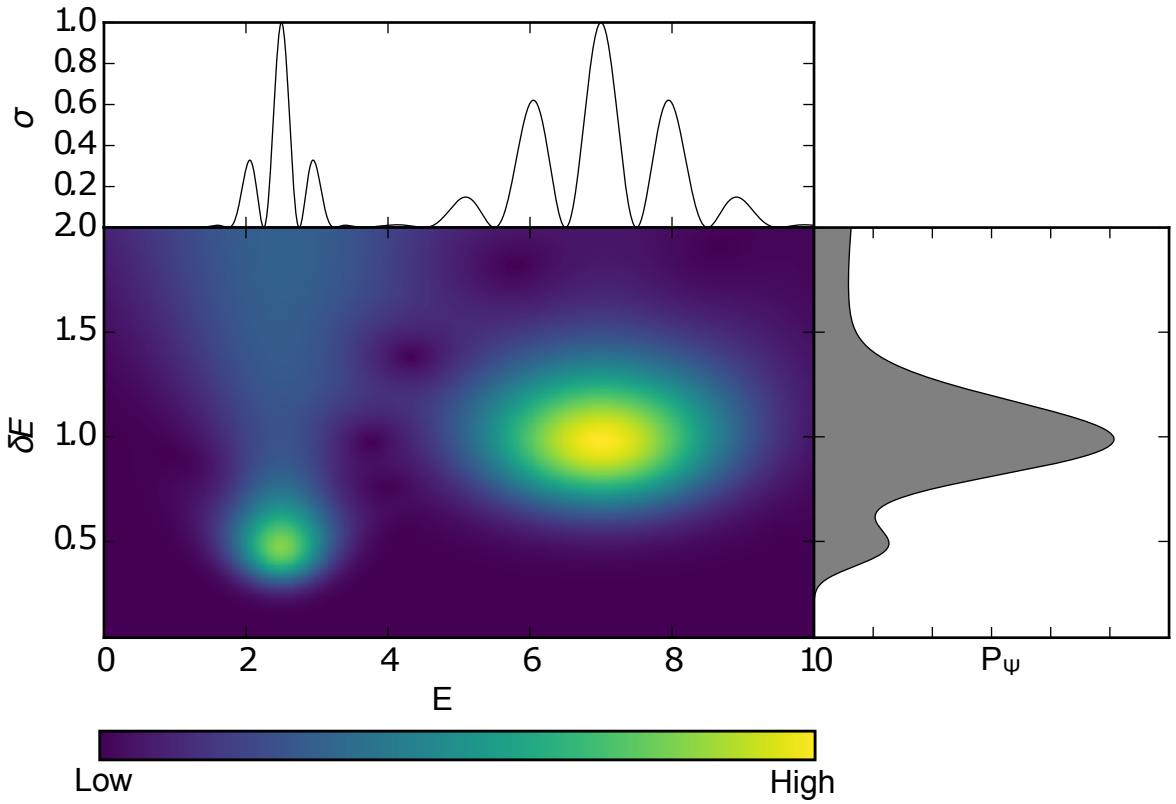

Figure 5.8: The CWT of the example spectrum defined in Equation (5.8). In this case all calculations use the wavelet scale $d = 0.8$. Displayed in this figure is the original spectrum $\sigma(E)$ (top panel), the wavelet transform, W_Ψ, (bottom left panel) and the wavelet power spectrum, P_Ψ, (bottom right panel). As it is an example spectrum, all units are arbitrary.

spectrum. Here the top panel displays the original, untransformed spectrum, $\sigma(E)$, and the bottom left panel displays $|W_\Psi|$, as a function of both E and δE. The bottom right panel displays P_Ψ as a function of δE. Both P_Ψ and $|W_\Psi|$ are always displayed in arbitrary units, since the absolute values have little physical meaning and depend heavily on the choice of normalisation of Ψ.

The example spectrum used for this demonstration is

$$\sigma(E) = e^{-5(E-2.5)^2}\cos^2\left(\frac{\pi E}{0.5}\right) + e^{-0.5(E-7.0)^2}\cos^2\left(\frac{\pi E}{1.0}\right). \tag{5.8}$$

This consists of two distinct periodic signals: one centred at $E = 2.5$ with a period of 0.5, and a second centred at $E = 7$ with a period of 1.0. It is clear from Figure 5.8 that the properties of these two signals are recovered instantly, with two distinct hot spots in W_Ψ, each corresponding to the two signals in the spectrum. Furthermore P_Ψ shows two peaks, known as characteristic scales, one for each signal.

The choice of the wavelet scale, d, is an important one, and dictates the trade-off between energy

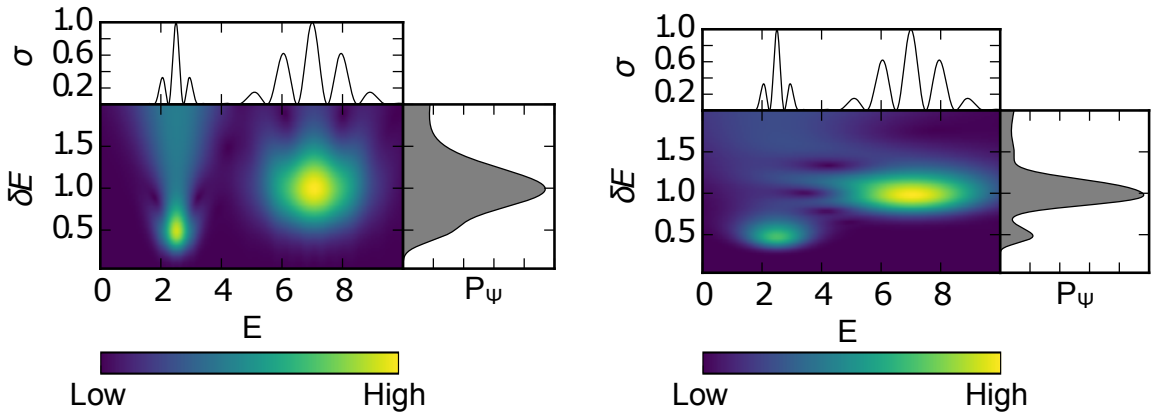

(a) $d = 0.5$ (b) $d = 1.5$

Figure 5.9: Two CWTs of the example spectrum defined for Figure 5.8, demonstrating the dependence of W_Ψ and P_Ψ on the wavelet scale d.

resolution, σ_E, and scale resolution, $\sigma_{\delta E}$, which are defined as

$$\sigma_{\delta E} = \frac{\delta E}{4d} \tag{5.9}$$

$$\sigma_E = 2d\delta E\,. \tag{5.10}$$

The effect of the choice of wavelet scale is shown in Figures 5.9a and 5.9b. A small d produces good energy resolution but poor scale resolution, and large d does the opposite. In the present work $d = 0.8$ is used in all cases as it gives the best balance for this work.

The wavelet transform may also be calculated using the Fourier and inverse Fourier transforms, defined in terms of frequency, ω, as

$$\hat{f}(\omega) = \mathrm{FT}_{x\to\omega}\left[f(x)\right] = \int_{-\infty}^{\infty} f(x)e^{-2\pi i x\omega}dx \tag{5.11}$$

$$f(x) = \mathrm{IFT}_{\omega\to x}\left[\hat{f}(\omega)\right] = \int_{-\infty}^{\infty} \hat{f}(\omega)e^{2\pi i x\omega}d\omega\,. \tag{5.12}$$

The wavelet transform and power spectrum are then defined in terms of the Fourier transform of the wavelet, $\hat{\Psi}(\omega,\delta E)$, and the Fourier transform of the spectrum, $\hat{\sigma}(\omega)$, as

$$\hat{\Psi}(\omega,\delta E) = \mathrm{FT}_{E\to\omega}\left[\Psi(E,\delta E)\right] \tag{5.13}$$

$$\hat{\sigma}(\omega) = \mathrm{FT}_{E\to\omega}\left[\sigma(E)\right] \tag{5.14}$$

$$W_\Psi(E,\delta E) = \mathrm{IFT}_{\omega\to E}\left[\hat{\sigma}(\omega)\hat{\Psi}(\omega,\delta E)\right] \tag{5.15}$$

$$P_\Psi(\delta E) = \int_{-\infty}^{\infty}\left|\hat{\Psi}(\omega,\delta E)\right|^2\left|\hat{\sigma}(\omega)\right|^2 d\omega\,. \tag{5.16}$$

Equation (5.15) is derived using the convolution theorem [135], and Equation (5.16) can be found in Ref. [130, p. 232]. Equation (5.13) can be solved analytically for the complex Morlet wavelet, giving

$$\hat{\Psi}(\omega,\delta E)=\delta E^{1-n}d^{3/2}\pi^{1/4}\left(\exp\left(-\frac{(2\pi d)^2}{2}\left(\delta E\,\omega-1\right)^2\right)-\exp\left(-\frac{(2\pi d)^2}{2}\left(\delta E^2\omega^2+1\right)\right)\right). \tag{5.17}$$

The Fourier transform of the spectrum however must be calculated numerically, in this work using the Fast Fourier Transform (FFT). Calculating $W_\Psi(E,\delta E)$ and $P_\Psi(\delta E)$ in Fourier space using Equations (5.13)-(5.17) is usually much more computationally efficient than doing so in energy space.

An important feature of the wavelet transform is the concept of vanishing moments. It can be shown that for a given wavelet, the following equation is true for $m<M$, where M is the vanishing moment of the wavelet

$$0=\int_{-\infty}^{\infty}E^m\Psi(E,\delta E)\,dE\,. \tag{5.18}$$

A wavelet with a vanishing moment M will therefore ignore polynomials up to order M-1. The complex Morlet wavelet has a vanishing moment of 2, and so ignores any constant and linear components in the spectra. This means that the CWT will ignore any components in the spectra that vary slowly enough with E such that they may be approximated as linear over the significant energy range dictated by δE. It is therefore possible, by only looking at scales up to some appropriately defined δE_{max}, to ignore the background contribution to the spectrum, focusing the analysis only on the resonant contribution. Here the background contribution represents all contributions to the spectrum apart from the resonant contribution, so the Rutherford contribution, potential contribution and any experimental background are collectively ignored. Any noise in the spectra will contribute at low δE, so a lower bound, δE_{min}, was set to ignore this contribution.

It was found that $\delta E_{\text{max}}=2$ MeV and $\delta E_{\text{min}}=0.04$ MeV produced a good separation of the resonant contribution from the background and noise in the present work. The CWTs of the measured spectra are plotted between these limits in Figure 5.10. The separation of the resonant contribution from the background and noise contributions is demonstrated by reconstructing the experimental spectra from W_Ψ using Equation (5.5), using only the scales between δE_{min} and δE_{max}. This is shown in Figure 5.11.

In all cases in this work the CWT is calculated between these limits, but W_Ψ and P_Ψ are usually plotted over a reduced range, up to δE = 1 MeV, because all of the behaviour of interest is found at low δE. The CWT of the data is plotted over the reduced range in Figure 5.12. It ought to be noted that the CWT is plotted over a slightly smaller energy range in Figure 5.10 than in Figure 5.12. This is because at the end of each spectrum there is an artificial feature where σ drops sharply to 0. At large δE this feature begins to dominate W_Ψ close to the upper boundary, and this dominates the visualisation of W_Ψ, making all other features seem less important. To avoid this, and focus on the real features in the

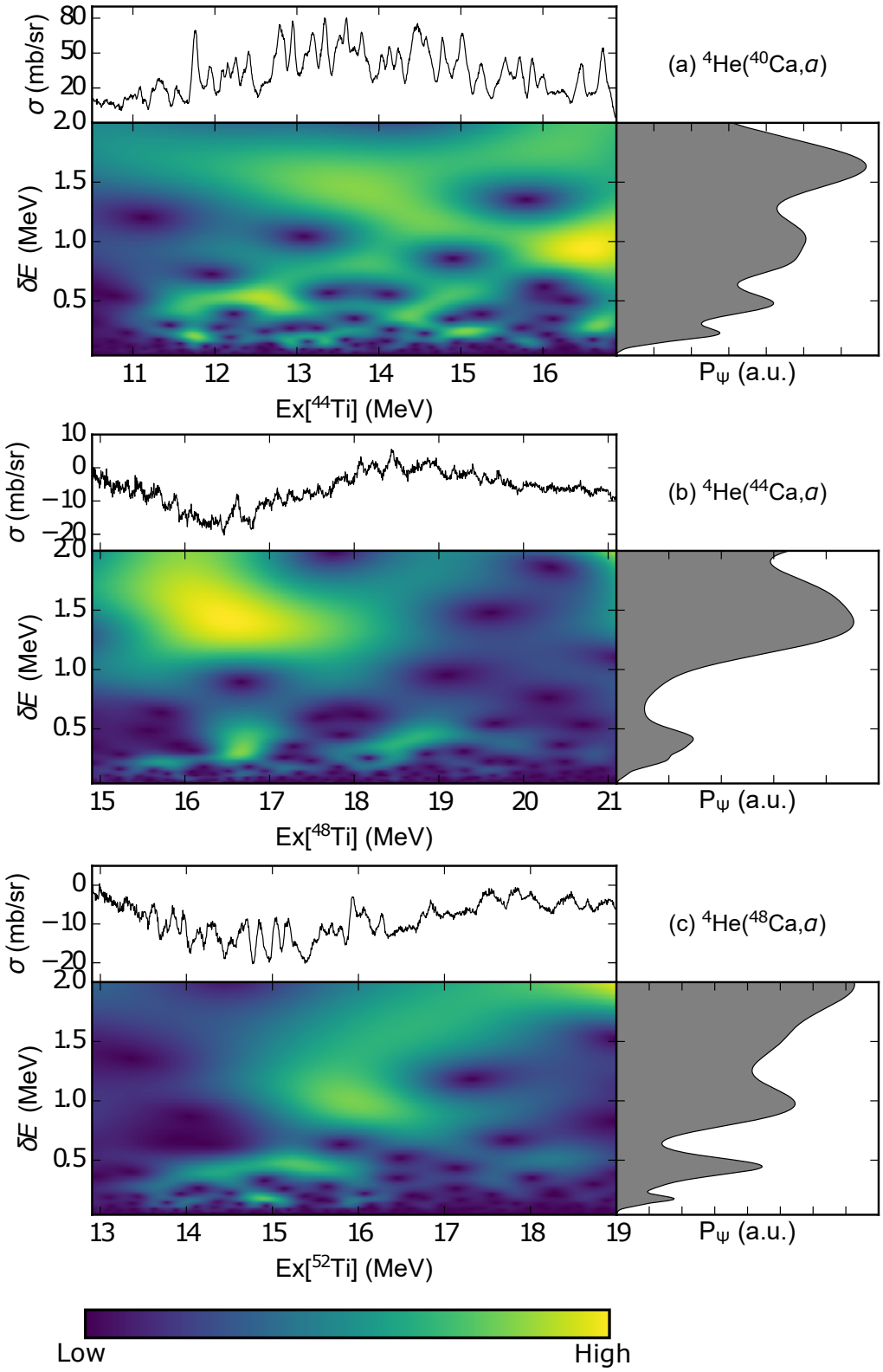

Figure 5.10: The CWT of the measured spectra over the range δE = 0.04 - 2.0 MeV. Here the Rutherford background is subtracted from the spectra prior to transformation.

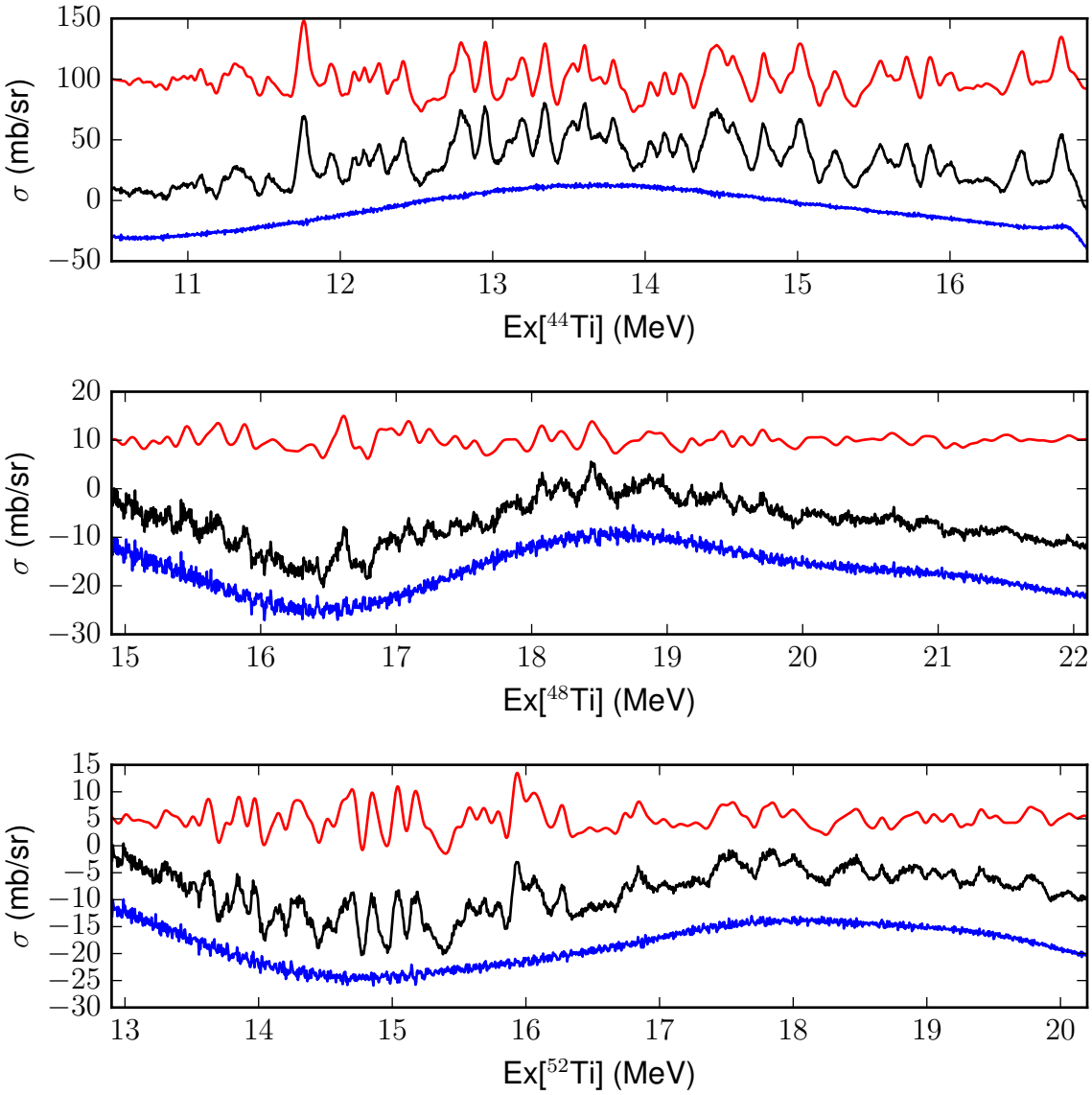

Figure 5.11: The separation of the spectra (black line) into resonant (red line) and background/noise components (blue line). Here the resonant contribution is a reconstruction of the spectrum from W_Ψ over the range δE = 0.04 - 2.0 MeV, and the background/noise contribution is the difference between this and the original spectrum. Resonant and background/noise components are shifted in y for clarity. The spectra have the Rutherford contribution subtracted.

spectra, the upper limit was reduced.

5.4.2 Fragmented Alpha Clustering

Fragmented α-clustering is the phenomenon whereby α-clustered states become fragmented into many states of the same J^π due to coupling to non-α-clustered states. In this section a formalism is developed to describe this behaviour mathematically, heavily based on the work by Bjørnholm & Lynn [136] for the treatment of fission isomers and double humped fission barriers in heavy nuclei.

As discussed in Section 2.1.1, it is possible to assign each minimum in the deformation potential energy surface calculated by the Nilsson-Strutinsky model to a different α-cluster structure. This concept can be generalised, implying that different nuclear structures occupy different minima in the potential energy surface. This idea provides the basis in this work for the mathematical description of the interplay between different structures within the same nucleus, allowing the question how does α-clustering manifest in nuclei when it is in competition with mean field type structures to be addressed. It is this interplay that leads to fragmented α-clustering.

The following discussion refers to deformation, β, which represents any general deformation and is limited to two deformation minima: the primary deformation minimum, β_{I}, and a secondary deformation minimum, β_{II}. It is assumed that a mean-field structure dominates at β_{I}, and α-clustering dominates at β_{II}. In order to treat the behaviour of the nucleus with respect to deformation explicitly, the nuclear hamiltonian, H, is split into a deformation contribution, H_{def}, a contribution from the intrinsic degrees of freedom, H_{int}, and a contribution which couples the deformation and intrinsic degrees of freedom, H_c,

$$H = H_{\mathrm{def}}(\beta) + H_{\mathrm{int}}(\xi) + H_c(\beta,\xi)\,. \tag{5.19}$$

This separation allows the nuclear energy levels to be characterised by their behaviour as a function of β, with states with wavefunctions that are localized in the primary potential minimum being identified as class-I states, and those with wavefunctions that are focused in the secondary potential minimum as class-II states. The class-I states, $|X^{(\mathrm{I})}_{\lambda_{\mathrm{I}}}\rangle$, have energies $E^{(\mathrm{I})}_{\lambda_{\mathrm{I}}}$, and the class-II states, $|X^{(\mathrm{II})}_{\lambda_{\mathrm{II}}}\rangle$, have energies $E^{(\mathrm{II})}_{\lambda_{\mathrm{II}}}$. It is then from these sets of class-I and class-II states that the final set of compound states, $|X_\lambda\rangle$, can be computed. This situation is depicted schematically in Figure 5.13 and is treated fully and in detail in Ref. [136], and leads to the eigenvalue equation

$$\begin{bmatrix} \boldsymbol{E}^{(\mathrm{I})} & \boldsymbol{H}_{\mathbf{c}}^{(\mathrm{I,II})} \\ \boldsymbol{H}_{\mathbf{c}}^{(\mathrm{II,I})} & \boldsymbol{E}^{(\mathrm{II})} \end{bmatrix} \begin{bmatrix} \boldsymbol{C}_{\boldsymbol{\lambda}}^{(\mathrm{I})} \\ \boldsymbol{C}_{\boldsymbol{\lambda}}^{(\mathrm{II})} \end{bmatrix} = E_\lambda \begin{bmatrix} \boldsymbol{C}_{\boldsymbol{\lambda}}^{(\mathrm{I})} \\ \boldsymbol{C}_{\boldsymbol{\lambda}}^{(\mathrm{II})} \end{bmatrix} \tag{5.20}$$

where $\boldsymbol{E}^{(\mathrm{I})}$ and $\boldsymbol{E}^{(\mathrm{II})}$ are both diagonal matrices containing the energies of the class-I and class-II states

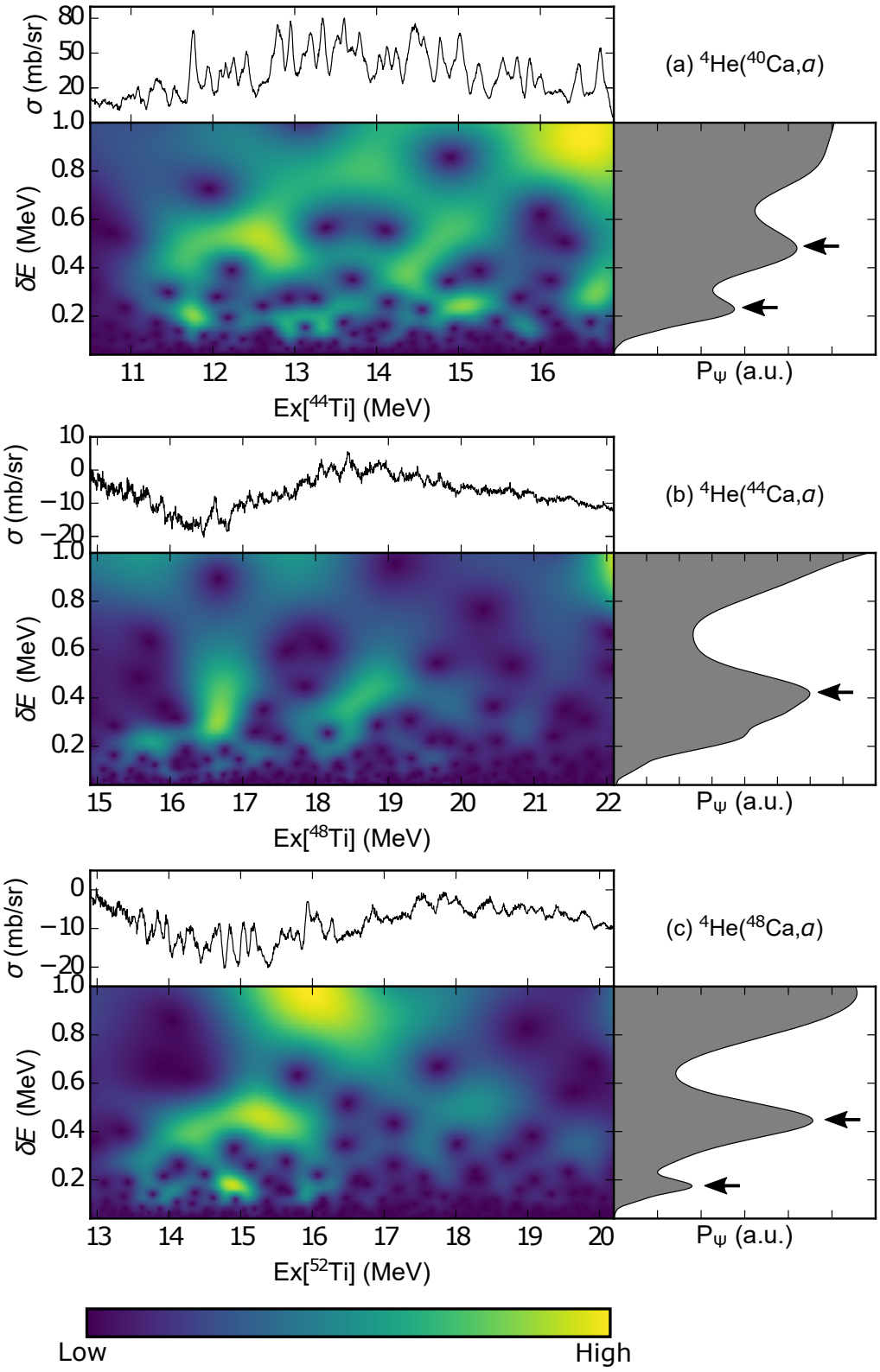

Figure 5.12: The CWT of the measured spectra over the range δE = 0.04 - 1.0 MeV. Here the Rutherford background is subtracted from the spectra prior to transformation. Characteristic scales are marked by arrows.

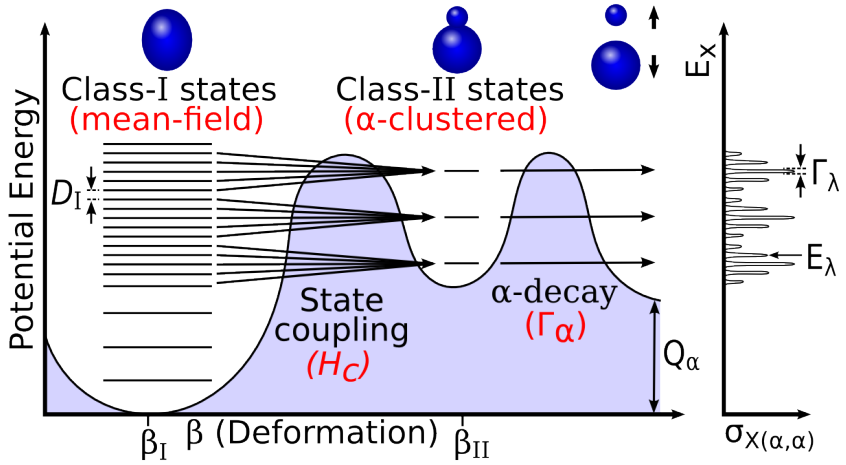

Figure 5.13: Left: A schematic illustration of a double humped fission barrier and its application to fragmented α-clustered states. Right: Schematic X(α,α) cross-section resulting from this structure. For simplicity the Rutherford contribution was ignored. This figure was adapted from [137, p. 97-98].

respectively, and $\boldsymbol{C}_{\boldsymbol{\lambda}}^{(\mathbf{I})}$ and $\boldsymbol{C}_{\boldsymbol{\lambda}}^{(\mathbf{II})}$ are column vectors, each containing the coefficients from which the compound state $|X_\lambda\rangle$ can be constructed using

$$|X_\lambda\rangle = \sum_{\lambda_\mathrm{I}} (\boldsymbol{C}_{\boldsymbol{\lambda}}^{(\mathbf{I})})_{\lambda_\mathrm{I}} |X_{\lambda_\mathrm{I}}^{(\mathrm{I})}\rangle + \sum_{\lambda_\mathrm{II}} (\boldsymbol{C}_{\boldsymbol{\lambda}}^{(\mathbf{II})})_{\lambda_\mathrm{II}} |X_{\lambda_\mathrm{II}}^{(\mathrm{II})}\rangle \,. \tag{5.21}$$

The matrices $\mathbf{H}_\mathbf{c}^{(\mathbf{I,II})}$ and $\mathbf{H}_\mathbf{c}^{(\mathbf{II,I})}$ contain the coupling terms between the class-I and class-II states, the elements of which are defined as

$$(\boldsymbol{H}_\boldsymbol{c}^{(\mathbf{I,II})})_{\lambda_\mathrm{I}\lambda_\mathrm{II}} = \langle X_{\lambda_\mathrm{I}}^{(\mathrm{I})} | H_c | X_{\lambda_\mathrm{II}}^{(\mathrm{II})} \rangle \tag{5.22}$$

$$(\boldsymbol{H}_\boldsymbol{c}^{(\mathbf{II,I})})_{\lambda_\mathrm{II}\lambda_\mathrm{I}} = \langle X_{\lambda_\mathrm{II}}^{(\mathrm{II})} | H_c | X_{\lambda_\mathrm{I}}^{(\mathrm{I})} \rangle \,. \tag{5.23}$$

These terms dictate the coupling strength, and will depend on both the overlap between the class-I and class-II states and the penetrability through the potential barrier separating the two minima. The overlap is only significant between states of the same total angular momentum, J, and parity, π, and so the coupling can be assumed to be zero between states with different J^π. This allows Equation (5.20) to be solved separately for each J^π.

In general Equation (5.20) must be solved numerically for $\boldsymbol{C}_{\boldsymbol{\lambda}}^{(\mathbf{I})}$, $\boldsymbol{C}_{\boldsymbol{\lambda}}^{(\mathbf{II})}$ and E_λ, given $\boldsymbol{E}^{(\mathbf{I})}$, $\boldsymbol{E}^{(\mathbf{II})}$ and $\boldsymbol{H}_\boldsymbol{c}^{(\mathbf{I,II})}$. This is done in the present work in Python using the `NumPy` function `numpy.linalg.eig()` [79].

Considering that the reduced width amplitude for the decay channel μ, $\gamma_{\lambda,\mu}$, is defined in Equation 3.40 to be proportional to the value of the wavefunction at the matching radius, $\langle R_\mu | X_\lambda \rangle$, the reduced width amplitude of $|X_\lambda\rangle$ can be calculated as follows from vectors containing the reduced width am-

plitudes of the class-I and class-II states, $\boldsymbol{\gamma_{\mu}^{(I)}}$ and $\boldsymbol{\gamma_{\mu}^{(II)}}$ respectively,

$$\gamma_{\lambda,\mu} = \boldsymbol{C_{\lambda}^{(I)}} \cdot \boldsymbol{\gamma_{\mu}^{(I)}} + \boldsymbol{C_{\lambda}^{(II)}} \cdot \boldsymbol{\gamma_{\mu}^{(II)}} \,. \tag{5.24}$$

From this set of $\gamma_{\lambda,\mu}$ and E_{λ} an experimental spectrum can be calculated. This was done using the Simplified $\boldsymbol{R}$-matrix theory discussed in Section 3.2.4. This formalism is used in this work to generate an excitation spectrum from sets of class-I and class-II states, defined by $\{\boldsymbol{E^{(I)}}, \boldsymbol{\gamma_{\mu}^{(I)}}\}$ and $\{\boldsymbol{E^{(II)}}, \boldsymbol{\gamma_{\mu}^{(II)}}\}$ respectively, and their coupling coefficients, $\boldsymbol{H_{c}^{(I,II)}}$. In addition to these it is necessary to define some additional parameters, which are required for the computation of the Simplified $\boldsymbol{R}$-matrix and dictate the nature of the background contribution to the spectrum and the experimental resolution. In the following sections the class-I and class-II states are chosen to simulate fragmented α-clustering.

5.4.3 Statistical Model of Fragmented Alpha Clustering

The goal of this section is to develop a model which allows the signature of a typical fragmented α-clustered state to be identified from the behaviour of the reaction cross-section. This was done by generating a regular excitation spectrum, comprised only of class-I states with a mean-field nature, and then coupling to it a set of class-II α-clustered states, using the mathematics discussed in Section 5.4.2, and observing how this affects the spectrum and its CWT.

In order to investigate this robustly statistical models were used to generate a generic set of class-I states in such a way as to mimic the states one may observe in a nucleus with a dominant mean-field structure. This is discussed further in the following section.

The problem was simplified by assuming that the simulation was performed over a small enough energy range such that any quantities which one would expect to vary slowly with energy can be assumed to be constant. In this case these quantities are P_L, f_R and $\phi_{J^{\pi}}$, as defined in Section 3.2.4.

5.4.3.1 Model Details

The class-I states were generated statistically, randomizing $E_{\lambda_{\mathrm{I}}}^{(\mathrm{I})}$, $\gamma_{\mu,\lambda_{\mathrm{I}}}^{(\mathrm{I})}$ and $J_{\lambda_{\mathrm{I}}}^{\pi}$ under certain constraints so as to produce the appropriate statistical distributions. The statistical distributions were chosen such that the class-I states produced would as best as possible represent a set of mean-field type states with random shell-model configurations. This is a problem that is addressed in great detail in Random Matrix Theory [138], which investigates the properties of the nuclear states that are produced given that the nuclear Hamiltonian is constructed with randomized matrix elements. Here only the relevant results are presented.

The reduced width amplitudes were constrained to follow a normal distribution, centred on 0, with

a variance of $\left\langle {\gamma_\mu^{(\mathrm{I})}}^2 \right\rangle$. This was originally proposed by Porter and Thomas [139], and has been shown to reproduce the distributions of experimentally determined resonance widths exceptionally well [140]. It follows the argument that;

> If the resonant states $|g_p\rangle$ are very complicated configurations over the channels α, then we should expect the reduced width amplitudes to be statistically distributed with a mean of zero. Because these amplitudes arise from many random influences in the Hamiltonian, we expect to be able to use the central-limit theorem, which says that the overall distribution of the $\gamma_{p\alpha}$ should be a normal distribution, centered here about zero. (Nuclear Reactions for Astrophysics, p. 315 [63])

Written formally it follows that $\gamma^{(\mathrm{I})}_{\mu,\lambda_\mathrm{I}}$ should follow the probability density function

$$P_\mu^{\mathrm{N}}(\gamma) = \frac{1}{\sqrt{2\pi}} \frac{1}{\sqrt{\left\langle {\gamma_\mu^{(\mathrm{I})}}^2 \right\rangle}} \exp\left(-\frac{\gamma^2}{2\left\langle {\gamma_\mu^{(\mathrm{I})}}^2 \right\rangle} \right). \tag{5.25}$$

Using Equation (3.45), this leads to the Porter-Thomas distribution for the partial widths, $\Gamma_\mu^{(\mathrm{I})}$, given in Ref. [63, p. 316]

$$P_\mu^{\mathrm{PT}}(\Gamma) = \frac{1}{\sqrt{2\pi}\left\langle \Gamma_\mu^{(\mathrm{I})} \right\rangle} \left(\frac{\Gamma}{\left\langle \Gamma_\mu^{(\mathrm{I})} \right\rangle} \right)^{-1/2} \exp\left(-\frac{\Gamma}{2\left\langle \Gamma_\mu^{(\mathrm{I})} \right\rangle} \right) \tag{5.26}$$

where $\left\langle \Gamma_\mu^{(\mathrm{I})} \right\rangle$ is the mean partial width for channel μ, and is defined as $\left\langle \Gamma_\mu^{(\mathrm{I})} \right\rangle = 2P_L \left\langle {\gamma_\mu^{(\mathrm{I})}}^2 \right\rangle$. Since P_L and $\left\langle {\gamma_\mu^{(\mathrm{I})}}^2 \right\rangle$ are, in the context of this simulation, both free variables, and are both only used to calculate $\left\langle \Gamma_\mu^{(\mathrm{I})} \right\rangle$, it is redundant to use both of them. As such, for this simulation, $\left\langle \Gamma_\mu^{(\mathrm{I})} \right\rangle$ is used to define the distribution of partial widths.

When discussing α elastic scattering measurements, the only important widths are the α-partial width $\Gamma_\alpha^{(\mathrm{I})}$, and the total width $\Gamma^{(\mathrm{I})}$. This means that rather than defining the mean partial width for every available open channel, the problem may be approximated by defining the mean partial width for the alpha channel, $\left\langle \Gamma_\alpha^{(\mathrm{I})} \right\rangle$, the mean partial width for all other channels, $\left\langle \Gamma_{\mu\neq\alpha}^{(\mathrm{I})} \right\rangle$, and the total number of open channels, N_μ. The total width may then be calculated by summing $N_\mu - 1$ independent samples of $P_{\mu\neq\alpha}^{\mathrm{PT}}$ and one sample of P_α^{PT}.

The second constraint was to choose $E_{\lambda_\mathrm{I}}^{(\mathrm{I})}$ and $J_{\lambda_\mathrm{I}}^\pi$ such that the nearest neighbour state spacing between states of the same J^π, $D_{J^\pi}^{(\mathrm{I})}$, follows the Wigner distribution [141]

$$P_{J^\pi}^{\mathrm{W}}(D) = \frac{\pi D}{2\left\langle D_{J^\pi}^{(\mathrm{I})} \right\rangle^2} \exp\left(-\frac{\pi D^2}{4\left\langle D_{J^\pi}^{(\mathrm{I})} \right\rangle^2} \right) \tag{5.27}$$

where $\left\langle D^{(\mathrm{I})}_{J^\pi} \right\rangle$ defines the mean state spacing for states of the same J^π. The Wigner distribution is derived under the assumption that adjacent energy levels feel a linear repulsive force. This level repulsion has the effect of regularising their spacings, producing a set of state spacings with a standard deviation approximately half that expected if the states were randomly with a uniform probability density function. The Wigner distribution has been shown to replicate experimental nearest neighbour state spacings, and those extracted from shell-model calculations, very well [138].

Since there is no level repulsion between states of differing J^π, the overall nearest neighbour state spacing, $D^{(\mathrm{I})}$, i.e. the state spacing irrespective of J^π, tends towards the Poisson distribution

$$P^{\mathrm{P}}(D) = \frac{1}{\langle D^{(\mathrm{I})} \rangle} \exp\left(-\frac{D}{\langle D^{(\mathrm{I})} \rangle} \right). \tag{5.28}$$

The Poisson distribution is generated in the case that all energy levels are random, sampled independently from a uniform probability density function. Figure 5.14 demonstrates how the overall state spacing distribution varies with the number of different spins. It is clear that by the time there are 5 distinct J^π in the spectrum, the distribution is almost indistinguishable from a Poisson distribution. The Poisson and Wigner distributions, and their expected standard deviations, are derived in Appendix E.

While constraining the nearest neighbour state spacing to follow the Wigner distribution should produce a set of $E^{(\mathrm{I})}_{\lambda_\mathrm{I}}$ representative of a typical mean-field type nucleus, it is important to note that it ignores higher order correlations which are observed in true state spacing distributions. For example if one were to look at the next-nearest neighbour state spacing distribution, the true distribution would be narrower than one would expect if the Wigner distribution were simply sampled twice [138]. This is a limitation of the current method.

Now the properties of the class-II states must be set. One would expect α-clustered states to have large $\gamma^{(\mathrm{II})}_\alpha$ and negligible $\gamma^{(\mathrm{II})}_{\mu\neq\alpha}$. The other parameters necessary to define a class-II state, $E^{(\mathrm{II})}$ and $J^\pi_{\lambda_\mathrm{II}}$ are not constrained in any way. This allows a statistical model like this to ask the question: given an α-clustered state of a certain J^π and at a certain excitation energy, on average what effect will this have on the CWT of the measured spectrum?

Finally the coupling between the class-I and class-II states must be defined. There are two possible approaches to dealing with this. The simplest is to assume that the coupling strength is constant between states with the same J^π, and zero otherwise, written explicitly as

$$(\mathbf{H_c^{(I,II)}})_{\lambda_\mathrm{I}\lambda_\mathrm{II}} = (\mathbf{H_c^{(II,I)}})_{\lambda_\mathrm{II}\lambda_\mathrm{I}} = H_c \delta_{J^\pi_{\lambda_\mathrm{I}} J^\pi_{\lambda_\mathrm{II}}}. \tag{5.29}$$

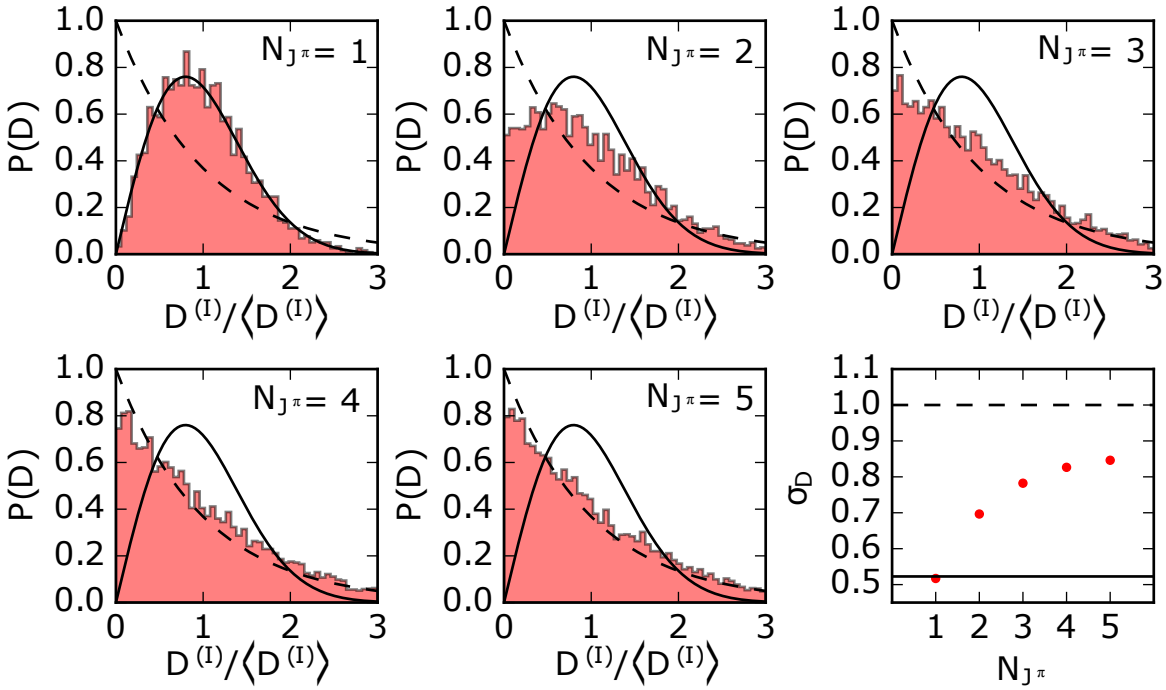

Figure 5.14: A Monte Carlo simulation showing the state spacing distributions for different numbers of unique J^π, N_{J^π}, (red histogram). This is plotted in comparison with a pure Wigner distribution (black solid line), and a pure Poisson distribution (black dashed line). The bottom right panel shows the how the standard deviation of the state spacing, σ_D, increases with N_{J^π}. Again in comparison with the true σ_D for the Wigner distribution (black solid line) and Poisson distribution (black dashed line). The simulation generates sets of excitation energies for each J^π by repeatedly sampling the Wigner distribution, and then combines N_{J^π} independently generated sets of excitation energies, before calculating the overall nearest neighbour state spacing $D^{(\mathrm{I})}$. Here it is assumed $\left\langle D^{(\mathrm{I})}_{J^\pi} \right\rangle$ is the same for all J^π.

Here H_c is the coupling constant and δ_{ij} is the kronecker delta. This assumption is known as the Uniform or Picket Fence approximation [136]. The benefit of this assumption is its simplicity, however it ignores the dependence that the coupling would have on the overlap between the class-I and class-II wavefunctions.

The second option is to assume that the coupling strength follows an appropriate statistical distribution, and to draw the elements of $\boldsymbol{H_c^{(I,II)}}$ from that distribution, similarly to the way that the class-I states are chosen. The appropriate distribution is argued to be a normal distribution, centred at 0, with variance $\langle H_c^2 \rangle$ [136]. This technique attempts to deal with the variability of the coupling matrix elements due to the variation in the class-I state structures, following the same argument as is made for the distribution of reduced widths by Porter and Thomas [139]. While it is a sensible assertion to use a normal distribution, and one would expect this to produce more realistic results than the Uniform approximation, this has not been verified experimentally. Therefore both of these techniques will be used, referred to as constant coupling and statistical coupling respectively, and the results compared.

The key observable that is dictated by the coupling strength is the spreading width, W, which is the energy range over which a given class-II state will spread. A small value for H_c will only permit the class-II state to couple to class-I states very close in energy, leading to a small spreading width, whereas a large H_c leads to a large spreading width. However W also depends on $D^{(\mathrm{I})}_{J^\pi}$, so in the following analysis the simulations will be defined using $\langle W \rangle$, and $\langle H_c \rangle$ can then be calculated using the following equation, derived in Ref. [142],

$$\left\langle H_c^2 \right\rangle = \frac{\langle W \rangle \langle D^{(\mathrm{I})}_{J^\pi} \rangle}{\pi} \,. \tag{5.30}$$

To summarise, using a combination of Porter-Thomas statistics and the Wigner distribution, a suitable ensemble of class-I states may be built up from the parameter set

$$\left\{ \left\langle D^{(\mathrm{I})}_{J^\pi} \right\rangle, \langle \Gamma^{(\mathrm{I})}_{\alpha} \rangle, \left\langle \Gamma^{(\mathrm{I})}_{\mu \neq \alpha} \right\rangle \right\} \,. \tag{5.31}$$

This set of class-I states may then be coupled to any number of class-II states to produce the final set of compound states, using either uniform or statistical coupling, each defined by the parameters

$$\left\{ \langle W_{\lambda_{\mathrm{II}}} \rangle, \Gamma^{(\mathrm{II})}_{\alpha,\lambda_{\mathrm{II}}}, E^{(\mathrm{II})}_{\lambda_{\mathrm{II}}}, J^\pi_{\lambda_{\mathrm{II}}} \right\} \,. \tag{5.32}$$

Finally a spectrum can be calculated from these compound states using the Simplfied R-Matrix discussed in Section 3.2.4. This calculation requires the definition of the parameters

$$\{ f_R, \phi_{J^\pi}, N_\mu, \sigma_R \} \tag{5.33}$$

where N_μ is the number of open channels, which must be greater than or equal to 1, since the α-channel must be open to populate the level. The experimental resolution, σ_R, was defined to be 45 keV at FWHM, to match the true experimental resolution. The other parameters, f_R and ϕ_{J^π}, dictate the background level and the type of interference between the resonances and the background. As discussed previously, for the purposes of this simulation it is assumed that the energy range is small enough that these variables can all be treated as constant.

5.4.3.2 Model Results

This procedure was used to simulate N unique spectra, half of which containing α-clustered class-II states, and half not. This ensemble of spectra, $\mathcal{E}_N$, may then be examined, using the CWT, to identify a signature of fragmented α-clustering that is observed consistently throughout $\mathcal{E}_N$. The observation of this signature in experimental spectra may then be used to identify fragmented α-clustering.

As the parameters used to generate the spectra in $\mathcal{E}_N$ are not known, they are randomised within reasonable limits. This ought to ensure that the resulting $\mathcal{E}_N$ is generally applicable, and not applicable only to spectra with, for example, a specific mean state spacing. These limits were chosen to ensure that:

1. The individual resonances are resolvable.
2. The α-clustered states are always fragmented.
3. The α-clustered states have significantly larger α-decay widths than the mean-field type states.

The limits for each parameter were chosen as follows, and the values summarised in Table 5.6:

$\left\langle \boldsymbol{D}^{(\mathrm{I})}_{J^\pi} \right\rangle$ The mean state spacing was chosen based on the measured level densities from TTIK measurements of α-elastic scattering of ^{32}S, ^{34}S and ^{40}Ca by Norrby *et al.*[67]. These spectra were analysed using the Simplified R-Matrix, giving a mean state spacing of 0.11, 0.10 and 0.054 MeV respectively. However these values correspond to the overall mean state spacing, $\left\langle D^{(\mathrm{I})} \right\rangle$, rather than the J^π specific state spacing required here. As such these measured state spacings can be treated as a reasonable lower bound for the J^π specific mean state spacing. The range chosen was 0.05 - 0.3 MeV.

$\boldsymbol{\Gamma}^{(\mathrm{II})}_{\alpha,\lambda_{\mathrm{II}}}$ The alpha width was chosen to be large, but small enough such that the widths of the fragmented levels would be smaller than the state spacing, ensuring that they would be resolvable. The range chosen was 87 - 113 keV. For each spectrum, all class-II states have the same width.

$\boldsymbol{E}^{(\mathrm{II})}_{\lambda_{\mathrm{II}}}$ These were randomized within the limits of the spectrum. There were anywhere between 1 and 3 clustered states used, and the central one was always fixed in the centre of the spectrum, to

ensure that there is always at least one set of fragmented states in the spectrum. However one would not expect the absolute values of $E^{(\mathrm{II})}_{\lambda_{\mathrm{II}}}$ to influence the behaviour of the spectral signature, rather they should just move the signature.

$\boldsymbol{J^{\pi}_{\lambda_{\mathrm{II}}}}$ The spins were randomized between 0 and 5, however again one would not expect the choice of spin to have a significant impact on the results of the CWT, as the angular distributions are not relevant here.

$\boldsymbol{\left\langle \Gamma^{(\mathrm{I})}_{\alpha} \right\rangle}$ This was chosen to be significantly smaller than $\Gamma^{(\mathrm{II})}_{\alpha,\lambda_{\mathrm{II}}}$, as one would expect the α-decay width of a mean-field type state to be on average much smaller than the α-decay width of an α-clustered state. The range chosen was 0.19 - 0.4 keV.

$\boldsymbol{\left\langle \Gamma^{(\mathrm{I})}_{\mu\neq\alpha} \right\rangle}$ This was chosen to be larger than $\left\langle \Gamma^{(\mathrm{I})}_{\alpha} \right\rangle$, but still of a similar order of magnitude. Since in these measurements the only other significant open decay channels are neutron and proton decay channels, one would expect larger widths than for the α channel, since the Coulomb barrier will be reduced. The range chosen was 0.76 - 1.28 keV.

$\boldsymbol{\langle W_{\lambda_{\mathrm{II}}} \rangle}$ This was chosen to ensure, at the lower bound that the class-II states would always couple to at least two class-I states, i.e. the α-clustered states would always be fragmented. The upper bound was chosen to ensure that the fragmented states would retain, to some extent, their localization, i.e. to prevent the class-II states simply coupling to all states in the spectrum. This range was chosen empirically to be 87 - 113 keV.

$\boldsymbol{f_R}$ The lower limit was chosen to be 0, i.e. no significant background contribution, and the upper limit was chosen such that f_R is much greater than the amplitude of the resonant contribution. The range chosen was 0 - 5 mb$^{1/2}$.

$\boldsymbol{\phi_{J^{\pi}}}$ The phases were randomized independently for each J^{π} between 0 and 2π to ensure that all types of interference with the background were accounted for.

$\boldsymbol{N_{\mu}}$ The number of open channels was chosen to be between 1 and 8 depending on the J^{π} of the state, since the angular momentum coupling strongly dictates the number of open channels.

$\boldsymbol{\sigma_R}$ The resolution was chosen to match the true experimental resolution, which was 45 keV at FWHM.

Two sets of spectra were generated from these parameters, both containing 2000 events, one using uniform coupling, $\mathcal{E}^{\mathrm{uni}}_{2000}$, and another using statistical coupling, $\mathcal{E}^{\mathrm{stat}}_{2000}$. The excitation energy range was fixed at 12-20 MeV, and the Q-value and nuclear masses used were for the ^{4}He(^{40}Ca,α) reaction, however one would not expect these parameters to have any bearing on the results of the simulation

Table 5.6: The parameters used for the statistical model of fragmented α-clustering. Each of the parameters was allowed to vary, uniformly, between the min and max values.

Parameter	Value		
	Min	Mean	Max
$\left\langle D^{(\mathrm{I})}_{J^\pi} \right\rangle$	0.05 MeV	0.175 MeV	0.3 MeV
$\langle W \rangle$	0.087 MeV	0.1 MeV	0.113 MeV
N_μ	1	4 or 5	8
$\left\langle \Gamma^{(\mathrm{I})}_\alpha \right\rangle$	0.19 keV	0.25 keV	0.4 keV
$\left\langle \Gamma^{(\mathrm{I})} \right\rangle$	2.46 keV	3.25 keV	4.15 keV
$\Gamma^{(\mathrm{II})}_\alpha$, $\Gamma^{(\mathrm{II})}$	87 keV	100 keV	113 keV
f_R	0	2.5	5

as long as the excitation energy range is significantly larger than the Q-value. This means that the results of these simulations should be applicable, at the very least, to all $^{\mathrm{X}}$Ca(α,$^{\mathrm{X}}$Ca) reactions.

The CWT was calculated for each simulated spectrum. The results of averaging the calculated $|W_\Psi|$ and P_Ψ are shown in Figure 5.15 for $\mathcal{E}^{\mathrm{uni}}_{2000}$ and Figure 5.16 for $\mathcal{E}^{\mathrm{stat}}_{2000}$. In each of these figures the average W_Ψ and P_Ψ are calculated separately for the spectra without fragmented α-clustered states, the spectra with the fragmented α-clustered states, and a set of spectra with fragmented states that have fixed $E^{(\mathrm{II})}_{\lambda_{\mathrm{II}}}$. It is clear that if uniform coupling is assumed, then the α-clustered spectra show, on average, an enhancement in P_Ψ at low δE. There is also a slight enhancement when statistical coupling is used, however it is not as clear. By examining the CWT of individual simulations, examples of which are also shown in Figures 5.15 and 5.16, it seems likely that this enhancement is generated by the increased likelihood of having a large characteristic scale at low δE if fragmented α-clustering is present in the spectrum. It is also clear by examining the average W_Ψ for the spectra with fixed $E^{(\mathrm{II})}_{\lambda_{\mathrm{II}}}$ that the α-clustered states produce hot spots in W_Ψ in line with the characteristic scale, at $E^{(\mathrm{II})}_{\lambda_{\mathrm{II}}}$.

This large characteristic scale and hot spots in W_Ψ is the signature of fragmented α-clustering. It arises because the spectrum in the vicinity of the class-II α-clustered states becomes dominated by the fragmented α-clustered states. Since these fragmented states all have a structure similar to the original α-clustered class-II state, they all have large Γ_α and small $\Gamma_{\mu\neq\alpha}$. This leads to consistently strong amplitudes for the fragmented resonances. Secondly, since these resonances will all have the same J^π, they will all interact with the background in the same way, and so all of the resonances will have similar shapes. Also their spacings will follow the Wigner distribution, which has a relatively small standard deviation, and as such the states will be quite regularly spaced. This combination of regularly spaced states all with similar amplitudes and shapes produces a strong periodic structure, which is picked out by the CWT, producing the hot spots and signature characteristic scale. Furthermore, this signature scale is likely to be the lowest peak in P_Ψ since the coupling procedure produces fragmented states that are, on average, more densely packed than the rest of the spectrum [136, p. 772].

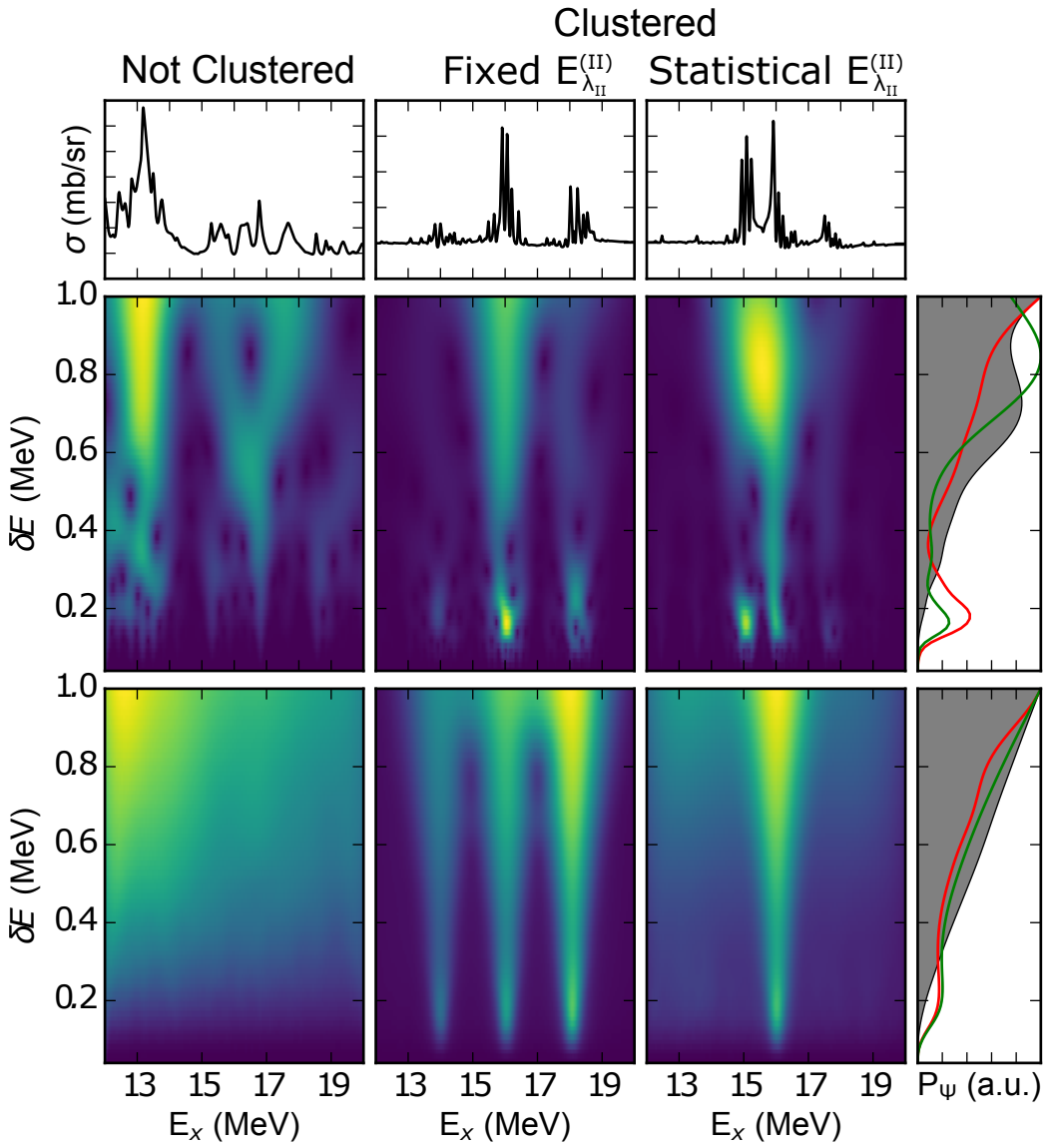

Figure 5.15: The average behaviour of the CWT of $\mathcal{E}^{\text{uni}}_{2000}$. Showing an example spectrum (top row), an example CWT (middle row), and the average CWT (bottom row), for spectra without any fragmented α-clustered states (left column), and with fragmented α-clustered states (middle and right columns). Right column displays P_Ψ calculated for each W_Ψ: the leftmost W_Ψ shown in grey, middle W_Ψ shown in red and rightmost W_Ψ shown in green. The results for the clustered spectra are shown both for randomised class-II state energies (right column) and fixed class-II state energies (middle column).

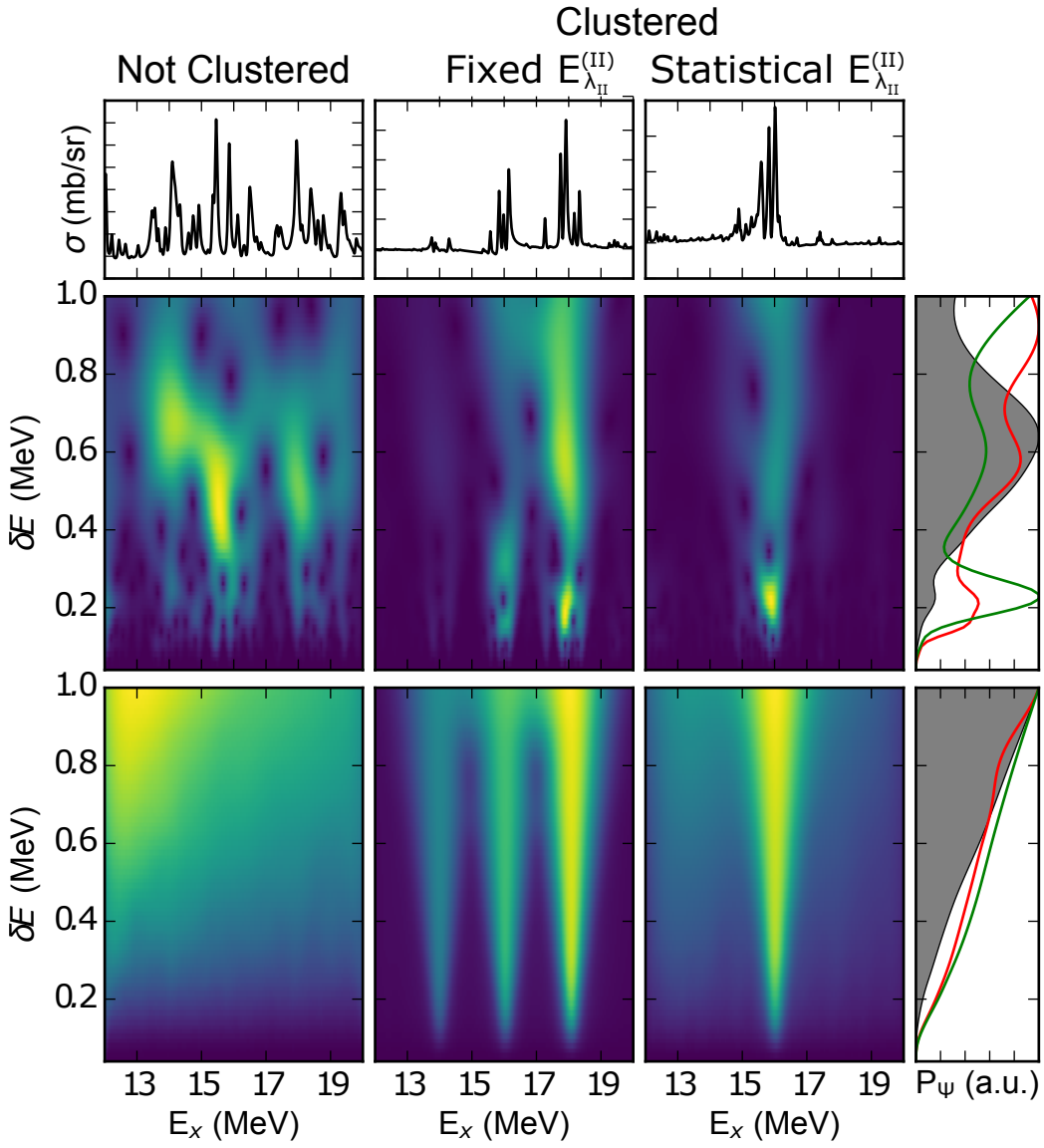

Figure 5.16: The average behaviour of the CWT of $\mathcal{E}^{\text{stat}}_{2000}$. Showing an example spectrum (top row), an example CWT (middle row), and the average CWT (bottom row), for spectra without any fragmented α-clustered states (left column), and with fragmented α-clustered states (middle and right columns). Right column displays P_Ψ calculated for each W_Ψ: the leftmost W_Ψ shown in grey, middle W_Ψ shown in red and rightmost W_Ψ shown in green. The results for the clustered spectra are shown both for randomised class-II state energies (right column) and fixed class-II state energies (middle column).

It is natural, therefore, that the signature will not be as clear in the case of statistical coupling, since the additional randomness introduced by the randomized coupling matrix elements acts to reduce this crucial consistent behaviour. However, one would still expect the signature to be present, it may just not be quite as obvious as it is in the case of uniform coupling. This is consistent with what is observed in the average P_Ψ, since there is still a slight enhancement at low δE, consistent with the signature observed for uniform coupling, it is just not as large an enhancement.

Looking at the CWT of the measured spectra in Figure 5.12, it can be seen that ^{44}Ti and ^{52}Ti contain an additional characteristic scale at low δE that ^{48}Ti does not. This suggests that ^{44}Ti and ^{52}Ti may both contain fragmented α-clustered states. However a more rigorous analysis is required before any conclusions can be made about this. To do this, techniques associated with Machine Learning are employed, in an attempt to understand the signature on a deeper level, and quantitatively analyse the data for a similar signature.

5.4.4 A Machine Learning Analysis of the Spectral Signature

5.4.4.1 Decision Trees and Random Forests

Machine learning refers to a field of computer science in which algorithms are developed which allow computers to learn patterns and make predictions without having those patterns and predictions explicitly written into the programs. A simple and widely used example of a machine learning algorithm is the Decision Tree (DT) [143]. A DT is a classification algorithm, which given a set of features, predicts a class associated with that set of features. It works by starting at the top of the tree, at the first 'node', and evaluating the criterion at that node with respect to the given features, before moving down the appropriate 'branch' depending on the result of that evaluation. At the end of that branch will either be another node, with a new criterion to be evaluated, or a 'leaf'. A leaf corresponds to the end of the DT, and outputs the predicted classification. This process is repeated, moving from node to node, until the algorithm reaches a leaf, at which point the prediction is made and the algorithm exits. The criteria assigned to each node must produce a True or False result. In the case of features with a discrete set of possible values, the criterion will either be an equal to or not equal to evaluation, and in the case of features with a continuous set of possible values, the criterion will either be greater than or less than an appropriately chosen threshold. An example of a simple DT, used to predict whether a given passenger aboard the Titanic would have survived or died, is shown in Figure 5.17. This DT uses three features to define the passenger: their sex, age and number of siblings/spouses (sibsp).

A DT is generated by 'training' it on a training data set, made up of many events for which the true classification is known, with the aim being of producing a DT which correctly classifies as many of

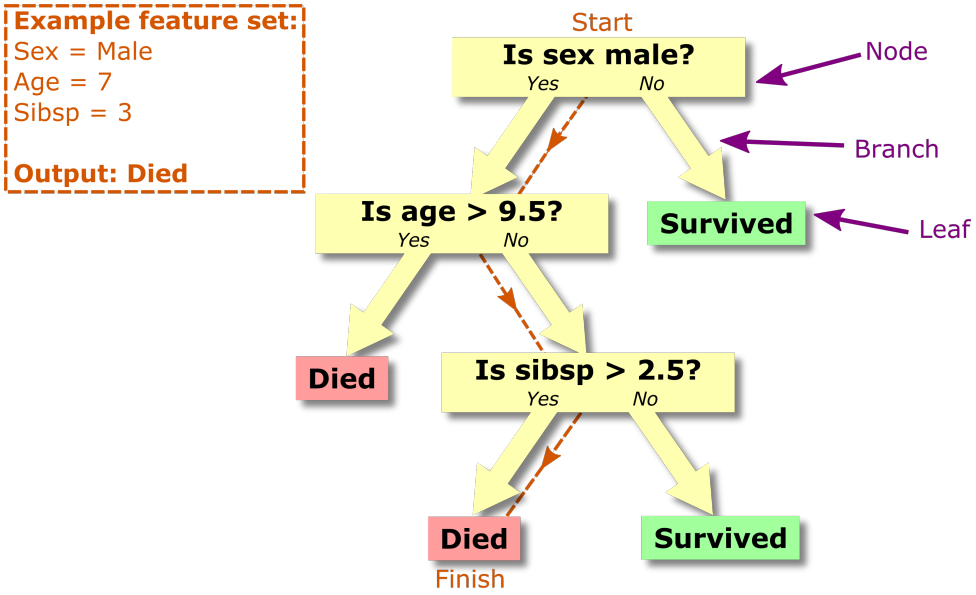

Figure 5.17: A simple example of a Decision Tree, used here to predict whether or not a given passenger aboard the Titanic will survive or die. Here three features are required for each passenger in order for the decision tree to make its classification: sex, age and number of siblings/spouses aboard (sibsp). The path of an example event is shown in orange. An example of a node, branch and leaf are annotated in purple. This figure was adapted from Ref. [144].

these events as possible. This proccess is known as supervised learning. This is done here using the greedy algorithm [145], which begins at the top of the tree and moves down, at each node choosing the optimal criterion to split the data on from all available features and thresholds. This process continues until either the data becomes perfectly classified, i.e. every leaf contains only data pertaining to a single classification, or the tree reaches some user-defined limit, for example the maximum depth of the tree. It is important to set an appropriate limiting criteria when using DTs to prevent overfitting to the training data [146].

DTs are exploited in a variety of ensemble machine learning techniques, where rather than using a single DT, many DTs are used simultaneously to produce a more accurate overall classification. In the present work, the Random Forest (RF) ensemble machine learning technique is used [147]. A RF trains many DTs independently, in each case introducing a degree of randomness into the training algorithm, such that each DT is slightly different. The randomness is introduced in two steps: first each DT is trained on a random subset of the training data, drawn from the training data set with replacement (a bootstrap sample). Secondly, when evaluating the feature to split on at each node, it is chosen from random subset of the available features.

When making a classification, a RF allows every DT to make an independent prediction, and then calculates the fraction of DTs which predict each class. This fraction is interpreted as the likelihood of that class being the correct classification. In the case where there are two possible classes (class-A and

class-B), a prediction threshold is used to provide a definitive classification. If class-A has a likelihood greater than the prediction threshold, then the RF outputs class-A, otherwise it outputs class-B. By default the prediction threshold is set to 0.5, but by adjusting this prediction threshold one may control how confident the algorithm must be to make a certain prediction. The fact that a RF returns both the predicted classification of an event and the likelihood that the classification is correct allows for a more informed and detailed analysis than is possible using a single DT. In the present work, all of the machine learning algorithms are implemented using the python module `scikit-learn` [148].

5.4.4.2 Understanding the Spectral Signature with Random Forests

In the present work RFs are used to classify spectra as either containing fragmented α-clustered states (clustered) or not containing any examples of such states (not clustered), based upon the CWT of the spectra. One would expect, if a signature of fragmented α-clustering exists, a RF ought to be able to characterise it, and then identify it in experimental spectra. Two RFs were trained, one on $\mathcal{E}^{\text{uni}}_{2000}$ and one on $\mathcal{E}^{\text{stat}}_{2000}$, to allow the effect of the coupling type on the signature to be understood. The output of these RFs is referred to as the clustering likelihood.

For simplicity the RFs were trained to identify the signature in P_Ψ alone, calculated for δE between 0 and 1. Rather than using the full P_Ψ spectrum as the feature set for each event, it was simplified by parametrising it in terms of characteristic scales. This was done by automatically identifying all of the peaks and troughs in P_Ψ and using their locations, $(\delta E_i, P_{\psi,i})$, as the features. The peaks and troughs were identified using an open source peak-finding algorithm [149]. It was important to use the troughs as well as the peaks as this provides some basic information on the shape of the peaks. The final feature set consisted of the locations of the N_{peaks} peaks and troughs with the lowest δE_i, and the total number of identified peaks and troughs. If there are fewer than N_{peaks} peaks or troughs identified in the spectrum, then the remaining slots were set to a peak position of $(1,0)$. This allows the P_Ψ for each event to be characterised by just $(4N_{\text{peaks}}+2)$ features. An example of this parametrisation is shown in Figure 5.18.

It is important to test the quality of the RF classifiers produced once they have been trained on the ensemble of spectra, i.e. how accurately they can now classify new spectra. This is analysed here using two metrics: The cross-validation score and a Receiver Operating Characteristic (ROC) curve. The cross-validation score is a simple measure which calculates how likely the trained RF is to produce the correct classification given a test data set. This is calculated by presenting the trained RF with a set of simulated spectra and observing the fraction which the RF classifies correctly as being either clustered or not clustered. It is important that the RF is tested using new spectra that have not already been used to train the RF, to avoid overfitting to the training data set [146]. The cross-validation is

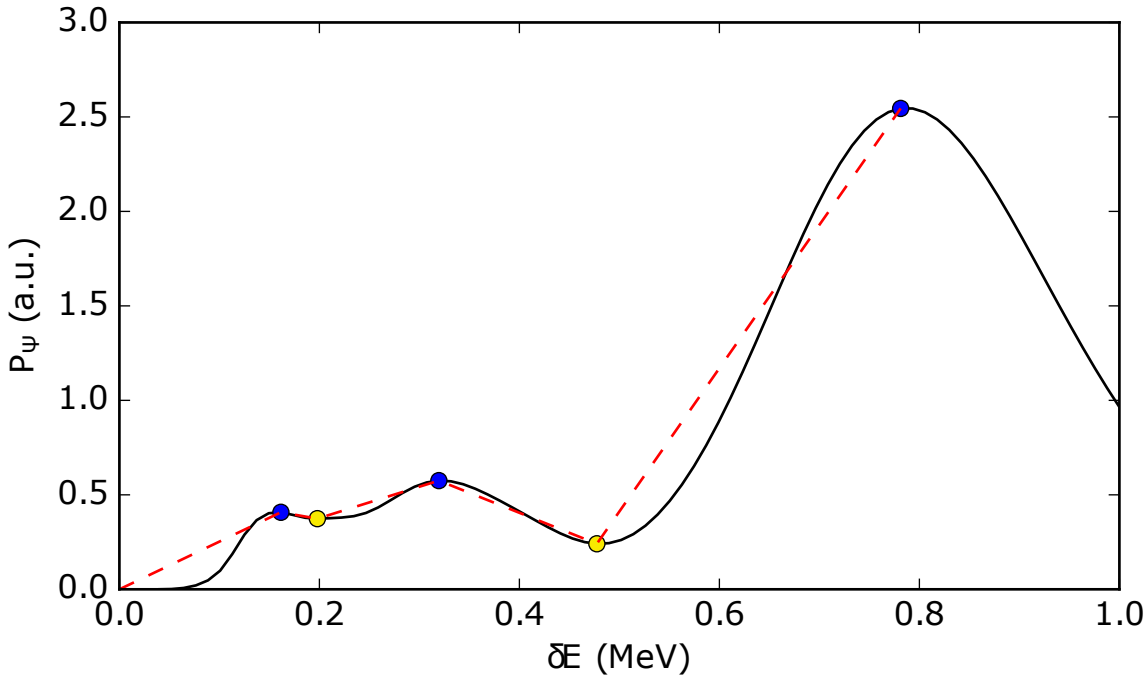

Figure 5.18: An example power spectrum (black line), characterised using only the identified peaks (blue points) and troughs (yellow points). The red dashed line demonstrates the approximation made using this technique. Here 3 peaks and 2 troughs are identified, so the remaining peaks and troughs would be set to (1,0).

calculated in this work using 10-fold cross-validation [150]. Here the training data set is split into 10 equally sized sub-sets. The RF is then trained on 9 of these sub-sets, leaving out one of the sub-sets, which is then used to test the RF. This procedure is repeated, leaving out each sub-set in turn, and the cross-validation score is calculated as the mean fraction of correctly classified events over all of the test subsets. The standard deviation of the fraction of correctly classified events gives an estimate of the error on the cross-validation score.

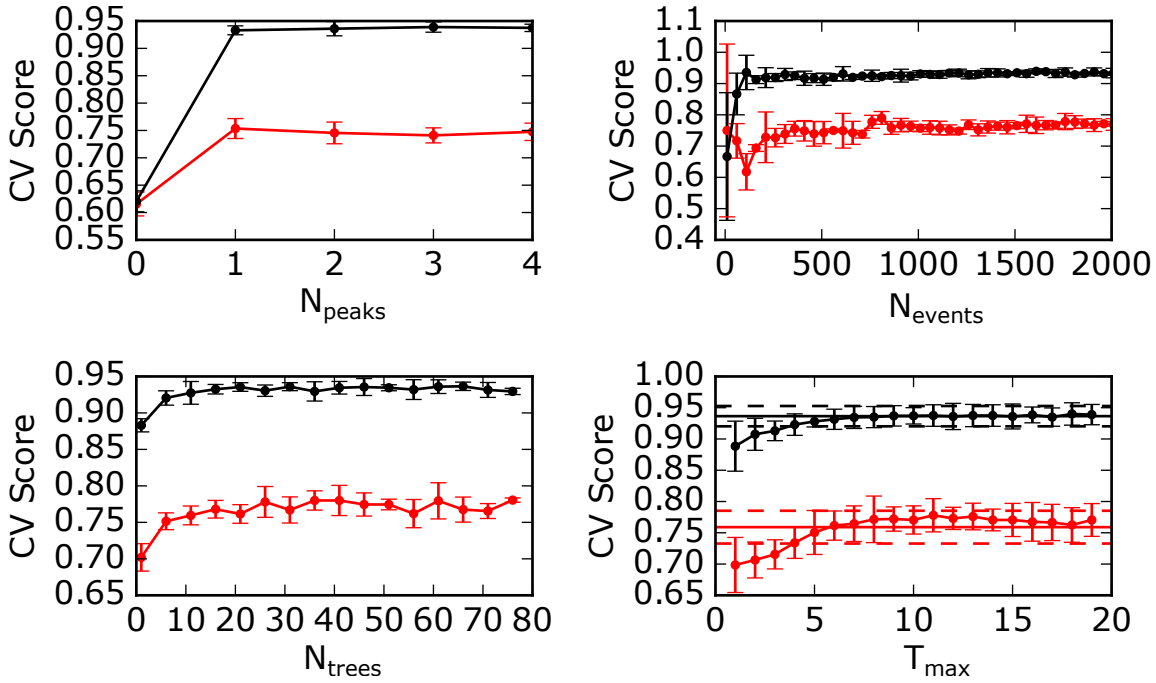

Figure 5.19: The 10-fold cross-validation score (CV score) as a function of various important input parameters to the RF algorithm. These are calculated for both the statistical coupling RF (red line), and uniform coupling RF (black line). All other input parameters are held fixed at the following values while the parameter in question is varied: $N_{\text{peaks}} = 5$, $N_{\text{events}} = 2000$, $N_{\text{trees}} = 200$, $T_{\text{max}} = 10$. In the plot of CV score as a function of T_{max}, the lines represent the CV score where the tree depth is unlimited.

The cross-validation score was used to choose the optimal parameters for the RFs: the number of peaks/troughs used in the parameter set, N_{peaks}, the number of events in the training data set, N_{events}, the number of DTs in the RF, N_{trees}, and the maximum DT depth, T_{max}. The cross-validation is plotted as a function of each of these parameters in Figure 5.19, and based on this the optimal parameters were taken to be: $N_{\text{peaks}} = 5$, $N_{\text{events}} = 2000$, $N_{\text{trees}} = 200$, $T_{\text{max}} = 10$[b]. To ensure the best possible results, all of these were taken to be well above the point at which the cross-validation score plateaus, limited instead by the corresponding increase in computational time, with the exception of T_{max}. T_{max} was taken to be as low as possible while maintaining an optimal cross-validation score to avoid overfit-

[b] Some of these values are beyond the ranges shown in Figure 5.19, as the ranges in the figure were reduced to emphasise the interesting behaviour at low values.

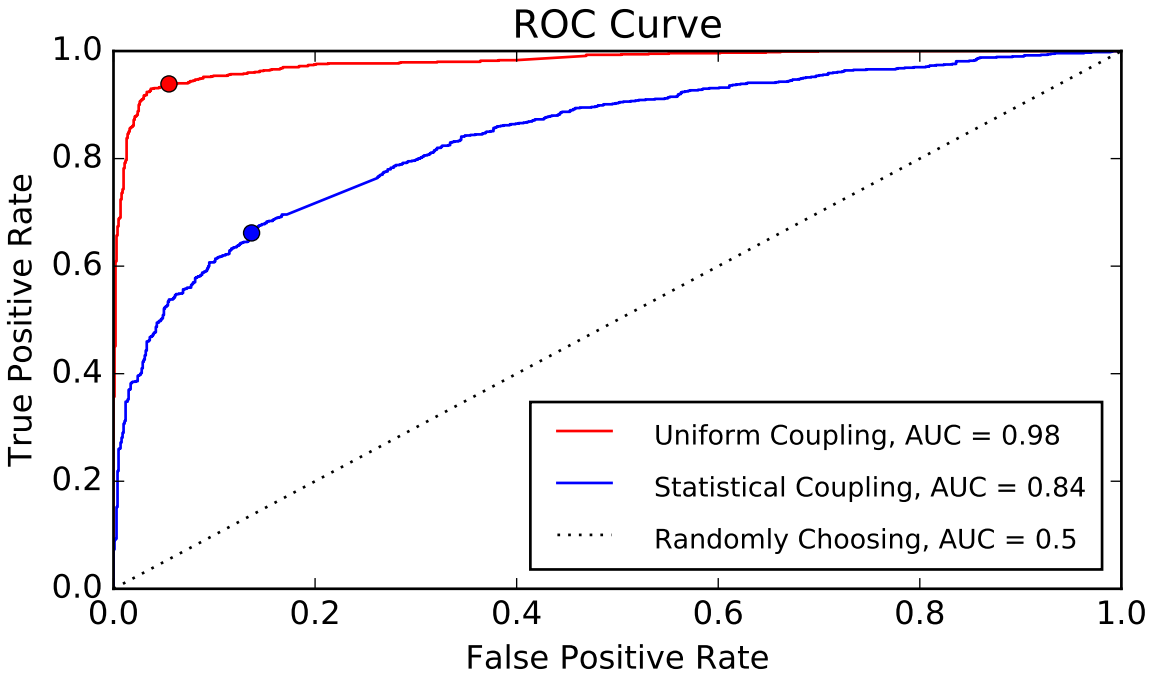

Figure 5.20: A ROC plot for both the uniform coupling RF and statistical coupling RF. The points identify the TPR and FPR when the threshold is set to 0.5, which is the threshold used in practice.

ting; the cross-validation score peaks close to $T_{\max} = 10$ for the statistical coupling RF, suggesting that above this the algorithm may overfit to the training data. Using these optimal parameters the cross-validation score for the uniform coupling RF was 0.94 ± 0.01 and for the statistical coupling RF it was 0.75 ± 0.02.

The second technique used to analyse the quality of the RFs was a ROC curve [151], plotted for each RF in Figure 5.20. A ROC curve is a parametric curve that plots the True Positive Rate (TPR) against the False Positive Rate (FPR), as a function of the prediction threshold. In this case the TPR corresponds to the fraction of clustered spectra that are correctly classified as such, and the FPR corresponds to the fraction of simulated spectra that are not clustered, that are falsely classified as clustered. An ideal RF would produce a ROC curve that passes through the top left most corner, where TPR = 1 and FPR = 0. A completely random classifier, which randomly assigns each spectrum a clustering likelihood with a uniform probability between 0 and 1, would produce a linear ROC curve between TPR=0,FPR=0 and TPR=1,FPR=1. Most ROC curves will fall somewhere between these two limits, and a better quality classifier will drag the curve closer to the top left corner, and further from the 'Randomly Choosing' line.

Another metric associated with the ROC curve is the Area Under the Curve (AUC) [152]. This is the area under the ROC curve, 0.5 for the Randomly Choosing ROC curve, and 1.0 for the perfect classifier.

A larger AUC corresponds to a better quality classifier, and can be interpreted as the probability that for a randomly chosen clustered spectrum and randomly chosen non-clustered spectrum, the classifier would produce a larger clustering likelihood for the clustered spectrum than the non-clustered spectrum. The AUCs for the uniform coupling RF and the statistical coupling RF are 0.98 and 0.84 respectively.

It is clear, by comparing the cross-validation scores, ROC curves and AUC values for the statistical coupling RF and uniform coupling RF that the signature is much easier to identify in the case of uniform coupling. It is still certainly possible to identify the signature using a RF in the case of statistical coupling, it is just not as reliable as in the uniform coupling case. This is consistent with the discussion at the end of Section 5.4.3, based on the averaged CWT over each ensemble of spectra, which suggested that the signature is much more prominent when uniform coupling is assumed. It is important to note, however, that this does not mean that the uniform coupling RF should be used rather than the statistical coupling RF. Uniform and statistical coupling correspond to two different approximations made when attempting to describe the coupling matrix elements, and while the case of uniform coupling produces a clearer signature of fragmented α-clustering, this does not make it more likely to be the correct assumption. In fact, as discussed in Section 5.4.3, statistical coupling is likely to be more physically accurate.

It is possible, within the framework of the RF, to calculate the relative importance of the features in classifying a spectrum. This is done by exploiting the fact that the most important parameters will be used as nodes at higher positions in the DTs. By taking the average node height for each feature over the entire forest of DTs, an estimate may be made for how important each feature is in classifying the training data set. More details on this procedure can be found in the `scikit-learn` user guide [148], and it is implemented for the RFs from the present work in Figure 5.21. It is clear from this that it is the first peak and first trough, which corresponds to the peak and trough with the lowest δE_i, that are the most important features. This is again consistent with the discussion in Section 5.4.3, where it is argued that the increase in P_Ψ at low δE is due to the increased likelihood of having a strong characteristic scale at low δE in α-clustered spectra. This is consistent also with the cross-validation score as a function of N_{peaks}, displayed in Figure 5.19, which shows that the cross-validation score plateaus after $N_{\text{peaks}} = 1$.

It is possible to investigate the nature of the signature in more detail by plotting decision surfaces. A decision surface is a calculation of the clustering likelihood as a function of any two features, averaged over all of the remaining features. This is calculated by re-training the RFs using only the two features of interest, rather than the full set of 22 features, and then calculating the clustering likelihood for all possible combinations of those two features and plotting this as a heatmap. This prevents the decision

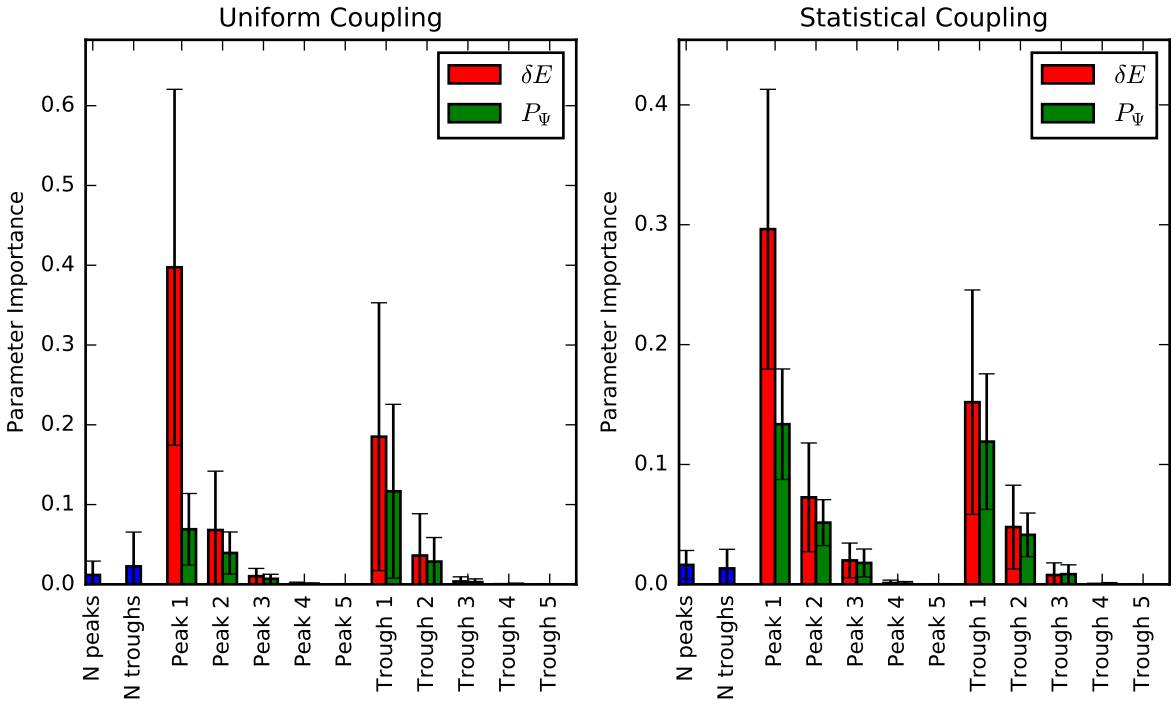

Figure 5.21: The relative importance of each feature in training the RF.

trees from splitting on any features apart from the two in question, effectively producing an average over all other features.

As it is the first peak and first trough that dominate the signature, the decision surfaces are plotted for all combinations of the 4 features associated with them: Peak 1 (δE_{p1},$P_{\Psi,p1}$) and Trough 1 (δE_{t1},$P_{\Psi,t1}$). These are shown for uniform coupling in Figure 5.22 and for statistical coupling in Figure 5.23. For each decision surface, the cross-validation score for the RF using only those two features is shown, which demonstrates how well that pair of features does at classifying the spectra.

For all feature combinations the decision surfaces for uniform coupling present a very clear and sharp separation between clustered and not clustered regions. It is this clear, sharp separation that leads to the high quality classifier, since it is generally quite easy to separate the two types of spectra. It is possible, by identifying regions in these decision surfaces with a very high clustering likelihood, to build up an understanding of what the signature of fragmented α-clustering actually is. These regions are marked A, B and C on Figure 5.22. Region A identifies the area where $\delta E_{p1} \lesssim 0.28$, region B the area where $\delta E_{t1} \lesssim 0.4$ and region C the area where $P_{\Psi,t1} \lesssim 0.5$. These three features combine to give a simplified understanding of the signature of fragmented α-clustering, which is the existence of the first characteristic scale at low δE, and that this scale ought to present as a narrow, well defined peak, followed by a deep trough.

It is also interesting to note that the boundary between the clustered and not clustered regions in

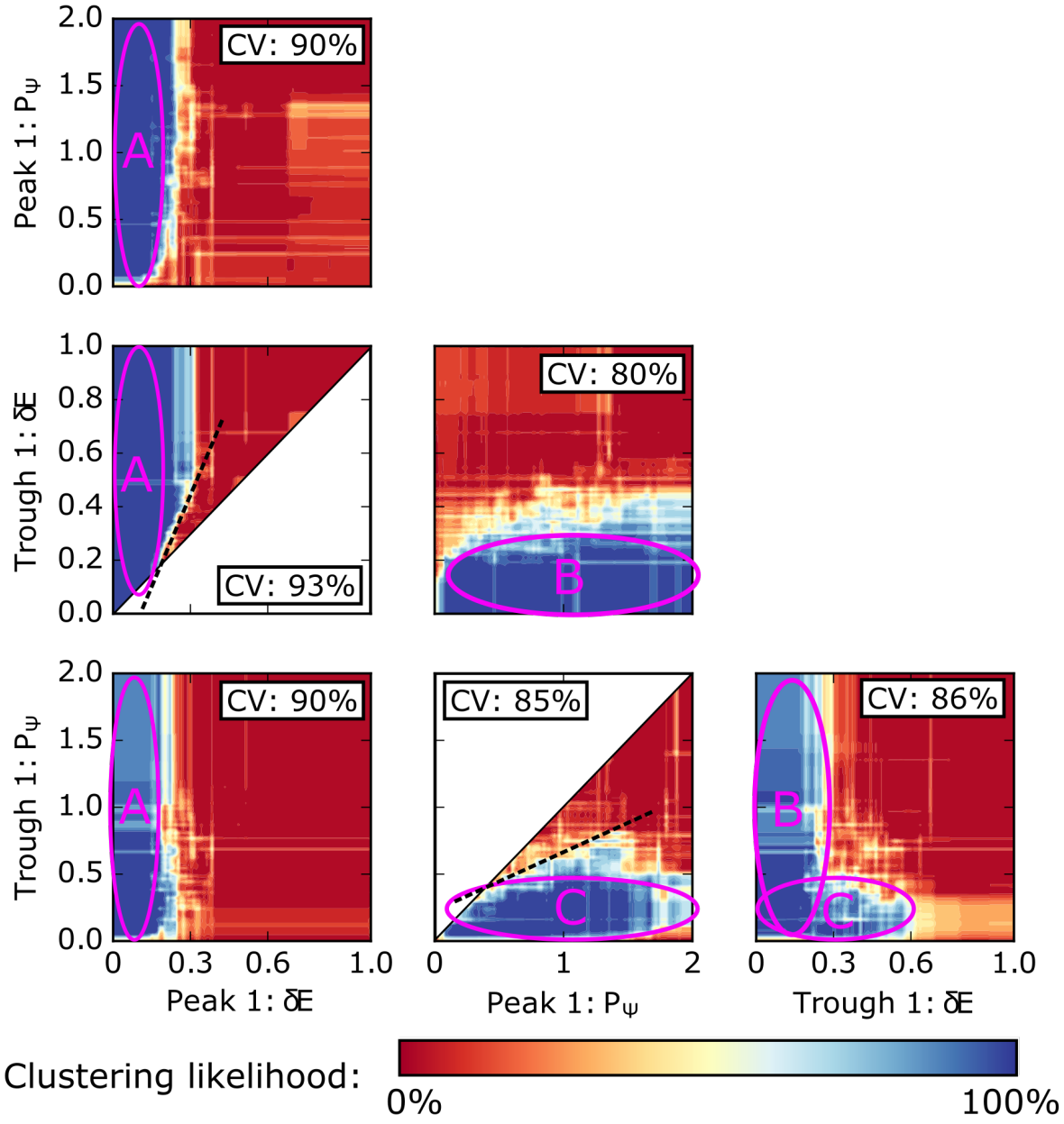

Figure 5.22: A set of decision surfaces for all possible pairs of the features of the first peak and first trough in the P_Ψ simulations, generated using uniform coupling. The cross-validation scores for the Random Forest trained only using those two features is inset in each plot. Regions of the surfaces that are invalid are left white. The regions marked as A, B and C in magenta are discussed in the text, as well as the dashed lines.

both the $P_{\Psi,p1}$ vs $P_{\Psi,t1}$ decision surface and the δE_{p1} vs δE_{t1} decision surface may be approximated, at least in part, by a linear line with a positive gradient. This is marked on Figure 5.22 by a dashed black line. This shows that in terms of the signature, it is usually the position of the first trough relative to the first peak that is important, rather than the absolute position of the first trough.

The statistical coupling decision surfaces show similar boundaries to the uniform coupling decision surfaces, suggesting that the signature presents in much the same way in the case of statistical coupling as it does for uniform coupling. The main difference is that the regions which were very definitely not clustered in the uniform coupling model generally have an increased clustering likelihood in the statistical coupling model, i.e. the RF is less confident when attempting to classify spectra as not clustered. This occurs because the additional level of randomness introduced by the statistically generated coupling matrix elements spreads the signature out in feature space, sometimes producing power spectra similar to those observed in spectra with no clustered states. This makes it much harder to say confidently that a given spectrum does not contain clustered states, and this is reflected in the decision surfaces not producing especially low clustering likelihoods. Overall this means that the signature does not change in the case of statistical coupling, there is just not as clear a separation between clustered and not clustered spectra.

5.4.4.3 Analysis of Experimental Data with Random Forests

It is now possible to apply the trained RFs to the ^{44,48,52}Ti data. Since the simulated spectra are generated under the assumption that the energy range is small enough to allow the penetrability and background contributions to be approximated as constants, and the data span a large energy range, this model cannot be compared with the P_Ψ of the entire spectrum. Instead P_Ψ is calculated for a 3 MeV window, and is then fed into the RF to produce a clustering likelihood for that region. This region is moved through the spectra to calculate the clustering likelihood over the entire energy range. The 3 MeV window size was chosen because it is small enough for the small energy range approximation to be valid, but large enough to ensure that local fluctuations in W_Ψ are averaged out, producing a P_Ψ containing only the truly significant characteristic scales. The results were compared with those produced using other window sizes, and similar results were found for windows between 2 and 6 MeV. It is important to note that the predictions made close to the boundaries of the spectra will be less reliable, as they will necessarily cover a window smaller than 3 MeV.

The results are shown in Figures 5.24 and 5.25 using the uniform coupling RF and statistical coupling RF respectively. While the two models predict consistent results for the ^{52}Ti spectrum, they differ greatly for ^{44,48}Ti. A comparison of the predictions made by each model with previous work on ^{44}Ti allows a comparison to be made regarding the quality of the underlying statistical coupling and uni-

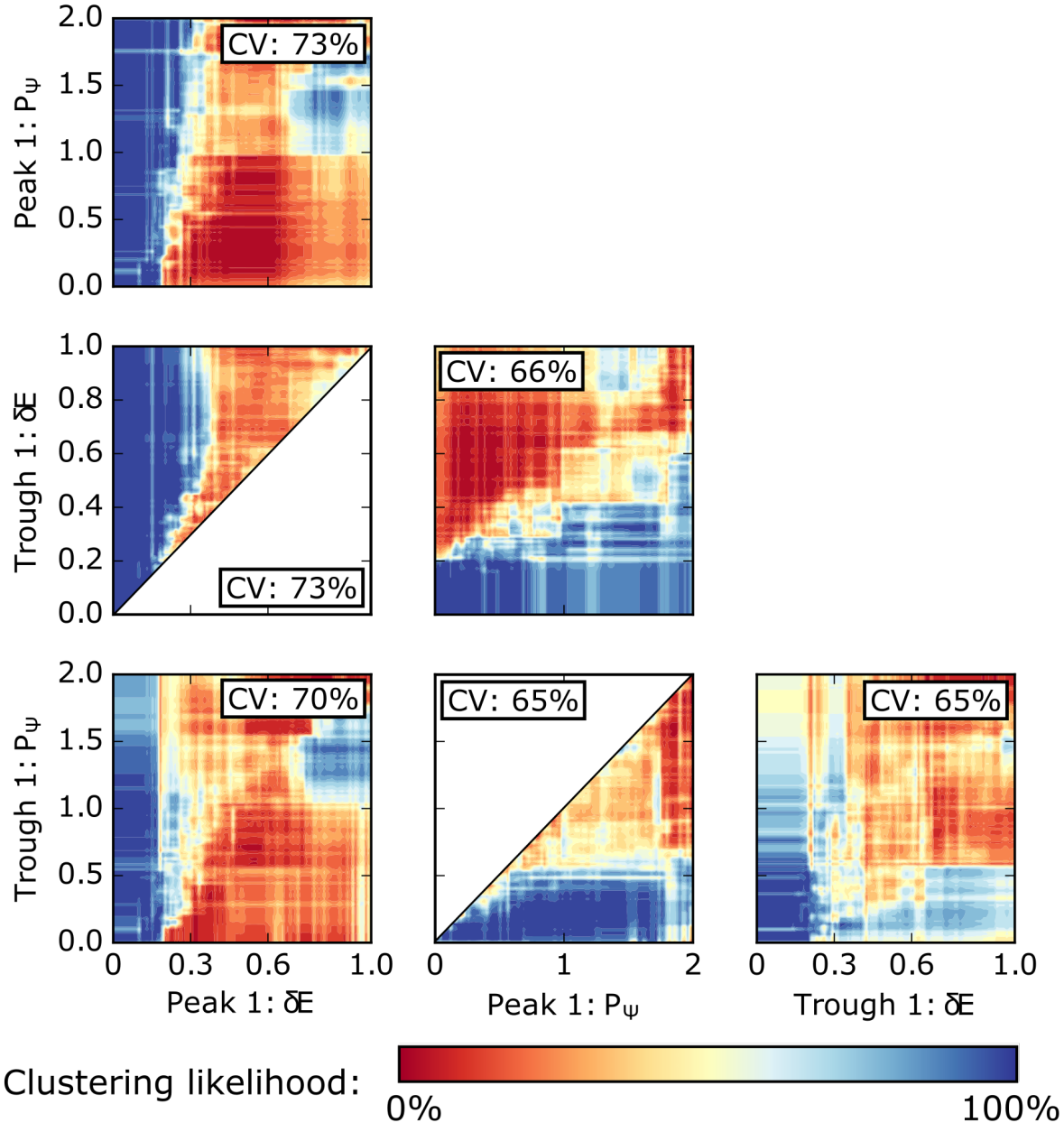

Figure 5.23: A set of decision surfaces for all possible pairs of the features of the first peak and first trough in the P_Ψ simulations, generated using random coupling. The cross-validation scores for the Random Forest trained only using those two features is inset in each plot. Regions of the surfaces that are invalid are left white.

form coupling approximations. It is clear from the literature discussed in Section 5.1 that fragmented α-clustered states have been observed in ^{44}Ti up to $\sim$ 14 MeV. There is some evidence for α-clustered states at excitation energies higher than this, however these have not been studied in enough detail to confirm whether they present as a group of fragmented states or as a single α-clustered state. A comparison with the two sets of predictions for the clustering likelihood in the ^{44}Ti spectrum clearly shows that the RF based on the statistical coupling assumption agrees with these previous studies, predicting fragmented α-clustered states consistently throughout the entire measured spectrum. By contrast the predictions of the RF based on uniform coupling vary, but at low energies where fragmented α-clustered states have been conclusively observed the RF predicts no α-clustered states. Based on this comparison the clustering likelihood calculated using the statistical coupling model is taken to be the most reliable metric, and the results produced by the uniform coupling model are rejected. This is consistent with the more physically realistic basis for the statistical coupling model, and shows that while the uniform model produces a clearer signature, it is useful only to help understand the properties of the signature, and does not perform well when compared directly with the data.

Focusing now only on the results produced by the statistical coupling RF, there is a clear signature of fragmented α-clustering identified by this algorithm throughout the entire ^{44}Ti spectrum, and below E_x $\sim$17.5 MeV in the ^{52}Ti spectrum. Above this threshold in ^{52}Ti the algorithm predicts that the spectrum is very unlikely to contain any fragmented α-clustered states. The clustering likelihood increases again at E_x $\sim$19.5 MeV, however this is very close to the edge of the spectrum, and is less reliable a result as a consequence. In fact, when one considers that the clustering likelihood is calculated for a 3 MeV window, these results suggest that there are no fragmented α-clustered states above E_x[^{52}Ti]$\sim$ 16.0 MeV (the lower boundary of a window centred on 17.5 MeV).

The results for ^{48}Ti are inconclusive. The clustering likelihood remains close to 0.5, oscillating between slightly above and slightly below this value for the majority of the spectrum. There are some regions, such as at E_x $\sim$ 18.5 MeV, where the clustering likelihood increases dramatically. However these regions all span a very small energy range, much smaller than the size of the 3 MeV window used to calculate it, suggesting that they are anomalous results. The only region of the ^{48}Ti spectrum that gives a high clustering likelihood over a significant energy region is at low energies, below E_x $\sim$ 16 MeV. It is possible that this may suggest fragmented α-clustered states in this energy range, however again these results are less reliable as they are close to the edge of the spectrum.

Another way it is possible to extract some understanding of the cluster structure in the ^{44,48,52}Ti data is based on the understanding of the signature provided by this machine learning analysis. As stated previously, the signature of fragmented α-clustering is a large characteristic scale at low δE, usually less than δE=0.28 MeV, and this characteristic scale is composed of hotspots in W_Ψ, each centred on the

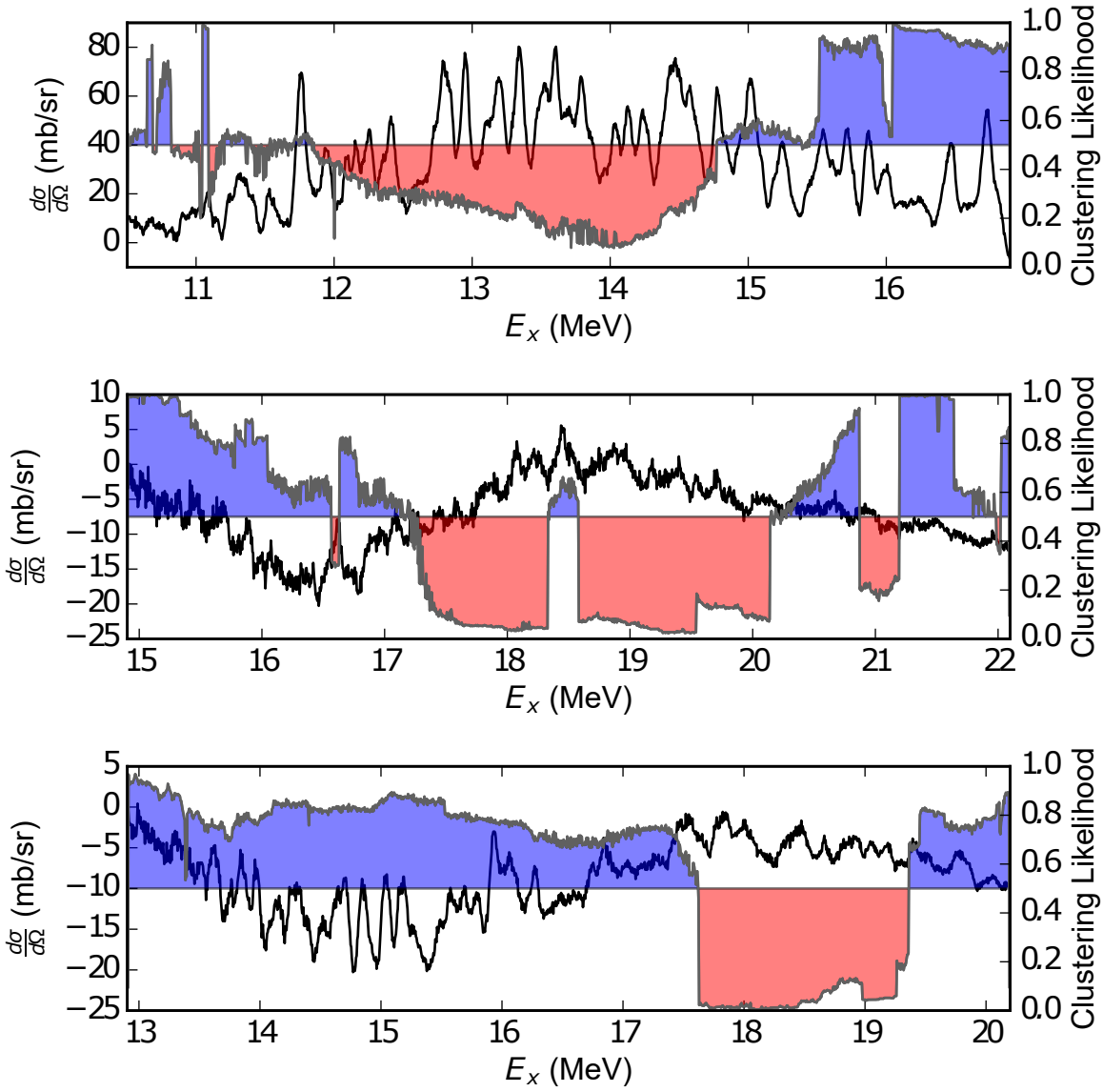

Figure 5.24: The result of the application of the RF trained on the uniform coupling data set, to the measured spectra: ^{44}Ti (top), ^{48}Ti (middle), ^{52}Ti (bottom). The clustering likelihood was calculated at each E_x for a 3 MeV window centred at that E_x. At the boundaries of the spectra the window size is reduced. Red regions are classified as not clustered, and blue regions are classified as clustered.

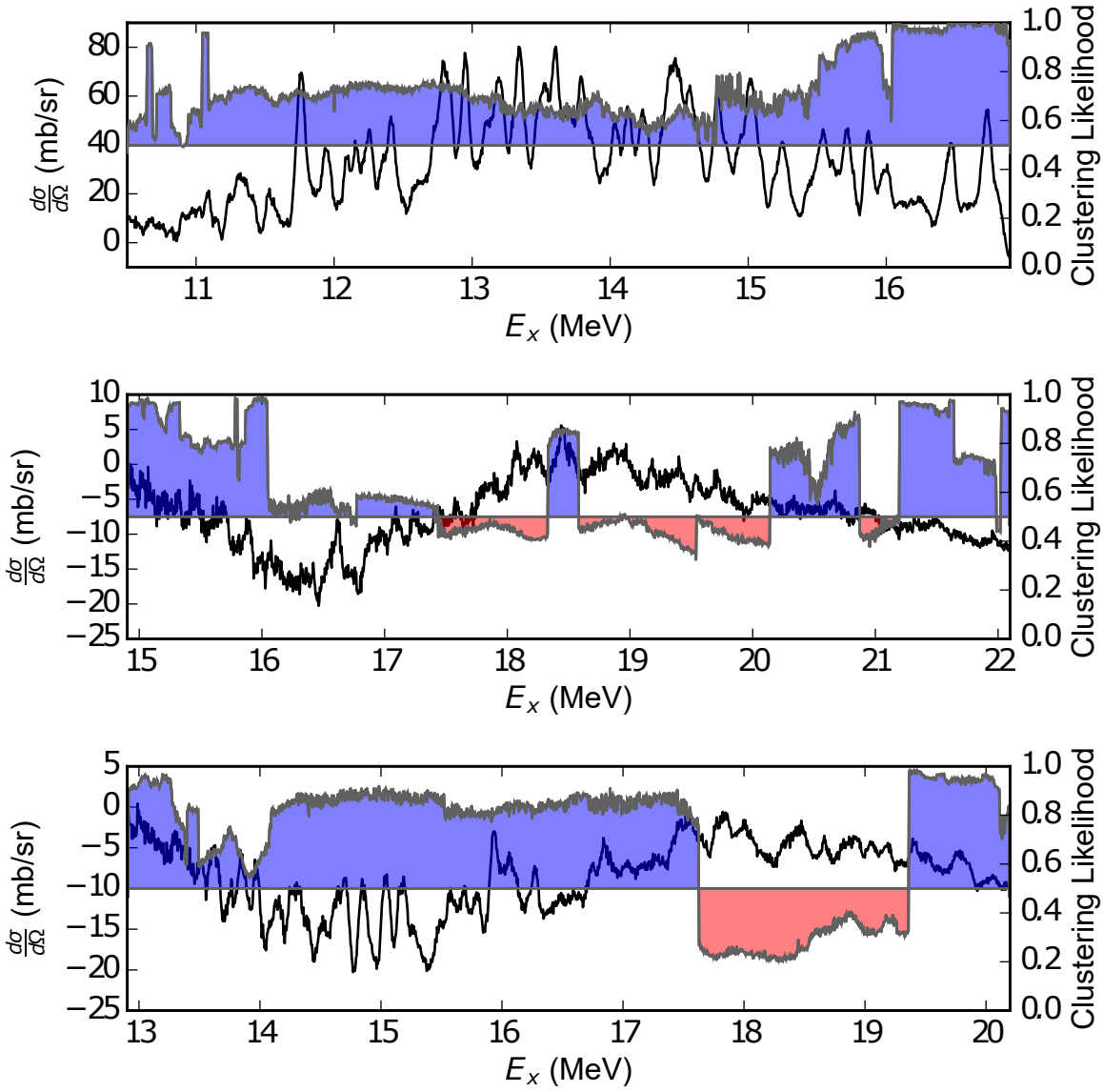

Figure 5.25: The result of the application of the RF trained on the statistical coupling data set, to the measured spectra: ^{44}Ti (top), ^{48}Ti (middle), ^{52}Ti (bottom). The clustering likelihood was calculated at each E_x for a 3 MeV window centred at that E_x. At the boundaries of the spectra the window size is reduced. Red regions are classified as not clustered, and blue regions are classified as clustered.

energies of the α-clustered class-II states. It can be seen in Figure 5.12 that both ^{44}Ti and ^{52}Ti present a characteristic scale at δE $\sim$0.2 MeV, and this scale is missing in ^{48}Ti. This suggests that this may be the signature characteristic scale. If one were to gate on this peak in W_Ψ, the hotspots should produce peaks at the energies of the α-clustered class-II states. This is done by calculating the fraction of W_Ψ that originates from within the boundaries of the signature peak: $[S_{\text{min}}, S_{\text{max}}]$, a quantity denoted here as F_Ψ. F_Ψ is defined as

$$F_\Psi(E) = \frac{\int_{S_{\text{min}}}^{S_{\text{max}}} |W_\Psi(E,\delta E)|^2 d\,\delta E}{\int_0^\infty |W_\Psi(E,\delta E)|^2 d\,\delta E}\,. \tag{5.34}$$

F_Ψ is overlayed on the experimental spectra for ^{44}Ti and ^{52}Ti in Figure 5.26. Clear peaks are identified in both spectra, suggesting the existence of α-clustered states at E_x = 11.19, 11.75, 12.37, 12.94, 13.36, 14.33, 14.8, 15.81 and 16.57 MeV in the ^{44}Ti spectrum, and at 3.66, 14.0 and 14.8 MeV in the ^{52}Ti spectrum. It is interesting to note the consistency between these results and the results of the direct application of the RF to the experimental data, which found that above 16 MeV in the ^{52}Ti spectrum there is very little evidence of any α-clustered structures, in contrast to ^{44}Ti where α-clustered type structures seem to be present throughout the measured energy range.

5.4.5 Picket Fence Model of Fragmented Alpha Clustering

As discussed in the previous sections, the spectral signature of fragmented α-clustering arises due to the increased consistency in the state spacings, widths and amplitudes of the resonances in the vicinity of a class-II α-clustered state. The Picket Fence model is the limiting case of this increasing consistency. Here the class-I states of a given J^π are uniformly distributed with a constant state spacing $D^{(\text{I})}_{J^\pi}$, and their configurations are all identical such that the coupling matrix elements follow the constant coupling approximation, and their $\gamma^{(\text{I})}_{\mu,\lambda_\text{I}}$ are constant,

$$\gamma^{(\text{I})}_{\mu,\lambda_\text{I}} = \gamma^{(\text{I})}_{\mu}\,. \tag{5.35}$$

The class-II states are suitably separated given the coupling strength, such that the class-II states may be considered one at a time. Or stated differently, no class-I state will couple significantly to more than one class-II state. This is particularly appropriate for the present case where the structure of the class-II states is dominantly α-clustered, since the states would be expected to follow a rotational band, with each J^π appearing once only. These assumptions simplify Equation 5.20 to produce the

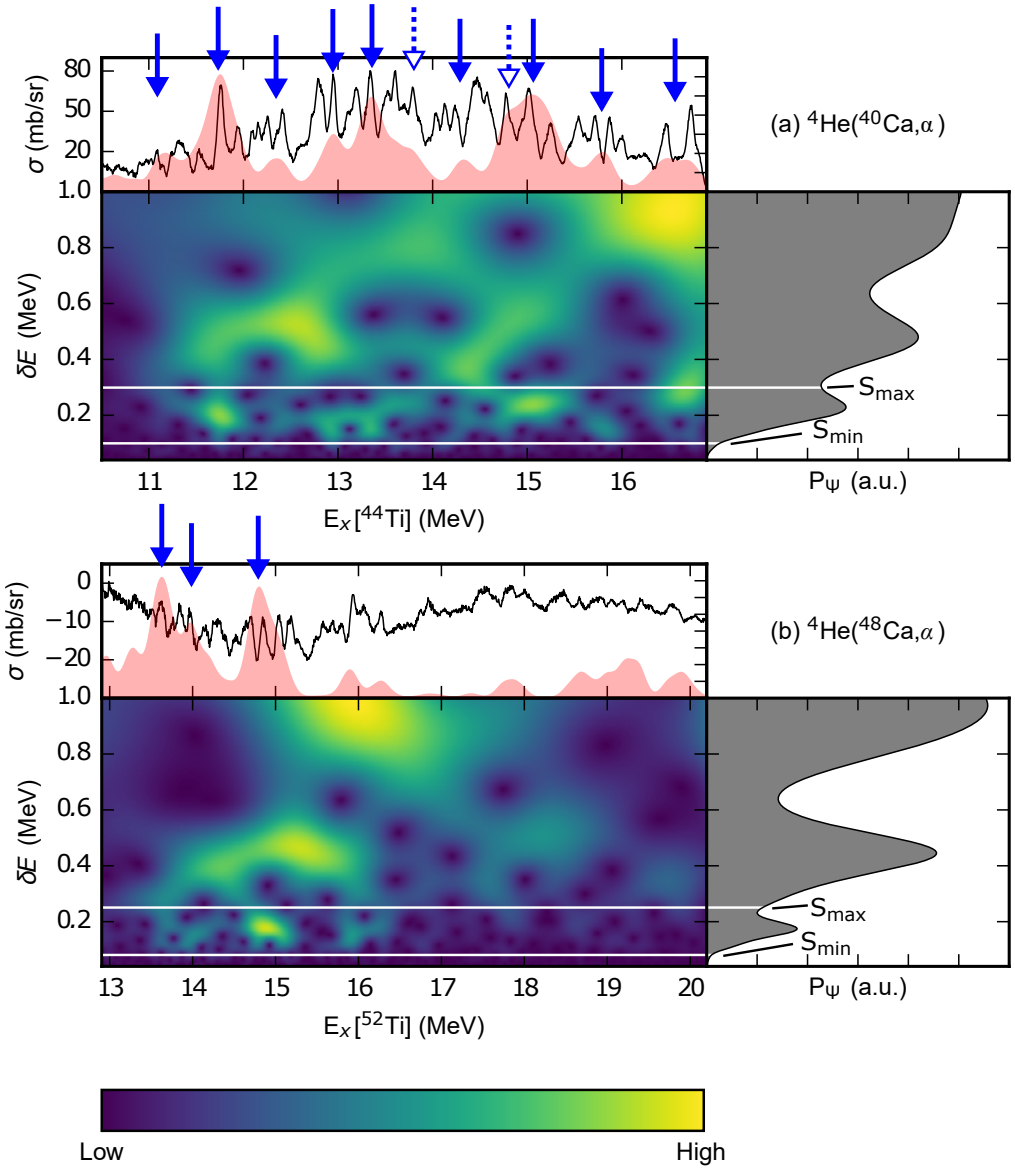

Figure 5.26: The F_Ψ analysis for ^{44}Ti (top) and ^{52}Ti (bottom). The light red overlay shows F_Ψ calculated using the boundaries $S_{\min}$ and $S_{\max}$ (white lines). Possible α-clustered states are indicated (blue arrows). Slight enhancements in F_Ψ which do not fully form peaks are indicated (blue dashed arrows), but these are not interpreted as possible α-clustered states.

following eigenvalue equation for N class-I states of a particular J^π

$$\begin{bmatrix} D^{(\mathrm{I})}_{J^\pi} & 0 & 0 & \cdots & 0 & H_c \\ 0 & 2D^{(\mathrm{I})}_{J^\pi} & 0 & \cdots & 0 & H_c \\ 0 & 0 & 3D^{(\mathrm{I})}_{J^\pi} & \cdots & 0 & H_c \\ \vdots & \vdots & \vdots & \ddots & \vdots & \vdots \\ 0 & 0 & 0 & \cdots & ND^{(\mathrm{I})}_{J^\pi} & H_c \\ H_c & H_c & H_c & \cdots & H_c & E^{(\mathrm{II})}_{J^\pi} \end{bmatrix} \begin{bmatrix} C^{(\mathrm{I})}_{\lambda,1} \\ C^{(\mathrm{I})}_{\lambda,2} \\ C^{(\mathrm{I})}_{\lambda,3} \\ \vdots \\ C^{(\mathrm{I})}_{\lambda,N} \\ C^{(\mathrm{II})}_{\lambda} \end{bmatrix} = E_\lambda \begin{bmatrix} C^{(\mathrm{I})}_{\lambda,1} \\ C^{(\mathrm{I})}_{\lambda,2} \\ C^{(\mathrm{I})}_{\lambda,3} \\ \vdots \\ C^{(\mathrm{I})}_{\lambda,N} \\ C^{(\mathrm{II})}_{\lambda} \end{bmatrix} . \tag{5.36}$$

This can now be diagonalised [136] to produce

$$E^{(\mathrm{II})}_{J^\pi} - E_\lambda = -\frac{\pi H_c^2}{D^{(\mathrm{I})}_{J^\pi}} \cot\left(\frac{\pi E_\lambda}{D^{(\mathrm{I})}_{J^\pi}}\right) \tag{5.37}$$

$$C^{(\mathrm{I})}_{\lambda,\lambda_\mathrm{I}} = -\frac{H_c}{E^{(\mathrm{I})}_{\lambda_I} - E_\lambda} C^{(\mathrm{II})}_{\lambda} \tag{5.38}$$

$$(C^{(\mathrm{II})}_{\lambda})^2 = \frac{H_c^2}{(E^{(\mathrm{II})} - E_\lambda)^2 + \frac{\pi^2 H_c^4}{D^{(\mathrm{I})\,2}_{J^\pi}} + H_c^2} . \tag{5.39}$$

Equation (5.37) must be solved numerically for E_λ, and then Equations (5.38) and (5.39) can be evaluated trivially. Following this a further simplifying assumption is made prior to the calculation of the resonance widths. Since the class-I states are assumed to be dominated by a mean-field structure, and the class-II states dominated by an α-clustered structure, it is assumed that $\gamma^{(\mathrm{II})}_\alpha \gg \gamma^{(\mathrm{I})}_\alpha$ and $\gamma^{(\mathrm{II})}_{\mu\neq\alpha} \ll \gamma^{(\mathrm{I})}_{\mu\neq\alpha}$, and as such the class-I contributions to the α partial width can be ignored, and conversely the class-II contributions to the partial widths for all other open channels can be ignored, simplifying Equations (5.24) and (3.45) to give

$$\Gamma_{\lambda,\alpha} = (C^{(\mathrm{II})}_{\lambda})^2 \, \Gamma^{(\mathrm{II})}_{\alpha} \tag{5.40}$$

$$\Gamma_{\lambda,\mu\neq\alpha} = \left(1 - (C^{(\mathrm{II})}_{\lambda})^2\right) \Gamma^{(\mathrm{I})}_{\mu\neq\alpha} . \tag{5.41}$$

From this calculated set of widths and energies for the compound states the spectra are calculated using the Simplified R-Matrix, in much the same way as was done for the statistical model of fragmented alpha clustering.

The picket fence model was used to simulate a single fragmented α-clustered state in Figures 5.27 and 5.28. It is clear from these figures that the spectral signature of fragmented α-clustering does indeed present in this limiting case, as expected, as a hotspot and a strong characteristic scale at low δE.

This model is also useful to test some assumptions upon which the statistical model is based. The

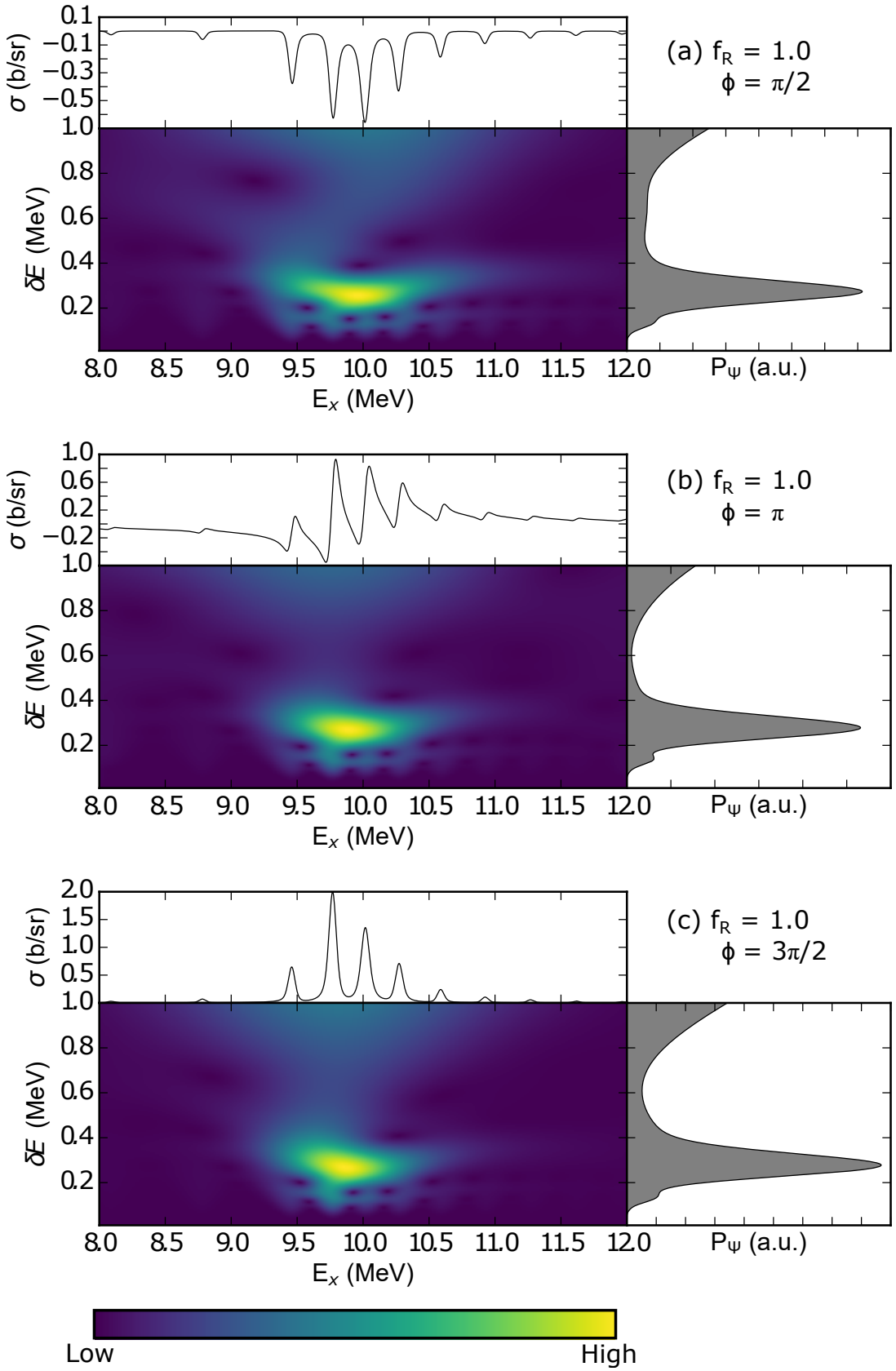

Figure 5.27: A single picket fence fragmented α-clustered state, calculated for varying ϕ, demonstrating the minimal effect the type of interference observed between the resonances and the background has on the spectral signature of fragmented α-clustering state. Other parameters used for calculation: $D^{(\mathrm{I})}_{J^\pi}$ = 0.35 MeV, $\Gamma^{(\mathrm{II})}_{\alpha}$ = 100 keV, $\Gamma^{(\mathrm{I})}_{\mu\neq\alpha}$ = 20 keV, H_c = 0.15 MeV$^{0.5}$.

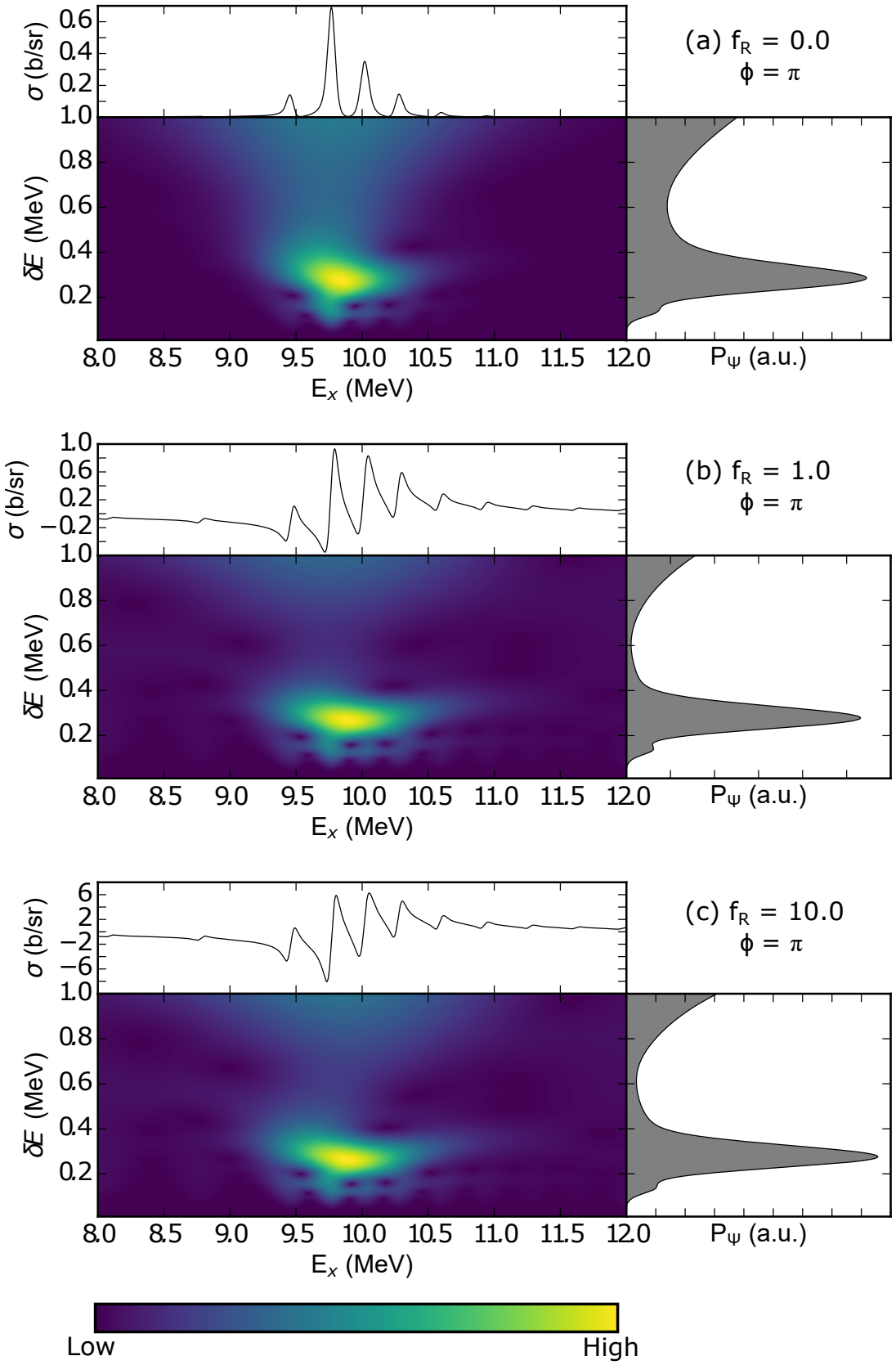

Figure 5.28: A single picket fence fragmented α-clustered state, calculated for varying f_R, demonstrating the minimal effect the type of interference observed between the resonances and the background has on the spectral signature of fragmented α-clustering state. Other parameters used for calculation: $D^{(\mathrm{I})}_{J^\pi}$ = 0.35 MeV, $\Gamma^{(\mathrm{II})}_{\alpha}$ = 100 keV, $\Gamma^{(\mathrm{I})}_{\mu\neq\alpha}$ = 20 keV, H_c = 0.15 MeV$^{0.5}$.

first of these is the assumption that the spectral signature is independent of the properties of the background to the spectrum, as long as the background varies slowly with E. Figures 5.27 and 5.28 show a range of calculations made for a single picket fence fragmented α-clustered state, whilst varying both the amplitude of the background f_R and the type of interference between the resonances and the background, dictated by ϕ_{J^π} . In all cases a clear signature of fragmented α-clustering is observed, confirming the assumption. Figure 5.27 demonstrates that the signature is largely independent of ϕ_{J^π}, and Figure 5.28 demonstrates that the signature is also independent of f_R.

As a further test of the hypothesis that the ^{44}Ti spectra is composed of fragmented α-clustered states, and that it is these states that are responsible for the signature observed in the CWT, the spectrum was simulated using the picket fence model. This was done up to $E_x[^{44}\text{Ti}] \sim 14$ MeV, since it is in this energy region that the α-clustered states are well understood from previous work, and are understood to be fragmented.

There are 5 previously measured α-clustered states in this energy region, with spins ranging from 0^+ to 4^+. The values for $E^{(\text{II})}_{\lambda_{\text{II}}}$ were taken from the work by Ohkubo *et al.* [120], given in Table 5.1. The values for $\Gamma^{(\text{II})}_{\alpha,\lambda_{\text{II}}}$ were calculated using the Wentzel-Kramers-Brillouin (WKB) method applied to an appropriately chosen Woods-Saxon squared potential. This calculation was performed by Soylu [153], and was implemented in much the same way as previous WKB calculations [154, 155]. An α-cluster preformation factor of 0.1 was used for all states, chosen to provide the best possible agreement with the measured spectrum.

As it was confirmed that the signature is independent of f_R and ϕ_{J^π}, these values were chosen arbitrarily. The remaining parameters: $\Gamma^{(\text{I})}_{\mu\neq\alpha}$, $D^{(\text{I})}_{J^\pi}$ and W were varied to produce the best possible agreement with the measured spectrum. It was observed in this process that $\Gamma^{(\text{I})}_{\mu\neq\alpha}$ had a negligible effect on the resulting spectrum, so this was set to 0. It is worth noting that the $(2J+1)$ factor in Equation (3.58) significantly reduces the amplitude of the 0^+ resonances, meaning they have a very small impact on the CWT. This meant that the properties of the 0^+ class-II state could not be tested here. The amplitudes of the 1^- resonances were amplified by a factor of 2.5 to reproduce their considerable observed amplification in the experimental spectrum. The explanation for this amplification is not understood. The final set of parameters used to generate the picket fence model of ^{44}Ti are given in Table 5.7, and the CWT of the model spectrum is compared with the data in Figure 5.29.

It is clear from inspection that the CWT of the picket fence model does a good job of reproducing the CWT of the measured spectrum. Both the first characteristic scale in P_Ψ and the corresponding hot spots in W_Ψ agree almost perfectly. There is a clear similarity between the features in both W_Ψ and P_Ψ at higher scales, however these aren't as well aligned. This is likely because of the simplicity of the model, and the assumption that every feature in the spectrum is a fragmented α-clustered state.

Table 5.7: The parameters used to produce the picket fence model of ^{44}Ti. Grey boxes indicate parameters that are constant for all states.

Parameter	Class-II State				
λ_{II}	0	1	2	3	4
$J^{\pi}_{\lambda_{\text{II}}}$	0+	1-	2+	3-	4+
$E^{(\text{II})}_{\lambda_{\text{II}}}$ (MeV)	11.19	11.8	12.28	12.86	13.42
$\Gamma^{(\text{II})}_{\alpha,\lambda_{\text{II}}}$ (keV)	50	94	105	128	98
$\Gamma^{(\text{I})}_{\mu\neq\alpha}$ (keV)	0				
$D^{(\text{I})}_{J^{\pi}}$ (MeV)	0.28				
W (keV)	93				
f_R (mb$^{0.5}$)	0				
$\phi_{J^{\pi}}$	3π /2				

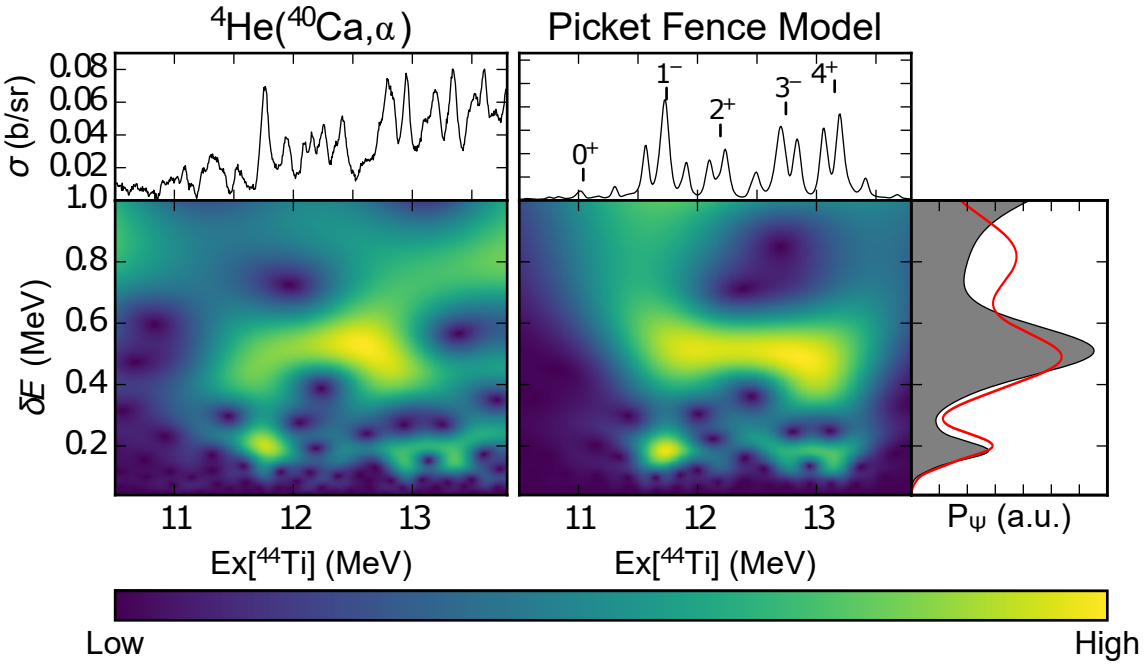

Figure 5.29: A comparison between the CWT of the experimental data for ^{44}Ti and a picket fence model, using the energies determined by Ohkubo *et al.* [120]. The red line represents P_{Ψ} for the data, and the grey area P_{Ψ} for the model. The other parameters used to produce this simulation are given in Table 5.7.

5.5 Discussion

5.5.1 Summary

Using the TTIK technique, measurements were made of the ^{4}He(^{40}Ca,α), ^{4}He(^{44}Ca,α) and ^{4}He(^{48}Ca,α) reactions, each at a scattering angle of 180°. Based upon these measurements the degree of α-clustering in ^{44}Ti, ^{48}Ti and ^{52}Ti was analysed. This was done by using the CWT to identify a signature of fragmented α-clustering in the measured spectra, a technique referred to as the spectral signature analysis.

The signature was understood and quantified using a Random Forest Classification algorithm applied to a set of simulated spectra. This demonstrated that the signature was a large, clear characteristic scale at low δE. This characteristic scale was observed to be composed of hot spots in W_Ψ, at the energies of the fragmented α-clustered states. Based on the spectral signature analysis, it seems clear that both ^{44}Ti and ^{52}Ti present fragmented α-clustered states in the measured energy regions. By contrast the results for ^{48}Ti were inconclusive, neither identifying fragmented α-clustered states nor confidently prohibiting their existence.

The application of the RF to the ^{44}Ti spectrum identified a clear signature of fragmented α-clustering throughout the measured energy range, a result consistent with previous work. The F_Ψ analysis identified 9 possible excitation energies of α-clustered states, spanning the entire measured energy range. Below $E_x[^{44}\text{Ti}]\sim 14$ MeV it was demonstrated that it is possible to reproduce many of the dominant features in the CWT using previously measured α-clustered states by Ohkubo *et al.* [120] and the picket fence approximation of fragmented α-clustering, confirming that the characteristic scales and hot spots in the spectrum are indeed generated by those fragmented α-clustered states.

The application of the RF to the ^{48}Ti spectrum did not conclusively identify the signature of fragmented α-clustering at any point in the measured energy range, with a clustering likelihood close to 0.5 for the majority of the energy range. This does not conclusively deny the existence of fragmented α-clustered states in ^{48}Ti either, however if they are present they do not exhibit the same characteristic signature that is observed in ^{44}Ti and ^{52}Ti.

The application of the RF to the ^{52}Ti spectrum suggests that fragmented α-clustered states exist below $E_x[^{52}\text{Ti}]\sim 16.0$ MeV, and above this threshold the existence of fragmented α-clustered states was shown to be unlikely. This is consistent with the F_Ψ analysis of ^{52}Ti, which identified three possible fragmented α-clustered states, at $E_x[^{52}\text{Ti}]\sim 13.66$, 14.0 and 14.8 MeV.

5.5.2 Clustering Discussion

An excellent one-to-one agreement is observed between previous measurements of α-clustered states by Ohkubo *et al.* [120] in ^{44}Ti, given in Table 5.1, and the states identified in the present work using the F_Ψ analysis. Following a simple comparison it is possible to assign the states measured here to these previously measured α-clustered states. This assignment is shown in Figure 5.30. It is important to note that the spins and parities are not measured in the present work, so these assignments are made based on the agreement in excitation energies alone.

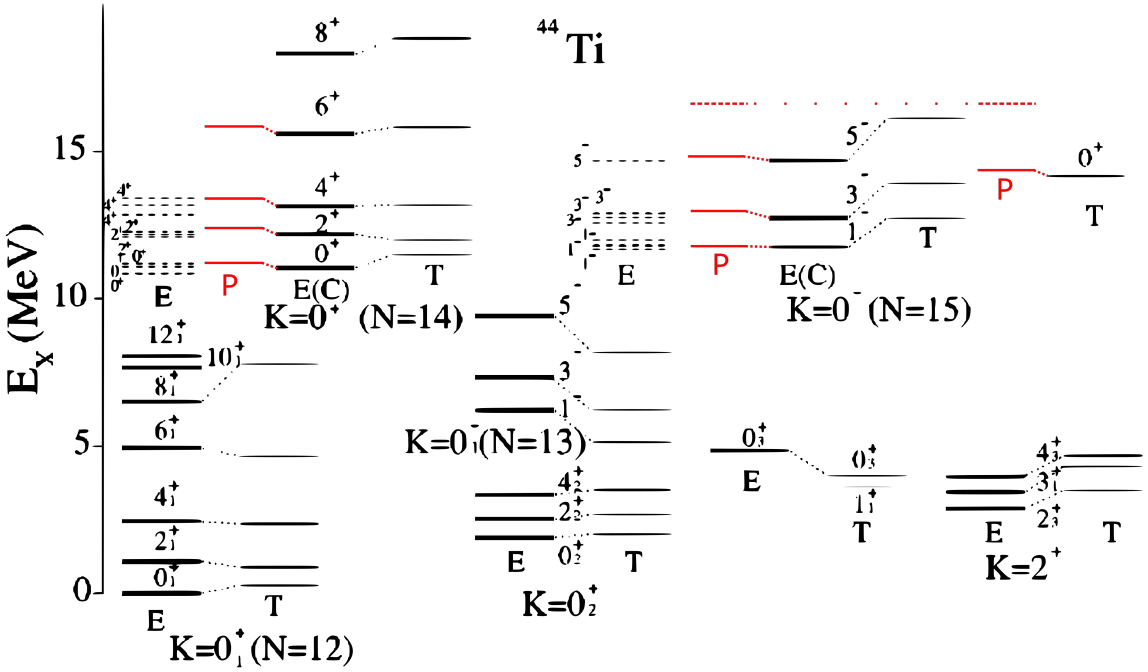

Figure 5.30: Previously measured α-clustered energy levels of ^{44}Ti, compared with predictions from an α-cluster model. Annotated with results from the present work (red), labelled P. The dashed red line indicates a measured state that does not have a valid assignment based on previous work. Theoretical energy levels (thin solid lines, labelled T) are compared with the experimental data (thick solid lines and labelled E). The fragmented experimental energy levels (E) are displayed by dashed lines and their centroid is indicated by the thick solid lines with label E(C). This figure was adapted from Ref. [120].

As the states must present as fragmented states to be measured using the present technique, all of these states may be assumed to be fragmented. This is in good agreement with previous work on the low lying members of the $N = 14$ and $N = 15$ bands, and it is the first observation of the fragmented nature of the 5^- and 6^+ states in these bands. This also may be the first experimental measurement of the 0^+ member of the predicted core-excited band. Finally a state is observed in the present work at 16.57 MeV, which cannot be assigned to any previously measured or predicted α-clustered states. It is possible that this state may be the 7^- member of the $N = 15$ band or the 2^+ member of the

core-excited band. It is interesting to note that all of the states measured in this work are measured at slightly higher energies than those presented by Ohkubo *et al.* [120]. This may indicate a slight error in the energy calibrations in either the present work or that presented by Ohkubo *et al.*.

This analysis suggests that α-clustering is a dominant component in describing the structure of ^{44}Ti and ^{52}Ti, but not in ^{48}Ti. This suggests that the doubly magic ^{40}Ca and ^{48}Ca cores play an important role in the existence of α-cluster structures in this mass region. It seems like the additional 4 neutrons in ^{48}Ti do not act as valence neutrons on the cluster structure, and instead act to destroy the cluster structure and revert to a mean-field dominated structure.

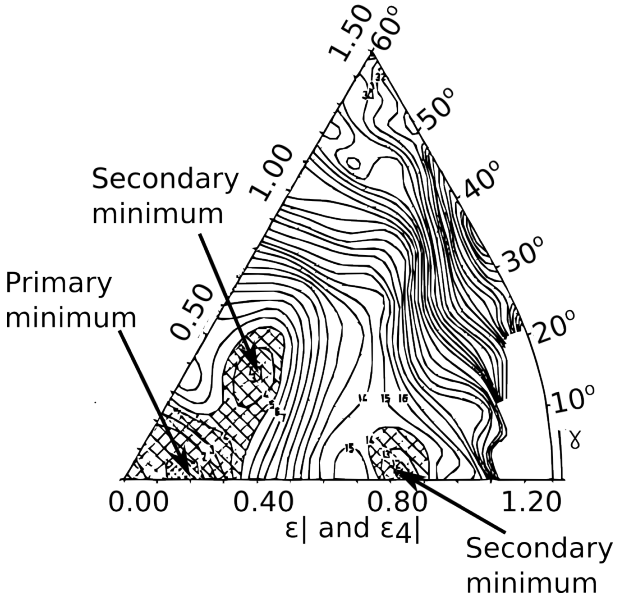

Figure 5.31: A Nilsson-Strutinsky calculation for ^{44}Ti, depicting one clear primary minimum and two clear secondary minima, marked. This figure is adapted from Ref. [53].

These results are consistent with the Nilsson-Strutinski calculation for ^{44}Ti [53], shown in Figure 5.31, which shows a secondary minimum with a prolate deformation, which could correspond to an α-^{40}Ca cluster structure. It would be an interesting comparison to perform a similar calculation for ^{48}Ti and ^{52}Ti, and observe the behaviour of this secondary minimum. If it were observed to disappear in the case of ^{48}Ti and then re-emerge in ^{52}Ti this would be very compelling evidence that that secondary minimum is indeed dominated by an α-cluster structure.

Chapter 6

Discussion

6.1 Summary

In this thesis ^{18}F and ^{44,48,52}Ti were investigated using the TTIK technique. A new method was developed to correct for the variable geometrical efficiency of the results, and the effective variable target thickness of TTIK measurements was discussed for the first time.

The excitation spectra of the ^{4}He(^{14}N,α) and ^{4}He(^{14}N,d)^{16}O reactions were extracted from the ^{18}F experiment, and a combination of these measurements and previous measurements of similar reaction channels were used to constrain a full $\boldsymbol{R}$-matrix fit, between E_x = 5.5 and 9 MeV. From this fit, the energy levels in ^{18}F were extracted and compared with previous work. In addition to suggesting new spin assignments for some previously measured states, this analysis identified 10 new states in ^{18}F.

Alpha-clustering in ^{18}F was analysed by comparing the results from this work with the predictions of a semi-microscopic α-^{14}N model by Buck *et al.* [105], which constructed the ^{14}N wavefunction by coupling an ^{16}O core to a proton and neutron hole. While the measurements made in this thesis were mostly consistent with the predictions of the model, one predicted state, the 3^+ state in the $K = 0$ rotational band, was identified at a significantly higher energy than predicted. This suggests that the structure of ^{18}F is still not thoroughly understood, and more theoretical calculations are required before deeper conclusions can be made in this direction.

The ^{4}He(^{40}Ca,α), ^{4}He(^{44}Ca,α) and ^{4}He(^{48}Ca,α) excitation spectra were extracted from the titanium experiment. These spectra were analysed using the newly developed Spectral Signature analysis, which exploited the likely fragmented nature of α-clustered states in this energy region of these nuclei to automatically identify them. This was implemented using the CWT and machine learning methods to compare the results of a statistical model of fragmented α-clustering with the measured spectra.

The Spectral Signature analysis indicated a large likelihood of the existence of fragmented α-clustered

states in both ^{44}Ti and ^{52}Ti, while the results for ^{48}Ti were inconclusive. While this is not a new result for ^{44}Ti, the existence of α-clustered states has not been observed previously in ^{52}Ti. One possible interpretation of the variation of the decreased clustering likelihood in ^{48}Ti is that the α-cluster structure may be more dominant in the presence of a doubly-magic core, however more work is required to substantiate this claim.

This analysis extracted the excitation energies of 9 fragmented α-clustered states in ^{44}Ti, which are in good agreement with previous measurements and models. It extracted none in ^{48}Ti and 3 in ^{52}Ti, however there exists no previous measurements with which these results can be compared.

6.2 The Spectral Signature Analysis

The spectral signature analysis appears to be a very powerful analytical technique for identifying fragmented α-clustered states. It actually exploits the high level density of the system and the fragmented nature of the states in order to identify them, which are both properties which effectively preclude a full $\boldsymbol{R}$-matrix analysis. Furthermore, it allows such states to be identified without having to rely on experimentally challenging angular distribution measurements. This is especially beneficial when analysing TTIK measurements.

Machine learning is a particularly powerful technique here, allowing the quantitative comparison of the simulated fragmented α-clustered states with the experimental work, producing results that are both more reliable and easier to compare. It may be possible to further develop and refine this technique, and some of the ways this may be done are discussed here.

In this work the machine learning analysis is applied not to the entire CWT, but instead only to the characteristic scales observed in P_Ψ. This was based on an initial analysis which suggested that the characteristic scales contained the majority of the signature of α-clustering, and so using only these as parameters would significantly reduce the parameter space while still producing a high quality classifier. This assertion seems to have been vindicated, however it may be possible by either introducing additional parameters to this parameter set or choosing an entirely new parameter set to improve the classifier. As has been discussed, an important part of the signature of fragmented α-clustering is the existence of hot-spots in W_Ψ. It is therefore natural to assume that, if appropriately parametrised, W_Ψ may provide an improved set of new parameters. The inclusion of W_Ψ in the parameter space may also allow the machine learning algorithm to identify the excitation energies of α-clustered states, in much the same way as was done in this work using the F_Ψ analysis, but in a more quantitative and rigorous way. It may be possible to use Principle Component Analysis (PCA) [148], or a similar technique, to automatically choose a good parameter set from the raw W_Ψ and P_Ψ spectra. This would also lead to

a deeper understanding of how the signature manifests.

While the RF is a very powerful classification algorithm, there is a plethora of different machine learning algorithms which could be tested. It is possible that a different classifier may be more applicable to the present problem, and hence would provide more reliable results. A range of different classification algorithms are discussed in Ref. [156].

It would also be of interest to vary the parameters used for the statistical model outside the ranges stated in Section 5.4.3, and observe how the signature changes and if under any conditions it disappears. This would allow conclusions to be drawn about how generally applicable this technique is. It also may be possible to use the machine learning algorithm to predict the value of certain parameters from the experimental data, for example one would expect to be able to infer a possible value of $\left\langle D^{(\mathrm{I})}_{J^\pi} \right\rangle$ from the δE of the first characteristic scale.

Furthermore, rather than using the statistical distributions derived from random matrix theory to simulate the set of class-I states, random matrix theory could be used directly. This would produce a set of states which necessarily follow the correct distributions, but also contain any higher order correlations between parameters which are ignored in the present model. If one were to go further, using more sophisticated nuclear models with which to compare the results of the CWT may yield more robust results, as is done in Refs. [132, 133] where the results of the CWT are compared with the Interacting Boson Model.

Finally it is important that this analytical technique is tested on other experimental data. An excellent testing ground for this technique would be the ^{32}S, ^{34}S, ^{36}Ar and ^{40}Ca spectra measured by Lonnroth *et al.* [68] and Goldberg *et al.* [69] and Norrby *et al.* [66, 67]. It was concluded, based on a Simplfiied R-Matrix analysis, that each of these nuclei present fragmented α-clustered states, and it would be interesting to observe whether a spectral signature analysis produces the same results.

6.3 Future Work

Alpha-clustering in ^{18}F still requires much theoretical work before it can be fully understood. The behaviour of the proton and neutron holes, and their interaction with the cluster structure, is still an open question. It is clear that a significant amount of resonant structure exists in ^{18}F up to at least 16 MeV, which has yet to be fully analysed. Further detailed measurements of ^{18}F using resonant scattering at a variety of angles and via a range of entrance and exit channels may provide the necessary constraints required to extend the $\boldsymbol{R}$-matrix analysis to these energies, allowing the extraction of structural information pertaining to ^{18}F in this region.

The Spectral Signature analysis that was performed on ^{44,48,52}Ti in this thesis ought to be applicable

to all nuclei in that mass region. The application of this to ^{45,46,47,49,50,51}Ti, (or the application of a refined version of this method), ought to provide a much clearer understanding of the development of α-clustering in this mass region.

In addition to the future work pertaining to the Spectral Signature analysis, discussed in the previous section, it is my opinion that there is much to be gained by the application of other image processing techniques to the analysis of resonant scattering spectra, especially those spectra obtained from TTIK measurements. For example, it is possible that deconvolution techniques may be applied to resonant spectra to reduce the effect of the experimental resolution on the data, allowing the spectra to be fitted without the incorporation of computationally expensive convolutions. By combining machine learning techniques with $\boldsymbol{R}$-matrix theory, it may be possible to automatically identify resonance energies, widths and spins in resonant scattering spectra, which can then be used as initial parameters for a full $\boldsymbol{R}$-matrix analysis. This would reduce the currently significant degree of human input required in $\boldsymbol{R}$-matrix fits, making them a more reasonable option for the analysis of complex spectra. Developments such as these, combined with the availability of exponentially increasing modern computational power, may shed light on nuclear phenomena which have previously been out of reach of experimental ventures.

Appendices

Appendix A

Coulomb Wavefunctions and the R-matrix

Throughout this section the book Nuclear Reactions for Astrophysics by Thompson and Nunes [63] is referenced extensively.

The $\boldsymbol{R}$-Matrix parameters are defined in terms of the regular and irregular coulomb wavefunctions $F_L(\eta,\rho)$ and $G_L(\eta,\rho)$, which are the solutions to the 3-dimensional Schrödinger equation for two particles interacting via the point coulomb potential, given in Equation (3.30). Here L defines the relative orbital angular momentum of the system, and η and ρ are defined in Equations (3.31) and (3.32). The coulomb wavefunctions are plotted as a function of E for the ^{14}N + α system in Figure A.1, for a range of values of L.

In $\boldsymbol{R}$-matrix theory the coulomb wavefunctions are used to define the penetrability, P_μ, shift function, S^0_μ, and hard sphere phase shift Ω_μ by matching them to the internal wavefunction at R_μ. This means that the coulomb wavefunctions are always evaluated at $\rho \to \rho_\mu = k_\mu R_\mu$. The parameters P_μ, S^0_μ and Ω_μ are defined as

$$P_\mu = \frac{\rho_\mu}{F^2_{L_\mu} + G^2_{L_\mu}} \tag{A.1}$$

$$S^0_\mu = \rho_\mu \frac{\frac{\partial F_{L_\mu}}{\partial \rho} F_{L_\mu} + \frac{\partial G_{L_\mu}}{\partial \rho} G_{L_\mu}}{F^2_{L_\mu} + G^2_{L_\mu}} - \beta R_\mu \tag{A.2}$$

$$\Omega_\mu = \exp\left(-i \frac{F_{L_\mu}}{G_{L_\mu}}\right) \tag{A.3}$$

where β is the boundary condition, discussed in Section 3.2.2.6. Of these parameters, P_μ has the clearest physical interpretation. Based on its relationship with the partial and reduced widths, given

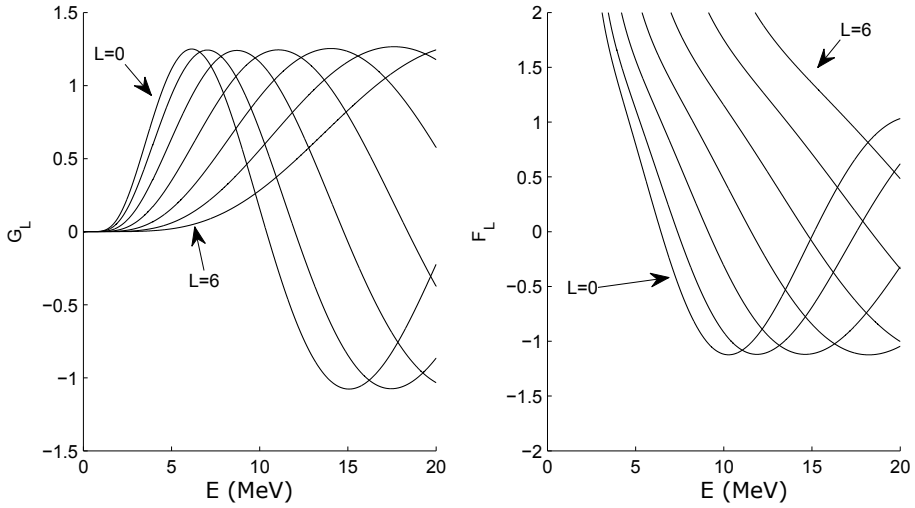

Figure A.1: Coulomb wavefunctions for the ^{14}N + α system, with $\rho = \rho_\mu$.

in Equation (3.45), it is interpreted as the likelihood of the particle pair in the channel μ tunnelling through the combined coulomb and centrifugal barriers. The energy dependence of this factor is shown in Figure A.2 for the ^{14}N + α system.

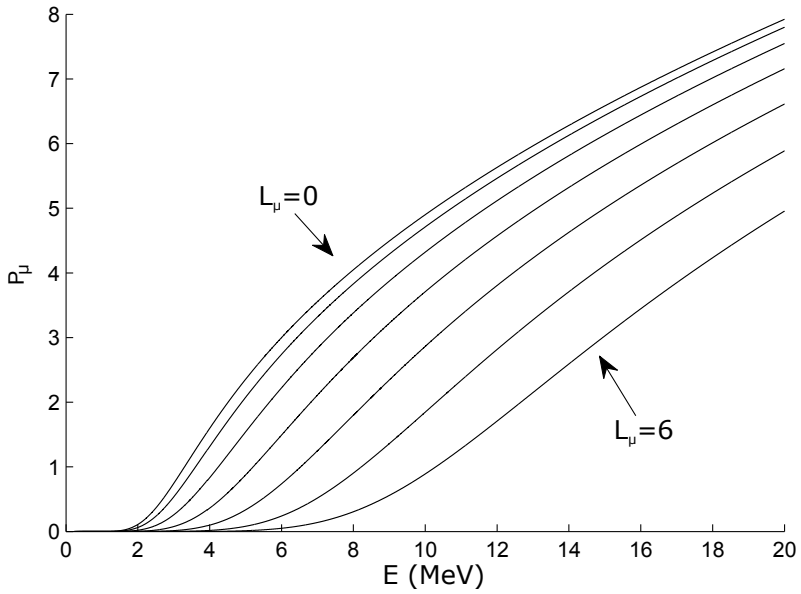

Figure A.2: Penetrabilities P_μ for the ^{14}N + α system.

Appendix B

Cyclotrons

A cyclotron is a type of particle accelerator, shown schematically in Figure B.1, which is used to produce accelerated ion beams in both of the experiments in this thesis. They are constructed of one or more 'D' shaped cavities, which are connected to a Radio Frequency (RF) power supply, and are therefore charged, generating a time varying electric field, $\vec{E}$. The D's are sandwiched by magnets, which produce a constant magnetic field, $\vec{B}$, across the D's. The ions which are to be accelerated are injected at the center of the cyclotron, and the $\vec{B}$-field causes them to move in a circular orbit. As the ions pass between the D's, they are accelerated by the $\vec{E}$-field. The frequency at which the $\vec{E}$-field varies is chosen such that the ions are accelerated as they pass through each gap, and so an overall net acceleration is generated.

As the ions are accelerated the radius of curvature of their path through the $\vec{B}$ increases, and eventually they will reach the extraction radius R_0, at which they enter the beam line at a specific energy E_0. It should be noted that the radius of curvature and the velocities of the ions vary in such a way so as to maintain a constant period of rotation, and so a constant frequency of the $\vec{E}$-field will continu-

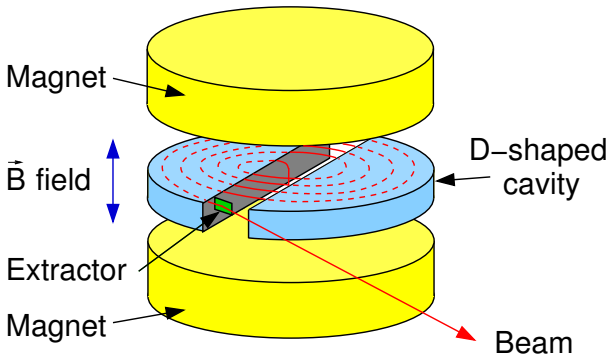

Figure B.1: A schematic diagram of a cyclotron with two D's, with the path on an ion shown in red. Figure reprinted with permission from Ref. [157].

ally accelerate the ions as they spiral out from the center of the cyclotron. The extraction radius and energy can be calculated by equating the centripetal and magnetic forces. This gives the dependence of the ion velocity, v, on the radius of extraction and the $\vec{B}$-field

$$\frac{mv^2}{R_0} = |\vec{B}|qv \tag{B.1}$$

$$v = \frac{|\vec{B}|qR_0}{m} \tag{B.2}$$

where q is the charge of the ion. From v the kinetic energy of the ion upon extraction, E_0, is evaluated as:

$$E_0 = \frac{|\vec{B}|^2 q^2 R_0^2}{2m} \tag{B.3}$$

This equation is entirely non-relativistic, and so at high energies relativistic effects must be accounted for. At relativistic energies the mass of the particle is no longer constant, which means that using a constant frequency $\vec{E}$-field to accelerate the ions becomes inefficient as the ions move out of phase with the $\vec{E}$-field at high energies. This may be corrected for by using a spatially varying $\vec{B}$-field, and there are a range of engineering solutions which accomplish this, leading to a diverse range of cyclotron designs, known as Azimuthally Varying Field (AVF) Cyclotrons.

B.1 The Birmingham MC40 Cyclotron

The cyclotron used for the ^{18}F experiment is the MC40 cyclotron at the University of Birmingham. The definition of MC40 means that the maximum energy it can accelerate protons to is 40 MeV. This can be used as a calibration to calculate the maximum energies that can be produced for the various charge states of ^{14}N

$$E_{\mathrm{N}} = E_\alpha \frac{q_{\mathrm{N}}^2}{q_p^2} \frac{m_p}{m_{\mathrm{N}}}$$

and these are given in Table B.1.

Table B.1: Maxmimum beam energies for each charge state in ^{14}N.

^{14}N Charge State	Maximum Beam Energy (MeV)
1+	2.85
2+	11.43
3+	25.71
4+	45.71
5+	71.43
6+	102.86
7+ (Fully Ionised)	140

Table B.2: The range of energies ($E_{\text{min}} - E_{\text{max}}$) that may be produced for each of the beams produced by the GANIL facility for the Ti experiment. The actual energy used is given by E.

Ion	Charge State	E_{min} (MeV)	E_{max} (MeV)	E (MeV)
^{40}Ca	7+	80.92	480.12	179.83
^{44}Ca	8+	96.08	570.09	206.59
^{48}Ca	9+	111.47	661.39	234.01

In the present experiment two beam energies were used: one at approximately 46 MeV and the other at 62 MeV [114]. It can be seen from Table B.1 that the first of these must correspond to the maximum energy of the 4+ charge state, whereas the second probably corresponds to the 5+ charge state at a slightly reduced extraction energy. This reduction may be produced by altering the extraction radius or the $\vec{B}$-field.

B.2 The GANIL Facility

The Titainum experimental work was performed at the GANIL facility in Caen, France. The CSS1 cyclotron was used in this experiment, full details of which can be found in Ref. [131]. This cyclotron has a 3 m extraction radius, and its $\vec{B}$-field ranges between 0.39 and 0.95 T. From these properties, Equation (B.3) can be used to calculate the range of energies that the beams used in this thesis may be accelerated to. These are shown in Table B.2.

Following extraction from the CSS1 cyclotron, but prior to entering the experimental chamber, the accelerated beams pass through a series of bending magnets. These magnets act to select the required beam energy from the cyclotron, as the magnetic field on these bending magnets must be set depending on the ion and energy required. This ensures that the specified beam energy is indeed being delivered to the reaction chamber, allowing an accurate determination of the beam energy.

Appendix C

Pile-up Probabilities

In this appendix the probability of producing a pile up event where two events occur simultaneously in the same strip, $P_{2,\text{strip}}$, is compared with the probability of a pile up event occurring where both events occur simultaneously in the same pixel, $P_{2,\text{pix}}$. Figure C.1 is used to aid the discussion. Here the fraction of all pile-up events that occur in the same pixel, given by $P_{2,\text{pix}}/P_{2,\text{strip}}$, which are therefore not caught by the data clean-up used in the experimental work in this thesis is calculated.

Given a probability of an event being measured per unit time and per unit area, P_0, the probability of it being measured within a given pixel of area, A_{pix} is given by

$$P_{1,\text{pix}} = P_0 A_{\text{pix}} \Delta t \,. \tag{C.1}$$

Where Δt is the time resolution of the detector. From this the probability for pile-up in the same pixel can be calculated as

$$P_{2,\text{pix}} = P_{1,\text{pix}}^2 = P_0^2 A_{\text{pix}}^2 \Delta t^2 \,. \tag{C.2}$$

By comparison, the area on the detector which would produce a pile-up event in the same strip, A_{strips}, is shown by the blue shaded region in Figure C.1, and is related to the area of a single pixel by

$$A_{\text{strips}} = (2N_{\text{strips}} - 1)A_{\text{pix}} \,. \tag{C.3}$$

Where N_{strips} is the number of strips on a single face of the detector, in this case 16. Therefore it is possible to calculate the probability of a pile-up event in the same strip, given as

$$P_{2,\text{strip}} = P_0^2 A_{\text{pix}} A_{\text{strips}} \Delta t^2 \,. \tag{C.4}$$

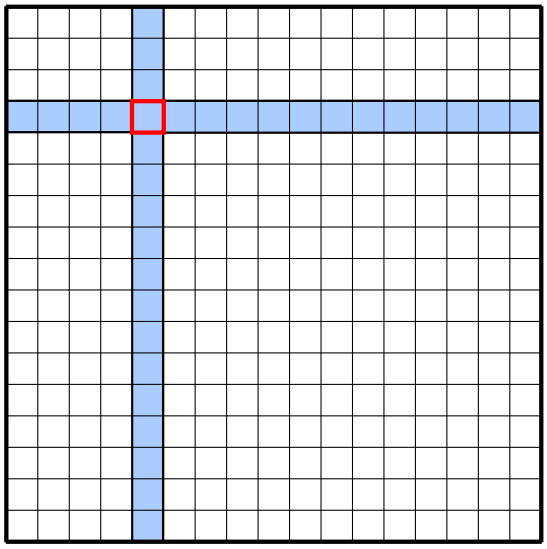

Figure C.1: A schematic diagram of a typical 16 strip DSSD. Shown here are the areas associated with a given pixel (red box), and the corresponding area inside which a second event must occur in order to produce a pile-up event (blue shading).

Combining Equations (C.2), (C.3) and (C.4) allows one to calculate the fraction of all pile-up events which occur in the same pixel;

$$\frac{P_{2,\mathrm{pix}}}{P_{2,\mathrm{strip}}} = \frac{1}{2N_{\mathrm{strips}} - 1} \tag{C.5}$$

For 16-strip detectors, this fraction is calculated to be approximately 3%.

Appendix D

^{18}F R-matrix Parameters

A full list of the $\boldsymbol{R}$-matrix parameters used in the ^{18}F fit are given in Table D.1. In the main fit, discussed in Section 4.4, the channel radii are calculated using Equation (3.26) with $r_0 = 1.35$. In addition to this, the fit was calculated using $r_0 = 1.45$. The differences in the physical parameters, E_x and Γ_μ, are defined as

$$\Delta\Gamma_\mu = \Gamma_\mu[r_0 = 1.35] - \Gamma_\mu[r_0 = 1.45] \tag{D.1}$$

$$\Delta E_x = E_x[r_0 = 1.35] - E_x[r_0 = 1.45]\,. \tag{D.2}$$

These values are given in brackets in Table D.1.

In an ideal fit, the values of $\Delta\Gamma_\mu$ and ΔE_x ought to be zero for all parameters, since the channel radii do not correspond to physical quantities, and so should not affect the physical parameters. In reality a robust analysis is indicated in the case that $\Delta\Gamma_\mu$ and ΔE_x are consistent with the errors on the parameters, σ_{Γ_μ} and σ_{E_x}. This consistency is demonstrated for the present work by analysing the distribution of $\Delta\Gamma_\mu/\sigma_{\Gamma_\mu}$ and $\Delta E_x/\sigma_{E_x}$, which for a robust fit ought to be normally distributed about 0 with a standard deviation less than 1. This is shown to be the case in Figure D.1, indicating a robust analysis.

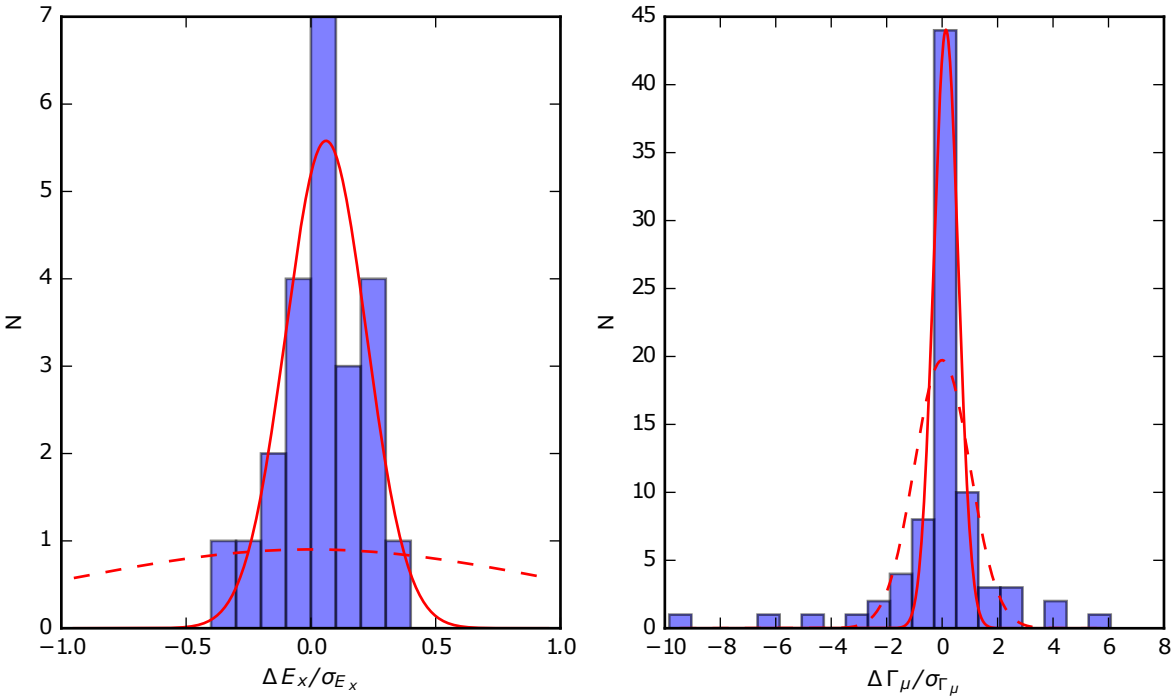

Figure D.1: Histograms (blue) of the channel radius variations of E_x (left) and Γ_μ (right), scaled by the errors on the parameters, with a Gaussian fit (red line). Fitted values for E_x: centroid = 0.06, standard deviation = 0.16 and for Γ_μ: centroid = 0.14, standard deviation = 0.45. 'Maximal' Gaussian distributions, corresponding to centroid = 0 and standard deviation = 1, are shown for comparison (red dashed line).

Table D.1: The parameters used in the fit. Here l denotes the orbital angular momentum, and s the channel spin. The numbers in brackets indicate the difference between these parameters, produced using $r_0 = 1.35$, and those produced when using $r_0 = 1.45$, as discussed in the text. The values for E_x and Γ_μ are rounded to the nearest keV, and the channels are only shown if the corresponding $\Gamma_\mu >$ 1 keV. The systematic error on E_x is $\pm$10 keV.

Levels		Decay Channels				
J^π	E_x (MeV)	Particle Pair	l	s	Γ_μ (keV)	γ_μ (MeV$^{1/2}$)
0^-	8.917 (0)	^{14}N + α_0	1	1	30 $\pm$ 4 (0)	+0.089 $\pm$ 0.006
		^{16}O + d_0	1	1	3 $\pm$ 1 (1)	+0.088 $\pm$ 0.008
		^{17}O + p_0	3	3	2 $\pm$ 4 (1)	-0.16 $\pm$ 0.15
		^{17}O + p_1	1	1	8 (1)	-0.094
1^-	6.654 (0)	^{14}N + α_0	1	1	39 $\pm$ 3 (2)	+0.39 $\pm$ 0.01
		^{17}O + p_0	1	2	21 $\pm$ 2 (0)	-0.53 $\pm$ 0.03
1^-	7.595 (0.14)	^{14}N + α_0	1	1	5 $\pm$ 1 (5)	+0.059 $\pm$ 0.007
		^{17}O + p_0	1	2	39 $\pm$ 11 (10)	+0.25 $\pm$ 0.04
		^{17}O + p_0	3	2	1 $\pm$ 6 (-25)	+0.4 $\pm$ 0.9
1^+	7.26 (0)	^{14}N + α_0	0	1	1 $\pm$ 1 (1)	-0.034 $\pm$ 0.009
		^{14}N + α_0	2	1	51 $\pm$ 6 (34)	-0.34 $\pm$ 0.02
		^{17}O + p_0	2	2	3 $\pm$ 1 (-11)	-0.24 $\pm$ 0.04
		^{17}O + p_1	0	1	5 (-27)	+0.212
1^+	7.947 (0.01)	^{14}N + α_0	0	1	1 $\pm$ 1 (-9)	-0.015 $\pm$ 0.016
		^{14}N + α_0	2	1	48 $\pm$ 6 (-21)	-0.19 $\pm$ 0.01
		^{17}O + p_0	2	2	12 $\pm$ 7 (10)	+0.25 $\pm$ 0.07
		^{17}O + p_0	2	3	10 $\pm$ 6 (-14)	-0.22 $\pm$ 0.07
1^+	8.326 (0)	^{14}N + α_0	0	1	421 $\pm$ 112 (3)	-0.46 $\pm$ 0.06
		^{14}N + α_0	2	1	12 $\pm$ 5 (-6)	+0.10 $\pm$ 0.02
		^{16}O + d_0	0	1	3 $\pm$ 1 (0)	+0.25 $\pm$ 0.05
		^{16}O + d_0	2	1	1 $\pm$ 0 (0)	+0.65 $\pm$ 0.1
		^{17}O + p_0	2	2	4 $\pm$ 3 (-4)	-0.14 $\pm$ 0.05

Continued on next page

Table D.1 – continued from previous page

Levels		Decay Channels				
J^π	E_x (MeV)	Particle Pair	l	s	Γ_μ (keV)	γ_μ (MeV$^{1/2}$)
		^{17}O + p_0	2	3	9 ± 2 (3)	-0.22 ± 0.02
		^{17}O + p_0	4	3	3 ± 3 (1)	-1.4 ± 0.9
		^{17}O + p_1	0	1	1 (0)	+0.039
1^+	8.678 (0)	^{14}N + α_0	0	1	92 ± 16 (5)	-0.18 ± 0.02
		^{14}N + α_0	2	1	44 ± 7 (0)	+0.19 ± 0.01
		^{16}O + d_0	0	1	8 ± 2 (0)	+0.16 ± 0.02
		^{17}O + p_0	2	2	1 ± 2 (-1)	+0.04 ± 0.08
		^{17}O + p_0	4	3	6 ± 4 (-1)	-1.4 ± 0.4
		^{17}O + p_1	0	1	69 (-2)	+0.255
1^+	8.801 (0)	^{14}N + α_0	0	1	162 ± 13 (1)	-0.201 ± 0.008
		^{14}N + α_0	2	1	90 ± 4 (0)	+0.189 ± 0.004
		^{16}O + d_0	0	1	6 ± 1 (1)	-0.106 ± 0.004
		^{17}O + p_0	2	2	9 ± 5 (2)	-0.14 ± 0.04
		^{17}O + p_0	2	3	3 ± 1 (0)	+0.08 ± 0.02
		^{17}O + p_1	0	1	12 (1)	-0.089
1^+	8.996 (0)	^{14}N + α_0	0	1	427 ± 114 (26)	+0.35 ± 0.05
		^{16}O + d_0	0	1	6 ± 2 (0)	-0.10 ± 0.01
		^{16}O + d_0	2	1	7 ± 2 (0)	+0.30 ± 0.04
		^{17}O + p_0	2	3	5 ± 4 (-2)	-0.11 ± 0.04
		^{17}O + p_0	4	3	7 ± 9 (-2)	-1.2 ± 0.8
		^{17}O + p_1	0	1	1 (0)	-0.032
2^-	6.832 (0)	^{14}N + α_0	1	1	98 ± 3 (0)	+0.553 ± 0.009
		^{14}N + α_0	3	1	10 ± 1 (-2)	+0.56 ± 0.03
		^{17}O + p_0	1	3	9 ± 2 (-1)	+0.30 ± 0.03
2^-	7.515 (0)	^{14}N + α_0	1	1	20 ± 3 (4)	-0.124 ± 0.009

Continued on next page

Table D.1 – continued from previous page

Levels		Decay Channels				
J^π	E_x (MeV)	Particle Pair	l	s	Γ_μ (keV)	γ_μ (MeV$^{1/2}$)
		^{14}N + α_0	3	1	33 ± 2 (2)	+0.37 ± 0.01
		^{17}O + p_0	1	2	5 ± 2 (5)	+0.10 ± 0.02
		^{17}O + p_0	1	3	3 ± 2 (-3)	-0.08 ± 0.02
2^-	8.212 (0)	^{14}N + α_0	1	1	11 ± 2 (7)	+0.096 ± 0.008
		^{14}N + α_0	3	1	79 ± 8 (7)	+0.47 ± 0.02
		^{16}O + d_0	1	1	3 ± 0 (0)	-0.67 ± 0.05
		^{17}O + p_0	1	2	18 ± 6 (1)	+0.19 ± 0.03
		^{17}O + p_0	3	2	15 ± 6 (3)	+1.0 ± 0.2
		^{17}O + p_0	1	3	2 ± 2 (1)	+0.06 ± 0.02
		^{17}O + p_0	3	3	21 ± 8 (-1)	+1.2 ± 0.2
		^{17}O + p_1	1	1	24 (-3)	-0.334
2^-	8.505 (0.01)	^{14}N + α_0	3	1	267 ± 39 (-34)	+0.71 ± 0.05
		^{16}O + d_0	1	1	10 ± 1 (0)	+0.47 ± 0.04
		^{17}O + p_0	1	2	78 ± 8 (-2)	-0.35 ± 0.02
		^{17}O + p_0	3	2	20 ± 12 (12)	+0.9 ± 0.3
		^{17}O + p_0	1	3	31 ± 5 (12)	+0.22 ± 0.02
		^{17}O + p_0	3	3	21 ± 8 (0)	-0.9 ± 0.2
		^{17}O + p_1	1	1	15 (8)	-0.214
2^-	8.667 (0)	^{14}N + α_0	1	1	0.5 ± 0.3 (-0.6)	+0.016 ± 0.005
		^{14}N + α_0	3	1	0.4 ± 0.5 (0)	+0.03 ± 0.01
		^{16}O + d_0	1	1	4 ± 6 (0)	+0.2 ± 0.1
		^{16}O + d_0	3	1	3 ± 4 (0)	+1.4 ± 0.9
		^{17}O + p_0	1	2	7 ± 11 (0)	-0.10 ± 0.07
		^{17}O + p_0	1	3	1 ± 4 (0)	+0.03 ± 0.09
		^{17}O + p_1	1	1	9 (0)	+0.143
3^-	7.208 (0)	^{14}N + α_0	3	1	0.6 ± 0.3 (0)	+0.07 ± 0.01

Continued on next page

Table D.1 – continued from previous page

Levels		Decay Channels				
J^π	E_x (MeV)	Particle Pair	l	s	Γ_μ (keV)	γ_μ (MeV$^{1/2}$)
3^-	7.306 (0)	^{14}N + α_0	3	1	42 ± 3 (1)	+0.77 ± 0.03
		^{17}O + p_0	1	2	15 ± 1 (-1)	+0.29 ± 0.01
		^{17}O + p_0	3	2	2 ± 1 (-1)	-0.9 ± 0.3
		^{17}O + p_0	1	3	4 ± 1 (1)	-0.16 ± 0.02
3^-	7.553 (0)	^{14}N + α_0	3	1	62 ± 2 (4)	+0.83 ± 0.01
		^{17}O + p_0	1	3	11 ± 1 (2)	-0.24 ± 0.01
		^{17}O + p_0	3	3	1 ± 0 (-5)	-0.4 ± 0.2
		^{17}O + p_1	3	0	1 (1)	+2.858
3^-	7.895 (0)	^{14}N + α_0	3	1	26 ± 2 (-2)	+0.247 ± 0.009
		^{17}O + p_0	1	2	9 ± 3 (1)	+0.11 ± 0.02
		^{17}O + p_0	3	2	9 ± 4 (0)	-0.8 ± 0.2
		^{17}O + p_0	3	3	1 ± 1 (-2)	-0.2 ± 0.1
3^-	8.951 (0)	^{14}N + α_0	3	1	1 ± 1 (0)	+0.028 ± 0.009
		^{17}O + p_0	3	2	7 ± 18 (-2)	-0.3 ± 0.3
		^{17}O + p_0	3	3	4 ± 10 (3)	+0.2 ± 0.3
3^+	7.711 (0)	^{14}N + α_0	2	1	56 ± 10 (-4)	+0.31 ± 0.03
		^{17}O + p_0	2	2	4 ± 2 (1)	-0.21 ± 0.06
		^{17}O + p_0	0	3	33 ± 7 (7)	+0.20 ± 0.02
		^{17}O + p_0	2	3	1 ± 2 (-1)	+0.09 ± 0.1
		^{17}O + p_0	4	3	1 ± 1 (1)	-1.4 ± 0.7
		^{17}O + p_1	2	1	11 (-1)	+0.986
3^+	8.363 (0)	^{14}N + α_0	4	1	4 ± 1 (0)	-0.13 ± 0.02
		^{17}O + p_0	2	2	1 ± 2 (-1)	+0.053 ± 0.06
		^{17}O + p_0	0	3	2 ± 3 (1)	-0.037 ± 0.02

Continued on next page

Table D.1 – continued from previous page

Levels		Decay Channels				
J^π	E_x (MeV)	Particle Pair	l	s	Γ_μ (keV)	γ_μ (MeV$^{1/2}$)
		^{17}O + p_0	2	3	3 ± 3 (2)	-0.091 ± 0.06
		^{17}O + p_1	2	1	21 (-2)	-0.48
3^+	8.858 (-0.02)	^{14}N + α_0	2	1	146 ± 16 (11)	-0.28 ± 0.02
		^{14}N + α_0	4	1	161 ± 50 (7)	+0.7 ± 0.1
		^{17}O + p_0	2	2	34 ± 16 (-1)	-0.31 ± 0.07
		^{17}O + p_0	0	3	10 ± 9 (-13)	-0.08 ± 0.04
		^{17}O + p_0	2	3	51 ± 13 (-4)	-0.37 ± 0.05
		^{17}O + p_1	2	1	4 (4)	+0.161
4^+	8.108 (-0.01)	^{14}N + α_0	4	1	2 ± 1 (1)	+0.31 ± 0.08
		^{17}O + p_0	2	2	2 ± 2 (-14)	+0.3 ± 0.2
		^{17}O + p_0	4	2	2 ± 3 (0)	-4 ± 3
		^{17}O + p_0	2	3	91 ± 34 (-5)	+2.0 ± 0.4
		^{17}O + p_0	4	3	1 ± 2 (0)	-2.0 ± 5
4^+	8.26 (0)	^{14}N + α_0	4	1	66 ± 23 (-6)	+0.8 ± 0.1
		^{17}O + p_0	2	2	19 ± 6 (0)	+0.37 ± 0.06
		^{17}O + p_0	4	2	3 ± 3 (1)	-1.9 ± 0.8
		^{17}O + p_0	2	3	9 ± 4 (0)	+0.25 ± 0.06
		^{17}O + p_0	4	3	1 ± 1 (0)	-0.8 ± 1.0

Appendix E

The Poisson and Wigner Distributions

In this appendix the nearest neighbour state spacing probability density function, P, is derived. This derivation is a more detailed version of the work done in Ref. [138]. P gives the probability of finding two energy levels spaced D apart. This probability is assumed to be independent of energy E. This is depicted in Figure E.1.

P is defined in general as;

$$P(D) = \frac{\int P_1(E+D|E)P_2(E+D|E)dE}{\int dE}\,. \tag{E.1}$$

Where $P_1(a|b)$ is the probability that there is a state at a, given that there is one at b, and $P_2(a|b)$ is the probability that there are no states between a and b. It is clear based on definition of P that P_2 can be rewritten as follows;

$$P_2(E+D|E) = 1 - \int_0^D P(D')dD'\,. \tag{E.2}$$

Secondly, P_1 may be simplified under the assumption that it is independent E;

$$P_1(E+D|E) = R(D)\,. \tag{E.3}$$

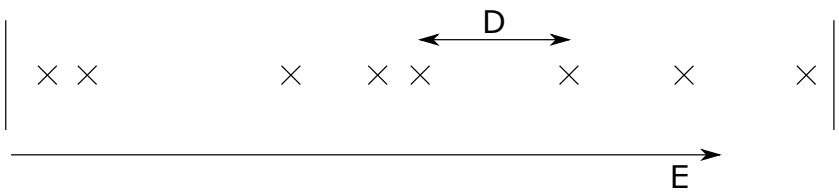

Figure E.1: A schematic diagram indicating how state spacing D and energy E are defined here. Crosses indicate energy levels.

Here $R(D)$ is known as the repulsion term, and it is the choice of this term that distinguishes between the Wigner and Poisson distributions. Substituting Equations (E.2) and (E.3) into (E.1) gives;

$$P(D) = R(D)\left(1 - \int_0^D P(D')dD'\right)\frac{\int dE}{\int dE} \tag{E.4}$$

$$= R(D)\left(1 - \int_0^D P(D')dD'\right). \tag{E.5}$$

Rearranging Equation (E.5) and substituting $f(D) = P(D)/R(D)$ gives;

$$\int_0^D R(D')f(D')dD' = 1 - f(D). \tag{E.6}$$

Then, using Leibniz Integral Rule, this can be formulated as the following first order differential equation;

$$\frac{df}{dD} = -R(D)f(D). \tag{E.7}$$

Finally, solving this using separation of variables, and substituting $f(D) = P(D)/R(D)$ to remove $f(D)$, gives;

$$P(D) = NR(D)\exp\left(-\int R(D)dD\right) \tag{E.8}$$

Where N is a constant of integration. At this point the choice of $R(D)$ can be made. The Poisson distribution assumes a constant for $R(D)$, since this implies that each state has an equal chance of being placed at any E, regardless of the locations of the other states. The Wigner distribution assumes a linear for for $R(D)$, pushing the states further apart. These are defined as follows;

$$R^{\mathrm{P}}(D) = \alpha \qquad \text{(Poisson state repulsion)}$$

$$R^{\mathrm{W}}(D) = \beta D \qquad \text{(Wigner state repulsion)}$$

Introducing these into Equation (E.8), and combining where possible the constants of integration, produces the following forms for the Poisson and Wigner distributions, P^{P} and P^{W} respectively:

$$P^{\mathrm{P}}(D) = N\exp\left(-\alpha D\right) \tag{E.9}$$

$$P^{\mathrm{W}}(D) = ND\exp\left(-\beta\frac{D^2}{2}\right) \tag{E.10}$$

The constants of integration are then calculated by normalizing P and defining the mean state

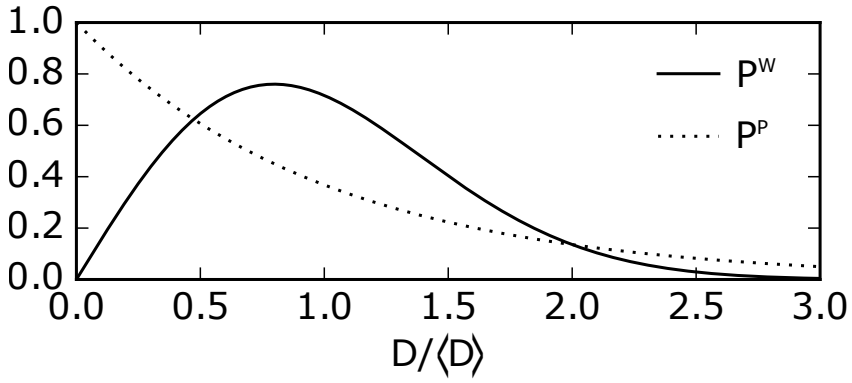

Figure E.2: The Poisson and Wigner distributions, P^{P} and P^{W} respectively.

spacing to be $\langle D \rangle$. These constraints are formalized as;

$$1 = \int_0^\infty P(D)\, dD \tag{E.11}$$

$$\langle D \rangle = \int_0^\infty DP(D)\, dD \tag{E.12}$$

These integrals were evaluated using Wolfram Alpha [158]. Finally this produces the following forms for the Wigner and Poisson distributions, plotted for comparison in Figure E.2;

$$P^{\mathrm{P}}(D) = \frac{1}{\langle D \rangle} \exp\left(-\frac{D}{\langle D \rangle}\right) \tag{E.13}$$

$$P^{\mathrm{W}}(D) = \frac{\pi D}{2\langle D \rangle^2} \exp\left(-\frac{\pi D^2}{4\langle D \rangle^2}\right). \tag{E.14}$$

The standard deviations for each distribution are calculated as follows;

$$\sigma^2 = \langle D^2 \rangle = \int_0^\infty (D - \langle D \rangle)^2 P(D)\, dD\,. \tag{E.15}$$

This integral was evaluated for both cases by using the results of the integral $\int_0^\infty x^n \exp(-ax^m)dx$, where $n = 0, 1, 2, 3$ and $m = 1, 2$, calculated using Wolfram Alpha [158]. The results are as follows;

$$\sigma_{\mathrm{P}} = \langle D \rangle \tag{E.16}$$

$$\sigma_{\mathrm{W}} = \langle D \rangle \sqrt{\frac{4}{\pi} - 1} \approx 0.5227 \langle D \rangle \tag{E.17}$$

Appendix F

Publication: Energy Levels of ^{18}F from the ^{14}N + α Resonant Reaction

PHYSICAL REVIEW C **90**, 024302 (2014)

Energy levels of ^{18}F from the ^{14}N + α resonant reaction

S. Bailey, M. Freer, Tz. Kokalova, S. Cruz, H. Floyd, and D. J. Parker
University of Birmingham, Birmingham, United Kingdom

(Received 30 April 2014; revised manuscript received 26 June 2014; published 5 August 2014)

Measurements were made of the differential cross section of the resonant reactions ^{4}He(^{14}N,α) and, ^{4}He(^{14}N,d)^{16}O with the intention of investigating the compound nucleus ^{18}F. These measurements were performed in inverse kinematics at a center-of-mass scattering angle of $\theta_{\text{c.m.}} = 180^\circ$ by using a thick ^{4}He gas target and a ^{14}N beam. Data were recorded which covered ^{18}F excitation energies from 5.5–16 MeV. An R-matrix analysis was performed on the data up to 9 MeV, and the energies, spins, parities, and partial widths were extracted. Nine new states have been identified in ^{18}F based on this analysis between 8.326 and 8.915 MeV.

DOI: 10.1103/PhysRevC.90.024302 PACS number(s): 21.10.−k, 24.30.−v, 21.60.Gx, 27.20.+n

I. INTRODUCTION

The idea that nucleons may cluster together to form substructures within nuclei is a well established principle in the case of many light α-conjugate nuclei. This idea has been extended to neutron-rich nuclei, where the extra neutrons are shared between the clusters, acting like valence neutrons to increase the binding energy [1,2]. There has been comparatively little work done, however, investigating the role of clustering in nuclei which deviate from α-conjugate nuclei in ways other than by the addition of neutrons.

^{18}F is interesting from a clustering perspective because of the comparisons that can be made with ^{20}Ne. The $\alpha + {}^{16}$O cluster-core structure has been found to be very prominent in ^{20}Ne [3], and it has been hypothesized that the similar $\alpha + {}^{14}$N structure may be observed in ^{18}F [4]. This structure can be described by $4p$-$2h$ excitations, with an additional proton and neutron being promoted to the s-d shell from the p shell, leaving two protons and two neutrons in the s-d shell, and one proton hole and one neutron hole in the p shell [5]. This leads to the idea that the structure could be thought of as an α cluster and an ^{16}O core, as has been observed in ^{20}Ne, with the addition of one proton and one neutron hole. It is the interplay between these proton and neutron holes and the cluster-core structure that provides the motivation for investigating ^{18}F.

Attempts have been made to study this structure previously by using the ^{14}N(^{7}Li,t)^{18}F α-transfer reaction [5,6] in 1968 and 1977. Difficulties arise in the analysis of these measurements, however, due to the nonzero spins of the nuclei involved. In fact, in this case up to five different transferred angular momenta can contribute incoherently to a direct α-transfer reaction [6]. This makes spin assignments based on angular distributions for states measured in this way extremely difficult, and the authors were forced to adopt less rigorous methods in order to infer some possible spin-parity assignments. Despite this, a possible $K^\pi = 1^+$ rotational band was identified up to $J^\pi = 7^+$, with states ranging from 1.701 to 13.937 MeV [6].

Additionally, a semimicroscopic calculation was performed in 1979, predicting α-clustered states in ^{18}F ranging from 1.6 to 19.65 MeV [4]. The states in this work formed two distinct rotational bands, $K^\pi = 1^+$ and $K^\pi = 0^+$. While the predicted $K^\pi = 1^+$ states agreed broadly with the assignments made using the α-transfer reaction, the $K^\pi = 0^+$ states are yet to be confidently assigned to experimental measurements.

In the current work ^{18}F was investigated by measuring the resonant elastic scattering of ^{14}N ions from α particles. It was expected that this technique would preferentially populate clustered states, because such states are expected to have increased α reduced widths. Properties of the compound nucleus ^{18}F were then extracted by using R-matrix theory, constrained by both these measurements and existing experimental data.

II. EXPERIMENTAL MEASUREMENTS, DATA ANALYSIS, AND RESULTS

Measurements were made of the ^{14}N + α resonant reaction by using the thick-target inverse kinematics (TTIK) technique detailed in Ref. [7]. E-ΔE particle identification was employed, allowing measurements to be made of three reactions simultaneously: ^{4}He(^{14}N,α), ^{4}He(^{14}N,d)^{16}O, and ^{4}He(^{14}N,p)^{17}O.

A. Experimental setup

The experiment was carried out using the MC40 Cyclotron at the University of Birmingham. The cyclotron was used to produce a ^{14}N beam at ∼46 MeV and ∼62 MeV, with beam currents typically ranging from 0.5 to 0.75 nA.

There was no direct measurement of the beam energies, and since this was the first example of a ^{14}N beam produced at this facility the energies stated were based solely on theoretical calculations. These calculations were very sensitive to the radius at which the beam was extracted from the cyclotron, which lead to an uncertainty on the beam energy of 10%. This uncertainty could, however, be resolved through data analysis. The beam energy resolution was estimated to be <100 keV, which is <22 keV in the center-of-mass frame.

Upon extraction the beam passed to the reaction chamber. A schematic diagram of the reaction chamber is shown in Fig. 1. As the ^{14}N beam travels through the ^{4}He gas it loses energy in accordance with the Bethe–Bloch formula for stopping power [8]. Since the excitation energy of the ^{18}F nucleus created in any given reaction is dependent entirely on the beam energy at the reaction point, this technique allows a range of excitation energies to be investigated in one experimental run.

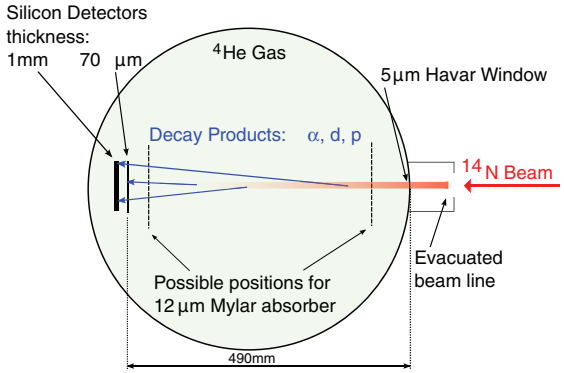

FIG. 1. (Color online) Schematic drawing of the reaction chamber.

The detectors were placed at 0° to the beam line and, since the measurements were made in inverse kinematics, this corresponded to a center-of-mass scattering angle of 180°. This is the ideal angle at which to make resonant-reaction measurements because it matches the minimum for the Rutherford cross section and the maximum for the nuclear amplitude, which produces the clearest possible resonance spectra.

It was crucial that the beam was stopped entirely before it reached the detectors at the end of the chamber in order to prevent damaging the detectors. This introduced a significant restriction on the beam energies and gas pressures that could be used, so a 12 μm mylar absorber was used in either of the positions shown in Fig. 1 to arbitrarily reduce the beam energy when necessary, providing an increased level of flexibility and control over the measured energy ranges.

The E-ΔE particle detection system made use of two double-sided silicon-strip detectors. The ΔE detector was 70 μm thick and the E detector was 1 mm thick. Both were square detectors with a side length of 50 mm.

Each of the detectors was separated into a front and back face, and then each face was further separated into 16 strips. One face consisted of horizontal strips, and the other of vertical strips. This allowed the position of a detected event to be assigned to a 3.13 × 3.13 mm pixel. This information was used to implement an efficiency correction, described in Sec. II D.

The detectors were calibrated by using the 3-α source ^{239}Pu^{241}Am^{244}Cm. For the calibration runs, the chamber was evacuated and the detectors were separated so that they each had a clear view of the source. This produced peaks in the energy spectra at three known energies 5.138, 5.457, and 5.759 MeV [9], to which a linear fit was performed individually for each detector strip. It was observed that the E detector had a 2 μm dead layer, which for a given measurement would lead to a fraction of the energy not being recorded. This was corrected for in the calibration by using LISE++ [10] to calculate the energy lost by each decay product to the dead layer, and then performing a particle-dependant calibration.

TABLE I. Spin and parity of the ground states (g.s.) and first-excited states of each decay product.

Reaction	Decay product	Energy (MeV)	J^π
^{4}He(^{14}N,α)	α	g.s.	0^+
		20.21[a]	0^+
	^{14}N	g.s.	1^+
		2.313	0^+
^{4}He(^{14}N,d)^{16}O	d	g.s.	1^+
	^{16}O	g.s.	0^+
		6.049[a]	0^+
^{4}He(^{14}N,p)^{17}O	p	g.s.	$\frac{1}{2}^+$
	^{17}O	g.s.	$\frac{5}{2}^+$
		0.871	$\frac{1}{2}^+$

[a]State too high to be populated in these measurements.

B. Inelastic contaminants

A difficulty encountered with this method is how to deal with inelastic contaminants. If, for example, a reaction decays by the $^{17}O^* + p$ channel rather than the $^{17}O + p$ channel, the decay products will be indistinguishable apart from an energy shift due to the energy lost to the residual ^{17}O nucleus. This means that measurements of the ^{4}He(^{14}N,p_0)^{17}O elastic scattering may be contaminated by the ^{4}He(^{14}N,$p_{1,2,3,\ldots}$)^{17}O inelastic reactions.

The ground and first-excited states for each of the decay products in the available channels for the $^{14}N + \alpha$ reaction are given in Table I. Both the deuteron and proton have no bound excited states, and the first-excited states of the closed-shell nuclei ^{16}O and ^{4}He are too high to be populated in these measurements. This leaves only the first-excited states of ^{14}N and ^{17}O that can be populated in this reaction, with the $^{16}O + d$ channel automatically free of inelastic contaminants.

The extent to which the inelastic contributions influenced the spectra were analyzed by identifying regions of the spectra which were guaranteed kinematically to be free of inelastic contaminants. This worked on the basis that the highest-energy events must originate from the collisions with the largest center-of-mass energy $E_{\text{c.m.}} = E_{\text{max}}$. However, if the reaction leaves a decay product in an excited state with an energy E^*, then the center-of-mass energy is reduced by E^*. This has the effect of shifting the events down in energy, leaving the region in the spectra with $E_{\text{c.m.}} > E_{\text{max}} - E^*$ free from inelastic contaminants.

This technique was implemented by altering the beam energy, absorber position, and gas pressure in order to control the maximum energy for each measurement. In total, six measurements were performed, resulting in four unambiguous energy ranges. The details of these measurements are given in Table II. Here the "Actual Beam Energies" are the energies extracted from the data analysis detailed in Sec. II D. By comparing the clean region from a given measurement to the same energy region in a different measurement, the effect of the inelastic contributions could be quantified and, if necessary, removed. An example of a raw spectrum and its inelastic-free region can be found in Fig. 2. It was observed that for the majority of the ^{4}He(^{14}N,α) reactions the inelastic contributions

TABLE II. The details of each of the measurements; all energies in MeV. The inelastic-free region refers to the ^{18}F excitation energy range for which the ^{4}He(^{14}N,α) reaction is free from inelastic contributions.

Measurement	Theoretical beam energy	Actual beam energy (*after window*)	Max. ^{18}F excitation energy	Inelastic-free region	Gas pressure (mbar)	Absorber position	Beam current (nA)
1	46	44.4 (*32.5*)	11.63	9.22–11.63	620	None	0.5
2	46	45.9 (*34.2*)	9.89	7.57–9.89	420	Window	0.5
3[a]	62	62.2 (*52.5*)	16.0	13.69–16.0	900	Detectors	0.5
4[a]	62	62.2 (*52.5*)	16.0	13.69–16.0	900	Detectors	0.25
5[b]	62	61.8 (*52.1*)	14.35	12.03–14.35	900	Window	<0.75
6[b]	62	61.8 (*52.1*)	14.35	12.03–14.35	850	Window	0.75

[a]Identical energy ranges, but with a different beam current.
[b]Identical energy ranges, but with a different gas pressure.

were orders of magnitude smaller than the elastic cross section, and so they were neglected. The only exception to this was the energy range from 10 to 11 MeV. Here it was observed that measurements three, four, five, and six all presented a greater yield than measurement one, which was guaranteed kinematically to be clean in this region. Therefore between 10 and 11 MeV only the data from measurement one were used.

However, in the case of the ^{4}He(^{14}N, p)^{17}O reaction, the inelastic contribution was significant. This was expected since the ground state of ^{17}O has a spin of $\frac{5}{2}^{+}$, while the first-excited state has a low energy of 0.871 MeV and a spin of $\frac{1}{2}^{+}$. This may introduce a preference for low-spin states in ^{18}F to decay to the first-excited state of ^{17}O since the decay products would carry away a smaller amount of angular momentum, reducing the size of the centrifugal barrier. Additionally, the proton measurements were contaminated by events which corresponded to protons being knocked out of the mylar absorber, and high-energy protons which punched through both detectors, producing an incorrect determination of the energy. These considerations led to the ^{4}He(^{14}N, p)^{17}O data not being used in the following analysis.

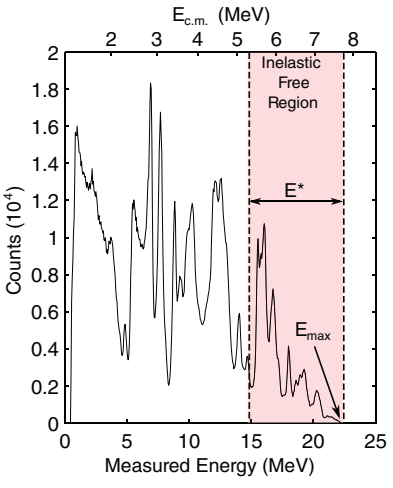

FIG. 2. (Color online) Raw Spectrum, prior to efficiency correction: Measurement 1 ^{4}He(^{14}N,α) data. The region marked is guaranteed kinematically to be free of inelastic contaminants in the α channel.

C. Data analysis and reduction

TTIK measurements are particularly advantageous from an experimental perspective since just one beam energy is required to make a measurement of a large range of excitation energies. This is in contrast with thin-target measurements which require many beam-energy steps to measure an equivalent spectrum. Additionally, the TTIK technique allows measurements to be made of 180° scattering, which is much more difficult when using a thin-target setup.

However, it is important to note that the spectra produced by TTIK measurements require a lot of preliminary analysis before they are in a useful form. This process requires some specific analytic techniques that are unique to TTIK measurements. These are detailed here.

For each event in this experimental setup, the measured quantities are the total kinetic energy of the decay product and the position of the event on the detector. Since the position resolution is limited to a 3.13-mm-square pixel, within this square the position is randomized in order to synthesize more continuous data. This is crucial to avoid any sharp discontinuities in the final spectra, which would otherwise arise due to the boundaries between the pixels.

From these properties, the excitation energy of the compound nucleus and the depth into the chamber that the reaction occurred is reconstructed. This is done by calculating the kinematics of the reaction and simulating the energy loss of the beam and the decay products through the gas by using LISE++ [10].

Since this technique relies on the energy loss of the beam through the target to measure a range of energies, the excitation energy is entirely dependant on the reaction position in the chamber. The high-energy events originate from the back of the chamber, close to the Havar window and far from the detectors, whereas the low-energy events occur close to the detectors. This leads to an energy-dependant geometrical contribution to the efficiency of the measurements, which must be corrected for.

This was done on an event-by-event basis by using both the position of the event on the detectors and the energy; the center-of-mass scattering angle was calculated. A limit

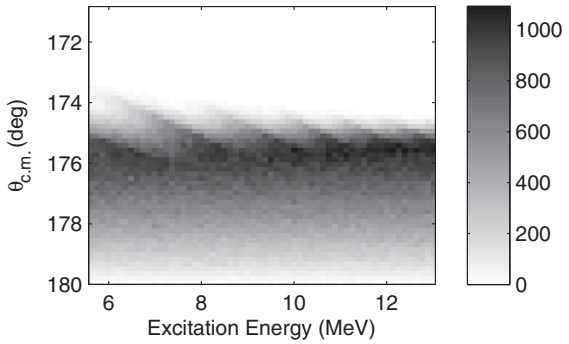

FIG. 3. A Monte Carlo simulation of the distribution of measured angles as a function of ^{18}F excitation energy, for measurement-one α particles.

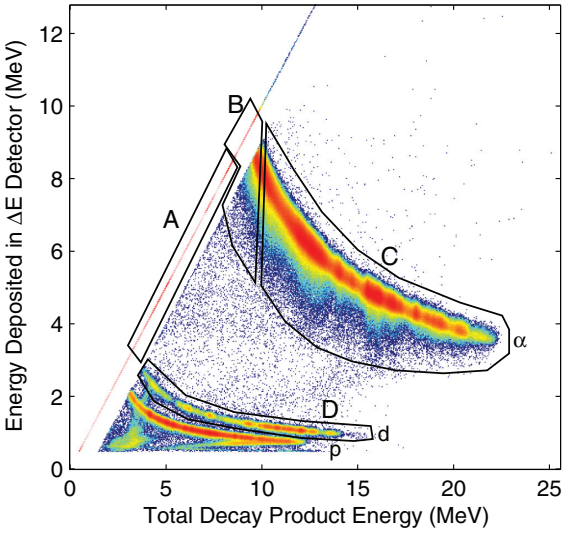

FIG. 4. (Color online) Particle-identification plot from measurement one. Windows A and C selected the ^{4}He(^{14}N,α) reaction and window D selected the ^{4}He(^{14}N,d)^{16}O reaction. Window B was discarded.

was then placed on the maximum-allowed deviation from 180° of the center-of-mass scattering angle, and events which were scattered outside of this range were discarded. In this case this range was set to be 5°, allowing measurements to be made in the range $175^\circ < \theta_{\text{c.m.}} < 180^\circ$. A Monte Carlo simulation was performed to simulate the distribution of angles that would be recorded using this technique as a function of energy. This simulation incorporated the energy loss, kinematics, and the fact that the detector was segmented into discrete pixels. The energy and angular straggling for the beam for a typical run were calculated using LISE++ [10] to be 0.07 MeV and 15 mrad in the window, 0.06 MeV and 8 mrad in the absorber, and 0.015 MeV and 20 mrad in the gas; however, these were determined to be small enough to neglect for the purposes of the simulation, since their only effect would be to smooth out some of the sharper features in the results.

An example of the resulting distribution is shown in Fig. 3. The aberrations at the 175° limit occur due to the finite pixel size on the detector. In general, these were too small to affect the measurements, with the exception of measurements three and four. In these cases the events occurred much closer to the detectors, which caused each individual pixel to subtend a larger solid angle, amplifying this effect and leading to a poor efficiency correction, especially for low-energy events. Based on this analysis, the center-of-mass angular range was determined to be $176.6^\circ \pm 1.2^\circ$, and the data from measurements three and four were discarded below 8 MeV.

D. Results

The measurements of the ^{4}He(^{14}N,α) and ^{4}He(^{14}N,d)^{16}O were extracted by windowing on the particle-identification plot, an example of which is shown in Fig. 4. The narrow diagonal line corresponds to particles which were stopped entirely by the ΔE detector. In an attempt to extend the α spectrum to lower energies, window A was used in addition to window C. This could be argued to consist purely of α particles because, if a deuteron or proton had the same total energy upon reaching the detectors, it would have made it through the ΔE detector and would have been measured in the E detector.

The E detector had a 1.5 MeV energy threshold, such that only events which were measured above this threshold were recorded. This was necessary to remove low-energy noise in the detector. This threshold manifests itself in the particle-identification plot as the gap between the thin diagonal line and the particle bands. The implications of this are that, if an α particle has sufficient energy to pass through the ΔE detector but then has less than 1.5 MeV remaining, the remaining energy will not be recorded and the particle will be moved artificially into the diagonal line. This generates a systematic error in region B, and hence it was discarded, leaving a gap in the middle of the ^{4}He(^{14}N,α) spectrum.

The excitation energy and efficiency correction were calculated by using the techniques detailed in Sec. II C. Since these techniques are very sensitive to the initial energy of the beam as it enters the chamber, and these initial beam energies were not well known, they were treated as free parameters in the analysis. They were altered to align the ^{4}He(^{14}N,α) data with the same reaction reported in Ref. [11], which made thin-target measurements by using a tandem accelerator and claimed to have an uncertainty associated with the energy below 1 keV. The beam energies produced by matching the present data to this work are reported in Table II as the "actual beam energies."

The detector resolution was calculated by measuring the widths σ of the peaks in the α calibration measurements and was found to be between 30 and 40 keV for each detector strip. From this, the resolution on the center-of-mass energy was calculated. This resolution depended on the decay products and the number of detectors used in the measurement. The

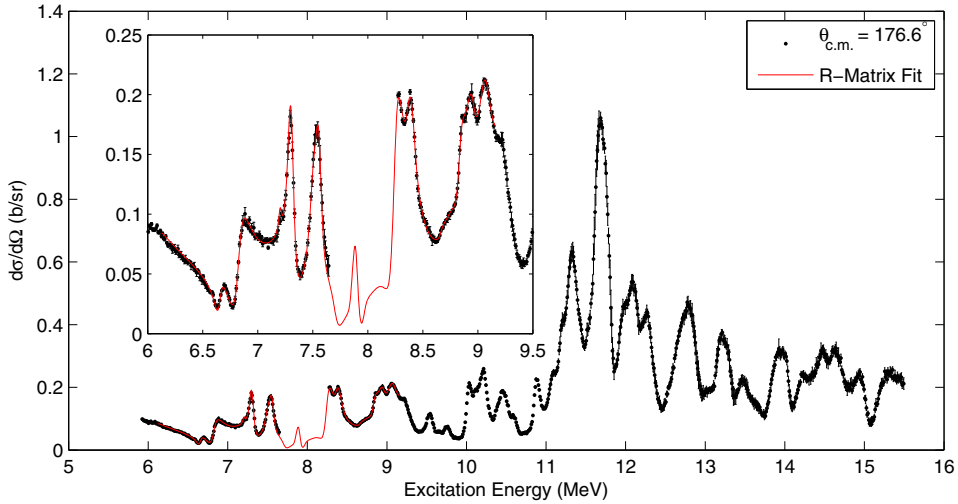

FIG. 5. (Color online) ^{4}He(^{14}N,α) cross section from the present work, plotted with the R-matrix fit convolved with the experimental resolution. Inset shows an enlarged view of the R-matrix fit; χ^2/d.o.f. = 2.6 (where "d.o.f." means "degrees of freedom").

resolution in the ^{4}He(^{14}N,α) measurement was calculated to be 11 keV for $E < 8$ MeV and 14 keV for $E > 8$ MeV. The resolution in the ^{4}He(^{14}N,d)^{16}O measurement was 15 keV.

Finally, the weighted average of the spectra from each measurement was calculated and then scaled to the Rutherford-scattering cross section at low energies in the ^{4}He(^{14}N,α) measurement, giving the final spectra shown in Figs. 5 and 6.

III. *R*-MATRIX ANALYSIS

In R-matrix theory, the differential cross section for a given reaction can be thought of as being made up of up to three components. These are the potential contribution, the resonant contribution and, in the case of elastic scattering, the Coulomb contribution. The resonant contribution is calculated from the properties of the resonant states in the compound nucleus in this case ^{18}F. The potential contribution is usually taken from hard-sphere scattering; however, in this case background poles were introduced in addition to this to self-consistently

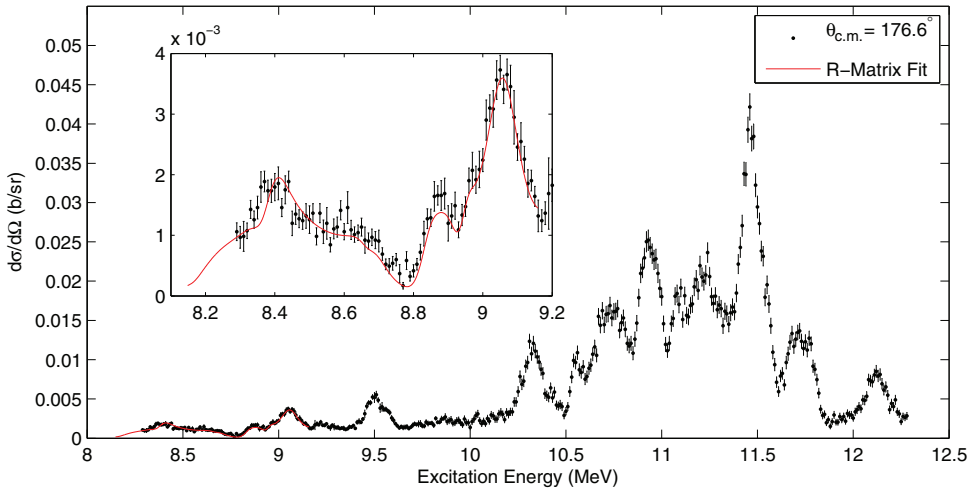

FIG. 6. (Color online) ^{4}He(^{14}N,d)^{16}O cross section from the present work, plotted with the R-matrix fit convolved with the experimental resolution. Inset shows an enlarged view of the R-matrix fit; χ^2/d.o.f. = 1.8.

TABLE III. A summary of the data sources used to constrain the R-matrix fit.

Reaction	$\theta_{\text{c.m.}}$	Energy range (MeV)	Measurement type	Reference
^{4}He(^{14}N,α)	176.6°	6–13	Thick target, inverse kinematics	Present work
^{4}He(^{14}N,d)^{16}O	176.6°	8.2–12.3	Thick target, inverse kinematics	Present work
^{14}N(α,α)^{14}N	169°	7–9.1	Thin target, normal kinematics	[11]
^{14}N(α,p)^{17}O	167°	7–9.1	Thin target, normal kinematics	[11]
^{14}N(α,p)^{17}O	141°	7–9.1	Thin target, normal kinematics	[11]
^{14}N(α,p)^{17}O	99°	7–7.9	Thin target, normal kinematics	[11]
^{16}O(d,α)^{14}N	166°	8.2–9.1	Thin target, normal kinematics	[15]

produce a more sophisticated potential contribution. Finally, the Coulomb contribution comes from the Coulomb repulsion of the nuclei and alone would produce pure Rutherford scattering. More detail can be found in Ref. [12].

An R-matrix analysis was performed on the data in order to extract the spins, parities, and partial widths of the resonant states in ^{18}F. This involved calculating the differential cross section for the appropriate reactions from the properties of the resonant states. These properties were then treated as free parameters, and the differential cross sections were fit to the experimental data. Additionally, the Brune transformation was employed, which allowed the partial decay widths and resonance energies to be used directly as free parameters in the fit, rather than the reduced-width amplitudes and R-matrix pole energies, which are less-physical quantities and therefore harder to fit. The details of this transformation can be found in [13]. The fit was performed using the code AZURE2, developed at the University of Notre Dame by Azuma *et al.* and detailed extensively in Ref. [14].

It was found that the spectra taken in the present work were not sufficient alone to fully constrain an R-Matrix fit, since the spins of the states could not be uniquely identified. This was due to two main factors; first, the lack of angular data meant that the spins could not be identified by analyzing angular distributions. Second, the nonzero spins of the decay products led to a range of different decay channels in a given state for each particle pair, each with a unique channel spin and orbital angular momentum. This made it very difficult to assign the spins based on the shape of the resonances and interference effects alone.

To resolve this issue, data from the literature were used in conjunction with the present work, further constraining the fit. These data sources are summarized in Table III. This allowed an R-matrix fit to be performed, but only up to 9 MeV which was the limit of the data from the literature. For the data from the present work, the fit was convolved with the experimental resolution. It was noticed that the ^{16}O(d,d)^{16}O measurement from Ref. [15] did not agree with the predicted Rutherford cross section at low energies. This was corrected for by rescaling both the ^{16}O(d,d)^{16}O and ^{16}O(d,α)^{14}N data by a factor of 1.1 prior to fitting. Both the original and rescaled data are shown in Fig 7.

The channel radii were calculated for each decay channel by using $R_{12} = R_0(A_1^{1/3} + A_2^{1/3})$, where R_0 was set to 1.35 fm. The best fits for each data source are shown in Figs. 7, 8, and 9, as well as the insets in Figs. 5 and 6. The parameters extracted from these calculations are given in Table IV, and nine new states have been observed ranging from 8.326 to 8.915 MeV. Varying the channel radii by 10% was found to have a negligible effect on the majority of the extracted parameters, and in all cases the parameters remained within errors, indicating a robust analysis.

Fitting these data sources simultaneously constrained the $^{14}\text{N} + \alpha_0$, $^{16}\text{O} + d_0$, and $^{17}\text{O} + p_0$ channels, providing reliable assignments for $\Gamma_{\alpha 0}$, Γ_{d0}, and Γ_{p0}. However, this still left the $^{17}\text{O} + p_1$ channel unconstrained, which was discussed in Sec. II B and was expected to be significant in some low-spin states. Therefore, Γ_{p1} was introduced as a free parameter without any data to directly constrain it. Since Γ_{p1} would contribute to the total width for each state, including it in the parameter space would lead to a more accurate description of the data and more reliable results. It was observed that the introduction of the p_1 channel significantly improved the χ^2/d.o.f. (where "d.o.f." means "degrees of freedom") of the fits, reducing it by between 10% and 50% for each data set.

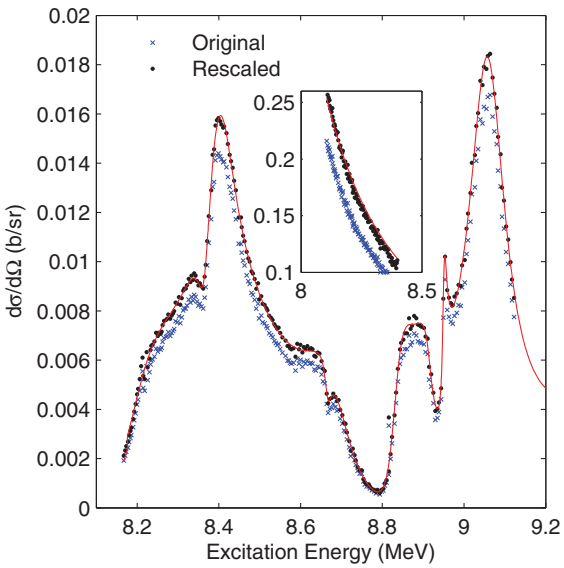

FIG. 7. (Color online) ^{16}O(d,α)^{14}N cross section at $\theta_{\text{c.m.}} = 166°$ from the work by Seiler *et al.* [15], with the present R-matrix fit. χ^2/d.o.f. = 2.9. Inset shows ^{16}O(d,d)^{16}O from the same work, at $\theta_{\text{c.m.}} = 166.5°$, compared with pure Rutherford scattering. Data rescaled by a factor of 1.1, as explained in the text.

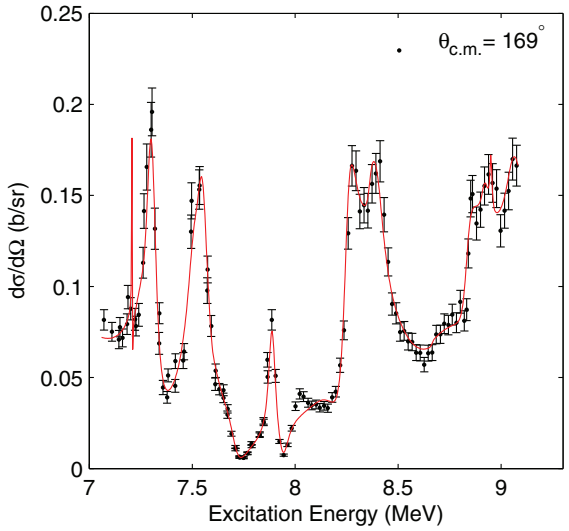

FIG. 8. (Color online) ^{14}N(α,α)^{14}N cross section from the work by Terwagne *et al.* [11], with the present *R*-matrix fit; χ^2/d.o.f. = 2.2.

States for which the total width was found to have a large Γ_{p1} component are indicated in Table IV, and these were found predominantly between 8 and 9 MeV, which was consistent with work by Seiler *et al.* [15].

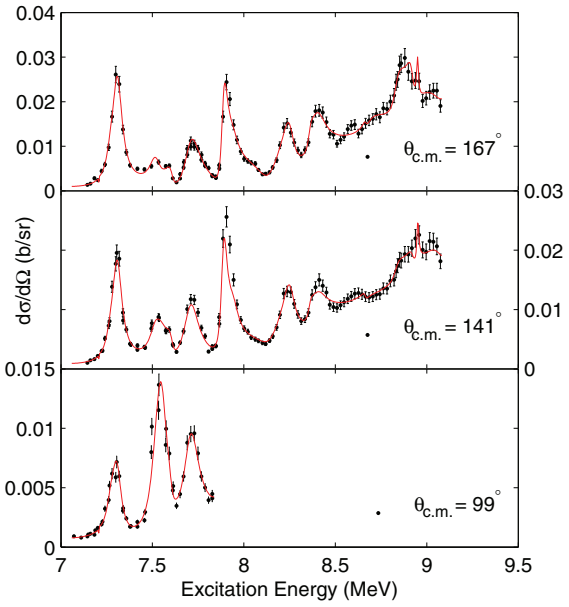

FIG. 9. (Color online) ^{14}N(α,p)^{17}O cross sections from the work by Terwagne *et al.* [11], with the present *R*-matrix fits; χ^2/d.o.f. = 1.6.

It should be noted that, while the *R*-matrix fits generally reproduce the data very well, with the χ^2/d.o.f. ranging between 1 and 3 over all data sets, there are some discrepancies at very low energies in the data from this work. This can be seen below 8.5 MeV in the ^{4}He(^{14}N,d)^{16}O spectrum. This is probably due to inadequacies of the energy-loss formulae used by LISE++ [10] at low energies, since the fit perfectly reproduces the same region of the ^{16}O(d,α)^{14}N spectrum from Ref. [15].

It was observed that there were some discrepancies between the spins and widths of some of the states extracted in this analysis and those measured previously. First, the spin assignments for the six states between 7.26 and 7.712 MeV were observed to disagree with a previous *R*-matrix fit by Gurbich *et al.* [17]. A likely explanation for this is that their fit was performed on a more limited data set, constraining only the α channel, and the introduction of more data from different decay channels in the present analysis led to a better constrained fit. It was found that, if these alternative spins were used in the present fit, and only the data in the α channel were used, a good fit was achieved with a χ^2/d.o.f. of 4.3. However, if the data constraining the proton and deuteron channels were added it became clear that the fit could not reproduce the data, with the χ^2/d.o.f. rising to ~100. The results from these fits are shown in Fig. 10. Additionally, the spin assignments from the present work were found to be consistent with those in the tabulations [16].

The present analysis seems to overestimate the total width for several states compared to previous measurements. In each case there is a reasonable explanation. The 2^- state at 6.832 MeV was measured in this work to have a width of 118 keV, compared with 88, 93, or 101 keV from previous measurements. This is only a relatively small increase, and may be due to the lack of ^{14}N(α,p)^{17}O data in this region, leading to poorly constrained partial widths.

Another case was the 1^+ state at 7.26 MeV. Here, the width was measured to be 61 keV, compared to 46.5 keV in the tabulations by Tilley *et al.* [16] and 35 keV in the work by Gurbich *et al.* [17]. However, the result is consistent with the *R*-matrix analysis performed by Kieser *et al.* [18], which produced a width of 60 keV, as well as that performed by Herring which produced a width of 62 keV [19]. It seems likely that the *R*-matrix fit by Gurbich *et al.* [17] may underestimate the width since they assign a spin of 4^+ to the state, which would significantly increase the centrifugal barrier and limit the width. Also, the widths given by Gurbich *et al.* [17] seem to be consistently underestimated for every state with spin assignments higher than in the present work and the tabulations of Ref. [16]. Taking this into account, with the exception of the tabulations by Tilley *et al.* [16], the width from the present work seems consistent with the majority of other sources, leading us to believe that our measurement is correct in this case.

The width of the 2^- state at 7.515 MeV is also larger than previous measurements suggest, with the present work recording a width of 62 keV compared with 39 keV in the work by Gurbich *et al.* [17] and 16.5 keV in the tabulations by Tilley *et al.* [16]. Again, it is likely that Gurbich *et al.* [17] underestimate the width due to an incorrect spin assignment;

TABLE IV. A comparison of the states identified in the present work with those in the tabulations compiled by Tilley *et al.* [16] and those from previous *R*-matrix fits by Gurbich *et al.* to ^{14}N(α,α)^{14}N data [17], Kieser *et al.* to ^{17}O(p,α)^{14}N data [18], and Herring to ^{14}N(α,α)^{14}N data [19]. The states from the tabulations are shown in bold. All energies are given in ^{18}F excitation energy. The systematic uncertainty on the resonance energies is ±10 keV. Uncertainties on the widths were calculated by using the MINOS error-analysis function in AZURE2, which individually fixed one parameter at a time and observed the effect on the χ^2.

Present work							Previous measurements				
E (MeV)	J^π	Γ (keV)	$\Gamma_{\alpha 0}$ (keV)	Γ_{d0} (keV)	Γ_{p0} (keV)	$\theta^2_{\alpha 0}$	E (MeV)	J^π	Γ (keV)	Decay	Ref.
6.654[a]	1^-	60 ± 6	39 ± 3		21 ± 2	0.216	6.647	1^-	59		[17]
							6.635	1^-	80		[18]
							6.664	1	93		[19]
							6.633	**1**	**80**	***p*,*α***	**[16]**
6.832[a]	2^-	118 ± 4	109 ± 3		9 ± 2	0.44	6.811	2^-	93		[17]
							6.807	2^-	88		[18]
							6.664	2	101		[19]
							6.809	**2^-**	**88**	***p*,*α***	**[16]**
(7.208)[c]	(3^-)	(0.6 ± 0.3)	(0.6 ± 0.3)		(<0.02)	(0.006)	7.20	3^-	3.1		[17]
							7.213	3,4,5	<4		[19]
							7.201	**(4^+)**	**< 6.5**	***p*,*α***	**[16]**
7.260	1^+	61 ± 6	53 ± 6		3.3 ± 1.1	0.082	7.269	4^+	35		[17]
							7.246	(1^+)	60		[18]
							∼7.29	1,2,3	∼62		[19]
							7.247	**(1^+)**	**46.5**	***p*,*α***	**[16]**
7.306[a]	3^-	63 ± 3	42 ± 3		20 ± 2	0.85	7.326	4^-	57		[17]
							7.294	3^-	60		[18]
							∼7.32	2,3,4	∼31		[19]
							7.315	**(3^-)**	**52**	***p*,*α***	**[16]**
7.515	2^-	62 ± 5	53 ± 4		9 ± 3	0.11	7.518	3^-	39		[17]
							7.528	**2^-**	**16.5**	***γ*,*p*,*α***	**[16]**
7.553[a]	3^-	75 ± 2	62 ± 2		12 ± 1	0.994	7.565	4^-	35		[17]
							7.532		**75**	***p*,*α***	**[16]**
7.595	1^-	46 ± 13	5 ± 1		40 ± 12	0.005	7.592	4^+	31		[17]
							7.555	**(1^-)**	**30**	***p***	**[16]**
7.711	3^+	106 ± 12	56 ± 10		39 ± 7	0.067	7.814	2^-	140		[17]
							7.685	**3^+,4^+**	**36**	***p*,*α***	**[16]**
							7.729	**>0**	**66**	***p*,*α***	**[16]**
7.895	3^-	45 ± 5	26 ± 2		19 ± 5	0.088	7.915	3^-	23		[17]
							7.899	**(2^-)**	**38**	***p*,*α***	**[16]**
7.947	1^+	70 ± 11	49 ± 6		22 ± 10	0.027	8.016	1^+	93		[17]
							7.941	**(1^+)**	**112**	***p*,*α***	**[16]**
							8.071	4^+	62		[17]
							8.064	**>3**	**60**	***p*,*α***	**[16]**
8.108	4^+	100 ± 35	1.7 ± 0.9		95 ± 35	0.14	**8.115**		**96**	***p***	**[16]**
8.212[b]	2^-	170 ± 15	90 ± 8	2.8 ± 0.2	55 ± 12	0.165	**8.209**	**2^-**	**52**	***p*,*α***	**[16]**
8.260[a]	4^+	100 ± 25	65 ± 20		32 ± 8	0.86	8.261	4^+	23		[17]
							8.238	**4^+**	**20**	***p***	**[16]**
8.326	1^+	450 ± 110	430 ± 110	6 ± 2	15 ± 5	0.16					
8.363[b]	3^+	32 ± 5	4 ± 1	0.119 ± 0.002	6 ± 5	0.011					
8.505[a]	2^-	440 ± 45	270 ± 40	10 ± 2	150 ± 20	0.37					
8.667[b]	2^-	<50	0.9 ± 0.5	<50	<11	0.001					
8.678[b]	1^+	220 ± 20	130 ± 20	8 ± 3	7 ± 4	0.041					
8.801	1^+	280 ± 15	250 ± 15	6.8 ± 0.3	13 ± 5	0.055					
8.858[a]	3^+	410 ± 60	310 ± 50	0.027 ± 0.001	95 ± 20	0.37					
8.917[b]	0^-	43 ± 6	30 ± 4	2.9 ± 0.5	<4	0.011					
8.951	3^-	<21	1.2 ± 0.7	0.4 ± 0.2	<20	0.001					
8.996	1^+	450 ± 115	430 ± 115	13 ± 7	12 ± 10	0.089	**9.02**	**(5^-)**			**[16]**

[a]Raised Wigner ratio in the α channel $\theta^2_{\alpha 0}$ suggests large α-cluster component in the structure.
[b]Fit suggests a significant ^{17}O + p_1 contribution to the total width.
[c]State is too narrow for the present data to provide a confident fit.

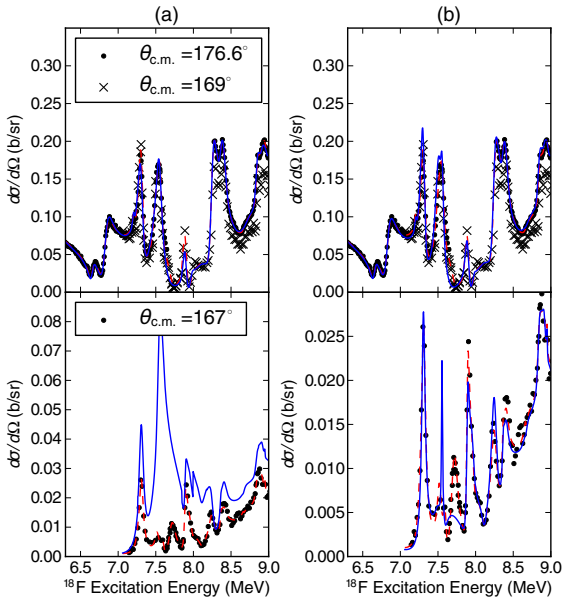

FIG. 10. (Color online) Comparison between the R-matrix fit from the present work (red dashed line) and the fit using the spins from Gurbich *et al.* [17] (blue line). Top row shows ^{4}He(^{14}N,α)^{14}N data from the present work and Ref. [11]. Bottom row shows ^{14}N(α, p_0)^{17}O data from Ref. [11]. (a) Fit only constrained by data in the α channel; χ^2/d.o.f. = 4.3. (b) Fit constrained by all data sets; χ^2/d.o.f. $\sim$ 100.

however, the width from the tabulations is more difficult to explain. It may be that there are in fact two states here with the same spin and parity, which cannot be resolved in this analysis. Another state was observed in a Breit–Wigner analysis of ^{17}O(p,α_0)^{14}N, ^{17}O(p,$p_1\gamma$)^{17}O, and ^{17}O(p,γ)^{18}F data by Sens *et al.* [20] at 7.446 MeV with undetermined spin and a width of 140 keV, which would be an appropriate candidate if it was measured to be the correct spin. If that was the case it may require a new measurement with improved resolution in order to separate the two states.

Another possible unresolved doublet is the 3^+ state at 7.711 MeV. In this case there are two possible states in the tabulations by Tilley *et al.* [16] at 7.685 and 7.729 MeV, each with ambiguous spin assignments and widths of 36 and 66 keV. In comparison, the present analysis provides a width of 106 keV. Again a repeat measurement with improved resolution may disentangle this doublet, allowing the widths to be accurately extracted.

In the previous work by Gurbich *et al.* [17] a 4^+ state was observed at 8.071 MeV with a width of 62 keV, which agrees with a state in the tabulations by Tilley *et al.* [16] at 8.064 MeV. While it is tempting to assign the 4^+ state at 8.108 MeV from the present work to these states, the partial widths indicate otherwise. A very small $\Gamma_{\alpha 0}$ and large Γ_{p0} implies that this state is in fact the 8.115 MeV state from the tabulations by Tilley *et al.* [16] which had previously only been measured to proton decay. Additionally, the total width of this state matches the width from the present work far better.

The 2^- state at 8.212 MeV and the 4^+ state at 8.26 MeV both dramatically overestimate the widths when compared with both the tabulations by Tilley *et al.* [16] and the parametrization by Gurbich *et al.* [17] However, in the present work nine new states have been observed, ranging from 8.236 to 9 MeV, and the introduction of these new states to the R-matrix calculation may strongly interfere with the states close to the boundary. This leads us to believe that the properties of these two states extracted in the present work are in fact more reliable than those from previous measurements.

Finally the 1^+ state at 8.996 MeV has only been tentatively assigned to the state from the tabulations by Tilley *et al.* [16] at 9.02 MeV. While this state is very close in excitation energy, the spin is significantly higher and is of opposite parity in the tabulations, and there is no measured total width with which a comparison could be made. Additionally, this state has only been observed in the ^{17}O(α,t)^{18}F proton-transfer reaction [21], which implies a large single-particle component to the state, which is not what is observed in the present analysis. If this assignment is incorrect, then the state from the present work would in fact correspond to a tenth new state in ^{18}F.

IV. DISCUSSION

By examining the Wigner ratios for the $^{14}\mathrm{N} + \alpha_0$ channel from the present R-matrix analysis, seven possible candidates for α-cluster states were identified: 6.654 MeV (1^-), 6.832 MeV (2^-), 7.306 MeV (3^-), 7.553 MeV (3^-), 6.654 MeV (1^-), 8.260 MeV (4^+), 8.505 MeV (2^-), and 8.858 MeV (3^+). These are highlighted in Table IV and compared with the states predicted by the semimicroscopic α-cluster calculation [4] in Fig. 11. The calculation was limited to positive-parity states only, so the following discussion focuses only on these.

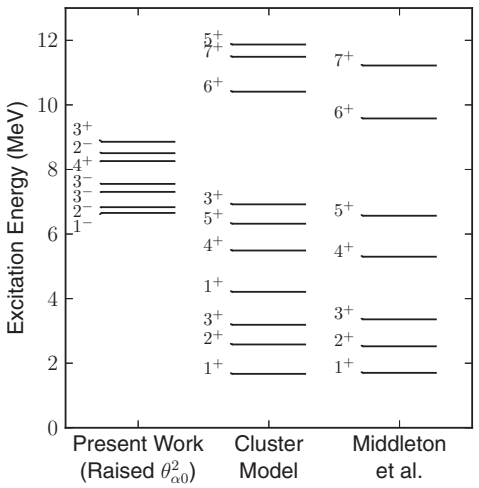

FIG. 11. Potential α-clustered states from the present work compared with those from the semimicroscopic-cluster model [4] and the experimental assignments by Middleton *et al.* [5]. States from the present work are identified as being α clustered if $\theta^2_{\alpha 0} > 0.2$.

The first predicted state in the relevant energy range is the 5^+ member of the $K^\pi = 1^+$ rotational band. This state was predicted to have an energy of 6.32 MeV [4] and was assigned to a 5^+ state which was found to be very strongly populated by the ^{14}N(^{7}Li,t)^{18}F α-transfer reaction at 6.567 MeV [5,6]. This state was also observed in α elastic-scattering measurements performed previously by Gurbich *et al.* [17] and was fit by using R-matrix theory as a 5^+ state at 6.567 MeV, with a width of 0.5 keV and $\Gamma_\alpha/\Gamma = 1$. This state was not observed, however, in the present work due to its very narrow width, which would have been entirely washed out by the experimental resolution. Despite this, it is expected that this state has been correctly assigned based on the previous experimental measurements. It is likely that its narrow width is simply a product of the state being close to the particle-decay threshold and having a large spin, producing a very large centrifugal barrier rather than any structural affects.

The second possible α-clustered state is the 3^+ member of the $K^\pi = 0^+$ rotational band. This state was predicted to have an energy of 6.92 MeV [4]. Some attempts have been made to assign this state to experimental measurements. The first candidate was a 3^+ state at 6.48 MeV; however, this has been discounted as it has been observed to contain considerable two-particle components [22] and, additionally, this would place the state below the 5^+ member of the $K^\pi = 1^+$ band, which is the opposite of what is predicted by the calculation. Another candidate has been suggested at 7.26 MeV by Middleton *et al.* [5]. This was observed to be very strongly populated in α-transfer reactions; however, further analysis by Sens *et al.* suggested that this may in fact be a 3^- state [20], and this was confirmed in the present R-matrix analysis. The present analysis has identified three 3^+ states at 7.712, 8.363, and 8.858 MeV. The 7.712 MeV state is the closest match to the theorized state in excitation energy; however, it has a relatively small Wigner ratio of $\theta^2_{\alpha 0} = 0.067$, which is uncharacteristic of α-clustered states. Additionally, this ratio may be reduced further because, when comparing this state to the tabulations, it seems likely that this may actually be two 3^+ states at 7.685 and 7.729 MeV, each with smaller widths and hence smaller Wigner ratios. The second candidate at 8.363 MeV also has a very small Wigner ratio of $\theta^2_{\alpha_0} = 0.011$, and there seems to be some evidence for a large Γ_{p1} component. This leaves the 3^+ state at 8.858 MeV which does present a large Wigner ratio of $\theta^2_{\alpha_0} = 0.37$, indicative of an α-clustered state. However, the energy of this state is 1.93 MeV higher than the calculated value.

Finally, the 5^+ member of the $K^\pi = 0^+$ band was investigated. This state was predicted at 11.87 MeV, and has yet to be assigned experimentally. A calculation was performed to predict what an α-clustered state at the Wigner limit, with the predicted energy and spin, would look like in the ^{4}He(^{14}N,α) spectrum. The result is shown in Fig. 12. The peak is very broad, so it is unlikely that it could be assigned to any of the strong, sharp resonances observed in this energy region. However, by comparing the state with the moving average of the data, it can be seen that there is a broad increase in cross section in this region, similar in shape and amplitude to the 5^+ peak. However, a full R-matrix analysis is required to see specifically how a state in this region would impact the spectrum. This, in turn, would require all the decay channels to be measured at this energy.

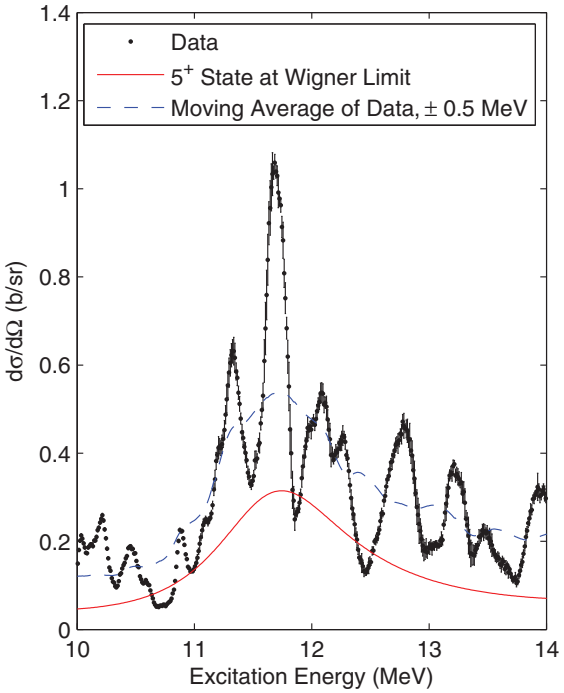

FIG. 12. (Color online) ^{4}He(^{14}N,α) cross section, compared with a theoretical calculation of the cross section generated from just one α-clustered state at the Wigner limit, predicted in Ref. [4], and the moving average of the data taken over a range of $\pm$0.5 MeV

V. CONCLUSIONS

Differential-cross-section measurements were made at 176.6° for the reactions ^{4}He(^{14}N,α) between 6 and 15.5 MeV in excitation energy and ^{4}He(^{14}N,d)^{16}O between 8.3 and 12.3 MeV. These measurements were used alongside data from previous work to constrain a full multichannel R-matrix fit to the α, deuteron, and proton channels between 6 and 9 MeV. From this fit, the energies, spins, parities, and partial widths of states in ^{18}F were extracted, and nine new states have been identified between 8.326 and 8.915 MeV. Furthermore, some discussion has been made based on a comparison between these measurements and some previous theoretical and experimental studies on the cluster structure of ^{18}F.

ACKNOWLEDGMENTS

The authors would like to thank the team at the University of Birmingham MC40 Cyclotron.

[1] M. Freer and A. C. Merchant, J. Phys. G **23**, 261 (1997).
[2] W. von Oertzen, M. Freer, and Y. Kanada-En'yo, Phys. Rep. **432**, 43 (2006).
[3] H. T. Richards, Phys. Rev. C **29**, 276 (1984).
[4] B. Buck, A. C. Merchant, and N. Rowley, Nucl. Phys. A **327**, 29 (1979).
[5] R. Middleton, L. M. Polsky, C. H. Holbrow, and K. Bethge, Phys. Rev. Lett. **21**, 1398 (1968).
[6] M. E. Cobern and P. D. Parker, Phys. Rev. C **15**, 1929 (1977).
[7] K. P. Artemov, O. P. Belyanin, A. L. Vetoshkin, R. Wolskj, M. S. Golovkov, V. S. Gol'dberg, M. Madeja, V. V. Pankratov, I. N. Serikov, V. A. Timofee, V. N. Shadrin, and J. Szmider, Sov. J. Nucl. Phys. **52**, 408 (1990).
[8] J. F. Ziegler, J. Appl. Phys. **85**, 1249 (1999).
[9] *Alpha spectrometry sources reference*, QSA Global, http://www.hightechsource.co.uk/Resources/Alpha.pdf, accessed Sept., 2013.
[10] O. B. Tarasov and D. Bazin, *Simulation of Fragment Separtors:*LISE++, http://lise.nscl.msu.edu/lise.html, nSCL/MSU, accessed Sept., 2013.
[11] G. Terwagne, G. Genard, M. Yedji, and G. G. Ross, J. Appl. Phys. **104**, 084909 (2008).
[12] A. M. Lane and R. G. Thomas, Rev. Mod. Phys. **30**, 257 (1958).
[13] C. R. Brune, Phys. Rev. C **66**, 044611 (2002).
[14] R. E. Azuma, E. Uberseder, E. C. Simpson, C. R. Brune, H. Costantini, R. J. de Boer, J. Görres, M. Heil, P. J. LeBlanc, C. Ugalde, and M. Wiescher, Phys. Rev. C **81**, 045805 (2010).
[15] R. F. Seiler, C. H. Jones, W. J. Anzick, D. F. Herring, and K. W. Jones, Nucl. Phys. **45**, 647 (1963).
[16] D. Tilley, H. Weller, C. Cheves, and R. Chasteler, Nucl. Phys. A **595**, 1 (1995).
[17] A. F. Gurbich, I. B. Radović, Z. Siketić, and M. Jakšić, Nucl. Instrum. Methods Phys. Res., Sect. B **269**, 40 (2011).
[18] W. Kieser, R. Azuma, and K. Jackson, Nucl. Phys. A **331**, 155 (1979).
[19] D. F. Herring, Phys. Rev. **112**, 1217 (1958).
[20] J. C. Sens, S. M. Refaei, and A. Pape, Phys. Rev. C **18**, 2007 (1978).
[21] M. Yasue, T. Hasegawa, S. I. Hayakawa, K. Ieki, J. Kasagi, S. Kubono, T. Murakami, K. Nisimura, K. Ogawa, H. Ohnuma, R. J. Peterson, H. Shimizu, M. H. Tanaka, and H. Toyokawa, Phys. Rev. C **46**, 1242 (1992).
[22] C. Rolfs, A. Charlesworth, and R. Azuma, Nucl. Phys. A **199**, 257 (1973).

Appendix G

Publication: Alpha Clustering in ^{18}F

Alpha clustering in ^{18}F

2014 J. Phys.: Conf. Ser. 569 012053

(http://iopscience.iop.org/1742-6596/569/1/012053)

Alpha clustering in ^{18}F

S Bailey[1], M Freer[1], Tz Kokalova[1], S Cruz[1,2], H Floyd[1] and D J Parker[1]

1 University of Birmingham, Birmingham, B15 2TT, UK

E-mail: s.c.bailey@pgr.bham.ac.uk

Abstract. We review some of the key experimental and theoretical studies of α-clustering in ^{18}F. Particular attention is given to the $4p$-$2h$ nature of such α-clustered states, and the interaction between the holes and clusters is examined in terms of both weak and strong-coupling regimes. The experimental work focuses on α-transfer spectroscopy and α resonant scattering as tools for investigating α-clustering.

1. Introduction

Alpha clustering is a well established concept in the structure of light α-conjugate nuclei [1]. Further to this, it has been shown that neutron-rich nuclei exhibit similar cluster structures with the additional neutrons playing the role of valence particles, contributing to the binding of the clusters in a way that resembles electrons in atomic molecules [2]. This has been investigated in detail recently both from theoretical and experimental perspectives, finding a lot of success in the $\alpha + x\text{n} + \alpha$ structures in Be isotopes [3, 4] and the $\alpha + x\text{n} + ^{16}$O structures in Ne isotopes [5, 6, 7]. There has been comparatively little work done, however, to investigate the persistence of cluster structure in isotopes which deviate from α-conjugate nuclei in ways other than the addition of valence neutrons.

^{18}F is of interest from a clustering perspective because of the predicted $\alpha + ^{14}$N structure, and how this compares with the $\alpha + ^{16}$O structure observed in ^{20}Ne [7]. It is thought that the cluster structure is amplified in ^{20}Ne by the large shell gap above the p shell, which provides a clear separation between the ^{16}O core and the α-cluster. The $\alpha + ^{14}$N structure is therefore expected to manifest itself in $4p$-$2h$ excitations of ^{18}F [8], displayed in Fig. 1. This produces a shell structure very similar to that of ^{20}Ne, again with a clear shell gap separating the α-cluster from the core, and deviating from ^{20}Ne only by the addition of one proton hole and one neutron hole in the p shell. It is the interplay between these proton and neutron holes and the cluster-core structure that motivates the present work on ^{18}F.

2. Hole-particle coupling

The regime which governs the coupling between the p shell holes and the s-d shell particles in $4p$-$2h$ states is extremely important for understanding the structure of ^{18}F. This coupling can either be described as weak-coupling or strong-coupling. In the weak-coupling picture, the particle wavefunctions are assumed to be similar to the eigenfunctions of ^{20}Ne, and the

[2] Present Address: Department of Physics and Astronomy, The University of British Columbia, 6224 Agricultural Road, Vancouver, BC V6T 1Z1, Canada

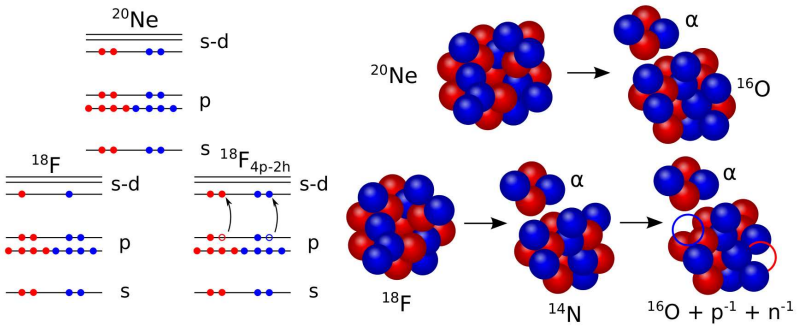

Figure 1. (Colour online) ^{18}F and ^{20}Ne from shell model (left) and cluster model (right) perspectives.

hole wavefunctions like that of the ^{14}N ground state [8, 9, 10]. This is interpreted as weak coupling since the interaction is expected to be well described as a small perturbation on these wavefunctions, leading to a structure very similar in nature to ^{20}Ne with some additional core excitations.

The strong-coupling model takes the opposite approach, asserting that the interaction between the holes and particles is too strong for the wavefunctions to be approximated in such a way. Instead more robust techniques are required, leading to more varied and exotic deformations and structures.

One of the earliest experimental investigations of hole-particle states in ^{18}F was performed in 1968 by Middleton *et al.* [8] using the ^{14}N(^{7}Li,t)^{18}F α-transfer reaction. It is expected that α-transfer reactions preferentially excite states formed by transferring all four nucleons into the same shell, leading to an amplified cross-section for 4*p*-2*h* states. In this work it was argued that this allowed the 4*p*-2*h* excitations to be identified by selecting states which were strongly populated by this reaction but weakly populated by one or two nucleon transfer reactions. However this may be an overly simplistic interpretation since it ignores the effects that the matching conditions have on the cross-section [11]. Additionally the nonzero spins of the nuclei involved in this reaction often lead to ambiguous angular distributions, making experimental J^π assignments very difficult [12].

Middleton *et al.* [8] reported six states to be likely 4*p*-2*h* candidates at 1.70, 2.52, 3.36, 4.23, 5.30 and 6.55 MeV using this technique. They go on to argue that these states can be well described by the weak-coupling model, coupling the ^{20}Ne ground state band to the $(1p_{1/2})_{1+}{}^{-2}$ hole configuration. The application of this model led to the following spin-parity assignments for the observed 4*p*-2*h* states, respectively: $J^\pi = 1^+, 2^+, 3^+, 1^+, 3^+$ and $(4^+, 5^+)$.

This weak-coupling description of the 4*p*-2*h* states was challenged following an extensive study of the structure of ^{18}F in 1973 by Rolfs *et al.* [13]. In this work the hole-particle states were investigated in detail using the ^{14}N(α,γ)^{18}F, ^{17}O(p,γ)^{18}F and ^{16}O(^{3}He,pγ)^{18}F reactions [13, Part III]. Following these measurements 5 states were identified as being members of a $K^\pi = 1^+$ rotational band of predominantly 4*p*-2*h* nature, at 1.701, 2.523, 3.358, 5.298 and 6.567 MeV. Spin-parity assignments were made based on measured branching ratios and angular distributions to be respectively $J^\pi = 1^+, 2^+, 3^+, 4^+$ and 5^+. The reduced α-widths were extracted for the 4^+ and 5^+ members, and in both cases were found to be exceptionally large.

It is clear that these states are the same states as those measured by Middleton *et al.* [8], with the exception that the 4.23 MeV state was found by Rolfs *et al.* to be unlikely to be 4*p*-2*h* in nature, and was instead assigned to be a $J^\pi = 2^{(-)}$ state of 3p-1h structure [13, Part IV]. Additionally the spin-parity assignment for the 5.298 MeV state disagrees with the assignment

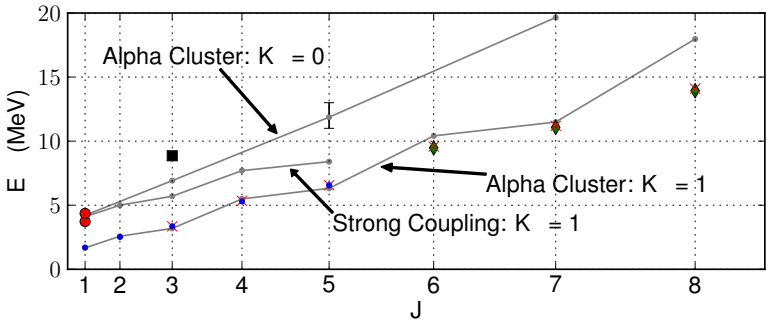

Figure 2. (Colour online) ^{18}F rotational bands, x-axis scaled as J(J + 1). Theoretical calculations displayed as lines (annotated), data displayed as points. Data from Rolfs *et al.* [13, Part III] (blue dots), Cobern *et al.* [12] (green diamonds), Etchegoyen *et al.* [15] (red crosses), Bailey *et al.* [16] (black squares/bars) and the Buck *et al.* mixed states assignment, see text [17] (red circles)

made based on the weak-coupling model by Middleton *et al.* [8]. These considerations led Rolfs *et al.* to reject the weak-coupling model in favour of the strong-coupling model.

A comparison was made between this band and a strong-coupling calculation performed in 1965 by Bassichis *et al.* [14], which predicted a $K^\pi = 1^+$, 4*p*-2*h* rotational band in ^{18}F. The gradient of the predicted band was found to be in excellent agreement with the measurements and it reproduced the observed zig-zagging in excitation energy, however the predicted band was shifted ≈ 2.5 MeV higher in energy. Rolfs *et al.* [13, Part III] speculated that based on the exceptionally large reduced α-widths observed for the 4^+ and 5^+ members, α-particle clustering may in fact play a prominent role in the structure of this band, and perhaps the explicit inclusion of α-clustering in the microscopic description of the band may reconcile this energy shift.

Based on these results it seems likely that the strong-coupling regime better describes the hole-particle coupling in ^{18}F, since the work by Rolfs *et al.* [13, Part III] is more extensive, allowing the spin-parity assignments to be made based on experimental measurements. Further to this, more α-transfer measurements have been made by Cobern *et al.* [12] and Etchegoyen *et al.* [15], extending the $K^\pi = 1^+$ rotational band observed by Rolfs *et al.* [13, Part III] from $J^\pi = 5^+$ up to 8^+. This rotational band is displayed in Fig. 2, with the band calculated using the strong-coupling model by Bassichis *et al.* [14] for comparison.

3. Alpha clustering

Based on the work by Rolfs *et al.* [13, Part III] it seems likely that there is a large α-cluster component to the structure of the $K^\pi = 1^+$ rotational band. A semi-microscopic calculation of α-cluster states in ^{18}F was performed in 1979 by Buck *et al.* [17]. In this work all four nucleons from which the α-particle is built up are placed in the *s*-*d* shell, enforcing the experimentally determined 4*p*-2*h* structure discussed previously. This leads to the ^{14}N core wavefunction being given by two *p* shell holes in the ^{16}O closed shell. Further details regarding this model can be found in Ref. [17].

This model produced two distinct rotational bands, one with $K^\pi = 1^+$ and one with $K^\pi = 0^+$. The states in the $K^\pi = 1^+$ band agreed exceptionally well with the experimentally determined states up to $J^\pi = 5^+$, however above this they began to diverge, with the calculated levels shifted higher in energy compared with the experimentally observed levels. This can be seen in Fig. 2. It was however explained by Buck *et al.* that this may be due to the way the nuclear

potential was modelled, since similar discrepancies have arisen in other calculations involving the same potential [17].

The extremely good agreement between observed and calculated levels in the $K^\pi = 1^+$ band leads us to believe that this is indeed an α-clustered $4p$-$2h$ rotational band. However if this model is correct, it should also be possible to identify the $K^\pi = 0^+$ rotational band. Buck *et al.* [17] assigned the 1^+ state in this band to two experimentally observed 1^+ states at 3.724 and 4.361 MeV. It is argued that this is due to mixing between this state and a $2p$ shell model state predicted to exist at a similar energy, causing the $4p$-$2h$ strength to be shared between both states. This hypothesis is confirmed to an extent experimentally by the slightly reduced cross-section for these states in α-transfer measurements [8]. However Buck *et al.* were unable to confidently assign any of the other members of this band.

4. ^{14}N + α resonant reaction

More recently a study of ^{18}F was performed in 2014 by Bailey *et al.* [16] using the α + ^{14}N resonant reaction to populate α-clustered states in the compound nucleus ^{18}F. The reduced widths of these states were then extracted by performing an R-Matrix fit simultaneously of these data and data from other sources covering the d + ^{16}O and p + ^{17}O channels [18, 19]. Bailey *et al.* [16] proceeded to assign the 3^+ state in the $K^\pi = 0^+$ band to a state at E_{ex} = 8.858 MeV, and also provided tentative evidence for the existence of the broad 5^+ state in the region between 11 and 13 MeV. The 3^+ assignment was made due its unusually large α-reduced width, however the state was predicted at 6.92 MeV, almost 2 MeV lower than observed. These assignments are compared with the calculated $K^\pi = 0^+$ band in Fig. 2.

5. Conclusion

It is clear that α-clustering plays a significant role in the structure of ^{18}F, with perhaps the strongest evidence coming from the excellent agreement between the $K^\pi = 1^+$ rotational band calculated using a semi-microscopic α-cluster model [17] and experimental observations made using α-transfer reactions [13, 12, 15]. However the $K^\pi = 0^+$ rotational band is still not fully understood, and there has yet to be any work done to investigate negative-parity α-clustered rotational bands.

References

[1] Freer M and Merchant A C 1997 *J. Phys. G: Nucl. Part. Phys.* **23** 261–322
[2] von Oertzen W, Freer M and Kanada-En'yo Y 2006 *Physics Reports* **432** 43 – 113
[3] Hiura J and Tamagaki R 1972 *Progress of Theoretical Physics Supplement* **52** 25–88
[4] Itagaki N and Okabe S 2000 *Phys. Rev. C* **61**(4) 044306
[5] von Oertzen W 2001 *Eur. Phys. J. A* **11** 403–411 ISSN 1434-6001
[6] Rogachev G V, Goldberg V Z, Lönnroth T, Trzaska W H, Fayans S A, Källman K M, Kolata J J, Mutterer M, Rozhkov M V and Skorodumov B B 2001 *Phys. Rev. C* **64**(5) 051302
[7] Richards H T 1984 *Phys. Rev. C* **29**(1) 276–283
[8] Middleton R, Polsky L M, Holbrow C H and Bethge K 1968 *Phys. Rev. Lett.* **21**(19) 1398–1401
[9] Arima A, Horiuchi H and Sebe T 1967 *Physics Letters B* **24** 129 – 131 ISSN 0370-2693
[10] Benson H and Flowers B 1969 *Nuclear Physics A* **126** 332 – 354 ISSN 0375-9474
[11] Brink D 1972 *Physics Letters B* **40** 37 – 40 ISSN 0370-2693
[12] Cobern M E and Parker P D 1977 *Phys. Rev. C* **15**(5) 1929–1932
[13] Rolfs C, Berka I, Trautvetter H, Azuma R, Kieser W, Litherland A and Charlesworth A 1973 *Nuclear Physics A* **199** 257 – 350 ISSN 0375-9474
[14] Bassichis W H, Giraud B and Ripka G 1965 *Phys. Rev. Lett.* **15**(25) 980–982
[15] Etchegoyen M, Sinclair D, Etchegoyen A and Moreno E 1983 *Nuclear Physics A* **402** 87 – 113 ISSN 0375-9474
[16] Bailey S, Freer M, Kokalova T, Cruz S, Floyd H and Parker D J 2014 *Phys. Rev. C* **90**(2) 024302
[17] Buck B, Merchant A and Rowley N 1979 *Nuclear Physics A* **327** 29 – 52 ISSN 0375-9474
[18] Terwagne G, Genard G, Yedji M and Ross G G 2008 *J Appl. Phys.* **104** 084909
[19] Seiler R F, Jones C H, Anzick W J, Herring D F and Jones K W 1963 *Nucl. Phys.* **45** 647–656

Appendix H

Publication: Alpha Clustering in Ti Isotopes: ^{40,44,48}Ca + α Resonant Scattering

EPJ Web of Conferences 113, 08002 (2016)
http://dx.doi.org/10.1051/epjconf/201611308002

Alpha clustering in Ti isotopes: ^{40,44,48}Ca + α resonant scattering

Sam Bailey[1,a], Martin Freer[1,b], Tzany Kokalova[1,c], Carl Wheldon[1], Robin Smith[1], Joseph Walshe[1], Lovro Prepolec[2], Neven Soić[2], Vedrana Tokić[2], Miguel Marqués[3], Lynda Achouri[3], Franck Delaunay[3], Marian Parlog[3], Quentin Deshayes[3], Beatriz Fernández-Dominguez[4], and Bertrand Jacquot[5]

[1] *School of Physics and Astronomy, University of Birmingham, Birmingham, B15 2TT, UK*
[2] *Institut Ruder Bošković, Bijenička cesta 54, 10000 Zagreb, Croatia*
[3] *Laboratoire de Physique Corpusculaire de Caen, 6 bd Maréchal Juin, 14050 Caen Cedex, France*
[4] *Universidade de Santiago de Compostela, Praza do Obradoiro, 15782 Santiago de Compostela, Spain*
[5] *Grand Accélérateur National d'Ions Lourds, Bd Henri Becquerel, BP 55027 - 14076 Caen Cedex 05, France*

Abstract. Measurements were made of the ^{4}He(^{40,44,48}Ca,α) resonant scattering reactions at 180° and up to $E_{c.m.}$ ~11.5 MeV, using the Thick Target Inverse Kinematics technique. These measurements are discussed, with a focus on assessing their usefulness for investigating α-clustering in medium mass ^{44,48,52}Ti nuclei.

1 Introduction

Clustering in nuclei allows the techniques of few-body physics to be applied to the many body nuclear problem, yet identifying nuclei which exhibit cluster structures is far from trivial. Alpha-clustering has been shown to play an important role in the structure of many α-conjugate and neutron rich light nuclei [1]. However, it is equally apparent that mean field approaches to nuclear structure describe the properties of heavy nuclei very well, suggesting that clusters do not contribute significantly to their structure. This leads to the question of to what extent does α-clustering persist into medium and heavy mass nuclei.

The core+Xn+α molecular cluster structure is an essential component in the structure of ^{20,21,22}Ne [2, 3]. Here ^{16}O acts as a core, and any additional neutrons act as valence particles providing additional binding to the α + ^{16}O cluster structure. This structure is thought to be exceptionally pronounced due to the inert nature of the doubly magic ^{16}O core. It has been hypothesized that ^{44}Ti may exhibit a similar cluster structure to ^{20}Ne, due to its doubly magic ^{40}Ca core. If confirmed this would provide evidence for α-clustering in medium mass nuclei.

In the present work ^{44,48,52}Ti are investigated, allowing the interaction of valence neutrons with the ^{40}Ca+α structure to be examined and compared with ^{20}Ne. Additionally since ^{48}Ca is also a doubly magic nucleus, this allows the evolution of this cluster structure across an entire shell to be explored.

[a] e-mail: s.c.bailey@pgr.bham.ac.uk
[b] e-mail: m.freer@bham.ac.uk
[c] e-mail: t.kokalova@bham.ac.uk

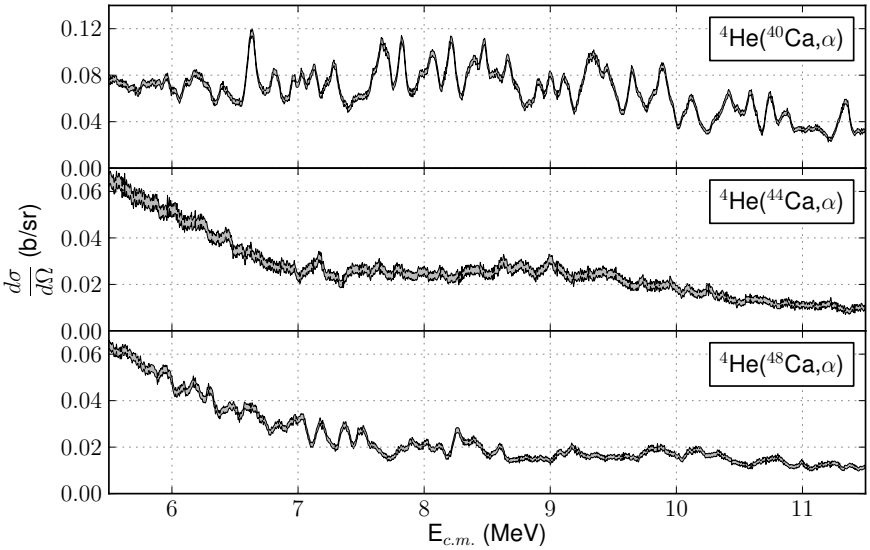

Figure 1. Measured spectra. All measurements taken at a scattering angle of 180° and normalized to the Rutherford scattering cross section at low $E_{c.m.}$. Grey region represents a 90% confidence interval.

2 Experimental Work

Measurements were made of the ^{4}He(^{40,44,48}Ca,α) resonant scattering reactions, at a scattering angle of 180° using the Thick Target Inverse Kinematics technique [4]. The experiment was performed at GANIL, France using ^{40,44,48}Ca beams incident on a thick ^{4}He gas target, with beam energies of 180, 207 and 234 MeV respectively. The scattered α-particles were measured using Double Sided Silicon Strip Detectors, which were placed at the end of the reaction chamber at 0° to the beam line, corresponding to a scattering angle of 180° in inverse kinematics. The beam loses energy as it traverses the gas, tracing out the continuous excitation spectra shown in Figure 1.

The resonant structure of these spectra is dependent entirely on the properties of the states in the compound nuclei: ^{44,48,52}Ti. This dependence is expressed using R-Matrix theory [5], which formulates explicitly the differential cross-section in terms of the energies, spins, parities and reduced widths of the compound nuclear states. The analysis will focus on developing techniques based on R-Matrix theory to probe the structure of ^{44,48,52}Ti, using these measurements of resonant structure. Since the states in these measurements are being populated through the α+^{40,44,48}Ca channels it is expected the α-clustered states will be preferentially populated, providing an excellent insight into the degree of α-clustering in ^{44,48,52}Ti.

References

[1] W. von Oertzen, M. Freer, and Yoshiko Kanada-En'yo, Physics Reports **432**, 43–113 (2006)
[2] W. von Oertzen, Eur. Phys. J. **A11**, 403 (2001)
[3] G. V. Rogachev et al., Phys. Rev. C **64**, 051320 (2001)
[4] K. P. Artemov et al., Sov. J. Nucl. Phys. **52**, 408–411 (1990)
[5] A. M. Lane and R. G. Thomas, Rev. Mod. Phys. **30**, 257 (1958)

Bibliography

1. Bailey, S. *et al.* Energy levels of ^{18}F from the ^{14}N+α resonant reaction. *Phys. Rev. C* **90,** 024302 (2 Aug. 2014) (cit. on pp. v, 23, 55, 62, 66, 77, 80, 81, 83, 89, 96).
2. Bailey, S. *et al.* Alpha clustering in ^{18}F. *J. Phys. Conf. Ser.* **569,** 012053 (2014) (cit. on pp. v, 55, 56).
3. Bailey, S. *et al.* Alpha clustering in Ti isotopes: ^{40,44,48}Ca + α resonant scattering. *EPJ Web of Conferences* **113,** 08002 (2016) (cit. on pp. v, 91).
4. Krane, K. *Introductory nuclear physics* (John Wiley & Sons, 1988) (cit. on pp. 1, 20, 27).
5. Epelbaum, E., Hammer, H.-W. & Meißner, U.-G. Modern theory of nuclear forces. *Rev. Mod. Phys.* **81,** 1773–1825 (4 Dec. 2009) (cit. on p. 1).
6. Weizsäcker, C. F. v. Zur Theorie der Kernmassen. *Zeitschrift für Physik* **96,** 431–458. ISSN: 0044-3328 (1935) (cit. on p. 1).
7. Bethe, H. A. & Bacher, R. F. Nuclear Physics A. Stationary States of Nuclei. *Rev. Mod. Phys.* **8,** 82–229 (2 Apr. 1936) (cit. on p. 1).
8. Meitner, L & Frisch, O. R. Disintegration of Uranium by Neutrons: a New Type of Nuclear Reaction. *Nature* **143,** 239 (1939) (cit. on p. 2).
9. Bohr, N. & Wheeler, J. A. The Mechanism of Nuclear Fission. *Phys. Rev.* **56,** 426–450 (5 Sept. 1939) (cit. on p. 2).
10. Mayer, M. G. On Closed Shells in Nuclei. II. *Phys. Rev.* **75,** 1969–1970 (12 June 1949) (cit. on p. 2).
11. Haxel, O., Jensen, J. H. D. & Suess, H. E. On the 'Magic Numbers' in Nuclear Structure. *Phys. Rev.* **75,** 1766–1766 (11 June 1949) (cit. on p. 2).
12. Caurier, E., Martínez-Pinedo, G., Nowacki, F., Poves, A. & Zuker, A. P. The shell model as a unified view of nuclear structure. *Rev. Mod. Phys.* **77,** 427–488 (2 June 2005) (cit. on p. 2).

13. Pauli, W. Über den Zusammenhang des Abschlusses der Elektronengruppen im Atom mit der Komplexstruktur der Spektren. *Zeitschrift für Physik* **31,** 765–783. ISSN: 0044-3328 (1925) (cit. on p. 2).

14. Bakken. Wikipedia Commons Image, https://commons.wikimedia.org/wiki/File:Shells.png (cit. on p. 3).

15. Ragnarstroberg. *Nuclear Binding Energies vs Liquid Drop* Wikipedia Commons Image, https://commons.wikimedia.org/wiki/File:Nuclear_BindingEnergies_vs_liquidDrop.png. License: Creative Commons Attribution-Share Alike 3.0 Unported, Accessed: 25/08/2016 (cit. on p. 3).

16. Brown, B. A. & Wildenthal, B. Status of the nuclear shell model. *Annu. Rev. Nucl. Part. Sci.* **38,** 29–66 (1988) (cit. on p. 2).

17. Koonin, S., Dean, D. & Langanke, K. Shell model Monte Carlo methods. *Phys. Rep.* **278,** 1–77. ISSN: 0370-1573 (1997) (cit. on p. 2).

18. Brown, B. The nuclear shell model towards the drip lines. *Prog. Part. Nucl. Phys.* **47,** 517–599. ISSN: 0146-6410 (2001) (cit. on p. 2).

19. Freer, M. & Merchant, A. C. Developments in the study of nuclear clustering in light even–even nuclei. *J. Phys. G: Nucl. Part. Phys.* **23,** 261–322 (1997) (cit. on pp. 2, 4, 6).

20. Von Oertzen, W., Freer, M. & Kanada-En'yo, Y. Nuclear clusters and nuclear molecules. *Phys. Rep.* **432,** 43–113 (2006) (cit. on pp. 2, 5, 12, 20, 21).

21. Hafstad, L. R. & Teller, E. The Alpha-Particle Model of the Nucleus. *Phys. Rev.* **54,** 681–692 (9 Nov. 1938) (cit. on pp. 2, 3).

22. Freer, M. *Clusters in Nuclei* Scholarpedia, http://www.scholarpedia.org/article/File:Haf_1.gif. Accessed: 25/8/2016 (cit. on p. 3).

23. Audi, G. & Wapstra, A. H. The 1995 Update to the Atomic Mass Evaluation. *Nucl. Phys. A* **595,** 409 (1995) (cit. on pp. 4, 6).

24. Barret, B. R., Mihaila, B., Pieper, S. C. & Wiringa, R. B. Ab initio calculations of light nuclei. *Nuclear Physics News* **13,** 17–23 (2003) (cit. on p. 4).

25. Hiura, J. & Tamagaki, R. Chapter II. Typical Realization of Alpha-Particle Model Aspects in Beryllium Region. *Progress of Theoretical Physics Supplement* **52,** 25–88 (1972) (cit. on pp. 4, 6, 20).

26. Hoyle, F. On Nuclear Reactions Occuring in Very Hot STARS. I. the Synthesis of Elements from Carbon to Nickel. *The Astrophysical Journal Supplement Series* **1,** 121 (1954) (cit. on p. 4).

27. Cook, C. W., Fowler, W. A., Lauritsen, C. C. & Lauritsen, T. B^{12}, C^{12}, and the Red Giants. *Phys. Rev.* **107,** 508–515 (2 July 1957) (cit. on p. 4).

28. Freer, M. *et al.* 2^+ excitation of the ^{12}C Hoyle state. *Phys. Rev. C* **80,** 041303 (4 Oct. 2009) (cit. on p. 4).

29. Freer, M. & Fynbo, H. The Hoyle state in 12C. *Prog. Part. Nucl. Phys.* **78,** 1–23. ISSN: 0146-6410 (2014) (cit. on p. 4).

30. Epelbaum, E., Krebs, H., Lee, D. & Meißner, U.-G. *Ab Initio* Calculation of the Hoyle State. *Phys. Rev. Lett.* **106,** 192501 (19 May 2011) (cit. on p. 4).

31. Kanada-En'yo, Y. & Kimura, M. in *Clusters in Nuclei: Volume 1* (ed Beck, C.) 129–164 (Springer Berlin Heidelberg, Berlin, Heidelberg, 2010). ISBN: 978-3-642-13899-7. doi:10.1007/978-3-642-13899-7_4 (cit. on pp. 4, 15).

32. Marín-Lámbarri, D. J. *et al.* Evidence for Triangular $\mathcal{D}_{3h}$ Symmetry in ^{12}C. *Phys. Rev. Lett.* **113,** 012502 (1 June 2014) (cit. on pp. 4, 17, 20).

33. Epelbaum, E., Krebs, H., Lähde, T. A., Lee, D. & Meißner, U.-G. Structure and Rotations of the Hoyle State. *Phys. Rev. Lett.* **109,** 252501 (25 Dec. 2012) (cit. on p. 4).

34. Funaki, Y. *et al.* Alpha Cluster States and Condensation in ^{16}O. *Progress of Theoretical Physics Supplement* **196,** 439–444 (2012) (cit. on p. 4).

35. Merchant, A. C. & Rae, W. D. M. in *Atomic and Nuclear Clusters: Proceedings of the Second International Conference at Santorini, Greece, June 28 – July 2, 1993* (eds Anagnostatos, G. S. & von Oertzen, W.) 82–87 (Springer Berlin Heidelberg, Berlin, Heidelberg, 1995). ISBN: 978-3-642-79696-8. doi:10.1007/978-3-642-79696-8_19 (cit. on p. 4).

36. Ikeda, K., Takigawa, N. & Horiuchi, H. The systematic structure-change into the molecule-like structures in the self-conjugate 4n nuclei. *Progress of Theoretical Physics Supplement* **68,** 464–475 (1968) (cit. on pp. 4, 5).

37. Cobern, M. E., Pisano, D. J. & Parker, P. D. Alpha-transfer reactions in light nuclei. III. $(^7Li, t)$ stripping reaction. *Phys. Rev. C* **14,** 491–505 (2 Aug. 1976) (cit. on pp. 5, 16).

38. Richards, H. T. Rotational bands in ^{20}Ne. *Phys. Rev. C* **29,** 276–283 (1 Jan. 1984) (cit. on pp. 5, 20).

39. Kanada-En'yo, Y., Kimura, M. & Horiuchi, H. Antisymmetrized Molecular Dynamics: a new insight into the structure of nuclei. *C. R. Phys.* **4,** 497–520. ISSN: 1631-0705 (2003) (cit. on pp. 5–7, 15).

40. Buck, B., Johnston, J. C., Merchant, A. C. & Perez, S. M. Cluster model of α decay and ^{212}Po. *Phys. Rev. C* **53,** 2841–2848 (6 June 1996) (cit. on p. 6).

41. Wang, S. M., Pei, J. C. & Xu, F. R. Spectroscopic calculations of cluster nuclei above double shell closures with a new local potential. *Phys. Rev. C* **87,** 014311 (1 Jan. 2013) (cit. on p. 6).

42. Itagaki, N. & Okabe, S. Molecular orbital structures in ^{10}Be. *Phys. Rev. C* **61,** 044306 (4 Mar. 2000) (cit. on pp. 6, 20).

43. Freer, M. *et al. Cluster Structure of* ^{12}C *and* ^{11}Be in *AIP Conference Proceedings* **1165** (2009) (cit. on p. 6).

44. Freer, M. *et al.* Exotic Molecular States in ^{12}Be. *Phys. Rev. Lett.* **82,** 1383–1386 (7 Feb. 1999) (cit. on p. 6).

45. Milin, M. & Von Oertzen, W. Search for molecular bands in 13C. *The European Physical Journal A-Hadrons and Nuclei* **14,** 295–307 (2002) (cit. on p. 6).

46. Avila, M. L. *et al.* α-cluster structure of ^{18}O. *Phys. Rev. C* **90,** 024327 (2 Aug. 2014) (cit. on pp. 6, 18).

47. Von Oertzen, W. Covalently bound molecular structures in the α + ^{16}O. *Eur. Phys. J. A* **11,** 403–411. ISSN: 1434-6001 (2001) (cit. on p. 7).

48. Rogachev, G. V. *et al.* Doubling of α-cluster states in^{22}Ne. *Phys. Rev. C* **64,** 051302 (5 Oct. 2001) (cit. on p. 7).

49. Bender, M., Heenen, P.-H. & Reinhard, P.-G. Self-consistent mean-field models for nuclear structure. *Rev. Mod. Phys.* **75,** 121–180 (1 Jan. 2003) (cit. on p. 8).

50. Casten, R. in, 332 (Oxford University Press, 2001) (cit. on p. 9).

51. Firestone, R. B. & Shirley, V. S. *Table of Isotopes* 8^{th} *ed.* (John Wiley & Sons, 1996) (cit. on p. 11).

52. Strutinsky, V. Shell effects in nuclear masses and deformation energies. *Nucl. Phys. A* **95,** 420–442. ISSN: 0375-9474 (1967) (cit. on p. 10).

53. Leander, G. & Larsson, S. Potential-energy surfaces for the doubly even N = Z nuclei. *Nucl. Phys. A* **239,** 93–113. ISSN: 0375-9474 (1975) (cit. on pp. 10, 147).

54. Fulton, B. R. & Rae, W. D. M. Fission of light nuclei. *J. Phys. G: Nucl. Part. Phys.* **16,** 333 (1990) (cit. on p. 10).

55. Brink, D. in *Proceedings of the International School of Physics Enrico Fermi* (ed Bloch, C.) **36** (1965), 247 (cit. on p. 13).

56. Peierls, R. E. & Yoccoz, J. The Collective Model of Nuclear Motion. *Proc. Phys. Soc. London, Sect. A* **70,** 381 (1957) (cit. on p. 13).

57. Zhang, J. & Rae, W. Systematics of 2-dimensional α-cluster configurations in 4N nuclei from 12C to 44Ti. *Nucl. Phys. A* **564,** 252–270. ISSN: 0375-9474 (1993) (cit. on pp. 13, 14).

58. Zhang, J., Rae, W. & Merchant, A. Systematics of some 3-dimensional α-cluster configurations in 4N nuclei from 16O to 44Ti. *Nucl. Phys. A* **575,** 61–71. ISSN: 0375-9474 (1994) (cit. on p. 13).

59. Nagatani, K. *et al.* Alpha transfer reaction $^{16}\mathrm{O}(^{14}\mathrm{N},\ ^{10}\mathrm{B})^{20}\mathrm{Ne}$ and high-spin states in $^{20}\mathrm{Ne}$. *Phys. Rev. C* **14,** 2133–2137 (6 Dec. 1976) (cit. on pp. 15, 16).

60. Kurath, D. Alpha-Structure Amplitudes for the $1p$ Shell. *Phys. Rev. C* **7,** 1390–1395 (4 Apr. 1973) (cit. on p. 15).

61. Erskine, J. R., Henning, W., Kovar, D. G., Greenwood, L. R. & DeVries, R. M. Nonpeculiar Behavior of the $(^{16}\mathrm{O},\ ^{12}\mathrm{C})$ Transfer Reaction in the $s-d$ Shell. *Phys. Rev. Lett.* **34,** 680–683 (11 Mar. 1975) (cit. on p. 15).

62. Bethge, K. Alpha-Particle Transfer Reactions. *Annu. Rev. Nucl. Sci.* **20,** 255–288 (1970) (cit. on pp. 15, 16).

63. Thompson, I. J. & Nunes, F. M. *Nuclear Reactions for Astrophysics* ISBN: 9780521856355 (Cambridge University Press, 2009) (cit. on pp. 16, 38, 43, 45–47, 49, 50, 115, 153).

64. Cobern, M. E. & Parker, P. D. $^{14}\mathrm{N}(^{7}\mathrm{Li},\ t)^{18}\mathrm{F}$. *Phys. Rev. C* **15,** 1929–1932 (5 May 1977) (cit. on pp. 16, 57–59, 86).

65. Artemov, K. P. *et al.* Effective method of study of alpha-cluster states. *Sov. J. Nucl. Phys.* **52,** 408–411 (3 1990) (cit. on pp. 18, 22).

66. Norrby, M. *et al.* Highly excited alpha-cluster states in ^{34}S. *Eur. Phys. Jour. A* **47.** ISSN: 1434-6001. doi:10.1140/epja (June 2011) (cit. on pp. 18, 39, 52, 94, 150).

67. Norrby, M. *et al.* Elastic alpha-particle resonances as evidence of clustering at high excitation in ^{40}Ca. *Eur. Phys. Jour. A* **47.** ISSN: 1434-6001. doi:10.1140/epja (Aug. 2011) (cit. on pp. 18, 39, 52, 94, 119, 150).

68. Lonnroth, T. *et al.* Highly excited alpha-cluster states in ^{32}S studied with the thick-target inverse kinematics method. *Eur. Phys. Jour. A* **46,** 5–16. ISSN: 1434-6001 (Oct. 2010) (cit. on pp. 18, 39, 52, 94, 150).

69. Goldberg, V. Z. *et al.* Observation of an alpha-cluster structure in ^{36}Ar. *Phys. At. Nucl.* **63,** 1518–1526. ISSN: 1063-7788 (Sept. 2000) (cit. on pp. 18, 39, 52, 94, 150).

70. Norrby, M. *Alpha-cluster structures in medium light nuclei* PhD thesis (Abo Akademi University, 2011) (cit. on p. 18).

71. Freer, M. *et al.* Resonances in ^{11}C observed in the ^{4}He(^{7}Be, α)^{7}Be and ^{4}He(^{7}Be, p)^{10}B reactions. *Phys. Rev. C* **85,** 014304 (1 Jan. 2012) (cit. on p. 18).

72. Freer, M. *et al.* Resonances in ^{14}C observed in the ^{4}He(^{10}Be, α)^{10}Be reaction. *Phys. Rev. C* **90,** 054324 (5 Nov. 2014) (cit. on p. 18).

73. Hernández, A. H. *et al.* Proton resonance reactions using thick targets in inverse kinematics. *Nucl. Instrum. Methods Phys. Res., Sect. B* **143,** 569–574. ISSN: 0168-583X (1998) (cit. on p. 18).

74. Walshe, J. *Resonant scattering studies of ^{24}Mg and ^{28}Mg and the search for nuclear water* PhD thesis (School of Physics and Astronomy, University of Birmingham, 2016) (cit. on pp. 18, 32, 33, 39).

75. Lutz, G. *Semiconductor Radiation Detectors* (Springer-Verlag Berlin Heidelberg, 2007) (cit. on p. 24).

76. Semiconductor, M. *W1 Product Specification* http://www.micronsemiconductor.co.uk/pdf/w1.pdf, Accessed 01/09/2016. <http://www.micronsemiconductor.co.uk/pdf/w1.pdf> (cit. on p. 24).

77. Bethe, H. A. & Ashkin, J. in *Experimental Nuclear Physics* 166 (J. Wiley, 1953) (cit. on p. 24).

78. Ziegler, J. F. The Stopping Power of Energetic Light Ions in Elemental Matter. *J Appl. Phys / Rev. Appl. Phys.* **85,** 1249 –1272 (1999) (cit. on pp. 24–26).

79. Jones, E., Oliphant, T., Peterson, P., *et al. SciPy: Open source scientific tools for Python* [Online; accessed 2016-09-01]. 2001–. <http://www.scipy.org/> (cit. on pp. 26, 113).

80. Tarasov, O. & Bazin, D. LISE++: Radioactive beam production with in-flight separators. *Nucl. Instrum. Methods Phys. Res., Sect. B* **266.** Proceedings of the XVth International Conference on Electromagnetic Isotope Separators and Techniques Related to their Applications, 4657–4664. ISSN: 0168-583X (2008) (cit. on p. 26).

81. Weick, H. & Geissel, H. *ATIMA: Calculations of energy loss and straggling in matter* Lise documentation: http://lise.nscl.msu.edu/4_20/lise_4_20.html. Accessed: 04/09/2016 (cit. on p. 26).

82. Clarke, N. Energy spread in thin absorbers. *Nucl. Instrum. Methods* **96,** 497–503. ISSN: 0029-554X (1971) (cit. on p. 37).

83. Marion, J. & Zimmerman, B. Multiple scattering of charged particles. *Nucl. Instrum. Methods* **51,** 93–101. ISSN: 0029-554X (1967) (cit. on p. 37).

84. Curtis, N. & Walshe, J. REX: A Monte Carlo simulation of thick gas target resonant scattering reactions. *Nucl. Instrum. Methods Phys. Res., Sect. A* **797,** 44–56. ISSN: 0168-9002 (2015) (cit. on pp. 38, 95, 97).

85. Starck, J. L., Pantin, E. & Murtagh, F. Deconvolution in Astronomy: A Review. *Publ. Astron. Soc. Pac.* **114,** 1051 (2002) (cit. on p. 39).

86. Lane, A. M. & Thomas, R. G. R-Matrix Theory of Nuclear Reactions. *Rev. Mod. Phys.* **30,** 257 –353 (Apr. 1958) (cit. on pp. 41, 42).

87. Sakurambo. *Li6-D Reaction* http://en.wikipedia.org/wiki/File:Li6-D_Reaction.svg. Accessed Sept 2013. May 2007 (cit. on p. 41).

88. Kapur, P. L. & Peierls, P. K. The dispersion formula for nuclear reactions. *Proc. Roy. Soc. London A* **166,** 277–295 (1938) (cit. on p. 42).

89. Wigner, E. P. & Eisenbud, L. Higher Angular Momenta and Long Range Interaction in Resonance Reactions. *Phys. Rev.* **72,** 29–41 (1 1947) (cit. on p. 42).

90. Rutherford, E. The Scattering of α and β Particles by Matter and the Structure of the Atom. *Phil. Mag.* **21,** 669–688 (1911) (cit. on p. 45).

91. Morrison, C. A. in *Angular Momentum Theory Applied to Interactions in Solids* 19–23 (Springer Berlin Heidelberg, Berlin, Heidelberg, 1988). ISBN: 978-3-642-93376-9. doi:10.1007/978-3-642-93376-9_2 (cit. on p. 46).

92. Brune, C. R. Alternative parameterization of R-matrix theory. *Phys. Rev. C* **66** (2002) (cit. on p. 48).

93. Gurbich, A. F., Radovic, I. B., Siketic, Z. & Jaksic, M. Measurements and evaluation of the cross-section for helium elastic scattering from nitrogen. *Nucl. Instrum. Methods Phys. Res., Sect. B* **269,** 40–44. ISSN: 0168-583X (2011) (cit. on pp. 50, 60, 61, 79, 82–86).

94. Press, W. H., Teukolsky, S. A., Vetterling, W. T. & Flannery, B. P. *Numerical recipes in C* (Cambridge university press Cambridge, 1996) (cit. on p. 52).

95. Riedhauser, S. R. ^{20}Ne states observed via $^{16}\mathrm{O}(\alpha,\alpha_0)^{16}\mathrm{O}$ and $^{16}\mathrm{O}(\alpha,\alpha_1)^{16}\mathrm{O}$. *Phys. Rev. C* **29,** 1961–1979 (6 June 1984) (cit. on p. 52).

96. De Boer, R. J. *Azure2* University of Notre Dame (cit. on p. 53).

97. Azuma, R. E. *et al.* AZURE: An R-matrix code for nuclear astrophysics. *Phys. Rev. C* **81** (2010) (cit. on p. 53).

98. Rolfs, C. *et al.* Nuclear structure of ^{18}F. *Nucl. Phys. A* **199,** 257–350. ISSN: 0375-9474 (1973) (cit. on pp. 55, 57–59).

99. Middleton, R., Polsky, L. M., Holbrow, C. H. & Bethge, K. Hole-Particle States in ^{18}F. *Phys. Rev. Lett.* **21,** 1398–1401 (19 Nov. 1968) (cit. on pp. 56–59, 86, 87).

100. Arima, A., Horiuchi, H. & Sebe, T. Weak coupling model of particles and holes in the sd shell nuclei. *Phys. Lett. B* **24,** 129–131. ISSN: 0370-2693 (1967) (cit. on p. 56).

101. Benson, H. & Flowers, B. A study of deformation in light nuclei: (II). Application to the even-parity states of the mass-18 nuclei. *Nucl. Phys. A* **126,** 332–354. ISSN: 0375-9474 (1969) (cit. on p. 56).

102. Brink, D. Kinematical effects in heavy-ion reactions. *Phys. Lett. B* **40,** 37–40. ISSN: 0370-2693 (1972) (cit. on p. 56).

103. Bassichis, W. H., Giraud, B. & Ripka, G. Projected Hartree-Fock Spectra in Light Nuclei. *Phys. Rev. Lett.* **15,** 980–982 (25 Dec. 1965) (cit. on pp. 57–59).

104. Etchegoyen, M., Sinclair, D., Etchegoyen, A. & Moreno, E. Spin determination via α-d angular correlations and α-transfer {DWBA} analysis in 18F high-energy states. *Nucl. Phys. A* **402,** 87–113. ISSN: 0375-9474 (1983) (cit. on pp. 57–59).

105. Buck, B., Merchant, A. & Rowley, N. Semi-microscopic calculation of α-cluster states in 18F. *Nucl. Phys. A* **327,** 29–52. ISSN: 0375-9474 (1979) (cit. on pp. 58, 59, 86–89, 148).

106. Rutherford, E. Collision of α Particles with Light Atoms. IV. An Anomalous Effect in Nitrogen. *Phil. Mag.* **37,** 581 (1919) (cit. on p. 59).

107. Herring, D. F., Chiba, R., Gasten, B. R. & Richards, H. T. $N^{14}(\alpha,\alpha)N^{14}$ and $N^{14}(\alpha,p)O^{17}$ Differential Cross Sections. *Phys. Rev.* **112,** 1210–1216 (4 Nov. 1958) (cit. on p. 59).

108. Herring, D. F. Energy Levels of F^{18}. *Phys. Rev.* **112,** 1217–1224 (4 Nov. 1958) (cit. on pp. 59, 82, 84).

109. Seiler, R. F., Jones, C. H., Anzick, W. J., Herring, D. F. & Jones, K. W. The Elastic Scattering of Deuterons by ^{16}O from 0.65 to 2.0 MeV. *Nucl. Phys.* **45,** 647–656 (1963) (cit. on pp. 59, 68, 78, 79, 81, 89).

110. Sens, J. C., Refaei, S. M., Mohamed, A. B. & Pape, A. Search for simple configurations in ^{18}F. I. The $^{17}O(p,p)^{17}O$ reaction. *Phys. Rev. C* **16,** 2129–2134 (6 Dec. 1977) (cit. on p. 60).

111. Sens, J. C., Refaei, S. M. & Pape, A. *Phys. Rev. C* **18,** 2007–2016 (5 Nov. 1978) (cit. on pp. 60, 85, 87).

112. Kieser, W., Azuma, R. & Jackson, K. The ^{17}O(p, α)^{14}N reaction: Physics and astrophysics. *Nucl. Phys. A* **331,** 155–179. ISSN: 0375-9474 (1979) (cit. on pp. 60, 82, 84).

113. Terwagne, G., Genard, G., Yedji, M. & Ross, G. G. *J Appl. Phys.* **104,** 084909 (2008) (cit. on pp. 60, 68, 78, 80, 83, 84, 89).

114. Parker, D. Private Communication. University of Birmingham. 2013 (cit. on pp. 61, 158).

115. Global, Q. *Alpha spectrometry sources reference* http://www.hightechsource.co.uk/Resources/Alpha.pdf. Accessed: September 2013 (cit. on p. 63).

116. Tilley, D., Weller, H., Cheves, C. & Chasteler, R. Energy levels of light nuclei A = 18–19. *Nucl. Phys. A* **595,** 1–170. ISSN: 0375-9474 (1995) (cit. on pp. 82, 84, 85).

117. Yasue, M. *et al.* Spectroscopic study of oxygen and fluorine isotopes with the $(\alpha$,3He) and $(\alpha$,t) reactions on O16,17,18. *Phys. Rev. C* **46,** 1242–1256 (4 Oct. 1992) (cit. on p. 86).

118. Rolfs, C., Charlesworth, A. & Azuma, R. Nuclear structure of ^{18}F: (I). Radiative capture experiments. *Nucl. Phys. A* **199,** 257–273. ISSN: 0375-9474 (1973) (cit. on p. 87).

119. Ohkubo, S. *Alpha-clustering and molecular structure of medium-weight and heavy nuclei* (Publication Office, Progress of Theoretical Physics, 1998) (cit. on pp. 91, 93).

120. Ohkubo, S., Hirabayashi, Y. & Sakuda, T. α-cluster structure of ^{44}Ti in core-excited $\alpha+^{40}$Ca model. *Phys. Rev. C* **57,** 2760–2762 (5 May 1998) (cit. on pp. 91–93, 143–147).

121. Kimura, M. & Horiuchi, H. Coexistence of cluster structure and superdeformation in ^{44}Ti. *Nucl. Phys. A* **767,** 58–80. ISSN: 0375-9474 (2006) (cit. on pp. 91, 92).

122. Artemov, K. P., Golovkov, M. S., Pankratov, V. V. & Rudakov, V. P. *Phys. At. Nucl.* **58,** 177 (1995) (cit. on pp. 92, 93).

123. Yamaya, T. *et al.* Existence of α-cluster structure in ^{44}Ti via the (^{6}Li, *d*) reaction. *Phys. Rev. C* **42,** 1935–1944 (5 Nov. 1990) (cit. on p. 92).

124. Frekers, D., Santo, R. & Langanke, K. Identification of quasimolecular resonances in low energy a-40Ca scattering and effects of compound nucleus excitation. *Nucl. Phys. A* **394,** 189–220. ISSN: 0375-9474 (1983) (cit. on pp. 92–94, 104).

125. Frekers, D. *et al.* Resonances in low energy40Ca(α,α)-scattering and quasimolecular band in44Ti. *Zeitschrift für Physik A Atoms and Nuclei* **276,** 317–324. ISSN: 0939-7922 (1976) (cit. on pp. 92, 93).

126. Michel, F., Reidemeister, G. & Ohkubo, S. Molecular interpretation of the oscillations of the fusion excitation function for the $\alpha+^{40}$Ca system. *Phys. Rev. C* **34,** 1248–1255 (4 Oct. 1986) (cit. on pp. 92, 93).

127. Rahman, M. A., Mecking, M. & Strohbusch, U. (6Li, d) reaction on sd-, fp- andg-shell nuclei in ZR- and FR-DWBA formalisms. *Il Nuovo Cimento A (1965-1970)* **105,** 859–864. ISSN: 1826-9869 (1992) (cit. on p. 93).

128. Fulbright, H. *et al.* Four-nucleon transfer via the (6Li, d) reaction. *Nucl. Phys. A* **284,** 329–364. ISSN: 0375-9474 (1977) (cit. on p. 93).

129. Fukada, M., Takimoto, M. K., Ogino, K. & Ohkubo, S. α cluster states in ^{44,46,52}Ti. *Phys. Rev. C* **80,** 064613 (6 Dec. 2009) (cit. on p. 93).

130. Van den Berg, J. C. *Wavelets in Physics* Paperback edition. ISBN: 0521533538 (Cambridge University Press, 2004) (cit. on pp. 94, 104, 105, 108).

131. National de physique nucleaire et de physique des particules, I. *The GANIL Cyclotrons* `sfp.in2p3.fr/accelerateur/cours/GANIL-CYCLOTRONS-corrected-reduit.doc`. Accessed: 5/9/2016 (cit. on pp. 95, 158).

132. Kalmykov, Y. *et al.* Fine Structure of the Gamow-Teller Resonance in ^{90}Nb and Level Density of 1^+ States. *Phys. Rev. Lett.* **96,** 012502 (1 Jan. 2006) (cit. on pp. 104, 150).

133. Shevchenko, A. *et al.* Fine Structure in the Energy Region of the Isoscalar Giant Quadrupole Resonance: Characteristic Scales from a Wavelet Analysis. *Phys. Rev. Lett.* **93,** 122501 (12 Sept. 2004) (cit. on pp. 104, 150).

134. Wasaka, T. *et al.* New candidate for an alpha cluster condensed state in ^{16}O(α,α') at 400 MeV. *Phys. Lett. B* **653,** 173 (2007) (cit. on p. 104).

135. Arfken, G. B., Weber, H. J. & Harris, F. E. *Mathematical methods for physicists: a comprehensive guide* (Academic press, 2011) (cit. on p. 108).

136. Bjørnholm, S. & Lynn, J. E. The double-humped fission barrier. *Rev. Mod. Phys.* **52,** 725–931 (4 Oct. 1980) (cit. on pp. 111, 118, 121, 140).

137. Vandenbosch, R. & Huizenga, J. R. *Nuclear Fission* ISBN: 0127108505 (Academic Press, 1973) (cit. on p. 113).

138. Brody, T. A. *et al.* Random-matrix physics: spectrum and strength fluctuations. *Rev. Mod. Phys.* **53,** 385–479 (3 July 1981) (cit. on pp. 114, 116, 168).

139. Porter, C. E. & Thomas, R. G. *Phys. Rev.* **104** (1956) (cit. on pp. 115, 118).

140. Moore, M. S. & Reich, C. W. *Phys. Rev.* **118** (1960) (cit. on p. 115).

141. Wigner, E. P. Random Matrices in Physics. English. *SIAM Rev.* **9,** 1–23. ISSN: 00361445 (1967) (cit. on p. 115).

142. Lane, A., Lynn, J. & Moses, J. Line shape in weak and intermediate coupling: Theory and practical fitting procedures. *Nucl. Phys. A* **232,** 189–199. ISSN: 0375-9474 (1974) (cit. on p. 118).

143. Apté, C. & Weiss, S. Data Mining Data mining with decision trees and decision rules. *Future Generation Computer Systems* **13,** 197–210. ISSN: 0167-739X (1997) (cit. on p. 124).

144. Milborrow, S. *CART tree titanic survivors* Wikipedia Commons Image, https://commons.wikimedia.org/wiki/File:CART_tree_titanic_survivors.png. License: Creative Commons Attribution-Share Alike 3.0 Unported, Accessed: 25/08/2016 (cit. on p. 125).

145. Buntine, W. & Niblett, T. A Further Comparison of Splitting Rules for Decision-Tree Induction. *Machine Learning* **8,** 75–85. ISSN: 1573-0565 (1992) (cit. on p. 125).

146. Dietterich, T. Overfitting and Undercomputing in Machine Learning. *ACM Comput. Surv.* **27,** 326–327. ISSN: 0360-0300 (Sept. 1995) (cit. on pp. 125, 126).

147. Liaw, A. & Wiener, M. Classification and regression by randomForest. *R news* **2,** 18–22 (2002) (cit. on p. 125).

148. Pedregosa, F. *et al.* Scikit-learn: Machine Learning in Python. *Journal of Machine Learning Research* **12,** 2825–2830 (2011) (cit. on pp. 126, 130, 149).

149. Negri, L. H. *PeakUtils* Python Package, https://pypi.python.org/pypi/PeakUtils. License: MIT, Date Accessed: 01/09/2016 (cit. on p. 126).

150. Refaeilzadeh, P., Tang, L. & Liu, H. in *Encyclopedia of Database Systems* (eds LIU, L. & ÖZSU, M. T.) 532–538 (Springer US, Boston, MA, 2009). ISBN: 978-0-387-39940-9. doi:10.1007/978-0-387-39940-9_565 (cit. on p. 128).

151. Jin, Y. *Multi-objective machine learning* (Springer Science & Business Media, 2006) (cit. on p. 129).

152. Batista, G. E.A.P. A., Prati, R. C. & Monard, M. C. A Study of the Behavior of Several Methods for Balancing Machine Learning Training Data. *SIGKDD Explor. Newsl.* **6,** 20–29. ISSN: 1931-0145 (June 2004) (cit. on p. 129).

153. Soylu, A. Private Communication. Niğde University, Turkey. 2015 (cit. on p. 143).

154. Pei, J. C. & XU, F. R. *Phys. Lett. B* **650,** 224 (2007) (cit. on p. 143).

155. Coban, A., Bayrak, O., Soylu, A. & Boztosun, I. *Phys. Rev. C* **85,** 044324 (2012) (cit. on p. 143).

156. Kotsiantis, S. B. Supervised machine learning: a review of classification techniques. *Emerging Artificial Intelligence Applications in Computer Engineering* (2007) (cit. on p. 150).

157. Curtis, N. Private Communication. University of Birmingham. 2015 (cit. on p. 156).

158. Wolfram|Alpha. Wolfram Alpha LLC, https://www.wolframalpha.com. Date accessed: 3/9/2016 (cit. on p. 170).